Characterisation of manganese alloy antiferromagnetic materials for property screening and for heterostructure effects

Ieuan Rhys Wilkes, MPhys (Oxon.)

PhD

University of York

Physics, Engineering and Technology

October 2024

Abstract

Faster, more efficient electronic devices are in constant demand in computing. Increasing climate change pressure makes energy efficiency paramount in modern technology. Current materials research includes investigation into spintronics to reduce energy usage and increase switching speed in memory technology. To increase device density, antiferromagnetic materials, with zero magnetization meaning resistance to external magnetic fields, are used. Antiferromagnetic spin orbit torque devices are considered excellent candidates for spintronic memory bits. Antiferromagnetic materials are explored in this thesis using ab-initio density functional theory to predict material properties, including structural, electronic and magnetic properties like magnetocrystalline anisotropy. Properties of several Mn-alloy collinear $L1_0$ and noncollinear $L1_2$ and $D0_{19}$ antiferromagnets were calculated. The magnetocrystalline anisotropy energy calculated for noncollinear antiferromagnets is restricted to specific high symmetry planes. Calculations show Mn-Ir alloys' immense magnetocrystalline anisotropy with 4.187 meV/FU and 6.26 meV/FU for $L1_0$ and $L1_2$ Mn-Ir, indicating these Mn-Ir alloys are materially and energetically efficient antiferromagnets for use in spintronic devices.

We investigate straining effects on $D0_{19}$ materials, finding distinct structural and magnetic property changes under ±6% (001) planar expansion strain. Weyl points appear consistently, shifting within $D0_{19}$ strained materials, by 0.22 eV in Mn_3Ge. This consistency maintains the electron mobility, maintaining switching speeds. We determine Weyl points are conserved in $D0_{19}$ antiferromagnets Mn_3Ge and Mn_3Sn.

We determined interface effects on $D0_{19}$ noncollinear antiferromagnets, including charge density changes, projected density of states, structural effects and electronic properties, characterising surfaces and platinum interfaces. We calculate Mn_3Ga surface magnetic moments cant significantly, to 44.66° , and platinum interface charge transfer of 1.795 e for Sn in Mn_3Sn, indicating major charge polarization at the interface. We see changes to manganese density of states by 0.4 eV at platinum interfaces, likely due to heterostructure straining. We conclude significant charge transfer helps stabilise interfaces magnetically, resulting in altered conductivity.

Declaration

I declare that this thesis is a presentation of original work and I am the sole author. This work has not previously been presented for an award at this, or any other, University. All sources are acknowledged as references.

"Ninety percent of most magic merely consists of knowing one extra fact." - Sir Terry Pratchett, *Night Watch*

Acknowledgements

Formal acknowledgements

To my supervisor, Professor Keith McKenna; I would like to extend my heartfelt thanks for all the support and guidance you have provided, going above and beyond to accommodate me under unusual and trying circumstances. I'd also like to thank Professor Jacek Dobaczewski and Dr. Aires Ferreira for their assistance as part of my thesis advisory panel. To Dr. Joseph Barker, I extend my thanks for his diligent cooperation with regard to research, for the use of his very effective program, JAMS, and for his intriguing questions during my first conference presentation. This work made use of the UK national high-performance computing service, ARCHER2. Access to ARCHER2 was granted as a part of the McKenna Materials Modelling Group, under their membership to the UK HPC Materials Chemistry Consortium founded by the EPSRC (EP/F067496 and EP/R029431 respectively), of whom I'd also like to thank. The University of York's VIKING cluster computing services were also used, and I am grateful for their support.

Informal acknowledgements

To my family; thank you for your love and support. You've helped me to get through the difficult times, and I will always be grateful to you for that. To my friends, thank you for the humour and experiences you have given me; I've become a better person because of you. To Tom and Alex especially, thank you for your support and for the fun chats in the office. To Spectrum First; thank you for focusing me on a healthy and better-organised path, it has helped me to become a more confident person.

Contents

Abstract I

Declaration II

Acknowledgements IV

List of Figures VIII

List of Tables XIV

1 Introduction 1
- 1.1 Introduction to spintronics 1
- 1.2 MRAM devices 2
- 1.3 Mn-based AFM materials 5
- 1.4 Computational modelling 6
- 1.5 Aims and objectives 10
- 1.6 Outline of thesis structure 11

2 Theory 12
- 2.1 Introduction 12
- 2.2 Schrödinger equation 14
  - 2.2.1 Schrödinger equation for many particle systems 14
  - 2.2.2 Born-Oppenheimer approximation and the Schrödinger equation 15
- 2.3 The theoretical basis of density functional theory 15
  - 2.3.1 Hartree-Fock method 15
  - 2.3.2 Hohenberg-Kohn 17
  - 2.3.3 Kohn-Sham 18
  - 2.3.4 Exchange-correlation functionals 20
  - 2.3.5 Generalized gradient approximation 21
  - 2.3.6 DFT with Hubbard U 22

2.3.7 Crystal structure 24
2.3.8 Born von Karman boundary conditions and Bloch's theorem 25
2.4 Computational implementation of density functional theory 25
2.4.1 Plane-wave basis set and k-point sampling 25
2.4.2 PAW methodology and Pseudopotentials 28
2.4.3 Spin-orbit coupling and noncollinear calculations 29
2.4.4 Band structure 31
2.5 Magnetism 32
2.5.1 Exchange interaction 33
2.5.2 Magnetic order 34
2.5.3 Temperature effects 35
2.5.4 Noncollinear antiferromagnets 36
2.5.5 Anisotropy 37
2.5.6 Magnetic dipole contributions 40
2.5.7 Magnetic frustration and Dzyaloshinskii-Moriya interactions 41
2.6 Summary 43

3 Collinear Mn-alloy antiferromagnetic materials 45
3.1 Introduction 45
3.2 Previous experimental results 47
3.3 Previous theoretical results 50
3.4 Structure and magnetic properties 53
3.4.1 Supercell for calculation 53
3.4.2 U-value and functional 54
3.4.3 Calculated properties of $\mathbf{L1}_0$ materials 56
3.4.4 Magnetic anisotropy 59
3.5 Discussion 62
3.5.1 Sources of inaccuracy 64
3.6 Conclusions 66

4 Noncollinear antiferromagnetic Mn-alloy materials 69
4.1 Introduction 69
4.2 Methods 75
4.3 Previous experimental results 78
4.3.1 $\mathbf{L1}_2$ materials 78
4.3.2 $\mathbf{D0}_{19}$ materials 80
4.4 Previous theoretical results 83

4.4.1 **L1**$_2$ Mn-alloys 83
4.4.2 **D0**$_{19}$ Mn-alloys 83
4.5 Results 86
4.5.1 Structure, magnetic and bulk properties 86
4.5.2 Strain and band structure 89
4.6 Discussion 95
4.6.1 Sources of inaccuracy 99
4.7 Conclusion 99

5 Interface effects on antiferromagnets 101
5.1 Introduction 101
5.2 Theory and methodology 103
5.2.1 Surface energy 103
5.2.2 Magnetic moment alignment 104
5.2.3 Bader charge analysis 105
5.2.4 Projected density of states 106
5.3 Previous experimental and theoretical data 106
5.4 Results 108
5.4.1 Layer optimisation at the surface 108
5.4.2 Magnetic and electronic effects at the surface 117
5.4.3 Randomised magnetic moments at the surface 129
5.4.4 Comparison of substrate interfaces 131
5.5 Discussion 135
5.5.1 Sources of inaccuracy 142
5.6 Conclusion 143

6 Conclusion 146

Acronyms 151

Bibliography 154

List of Figures

1.1 A Simple STT-AFM magnetic memory. The write spin current can reorient the magnetic configuration in accordance to its polarization, which alters the resistance state of the device. 5

1.2 The three major groups of materials, based on Strukturbericht notation. a) $L1_0$, b) $L1_2$, and c) $D0_{19}$, all shown in the (001) plane 7

2.1 MnGa in the ferromagnetic state will have varying magnetic moment with U. The dashed line provides a guide to the eye. 23

2.2 A monoclinic Bravais lattice, illustrating the structural parameters a, b, c, α, β and γ that define the Bravais lattices 24

2.3 2D k-point sampling grid over a square Brillouin zone, the extent of which is $\frac{2\pi}{a}$, where a is the lattice spacing. The Γ-point is the k-point where $\mathbf{k} = (0, 0, 0)$ 27

2.4 The approximation of the pseudopotential as a function of r. r_c is the cutoff radius under which the approximation is no longer valid. Here, the dashed lines represent pseudopotential wavefunctions and potentials ψ_{PS} and V_{PS}. 28

2.5 3D representation of noncollinearity. The red arrows represent the canting magnetic moments. 31

2.6 Band structures calculated using generalized gradient approximation (GGA) for a) silicon, a semiconductor, b) platinum, a transition metal. 32

2.7 Band structure for $L1_2$-Mn_3Ir over a range of 2 eV. Note the x-axis contains four high-symmetry k-points. 33

2.8 The Néel temperature T_N, shown here as a point on a magnetic susceptibility vs temperature graph. 37

2.9 A hexagonal noncollinear antiferromagnetic arrangement. The magnetic moments lie in-plane with differing angles. 38

2.10 a) A hexagonal system with the easy axis labelled, b) the minimum energies of the system, known as an “easy cone” 39

2.11 a) A three-component triangular antiferromagnet, b) the according magnetic moments 42
2.12 The magnetic ordering of bulk Mn_3Ge. The purple atoms represent manganese, the grey atoms represent germanium 44

3.1 The various magnetic configurations investigated. From top left, clockwise; a) A-phase antiferromagnetic, b) C-phase antiferromagnetic, c) G-phase antiferromagnetic, d) ferromagnetic 46
3.2 An example of the unit cell we use. Collinear $L1_0$-MnIr unit cell complete with ground-state magnetic moment vectors on display. Purple atoms represent Mn, green atoms represent Ir 52
3.3 Calculated properties of $L1_0$ MnGa using different functionals and Hubbard U values. a, b) Lattice parameters for various functionals, where the blue line represents the experimental a lattice parameter and the gold line represents the experimental c lattice parameter. c, d) Magnetic moments for various functionals, where the red line is the experimental magnetic moment. e, f) the MAE magnitude, where the red line is the experimental MAE. 55
3.4 Calculated magnetic ordering of $L1_0$ MnGa using different U values, in this example using PBEsol as a GGA. Positive values indicate higher-energy ordering than the FM configuration. 56
3.5 Calculated spin-orbit contribution of the magnetic anisotropy of $L1_0$ MnIr and MnPt within a supercell of eight primitive cells, where theta (θ) represents the angle away from the perpendicular to [001], and phi (ϕ) the angle from [100] 59
3.6 Total density of states for MnIr. We note the effect of simulating spin-orbit coupling (SOC) effects has small but significant changes to the density of states, in particular shifting peaks. 65

4.1 Magnetic moment configuration for $L1_2$ Mn_3Ir a) viewed from the side b) viewed along [1-11]. The green atoms are Ir, and the purple atoms are Mn. 70
4.2 a) Atomic configurations for Mn_3Ga, Mn_3Ge and Mn_3Sn, where purple atoms are the Mn atoms and the grey atoms are the Ga/Ge/Sn (inset; magnetic moment configuration), b) a magnetic moment configuration of such alloys rotated by 150°, where the purple atoms are the Mn and the grey atoms are the Ga/Ge/Sn. 72

4.3 Rotation of magnetic moments about the [1-11] axis for Mn_3Ir: a) 0°, b) 90° anticlockwise, c) 180° anticlockwise. The green atoms are Ir, and the purple atoms are Mn. 76

4.4 Example of the effect of the rotation of the quantization axis in-plane for Mn_3Ir. 77

4.5 Mn_3Ir simulated structure with magnetic moments, positioned along the [1-11] axis. 86

4.6 Mn_3Ga simulated structure with magnetic moments, viewed in the (001) plane. The green atoms are Ga, the purple atoms are Mn. . 88

4.7 Mn_3Ge simulated structure with magnetic moments, viewed in the (001) plane. The grey atoms are Ge, the purple atoms are Mn. . 88

4.8 Mn_3Sn simulated structure with magnetic moments, viewed in the (001) plane. The grey atoms are Sn, the purple atoms are Mn. . 89

4.9 Variation of magnetic moment with strain for the $D0_{19}$ materials. 91

4.10 Energy of formation trends and c lattice parameter variation for strained $D0_{19}$ materials a,b) Mn_3Ga, c,d) Mn_3Ge, e,f) Mn_3Sn. . . 92

4.11 Band structures for various strains and materials. The red circles indicate the Weyl points present in these band structures. 94

5.1 Randomisation procedure for magnetic moments within a limit. a) vector sum of random vector (gold) and bulk moment (red), with resultant moment (blue). b) new moment rescaled to correct magnitude in limited region, θ; in this work, θ is limited to ±16°. 105

5.2 Projected density of states of Mn_3Ge in bulk. The density of states is broken down into the various electronic cloud contributions for Mn and Ge. As can be seen in the figure, the largest contribution to the density of states is the Mn d-cloud. 107

5.3 Mn_3Sn, (100)-A, with two surfaces exposed to vacuum. The grey atoms represent Sn, and the purple atoms represent Mn 109

5.4 The change in thickness, marked by a red arrow, at the surface over each layer for the (001)-Mn_3Sn termination. The ellipsis indicates continuation of the supercell. 110

5.5 The surface terminations for the $D0_{19}$ materials with Mn_3Sn used as an example. a) and b) are the (100) terminations, respectively called (100)-A and (100)-B, c) and d) are the (010) terminations, labelled (010)-A and (010)-B respectively, and e) is the (001) termination, called A. The grey ellipsis indicates the continuation of the supercell of atoms and the green box indicates the surface layer. 111

5.6 Mn_3X slabs with (001) surfaces, pictured in the (100) plane to show surfaces from the side, to observe the displacement from the surface. a) Mn_3Ga, where the green atoms represent Ga, b) Mn_3Ge, where the dark grey atoms represent Ge, c) Mn_3Sn, where the light grey atoms represent Sn. Purple atoms represent Mn. The grey ellipsis indicates the continuation of the supercell of atoms and the green box indicates the surface layer. 112
5.7 The variation of the chemical potential μ with the surface termination and Mn-richness on the (100)-Mn_3Ga surface. The blue region indicates the stable chemical potential values. a) the variation in the chemical potential in Ga, b) the variation in chemical potential for Mn. 113
5.8 Mn_3X slabs with (100) surfaces, pictured in the (001) plane to show surfaces from the side, to observe the displacement from the surface. a) Mn_3Ga (100)-A, b) Mn_3Ga (100)-B, c) Mn_3Ge (100)-A, d) Mn_3Ge (100)-B, e) Mn_3Sn (100)-A, f) Mn_3Sn (100)-B. Grey atoms represent Ga, Ge and Sn, purple atoms represent Mn. The grey ellipsis indicates the continuation of the supercell of atoms and the green box indicates the surface layer. 114
5.9 Mn_3X slabs with (010) surfaces, pictured in the (001) plane to show surfaces from the side, to observe the displacement from the surface. a) Mn_3Ga (010)-A, b) Mn_3Ga (010)-B, c) Mn_3Ge (010)-A, d) Mn_3Ge (010)-B, e) Mn_3Sn (010)-A, f) Mn_3Sn (010)-B. The grey ellipsis indicates the continuation of the supercell of atoms and the green box indicates the surface layer. Green atoms represent Ga, grey atoms represent Ge/Sn, and purple atoms represent Mn. 115
5.10 The angles θ and ϕ used to describe the canting of magnetic moments, projected onto a (001) Mn_3X surface. The green arrow is an example of a magnetic moment with significant variation in θ and ϕ, where the green dashed lines illustrate the displacement. . 117
5.11 PDOS graphs in the (001) direction. a) Mn_3Ga, b) Mn_3Ge, c) Mn_3Sn. The red boxes indicate the regions of interest for PDOS analysis, due to the peaks contained within. 119

5.12 The magnetic moments and PDOS selection regions for Mn_3X alloys along the (001) direction. a) Mn_3Ga, b) Mn_3Ge, c) Mn_3Sn. The grey ellipsis indicates the continuation of the supercell of atoms. The gold box represents the surface layer, and the blue box represents the bulk layer. 120
5.13 Bader charge deviation from bulk average for the Ga atoms within the (001) surface slab. 120
5.14 The PDOS of the Mn_3Ga (100) surface in comparison to the bulk for a) (100)-A and b) (100)-B. The red boxes indicate the regions of interest for PDOS analysis, due to the peaks contained within. 122
5.15 The magnetic moments and PDOS selection regions for Mn_3X alloys along the (100) direction. a) Mn_3Ga (100)-A, b) Mn_3Ga (100)-B, c) Mn_3Ge (100)-A, d) Mn_3Ge (100)-B, e) Mn_3Sn (100)-A, f) Mn_3Sn (100)-B. The grey ellipsis indicates the continuation of the supercell of atoms. The gold box represents the surface layer next to vacuum, and the blue box represents the bulk layer. The grey atoms represent Ga. Ge and Sn. The purple atoms represent Mn. The surfaces for secondary materials (X) with the same chemical group have similar surface magnetization formation angles, indicating surface canting has some direct dependence on the group electronic structure. 123
5.16 The PDOS of the Mn_3Ga (010) surface in comparison to the bulk for a) (010)-A and b) (010)-B. The red boxes indicate the regions of interest for PDOS analysis, due to the peaks contained within. 124
5.17 The magnetic moments and PDOS selection regions for Mn_3X alloys along the (010) direction. a) Mn_3Ga (010)-A, b) Mn_3Ga (010)-B, c) Mn_3Ge (010)-A, d) Mn_3Ge (010)-B, e) Mn_3Sn (010)-A, f) Mn_3Sn (010)-B. The grey ellipsis indicates the continuation of the supercell of atoms. The gold box represents the surface layer next to vacuum, and the blue box represents the bulk layer. 125
5.18 The PDOS of Mn_3Ge's (100) surface in comparison to the bulk for a) (100)-A and b) (100)-B. The red boxes indicate the regions of interest for PDOS analysis, due to the peaks contained within. . . 125
5.19 The PDOS of Mn_3Ge's (010) surface in comparison to the bulk for a) (010)-A and b) (010)-B. The red boxes indicate the regions of interest for PDOS analysis, due to the peaks contained within. . . 126

5.20 The PDOS of Mn_3Sn's (100) surface in comparison to the bulk for a) (100)-A and b) (100)-B. The red boxes indicate the regions of interest for PDOS analysis, due to the peaks contained within. . . 128
5.21 The PDOS of Mn_3Sn's (010) surface in comparison to the bulk for a) (010)-A and b) (010)-B. The red boxes indicate the regions of interest for PDOS analysis, due to the peaks contained within. . . 129
5.22 Example of 30%, or up to 16° randomized magnetic moment at the surface of a (100) Mn_3Sn slab. The moments in the gold circles are those that are randomized. The grey ellipsis indicates the continuation of the supercell of atoms. 130
5.23 Platinum density of states (DOS). We can see the most significant region of this density of states exists below 0 eV. 132
5.24 Translations of the $D0_{19}$ (purple and grey atoms) materials relative to platinum (white). a) the zero translation configuration, I. b) configuration II and c) configuration III, translations along the b-direction. d) configuration IV and e) configuration V along the a-direction. 133
5.25 The Mn-PDOS graphs of the $D0_{19}$ materials interfacing with platinum. a) is Mn_3Ga, b) is Mn_3Ge, and c) is Mn_3Sn. The red boxes indicate regions of interest for PDOS analysis, due to the peaks contained within. 134
5.26 Magnetic moments and PDOS regions for the Pt-Mn_3X heterostructure models. a) Mn_3Ga (green and purple atoms), b) Mn_3Ge (grey and purple atoms), c) Mn_3Sn (grey and purple atoms). The gold boxes represent the PDOS bulk region within the Mn_3X material, and the green boxes represent the PDOS interface region for the Mn_3X material. 134

List of Tables

3.1 Experimentally determined properties of $L1_0$ Mn-alloys including lattice parameters, magnetic structure, and MAE. 47
3.2 Theoretical parameters for $L1_0$ Mn-alloys, including lattice parameters, magnetic structure, and MAE. 50
3.3 Results for structural and magnetic properties with comparison to the relevant experimental values 57
3.4 SOC anisotropy results and DAE contributions for the calculations, with comparison to reference data 61
3.5 Comparison of the structural parameters of each of the materials in this chapter compared to experimental and theoretical parameters 62
3.6 Comparisons of the magnetic moments of experimental and theoretical literature vs. the calculated results 63
3.7 Comparisons of the magnetic anisotropy energy (MAE) of experimental and theoretical literature vs. the calculated results 64

4.1 Experimental parameters for $L1_2$ and $D0_{19}$ materials, including lattice parameters, magnetic structure and plane where magnetic moments are flat, and MAE. 79
4.2 Theoretical parameters for $L1_2$ Mn-alloys, including lattice parameters, magnetic structure and plane where magnetic moments are parallel, and MAE. 84
4.3 Calculated parameters for $D0_{19}$ materials, including lattice parameters, magnetic structure, and MAE 87
4.4 Calculated parameters for $D0_{19}$ materials under strain, extracting data from Figure 4.10. The resultant amplitude of the energy of formation, the energy of formation minimum of the strain and the c-lattice parameter at the minimum are given to elucidate on the primary effects of the strain. 92
4.5 Comparison of the structural parameters of each of the materials in this chapter compared to experimental and theoretical parameters 95

4.6 Comparisons of the magnetic moments and MAE of experimental and theoretical literature vs. the calculated results 96

5.1 Summary of the data from previous experimental and theoretical studies 107
5.2 Expansion length for the first three layers of each material and surface. 110
5.3 Calculated results for structural and magnetic properties of the $D0_{19}$ materials 115
5.4 Angular deviation at the surfaces from bulk. 118
5.5 Bader charge variation for the differing terminations of surfaces . 121
5.6 Bader charge difference at the interface with platinum, where metal X represents Ga, Ge and Sn. 135
5.7 Angular deviation at the interface with platinum. 136
5.8 Comparison of charge transfer effects for the (001)-direction material surfaces and iterfaces with platinum. 137

Chapter 1

Introduction

1.1 Introduction to spintronics

Spintronics, a technology utilising both the intrinsic spin and charge of an electron for device functionality as opposed to only charge, is a relatively new avenue of research [1]. Initial spintronics research began in the 1970s [2]. The major discoveries to facilitate spintronic applications occurred in the 1980s; injection of a spin-polarized current between ferromagnetic and normal metals [3] as well as the discovery of giant magnetoresistance, the property of a material defining the change of its electrical resistance within an external magnetic field [4, 5]. Modern technologies based on spintronics include hard drive read heads, which use giant and tunnelling magnetoresistance effects to read the data by measuring resistance across the read head, and magnetoresistive random access memory (MRAM) devices, which use ferromagnet based magnetic tunnel junctions [6].

The change from resistive charge-based devices to purely spin-based devices would deliver a large increase in energy efficiency by reducing losses to electrical resistance, resulting in the general improvement overall for a device using this type of architecture in terms of energy usage [7]. This is beneficial to both the reduced environmental contribution by information and communication technology industries to global climate change and to costs of processing and storage, the former of which continues to increase [8].

Silicon integrated spintronic devices have many explicit benefits over equivalent integrated silicon devices that make them favourable to research. One of the most extreme advantages is the switching speed increase from silicon architecture to spintronic architecture, increasing switching speed from 0.5 THz to well over 1 THz speed [9, 10, 11]. This massive improvement in switching speed is thanks to the rapid nature of spin fluctuations, which progresses extremely quickly compared to charge dynamics. This would result in significant improvements in computational switching speeds and thus faster processing capability.

Alongside ferromagnetic materials in devices, there is a newer form of spintronic technology that focuses on antiferromagnetic materials [10]. These materials, whilst more complex to measure experimentally due to the antiferromagnet producing no resultant magnetization, are more likely to be useful in dense networks of devices due to their minimal stray fields and insensitivity to external fields [12, 13]. As such, investigation into antiferromagnetic spintronic devices, particularly the antiferromagnetic materials, may provide increased advantages over ferromagnetic devices in future computation architecture [14]. We acknowledge that a large array of materials and methods are used in this research, and take particular notice of the rare nature of components of several popular candidate alloys such as MnPt and MnIr. Being able to find less materially costly alloys would be of great benefit, both economically and environmentally, and is an ongoing aspect of research.

Alongside this, the low magnetic field sensitivity of antiferromagnetic spintronic systems is highly advantageous. Due to the high field resistance of antiferromagnetic systems, on local scales these devices will not interfere with adjacent devices, making the potential density of spintronic devices very high compared to silicon and ferromagnet-based spintronic devices [15, 7]. The resistance to external magnetic fields also brings significant benefits, drastically improving the retention of data in memory devices and permitting the realisation of high-field applications.

1.2 MRAM devices

Many differing spintronic technologies are on the market currently. We focus here on memory devices, as these are currently one of the largest potential commercial applications for spintronic devices. We will specifically discuss the architecture of the most common spintronic memory device in production, MRAM, in order to highlight current capabilities. We will also highlight improvements the antiferromagnetic spintronic devices can provide.

MRAM is based on magnetoresistive phenomena, specifically tunnelling magnetoresistance (TMR). TMR is a quantum mechanical effect in a system of two ferromagnets separated by an insulator whereby, should the insulating layer be thin enough, the electron may "tunnel" through the insulating layer between the ferromagnets. The simplest form of MRAM device utilises this phenomena through the difference in resistive state of a current across two ferromagnetic (FM) layers, separated by a thin insulator. One layer has a magnetisation direction that will not be changed in the device, the "pinned" layer, which is pinned using an antiferromagnetic layer [16]. The other will be changed during device use relative to the fixed layer (and will be called the "write" layer); the ability to reorient this direction under current application makes this device writeable [17]. The energy difference between specific directions of magnetic quantisation axis (a separate quantity to the magnetic moment, whereby the quantisation axis defines the relative directions of the magnetic moment) within a crystalline material is called the magnetocrystalline anisotropy energy, and leads to "preferred" orientations that are energetic minima. After a pair of orthogonal fields, generated from the Biot-Savart law from two orthogonal currents, are applied to orient the (ferro)magnetic field in the write layer to rotate the magnetization axis, the electrical resistance can be measured through both to determine the state (via TMR) [17]. The change in the relative magnetization direction delivers a resistance difference between the differing magnetic states of the material due to the differing magnetic interaction with the spin polarization between the materials. This difference in resistance is based on the energy barrier to electrons tunneling through the material and entering differing polarization states at the Fermi energy, reducing the tunneling probability in states of dissimilar polarization and forming the magnetoresistance. The resistive state in most MRAMs is normally a difference in magnetization orientation of 180°. Usually, a low resistance state corresponds to parallel magnetisation as the tunneling probability is highest in this system. To understand the reasoning for this, we may write the difference in the resistive state between these parallel and anti-parallel states as a ratio,

$$TMR = \frac{R_{AP} - R_P}{R_P}, \tag{1.1}$$

where R_{AP} is the antiparallel state resistance and R_P is the parallel state resistance. By defining the spin-polarization of the tunnelling electrons to be the fractional difference in the spin dependent density of states (D) at the Fermi energy, E_F,

$$P_n = \frac{D_\uparrow(E_F) - D_\downarrow(E_F)}{D_\uparrow(E_F) + D_\downarrow(E_F)}, \tag{1.2}$$

where n is the index for the region of interest, the spin-up configuration indicates electrons with alignment parallel to the external field and down represents anti-parallel alignments. We may use Equation 1.1 and the relations $R_P = D_{\uparrow 1}(E_F)D_{\uparrow 2}(E_F)+D_{\downarrow 1}(E_F)D_{\downarrow 2}(E_F)$ and $R_{AP} = D_{\uparrow 1}(E_F)D_{\downarrow 2}(E_F)+D_{\downarrow 1}(E_F)D_{\uparrow 2}(E_F)$ to produce the following relation,

$$TMR = \frac{2P_1P_2}{1 - P_1P_2}, \tag{1.3}$$

where we see the TMR becomes infinite if the materials are fully polarized into parallel and anti-parallel alignments, and zero for identical alignments. The unfortunate consequence of using current-generated magnetic fields to reorient the ferromagnetic axis in the materials is that the fields may affect neighbouring devices that are in close enough proximity to be influenced by said magnetic field, a significant consequence in dense architecture, resulting in the need for low component density due to these stray field interactions [7]. For all practical MRAMs, spin transfer torque (STT) is used to rotate the ferromagnetic axis of magnetization via polarised electron currents [18, 19]. STT is the process whereby the magnetic orientation of a material is modified by an injected spin-polarised current, whereby the mismatch in the magnetic orientation and the spin polarisation induces a torque on the magnetic moments within the write layer. This reduces the field leak problem, which allows for denser arrays due to the lower magnetic field influence, and lower currents are used in device operation due to the lower energy cost of rotating the magnetic moments. The detriment to the STT-MRAM is a reduced TMR ratio compared to non-STT-MRAMs, due to the bias voltage needed to achieve high switching speeds [7].

Other devices operate using spin-orbit torque (SOT) operations, another spin-torque phenomenon. Whilst STT-MRAM uses the same current path for read and write lines, the SOT-MRAM uses a separate write line under the pinned layer to alter the quantisation axis direction using the torque from a polarised current in the write layer, using the spin-orbit torque to switch the magnetic moments; the spin density originates from the spin-orbit coupling, and magnetic forces between the spin-orbit coupling from the spin current in the write line and the magnetic moments transfers angular momentum to the moments, resulting in their rotation [20]. For parallel and anti-parallel systems, this corresponds to the direction of current in the write line. This method usually results in faster switching and lower power consumption, as well as having the inherent benefit of separating the read and write lines [19].

A variant of STT/SOT-MRAM that shows a lot of promise is a version that uses antiferromagnetic (AFM) read and write layers as opposed to FM layers. AFM-based memory devices are comparatively similar to the STT/SOT-MRAM systems, in that they also use STT or SOT to alter their AFM domain orientation. However, we may note that the simplest AFM device is rather different to a simple STT/SOT-MRAM device in its construction. Instead of two FM layers, two AFM layers are used, separated by a nonmagnetic layer [21]. In this case, the quantisation axis of the AFM configuration in the write layer is rotated using a polarised current, and the resistance state is measured to determine the logic state of the device (Figure 1.1). This means the AFM-MRAMs have a very small footprint in comparison to the FM-MRAM device clusters, and a very compact and dense configuration of memory devices can be produced.

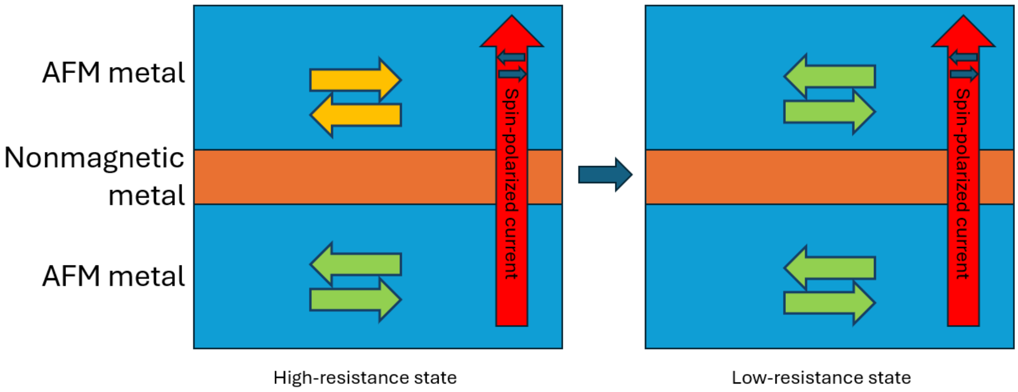

Figure. 1.1: A Simple STT-AFM magnetic memory. The write spin current can reorient the magnetic configuration in accordance to its polarization, which alters the resistance state of the device.

AFM materials do however come with the complexity that measurement of magnetic properties, such as the exact magnetic ordering, within the material is extremely difficult due to the nature of the magnetic structure. This makes measurement and control of these properties more difficult in practice, and so can be difficult to directly alter in some devices. Alongside this, developing AFM materials and devices can be significantly more difficult due to the AFM nature of the materials making changes and measurement of certain properties extremely difficult. For the magnetoresistance, the AFM devices must match high-resistance configurations with low-resistance configurations, a situation that can be more complex than for FM devices as configurations with magnetic moments at 180° from each other are often degenerate in energy. Orientation of these magnetic moment configurations can be difficult to determine experimentally. The TMR ratio is lower in SOT-AFM devices than for MRAM devices, with devices having a TMR ratio up to 110% [21].

1.3 Mn-based AFM materials

From previous studies, we note that a specific group of materials, namely Mn-based AFM materials, have shown particular promise in spintronic applications, such as the anomalous (and topological) Hall effects, anomalous Nernst effect, spin-Hall effects and terahertz electrical responses [22]. This includes the work by Shi et al [21], whereby Mn_3Pt was used to facilitate an all-AFM memory device, and Yan et al's study on strained MnPt devices, which reached a TMR ratio of 11.2% [23].

We note that there are two major classifications for the Mn-based AFM alloys we will be discussing. The first are collinear AFM materials, where the quantisation axis, and therefore direction, of the magnetic moments can be defined as parallel to all magnetic moments in the system. The second classification is the noncollinear AFM materials. These materials cannot be defined by making the magnetic quantisation axis (anti-)parallel to the direction of all magnetic moments; either some moments, or all moments, exist at some differing angle to any selection of quantisation axis of the material. The configurations of magnetic moments maintain zero magnetic moment overall. The collinear materials have a simpler magnetic ordering than the noncollinear materials, though the noncollinear materials are common in nature and can generate unconventional behaviour magnetically [24]. Structurally, the collinear and noncollinear materials can be broken down into three classifications based on Strukturbericht notation; $L1_0$, $L1_2$, and $D0_{19}$ [25, 26]. The $L1_0$ materials are tetragonal, the $L1_2$ materials are cubic and the $D0_{19}$ materials are hexagonal (Figure 1.2). The variation of these material structures will affect the magnetic orientations and thus magnetic configurations of these materials.

The different AFM configurations, during use in the write layer of a memory bit, may have varying relative orientations of the magnetic moments that are symmetrically equivalent, producing a difference in energetic variation for tunneling and magnetic anisotropy effects [21]. This difference in energy is a huge benefit to potential device applications in terms of controlling the magnetoresistance of a device. Consequentially, it is then possible to screen for materials with optimal magnetic anisotropy energy barriers between resistance states by finding the magnetic anisotropy energies for specific magnetic configurations. Consequentially, the materials can then be tuned to access specific resistance states based on material selection and magnetic moment configuration, augmenting device performance.

1.4 Computational modelling

There are many competing methods and tools that can be used for simulating materials. We first note that the modelling of electronic systems is a complex task. The inclusion of multiple electron states and multiple atoms in large num-

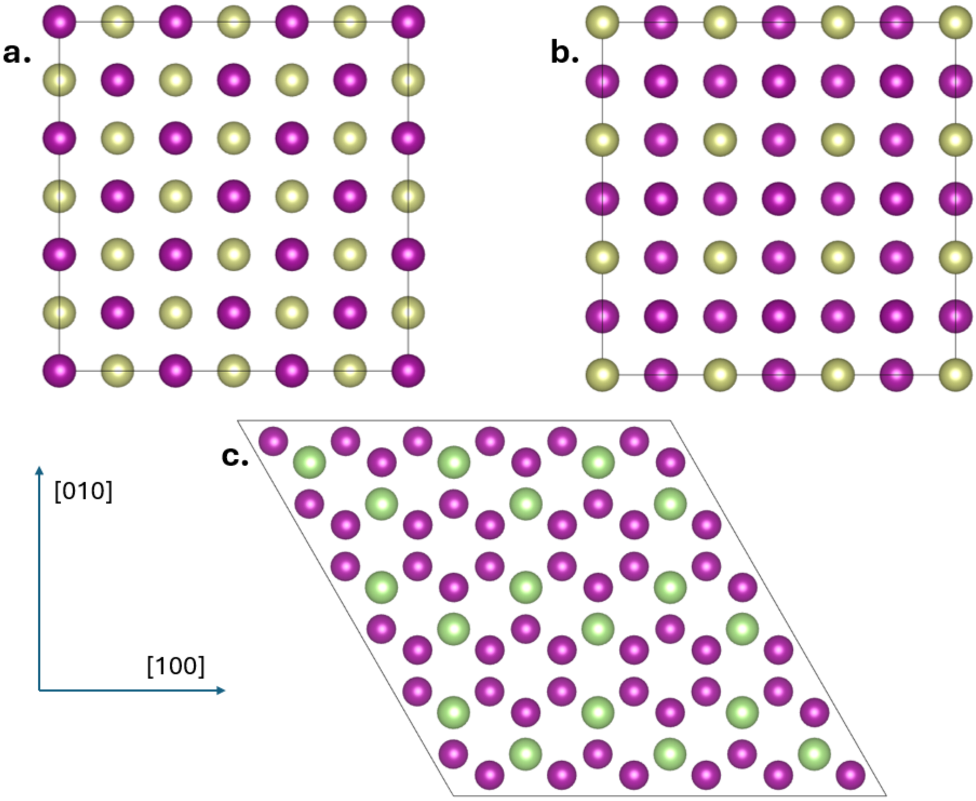

Figure. 1.2: The three major groups of materials, based on Strukturbericht notation. a) L1_0, b) L1_2, and c) D0_{19}, all shown in the (001) plane

bers means the capability to directly compute a property of a system to an exact level is limited, and approximations must be made. Alongside this, the need for the inclusion of spin properties adds further complexity. Methods that take reasonable approximations to solve the systems they calculate can be deployed, including simplified dipole equations based on nearest-neighbour approximations. There are many methods used to simulate a material, including atomistic methods, whereby the system is modelled on a discrete (atom-level) scale, commonly used for more numerous systems of magnetic ions; micromagnetic methods, where the length-scale of simulation is on the order of micrometres, and is used for simulations requiring larger-scale simulation; and all-electron methods, where electrons are considered explicitly without potential approximations, used for more precise calculations and radiation interaction simulations. The tool that is most commonly used for these applications, however, is *ab initio* density functional theory (DFT). The benefit of *ab initio* DFT is the predictive nature of the *ab initio* methodology, allowing us to predict the properties of materials and therefore allow for screening of materials to enable more targeted work in future by eliminating candidate materials that need to be tested [27]. This not only saves time but also saves further resources by eliminating undesirable candidates, as well as meaning experimental results may be estimated from the outset, determining necessary measurements and the region of experimental observation needed for certain characteristics. An example of this is the work by Park et al [28], where multiple members of the manganese binary alloys have their antiferromagnetic properties predicted using *ab initio* methods.

Theoretical approaches also offer the ability to model accurate representations of systems with a level of flexibility that is difficult to achieve in experiment. Atomistic simulations in particular allow for more specific initialisation than experiment may easily allow for. This includes identifying properties of specific atoms in a system and varying thickness of substrates. As such, specific applications can be explored that may supplement experimental work and help to provide additional support for experimental results, like that in Dutta et al's study of $Ba_2CoGe_2O_7$ [27], where the magnetic moment of $Ba_2CoGe_2O_7$ Co^{2+} ion was calculated alongside the band gap in the antiferromagnetic state, as well as the work by Niazi et al [29], where MnNi was investigated as to the layer dependence of the magnetic moment of the Mn species. This allows for rapid characterisation of materials in timeframes that wouldn't be plausible experimentally. Calculation of properties that are difficult to probe, such as the magnetic anisotropy energy, may be carried out [30]. Fewer precious metals therefore need to be used up during research, lessening environmental impact.

As previously mentioned, DFT modelling is an ab-initio approach. There are many DFT programs like the Vienna ab-initio simulation program (VASP) [31, 32, 33, 34], a plane wave basis set DFT solver that uses the projector augmented wave method, or the Cambridge serial total energy package (CASTEP) [35], a density functional theory solver using the plane-wave pseudopotential method that can use norm-conserving and Vanderbilt ultrasoft pseudopotentials also. For VASP, the major benefit is the additional data processing options it has such as projected density of states (PDOS) evaluation (CASTEP requires a secondary program, OPTADOS, for this), whereas CASTEP would be better for calculations that may also investigate perturbation effects like phonon exploration as per the work by Ngobe et al [36]. CP2K may also be used, which is able to perform DFT calculations (based on the Gaussian and plane wave approaches and atomic orbital basis sets) with local density approximation (LDA) and GGA, as well as Moller-Plesset and random phase approximation. This makes CP2K better suited to quantum chemistry applications which require more resources to do this type of calculation [37]. These software packages are well-established and have support for both serial and parallel calculation. VASP is often preferred due to this program having the best balance of good parallelisation and a wide array of post-DFT options.

DFT is used to calculate a wide variety of properties in this work, however some properties we are interested in are not calculated via DFT applications due to their small contribution or due to an approximation. For the magnetic dipole-dipole interaction contribution to the magnetic anisotropy energy, described as the interaction of neighbouring dipoles with each other and therefore the change in energy induced by the rotation of these dipoles, we use simplistic micromagnetic approaches instead to calculate this property. Vampire is an example of a calculation package that may use a micromagnetic approach [38], using the Stochastic Landau-Lifshitz-Gilbert equation and (constrained) Monte-Carlo metropolis algorithms to solve for properties of systems [39] that is able to calculate the magnetic dipole-dipole interaction contribution. Similarly, Just Another Magnetic Simulator (JAMS) [40], a simple magnetic system calculator, determines the magnetic dipole-dipole energy by calculating the dipole interaction as a sum over dipoles inside a sphere with a cutoff radius, which may be used to find the magnetic dipole anisotropy contribution to the magnetic anisotropy. In the theoretical work by Jenkins et al [41], dipole-dipole interaction is used to determine the stray fields in a simulated CoFeB ferromagnetic layer. Micromagnetic dipole-dipole calculations will not make the same approximations as atomistic simulations due to their exclusive use of magnetic moments and position and thus are used to resolve magnetic dipole-dipole contributions to the magnetic anisotropy energy. As we need only the dipole-dipole contribution and no additional micromagnetic information, we may elect to use JAMS as our main tool for this format of calculation.

1.5 Aims and objectives

We aim to investigate whether simulation methods can be used for directly comparing AFM materials to each other, in a way that is predictive and comparable to experiment. On top of this, for desirable materials, understanding stress and strain typically applied to heterostructures of these materials and what their effect is on the electronic properties is a crucial predictive aspect for experimental comparison that we will undertake for $D0_{19}$ materials. We aim to determine the relationship between stress and electronic properties (such as band structure) and structural properties. Also, to understand the boundaries of these materials, we aim to investigate the material properties at a surface and interface with a nonmagnetic metal, in order to effectively predict its behaviour. The specific objectives of the work presented in this thesis are:

1. To employ theoretical methods to calculate properties of bulk AFM $L1_0$, $L1_2$, and $D0_{19}$ materials, specifically the structural properties, magnetic properties and select electronic properties like the band structure and charge distribution for certain materials. The main theoretical methods are *ab initio* approaches to determine the structural and magnetic properties including magnetocrystalline anisotropy energy, with supplementary use of specific solvers for this avenue of research to calculate the magnetic dipole-dipole contribution to the magnetic anisotropy.
2. To expand on the calculation of properties and develop a comparable and consistent approach based on theoretical methods to characterise the $L1_0$, $L1_2$, and $D0_{19}$ Mn-alloy materials. By using a consistent approach, the comparability of the properties of these materials suffers no difference in systematic errors and can thus be compared directly and can be used to compare configurations of differing magnetic ordering. In order to have a reasonable size of sample AFM materials, we limit this investigation to a subset of Mn-alloys. We will characterise the $L1_0$, $L1_2$, and $D0_{19}$ materials, including determining the energetic changes related to magnetic anisotropy and investigate the relationships between certain practical effects and the properties of these materials.
3. Alongside the characterisation of the material in ground state, we will simulate

$D0_{19}$ materials under strain. The $D0_{19}$ materials are assessed for the changes in properties whilst under compressive and extensive strain up to ±6%, with the band structure being assessed across the strains for changes in the electronic properties. We will determine the change in Weyl points on the band structure to track the changes.

4. We will also assess the properties of materials at their surfaces and interfaces to determine the interface properties to be expected from thin films or heterostructure couplings of these materials, which will be necessary knowledge for potential use in a device. To fully understand the interaction between two materials as heterostructures, we aim to characterise a heterostructure of each of the $D0_{19}$ materials and a non-magnetic metal, platinum. By doing this, we can examine the predicted properties of such a union, including Bader charge analysis of charge distribution and the partial density of states. This will elucidate on the interface interaction within SOT memory devices and valves.

1.6 Outline of thesis structure

This thesis has the following structure. In Chapter 2, the theoretical background and methods for the work collated within this thesis is discussed; the underlying principles used to calculate the properties of manganese alloys are detailed. In Chapter 3, results for the $L1_0$ material investigation are presented, giving a full determination of the various structural and magnetic properties of this set of materials and noting their similarities and dissimilarities. We use these materials to act as comparison for our method to experiment and theory. After the $L1_0$ materials we discuss the $L1_2$ and $D0_{19}$ materials in Chapter 4, results for $D0_{19}$ and $L1_2$ noncollinear materials are also presented and discussed. We also add into this section the various discussions on band structure and strain, relevant properties for potential device application. We note that the noncollinear materials operate with similar structural effects under strain but differ greatly electronically. Chapter 5 includes the discussion of the surfaces and heterostructures of the $D0_{19}$ materials, discussing optimal surface layers and the effect of substrates on these materials. Finally, the conclusions are presented in Chapter 6.

Chapter 2

Theory

2.1 Introduction

The calculation of properties of materials is a useful tool in a wide array of scientific pursuits, particularly in systems or conditions that would be expensive or impractical to create, and for properties that are challenging to probe experimentally. Due to their zero net magnetisation, the magnetic properties of antiferromagnetic materials studied in this thesis are challenging to determine experimentally, and so predictive material modelling can provide an expedient method for evaluating and comparing multiple materials that are candidates for further research due to their potential magnetic properties [42, 43, 44, 45]. For antiferromagnetic materials, which have an inherently difficult magnetic structure to assess, materials simulation provides a far easier way of evaluating said structure by evaluating atomic-level magnetic properties directly. There are several modelling approaches for modelling magnetic materials, including ab-initio (a first-principles approach without any prior parameterization) [28], semi-empirical (using established data, usually in a database, to parameterize the calculation like micromagnetic simulation [46]) [43] and empirical methods (calculations that are fully parameterized by existing data) [47]. In this thesis the majority of results are obtained using ab-initio modelling. We note various types of approximations can be used for ab-initio calculations, including GW approximation, density functional perturbation theorem (DFPT), and time-dependent density functional theory (DFT). The work in this thesis focuses on the application of DFT to model the properties of antiferromagnetic (AFM) materials.

There are a wide array of methods for modelling magnetic materials. In particular, examples include micromagnetic approaches, atomistic approaches and quantum mechanical approaches. Micromagnetic approaches are a more simple method of magnetic simulation, with the purpose of solving for the spatial distribution of magnetization distribution within a system. These approaches are normally used to determine the magnetic properties of systems on length scales where atomic structure interaction is averaged out, i.e. on the order of cubic nanometres, averaging over the magnetic properties within. This allows for the simulation of magnetic structures and domains in a high-level manner obeying the continuum approximation. Examples of micromagnetic simulation tools include the object-oriented micromagnetic framework project (OOMMF) [48].

In a similar way, atomistic simulation maintains the method of averaging out the contribution from atomic structure interaction. However, the magnetic properties are instead calculated though using a model that considers atomic magnetic moment rather than averaging over some length scale, resulting in a simulation method that is able to model structures like ferrimagnetic and antiferromagnetic materials. However, these simulations are normally more costly in terms of resources and take more time to run. Examples of tools that use this type of simulation include Vampire [38].

Quantum mechanical approaches to modelling magnetic materials aim to solve (by approximation) the many-body Schrödinger equation in order to determine the properties of a system, both structural and electronic. The inclusion of calculating the structural properties provides a more in-depth theoretical approach. Whilst utilising several approximations, the results are still very accurate and the quantum mechanical method has become very popular for use in computational chemistry, though it should be cautioned this approach limits simulation size to hundreds of atoms due to CPU requirements [49]. Examples of tools that use quantum mechanical approaches include DFT based programs such as Vienna ab-initio simulation program (VASP) [31, 32, 33, 34] and the Cambridge serial total energy package (CASTEP) [35].

The primary aim of this work is to predict the properties of antiferromagnetic materials. Predicting the magnetic properties theoretically using *ab initio* methods can be especially useful for screening candidate materials for purposes such as spintronic memory devices and spin valves [50, 51].

This theory chapter starts with a discussion of some basic concepts important for *ab initio* materials modelling, for example the Schrödinger equation and crystal structure, in section 2.2. We then proceed onto an introduction to DFT, including the work by Hohenberg, Kohn and Sham, as well as exchange-correlation (XC) functionals and generalised gradient approximations, and Hubbard U theory in section 2.3. Discussion on the use of DFT in our calculations, as well as discussing additional important theory that must be understood in order to use DFT programs such as k-point sampling, planar augmented wave methodology, pseudopotentials, use of spin-orbit and noncollinear magnetic moments, and Hubbard U implementation is undertaken in section 2.4. Finally, we discuss magnetism and the nature of magnetic materials to provide a basis for understanding of the simulation work presented in this thesis in section 2.5, summarizing the chapter in section 2.6.

2.2 Schrödinger equation

The understanding of crystal structure and the properties thereof forms the basis of the work performed in this thesis. In this section, we present an overview of the key approaches and approximations employed to obtain the results presented in this thesis.

2.2.1 Schrödinger equation for many particle systems

The Schrödinger equation forms the basis for effective calculation of the properties of a quantum system [52]. It represents a Hamiltonian that can describe the dynamics of the system. In many particle systems, there can be considerable difficulty solving these equations exactly, often leading to very resource- and time-intensive calculations or outright inability to calculate the solution. This is due to the interacting nature of multiple particles; where single particles rely only on their position and momentum, the many-particle system requires the interaction of particles within the system to be taken into account, including electromagnetic interactions and spin effects.

The time-independent Schrödinger equation for the electronic and ionic components of a system is simply expressed as,

$$
\begin{aligned}
&\hat{\mathcal{H}}\psi(\mathbf{r_1}, ..., \mathbf{r_i}, ...\mathbf{r_N}, \mathbf{R_1}, ..., \mathbf{R_j}..., \mathbf{R_M}) \\
&= [\hat{\mathbf{T}}_e + \hat{\mathbf{T}}_n + \hat{\mathbf{V}}_{ext} + \hat{\mathbf{U}}_{ee} + \hat{\mathbf{U}}_{nn} + \hat{\mathbf{U}}_{ne}]\psi(\mathbf{r_1}, ..., \mathbf{r_i}, ...\mathbf{r_N}, \mathbf{R_1}, ..., \mathbf{R_j}..., \mathbf{R_M}) \\
&= E\psi(\mathbf{r_1}, ..., \mathbf{r_i}, ...\mathbf{r_N}, \mathbf{R_1}, ..., \mathbf{R_j}..., \mathbf{R_M}),
\end{aligned}
\tag{2.1}
$$

where $\hat{\mathbf{T}}_e$ is the electron kinetic energy operator, $\hat{\mathbf{T}}_n$ is the ionic kinetic energy operator, $\hat{\mathbf{U}}_{ee}$ is the electron-electron interaction potential operator, $\hat{\mathbf{U}}_{nn}$ is the ion-ion interaction potential operator, $\hat{\mathbf{U}}_{ne}$ is the ion-electron interaction potential operator, $\hat{\mathbf{V}}_{ext}$ is the external potential operator, $\mathbf{R}_n$ are the atomic coordinates of M ions and $\mathbf{r}_i$ are the electron coordinates of N electrons [53]. This equation is antisymmetric with respect to both the spin and spatial electron coordinates and adheres to the Pauli exclusion principle.

2.2.2 Born-Oppenheimer approximation and the Schrödinger equation

The Born-Oppenheimer approximation is where we begin to deal with specific atomistic/electronic approximations. Consider here a system of atoms that are interacting [54]. The mass of the nucleus of an ion is far larger than that of the electron. This allows us to decouple the dynamics of electrons and ions. The Born-Oppenheimer approximation sets the wavefunction as a product of ionic and electronic wavefunctions, $\psi = \phi_e \phi_N$ [55]. Due to the short timescale producing a "clamped-nuclei" approach, the potential term related to the nucleus interaction, $\mathbf{U}_{nn}$, may be neglected as in this case $\mathbf{R}$ is simply a parameter, meaning $\mathbf{U}_{nn}$ becomes a constant that simply shifts the eigenvalues by some constant amount. Re-applying to the respective particles, we find the time-independent Schrödinger equations for the electron and the nucleus (such as Equation 2.1) may be separated into electronic and nucleic contributions. These equations then become

$$\begin{aligned} &\hat{\mathcal{H}}_e(\mathbf{r_1}, ..., \mathbf{r_i}, ...\mathbf{r_N}, \mathbf{R_1}, ..., \mathbf{R_j}..., \mathbf{R_M})\psi_e(\mathbf{r}_i; \mathbf{R}_N) \\ &= E_e(\mathbf{r_1}, ..., \mathbf{r_i}, ...\mathbf{r_N}, \mathbf{R_1}, ..., \mathbf{R_j}..., \mathbf{R_M})\psi_e(\mathbf{r_1}, ..., \mathbf{r_i}, ...\mathbf{r_N}, \mathbf{R_1}, ..., \mathbf{R_j}..., \mathbf{R_M}), \end{aligned} \tag{2.2}$$

$$(\mathbf{\hat{T}_n} + E_e(\mathbf{R_1}, ..., \mathbf{R_j}..., \mathbf{R_M}))\psi_n(\mathbf{R_1}, ..., \mathbf{R_j}..., \mathbf{R_M}) = E\psi_n(\mathbf{R_1}, ..., \mathbf{R_j}..., \mathbf{R_M}), \tag{2.3}$$

where $\hat{\mathcal{H}}_e = \mathbf{\hat{T}_e} + \mathbf{\hat{U}_{ee}} + \mathbf{\hat{V}_{ext}}$ [56].

DFT aims to solve Equation 2.2 for many-electron systems. It is very hard to solve this equation as the inter-electronic potential prevents the separation of the equation to single-particle equations, making the solution far more challenging. Whilst it is possible to solve this Hamiltonian explicitly for trivial cases, it is unfeasible for large systems due to computational resources needed.

2.3 The theoretical basis of density functional theory

2.3.1 Hartree-Fock method

The Hartree-Fock method is one of the foundational steps to the approach in DFT [57]. This method allows us to represent, via Slater determinant, the wave function of an N-particle system as N spin-orbitals. We begin with the original wavefunction, $\psi(\mathbf{r}_1, \mathbf{r}_2, ...\mathbf{r}_n)$, where $\mathbf{r}_n$ is the n^{th} electron coordinate; we note we need to produce a wavefunction that is represented by the separate spin-orbital wavefunctions. To obey antisymmetry requirements, we define the wavefunction as a Slater determinant,

$$\psi(\mathbf{r}_1, \mathbf{r}_2, ...\mathbf{r}_n) = \frac{1}{\sqrt{N!}} \begin{bmatrix} \phi_1(\mathbf{r}_1) & \phi_2(\mathbf{r}_1) & ... & \phi_n(\mathbf{r}_1) \\ \phi_1(\mathbf{r}_2) & \phi_2(\mathbf{r}_2) & ... & \phi_n(\mathbf{r}_2) \\ \vdots & \vdots & \ddots & \vdots \\ \phi_1(\mathbf{r}_n) & \phi_2(\mathbf{r}_n) & ... & \phi_n(\mathbf{r}_n) \end{bmatrix}, \tag{2.4}$$

maintaining antisymmetry via Pauli exclusion [56]. We may then apply the variational principle in order to obtain the Fock equation,

$$\epsilon_i \phi_i = h^1(\mathbf{r}_i)\phi_i(\mathbf{r}_i) + J(\mathbf{r}_i)\phi_i(\mathbf{r}_i) - K(\mathbf{r}_i)\phi_i(\mathbf{r}_i) \tag{2.5}$$

where the one-electron Hamiltonian, $h^1(\mathbf{r}_i) = \frac{1}{2}\boldsymbol{\nabla}^2 + V_{ext}(\mathbf{r}_i)$, J is the Coulomb term and K is the energetic exchange term, the term that determines the exchange energy arising from the exchange statistics of the electrons occupying the same orbit, both defined as

$$J(\mathbf{r}_i) = \sum_{j=1}^{N} \int d\mathbf{r}_j \frac{\rho(\mathbf{r}_j)}{|\mathbf{r}_i - \mathbf{r}_j|}, \tag{2.6}$$

where $\rho(\mathbf{r}_j)$ is the electron density and

$$K(\mathbf{r}_i)\phi_i(\mathbf{r}_i) = \sum_{j=1}^{N} \phi_j(\mathbf{r}_i) \int d\mathbf{r}_j \frac{\phi_j^*(\mathbf{r}_j)\phi_i(\mathbf{r}_j)}{|\mathbf{r}_i - \mathbf{r}_j|}. \tag{2.7}$$

Exchange itself can be defined as the constraint on the states of two indistinguishable particles, in particular the effects of the exchange of two bodies in a system.

It is then a matter of reformulating this into a typical single-electron wavefunction. Expressing a new operator, the Fock operator, as a sum of one-electron operators (represented with a (1)),

$$\hat{F}(1)\phi_j = \hat{\mathcal{H}}^{core}(1)\phi_j + \sum_{j=1}^{N/2}[2\hat{J}_j(1) - \hat{K}_j(1)]\phi_j. \tag{2.8}$$

The Hartree-Fock wave functions (for one electron) may be determined by setting the Fock operator as an eigenfunction equation,

$$\hat{F}(1)\phi_i = \epsilon_i \phi_i(1), \tag{2.9}$$

where all $\phi_i(1)$ are one-electron wave functions.
We note that the exclusion of electron correlation in this method has been accounted for in post-Hartree-Fock methods, as Hartree-Fock does not account for electron correlation beyond Pauli exchange [58].

2.3.2 Hohenberg-Kohn

The Hohenberg-Kohn theory provides a connection between ground-state electron density and external potential of a many-body system, which will allow the many-body problem to be vastly simplified by expressing the ground state energy in terms of a functional of the ground state density [59]. Consider the Hamiltonian for two many electron and nuclei systems with differing external potentials in terms of component operators,

$$\begin{aligned} \hat{\mathcal{H}} &= \hat{T}_e + \hat{V}_{ee} + \hat{V}_{ext}, \\ \hat{\mathcal{H}}' &= \hat{T}_e + \hat{V}_{ee} + \hat{V}'_{ext}. \end{aligned} \tag{2.10}$$

It can be proved that there is a singular electron density that corresponds with the ground state energy for a given V_{ext} via *reductio ad absurdum*, or proof by self-contradiction (the first Hohenberg-Kohn theorem). In a system where the energy $E \neq E'$,

$$E < \langle \psi' | \hat{\mathcal{H}} | \psi' \rangle = \langle \psi' | \hat{\mathcal{H}}' | \psi' \rangle + \langle \psi' | \hat{\mathcal{H}} - \hat{\mathcal{H}}' | \psi' \rangle \tag{2.11}$$

$$E < \langle \psi' | \hat{\mathcal{H}} | \psi' \rangle = E' + \langle \psi' | \hat{T} + \hat{V}_{ee} + \hat{V}_{ext} - \hat{T} - \hat{V}_{ee} - \hat{V}'_{ext} | \psi' \rangle \tag{2.12}$$

$$E < E' + \int \rho(\mathbf{r})(\hat{V}_{ext} - \hat{V}'_{ext}) d\mathbf{r} \tag{2.13}$$

$$E' < E - \int \rho(\mathbf{r})(\hat{V}_{ext} - \hat{V}'_{ext}) d\mathbf{r}. \tag{2.14}$$

We then combine Equations 2.13 and 2.14 via addition,

$$E + E' < E + E'. \tag{2.15}$$

The result is a contradiction, so there are no two V_{ext} that have the same ground state. V_{ext} is uniquely defined by ground state electron density. We may then assign a unique electron density to the ground state, $\rho_0(\mathbf{r})$, making E a functional of ρ_0 (whereby a functional is a specific type of function that maps a space into the field of real or complex numbers),

$$E[\rho_0] = T[\rho_0] + E_{ee}[\rho_0] + E_{ne}[\rho_0]. \tag{2.16}$$

Here, E_{ne} is the energy associated with the new external potential, where the new external potential is the nuclei attraction-defined potential as the potential is fully defined by this in this case. $T(\rho_0) + E_{ee}(\rho_0)$ is universally valid (not dependent on the system under study due to the dependent components being isolated to the external potential) and will be combined into one term, $F_{HK}(\rho_0)$. We may then express this E_{Ne} energy term as a function of the electron density,

$$E_{ne}[\rho_0] = \int \rho_0(\mathbf{r})\hat{V}_{ne}(\mathbf{r})d\mathbf{r}. \tag{2.17}$$

We may then note the overall equation for the energy,

$$E[\rho_0] = F_{HK}[\rho_0] + \int \rho_0(\mathbf{r})\hat{V}_{ne}(\mathbf{r})d\mathbf{r}, \tag{2.18}$$

defines the ground state energy for some external potential, which we may write as V_{ext}. As the Hamiltonian operator is uniquely determined by the ground state density, all properties of all states are determined by the ground state density. We may then use this conclusion, as well as noting $F_{HK}(\rho)$ delivers the lowest energy if and only if ρ_0 is used as the input. By variational principle, this results in the second Hohenberg-Kohn equation,

$$E[\rho'] = F_{HK}[\rho'] + E_{V_{ext}}[\rho'] \geq E_0 = E[\rho_0], \tag{2.19}$$

whereby the functional that determines the ground state energy gives the lowest energy if and only if ρ_0 is used [60].

2.3.3 Kohn-Sham

The Kohn-Sham equation expands on the work by Hohenberg and Kohn by demonstrating the many-body hamiltonian can be simplified using "non-interacting electrons" to take the many-body system and make it into many one-body systems parameterized by an augmented potential alone [61]. The derivation begins by re-establishing the energy terms; we split the $E_{ee}(\rho)$ and $E_{Ne}(\rho)$ terms into contributions from the exchange correlation energy (defined as the energy of an electron interacting with the exchange-correlation hole charge density at some coordinate $\mathbf{r}'$) and the Hartree energy (the classical electrostatic energy),

$$E[\rho] = T[\rho] + E_H[\rho] + E_{xc}[\rho] + \int \rho(\mathbf{r})\hat{V}_{ext}(\mathbf{r})d\mathbf{r}, \tag{2.20}$$

where $T[\rho]$ is the kinetic energy component of the total energy functional, $E_{xc}[\rho]$ is the exchange correlation energy, and $E_H[\rho]$ is the Hartree energy. Next, it is useful to combine potentials as a single effective potential, V_{eff},

$$V_{eff}(\mathbf{r}) = V_{ext}(\mathbf{r}) + e^2 \int \frac{\rho(\mathbf{r'})}{|\mathbf{r} - \mathbf{r'}|} d\mathbf{r'} + \frac{\delta E_{xc}[\rho]}{\delta \rho(\mathbf{r})}, \tag{2.21}$$

where $\frac{\delta E_{xc}[\rho]}{\delta \rho(\mathbf{r})}$ is the XC potential.
Using a Lagrange multiplier, μ, to constrain the number of electrons to N, we may write the total energy as a functional of the electron density,

$$\frac{\delta}{\delta \rho(\mathbf{r})}[E[\rho(\mathbf{r})] - \mu \int \rho(\mathbf{r})d\mathbf{r}] = 0, \tag{2.22}$$

and so we can write μ as

$$\mu = \frac{\delta T[\rho]}{\delta \rho(\mathbf{r})} + V_{eff}(\mathbf{r}) = \frac{\delta E[\rho(\mathbf{r})]}{\delta \rho(\mathbf{r})}, \tag{2.23}$$

which is the equation for a group of non-interacting particles moving in an equivalent potential to V_{eff} [62]. We can then solve the single-electron Schrödinger equations,

$$\epsilon_i \phi_i(\mathbf{r}) = (T_i + V_{eff})\phi_i(\mathbf{r}). \tag{2.24}$$

Note that this system is restricted, in that there are an equal number of up- and down-spins.
This should be solved self-consistently with

$$\rho(\mathbf{r}) = \sum_{i=1}^{N} |\phi_i(\mathbf{r})|^2. \tag{2.25}$$

The result is an energy (Equation 2.24) constructed from single-electron equations dependent on the electron density; so, we can solve for the energy of the system as a sum orbital energies,

$$E[\rho(\mathbf{r})] = \sum_{i}^{N} \epsilon_i - \frac{e^2}{2} \int \frac{\rho(\mathbf{r})\rho'(\mathbf{r})}{|\mathbf{r} - \mathbf{r'}|} d\mathbf{r} d\mathbf{r}' + E_{xc}[\rho(\mathbf{r})] - \int V_{xc}[\rho(\mathbf{r})]\rho(\mathbf{r}) d\mathbf{r}. \quad (2.26)$$

Unrestricted Kohn-Sham can be solved by splitting the electron density into spin-up and spin-down components, and solving the Kohn-Sham equations for the separate contributions of the kinetic and XC interactions from the spin-up and spin-down components of the electron density. As the two contributions and their respective Hamiltonians are coupled via the total density, they must be solved simultaneously via the self-consistent field (SCF) procedure, an iterative method of solving the Kohn-Sham equations.

2.3.4 Exchange-correlation functionals

Despite the combined effective potential being a very useful tool in the theory of DFT, we do still need to approximate the exchange-correlation (XC) potential in order to calculate the effective potential [63]. The local density approximation (LDA) to the XC energy is given by

$$E_{xc}[\rho(\mathbf{r})] = \int \rho(\mathbf{r}) \epsilon_{xc}[\rho(\mathbf{r})] d^3\mathbf{r}, \quad (2.27)$$

where $\epsilon_{xc}[\rho]$ is the XC energy per particle of a homogeneous electron gas of charge density equal to ρ [64]. The XC energy, $\epsilon_{xc}[\rho]$, can be decomposed into exchange and correlation contributions,

$$\epsilon_{xc}^{LDA}[\rho] = \epsilon_{x}^{LDA}[\rho] + \epsilon_{c}^{LDA}[\rho], \quad (2.28)$$

with the exchange component for a homogeneous electron gas, ϵ_x^{LDA}, becoming

$$\epsilon_x^{LDA}[\rho(\mathbf{r})] = \frac{3}{4}(\frac{3}{\pi})^{\frac{1}{3}} \int [\rho(\mathbf{r})]^{\frac{4}{3}} d^3\mathbf{r}. \quad (2.29)$$

The correlation term is then approximated by fitting to various calculations, mostly quantum Monte-Carlo simulations to within 2 milli-Hartree; many variations exist of the approximation, such as the high- and low-density limits [65]. Several intermediate density calculations have been reported also [66]. For the spin-polarized system, where $\rho = \rho^{\uparrow} + \rho^{\downarrow}$, we may write the exchange term as

$$\epsilon_x^{LDA}[\rho^{\uparrow}(\mathbf{r}), \rho^{\downarrow}(\mathbf{r})] = \frac{3}{4}(\frac{3}{\pi})^{\frac{1}{3}} \int (\rho^{\uparrow}(\mathbf{r})^{\frac{4}{3}} + \rho^{\downarrow}(\mathbf{r})^{\frac{4}{3}}) d^3\mathbf{r}. \quad (2.30)$$

2.3.5 Generalized gradient approximation

The generalized gradient approximation (GGA)s improve upon the local density approximation (LDA) by expressing the exchange-correlation (XC) energy per particle ϵ_{xc} as a functional of two parameters; the electron density ρ, and its gradient $|\nabla\rho|$, such that

$$E_{xc}^{GGA}[\rho(\mathbf{r})] = \int \rho(\mathbf{r})\epsilon_{xc}[\rho(\mathbf{r}), |\nabla\rho(\mathbf{r})|]d\mathbf{r}, \tag{2.31}$$

where $E_{xc}^{GGA}[\rho]$ is the GGA XC energy [64]. There are a wide array of different generalized gradient approximation (GGA)s that differ in the parameterisation of ϵ_{xc}. It is therefore wise to use the GGA that most effectively replicates the properties of the material under investigation.

GGAs can be more accurate than LDAs at calculating the exchange and correlation energies due to the dual dependence on both the electron density and its gradient, which can improve on ground state energies. GGAs tend to underbind the molecules and crystals compared to local density approximation (LDA)s typically overbinding. The GGA approximations PW91 [67, 68], Perdew, Burke and Ernzerhof (PBE) [69] and revised PBE (rPBE) [70], for example, produce fairly similar results and describe metals and calculations within the bulk of solids fairly well. GGA can form a correction term for the LDA functional,

$$\epsilon_{xc}^{GGA}[\rho] = \epsilon_{xc}^{LDA}[\rho] + \Delta\epsilon_{xc}\left(\frac{|\boldsymbol{\nabla}\rho|}{\rho^{\frac{4}{3}}}\right), \tag{2.32}$$

improving upon the overbinding inherent in the LDA approach by reducing it. For spin-polarized calculations, this is modified as a straightforward generalization for $\rho = \rho^{\uparrow} + \rho^{\downarrow}$,

$$E_{xc}^{GGA}[\rho^{\uparrow}(\mathbf{r}), \rho^{\downarrow}(\mathbf{r})] = \int \rho(\mathbf{r})(\epsilon_{xc}[\rho^{\uparrow}(\mathbf{r}), |\nabla(\rho^{\uparrow}(\mathbf{r}))|] + \epsilon_{xc}[\rho^{\downarrow}(\mathbf{r}), |\nabla(\rho^{\downarrow}(\mathbf{r}))|])d^3\mathbf{r}, \tag{2.33}$$

altering the Kohn-Sham equation to be

$$\begin{aligned} E[\rho(\mathbf{r})] = \sum_{i}^{N} \epsilon_i - \frac{e^2}{2} \int \frac{\rho^{\uparrow}(\mathbf{r})\rho^{\uparrow\prime}(\mathbf{r})}{|\mathbf{r}-\mathbf{r}'|} d\mathbf{r} d\mathbf{r}' - \frac{e^2}{2} \int \frac{\rho^{\downarrow}(\mathbf{r})\rho^{\downarrow\prime}(\mathbf{r})}{|\mathbf{r}-\mathbf{r}'|} d\mathbf{r} d\mathbf{r}' \\ - \int V_{XC}[\rho^{\uparrow}(\mathbf{r})]\rho^{\uparrow}(\mathbf{r}) d\mathbf{r} - \int V_{XC}[\rho^{\downarrow}(\mathbf{r})]\rho^{\downarrow}(\mathbf{r}) d\mathbf{r} \\ + \int \rho(\mathbf{r})(\epsilon_{xc}[\rho^{\uparrow}(\mathbf{r}), |\nabla(\rho^{\uparrow}(\mathbf{r}))|] + \epsilon_{xc}[\rho^{\downarrow}(\mathbf{r}), |\nabla(\rho^{\downarrow}(\mathbf{r}))|]) d^3\mathbf{r}. \end{aligned} \tag{2.34}$$

2.3.6 DFT with Hubbard U

Hubbard potential

The self-interaction error (SIE) results from the spurious interaction of a particle with itself in approximate DFT. The SIE comes from the non-zero sum of the Hartree term for a single-electron in Kohn-Sham DFT, which is of course non-physical [71]. This interaction should be cancelled out by the XC energy in exact DFT, but for approximate XC functionals it is not [72]. This error is not significant in Hartree-Fock approaches as the Coulomb term cancels completely, but the Hartree-Fock neglects the electron correlation entirely based on approximation.

In DFT, correction of the self-interaction error is needed for accurate predictions. The density functional theory with Hubbard U (DFT+U) method aims to approximately correct for SIE by augmenting components of the Coulomb contribution and exchange contribution in the Hamiltonian [73, 74]. The DFT+U method is used to improve the prediction of electron localisation. This is especially important for this work as the DFT+U method will significantly affect the magnitude of magnetic moments and magnetic anisotropy energies.

Description of the model

To implement the correction into DFT, we can apply the local Hubbard U term to the d and f group electrons within the ions. We separate the d and f groups from the s and p groups, which can be adequately described without the DFT+U approximation. The method of implementation used in VASP here is the formalism of Dudarev et al [75], a method that effectively adds a penalty functional to the semilocal total energy expression to alter the electron localisation, insofar as the potential becoming repulsive for electrons occupying a state by less than half, and attractive otherwise. This functional causes changes to calculated properties of the system based on the magnitude of the correction, such as the magnetic moment of Mn of the system (Figure 2.1). The electron localisation is combined here as U, for an energy of

$$E_{DFT+U} = E_{LSDA} + \frac{U}{2}\sum_{\sigma}\left[\left(\sum_{m_1} n^{\sigma}_{m_1,m_1}\right) - \left(\sum_{m_1,m_2} n^{\sigma}_{m_1,m_2} n^{\sigma}_{m_2,m_1}\right)\right], \qquad (2.35)$$

where n^{σ} is the idempotentic on-site occupancy matrix, m_1 and m_2 are the particles of significant magnetic moment, and E_{LSDA} is the energy of the system in the local spin density approximation (an extension of LDA that takes into account the relative spin projections of the electrons). n^{σ} may be written as

$$n^{\sigma}_{m_1,m_2} = \sum_{n,\mathbf{k}} f^{\sigma}_{n,\mathbf{k}} \left\langle \psi^{\mathbf{k},\sigma}_{n} \right| P_{m_1,m_2} \left| \psi^{\mathbf{k},\sigma}_{n} \right\rangle, \qquad (2.36)$$

where $f^{\sigma}_{n,\mathbf{K}}$ is the occupation of a Kohn-Sham state, with values between 0 and 1 for the system with electronic spin, and P_{m_1,m_2} are the projection operators acting on a localised state [76]. These projection operators will be discussed further in section 2.4.2.

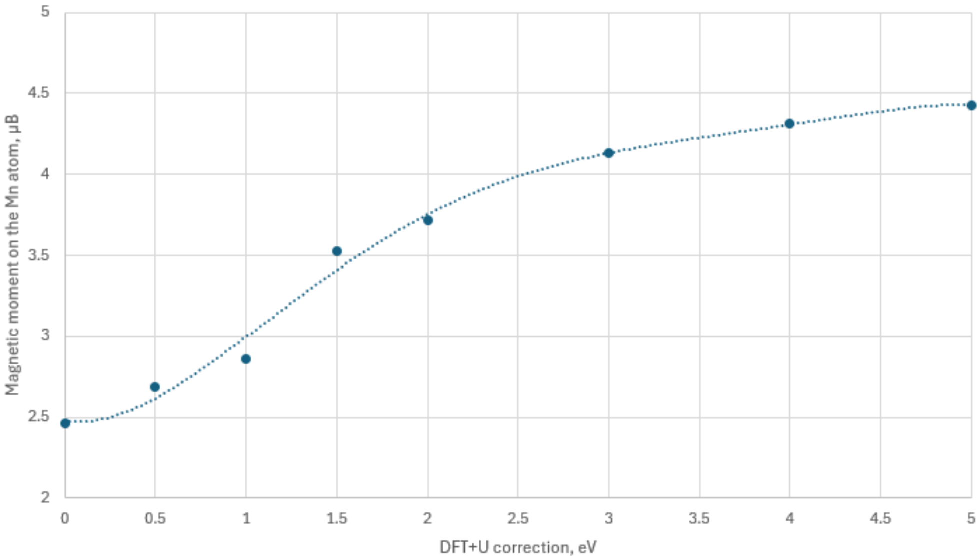

Figure. 2.1: MnGa in the ferromagnetic state will have varying magnetic moment with U. The dashed line provides a guide to the eye.

2.3.7 Crystal structure

A crystal structure is defined as a solid structure, within which the atoms are arranged in a highly ordered microscopic structure across all directions, forming a crystal lattice. The long range order may be represented by an array of discrete points (the basis) that repeat infinitely and crystals are generated by a set of translation (primitive) vectors applied to these points. A Bravais lattice is generated from the symmetry of the infinitely-repeating primitive vectors. There are 14 Bravais lattices that are symmetrically feasible [77, 78]. By repeating the translation of these points across a space using the primitive vectors, a lattice may be generated, which may then be populated by the basis, generating a structure.
Structural parameters determine the geometry of unit cells in a crystal. Usually, there are three length parameters, representing the three basis vectors of the Bravais lattice, usually labelled a, b and c respectively, and three angular parameters, α, β, and γ, shown in Figure 2.2. The structures may also be organised into 219 separate space groups, defined as the symmetry group of a set of points that repeat in (three-dimensional) space. These groups are collated based on the symmetry of the structural configuration of a material.

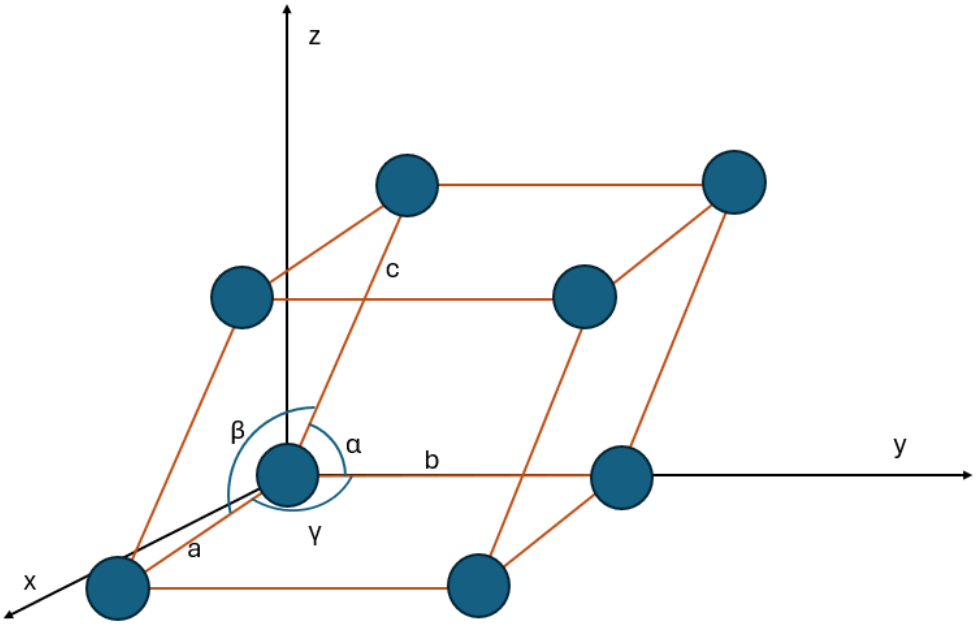

Figure. 2.2: A monoclinic Bravais lattice, illustrating the structural parameters a, b, c, α, β and γ that define the Bravais lattices

2.3.8 Born von Karman boundary conditions and Bloch's theorem

The Born von Karman boundary conditions, are a set of periodic boundary conditions that restrict a wavefunction to be periodic on a certain Bravais lattice [78]. Each cell is approximated to repeat infinitely along the basis vectors and tessellates into a full crystal structure. Periodicity is assumed here throughout this work for bulk structures.

Bloch's theorem builds on the Born von Karman boundary conditions. The theorem postulates solutions to a Schrödinger equation in a crystal can be expressed as plane waves modulated by periodic functions over the basis vector [79]. This theorem and subsequent work will assume Born von Karman boundary conditions,

$$\psi(\mathbf{r} + N_i\mathbf{a}_i) = \psi(\mathbf{r}), \tag{2.37}$$

where N_i is an integer in direction i representing a number of primitive cells below the maximum extent in some direction and $\mathbf{a_i}$ is a primitive vector of the crystal. We may define Bloch's theorem, stating that the Schrödinger equation with periodic potential is defined by plane waves modulating periodic functions. This is represented by the following equation,

$$\psi_{m\mathbf{k}}(\mathbf{r}) = e^{i\mathbf{k}\cdot\mathbf{r}}u_{m\mathbf{k}}(\mathbf{r}), \tag{2.38}$$

where m is the band index, $\mathbf{k}$ is the wave vector, and $u_{m\mathbf{k}}(\mathbf{r})$ is a function with the same periodicity as the crystal.

2.4 Computational implementation of density functional theory

2.4.1 Plane-wave basis set and k-point sampling

Plane-wave basis sets

A plane-wave basis set (PWBS) can be used as a set of functions to expand electron wavefunctions at each k-point [80]. The exponent of such a wavefunction's oscillating term includes wave vectors, and is described as above in Equation 2.38. One useful component of a PWBS is the ability to limit the basis set size by placing a limit on the kinetic energy $E_j = \frac{|\mathbf{G}_j|^2}{2}$; the cutoff energy defines the largest wave vectors in the basis set, whereby $\mathbf{G}$ is the reciprocal lattice vector, a vector constructed of translation vectors $\mathbf{T_n}$ such that $\mathbf{G} \cdot \mathbf{T_n} = 2\pi \times \textit{integer}$ [81, 82].

We also benefit from the same basis set for molecules and solids, making this calculation scalable for supercell calculations.

k-point sampling

Sampling over the Brillouin zone (the first Brillouin zone is defined as the locus/set of points in reciprocal space that is closer to some specified point, normally the gamma point, than any other set of reciprocal lattice points, and without crossing Bragg planes [83]) is necessary to calculate many properties. As such, we must integrate properties at each k-point over this zone. However, this can become a very complex integral to solve, and would be approximated well by a (weighted) sum over specific k-points. We may note that the occupancy of states $f(E)$ according to Fermi-Dirac statistics, expressed as

$$f(E) = \frac{1}{1 + e^{\frac{E-E_F}{K_B T}}}, \tag{2.39}$$

tends to zero in the lower temperature regimes for $E > E_F$ and to one for $E < E_F$ [80, 81]. Noting Pauli exclusion, we note that no two electrons can be in the same set of quantum numbers, and the temperature limit means electrons cannot change state. We therefore acknowledge the electron enthalpy must be minimal and all lowest states are filled. As such, the k-points that are allowed are only those that have a corresponding energy value below the Fermi energy, represented in momentum space by the according momentum value k_F. To calculate a function with complete lattice symmetry, $f(\mathbf{k})$, we make use of symmetrized plane waves. We may then make further generalisations in the crystal, insofar as having a periodic system [82],

$$\psi_{nk}(\mathbf{r}) = \frac{1}{\sqrt{V}} \sum_{\mathbf{G}} C_{n,k,\mathbf{G}}(\mathbf{G}) e^{i(\mathbf{k}+\mathbf{G})\cdot\mathbf{r}}, \tag{2.40}$$

and the electron density $\rho(\mathbf{r})$ is

$$\rho(\mathbf{r}) = \frac{1}{\Omega_k} \int |\psi_{mk}(\mathbf{r})|^2 d^3\mathbf{k} \approx \frac{1}{N_k} \sum_{k} |u_{mk}(\mathbf{r})|^2. \tag{2.41}$$

The other properties can be calculated by summing over $\mathbf{k}$ for these properties at each k-point for the result of calculating these properties at each k-point. We use the density calculated via Equation 2.41 alongside the SCF method to self-consistently solve the Kohn-Sham equations.

The discrete nature of the k-points being used to generate the sampling grid, as

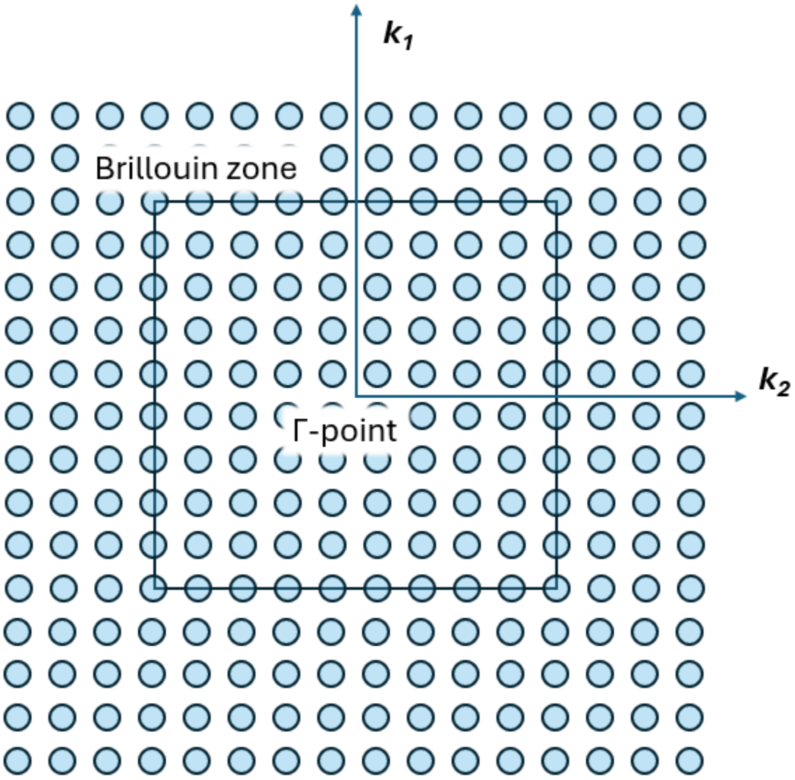

Figure. 2.3: 2D k-point sampling grid over a square Brillouin zone, the extent of which is $\frac{2\pi}{a}$, where a is the lattice spacing. The Γ-point is the k-point where $\mathbf{k} = (0, 0, 0)$

shown in Figure 2.3 which is an example of a gamma-centred grid [84], means we can sample the Brillouin zone as a sum at these specific points mentioned earlier. A Monkhorst-Pack k-point grid, defined as a uniform grid of k-points within a Brillouin zone with no set centering, will not necessarily include the gamma point for all selections of k-point density, instead being homogeneously distributed along the lattice vectors in the Brillouin zone [85]. The periodic lattice needs a finite number of k-points in periodic directions in order for the variation in energy term coefficients to be calculated, so we need to ensure a discrete evaluation grid is developed for these calculations. We therefore may specify a set number in specific directions to facilitate varying geometries and periodicities of lattices, with a high enough number of k-points to specify a consistent result. As the lattice is periodic and symmetric, it is worth noting many k-points are equivalent, and as such the number of k-points needed to fully assess a Brillouin zone is reduced.

2.4.2 PAW methodology and Pseudopotentials

To fully discuss pseudopotentials, we must first discuss core electron orbitals. Core electron orbitals are filled orbitals deep within the orbital structure close to the nucleus. The orbitals are approximated to be localised around one atom. The core and valence electron orbitals are orthonormal. The valence orbitals are only included in calculation as the core orbitals are located about the nucleus in order to augment the electrostatic properties correctly such as the resultant charge (this is the frozen core approximation, whereby the core electrons are considered as being a non-polarizable and rigid component of the ionic core) [86].

Pseudopotentials are an attempt to alter the potential to produce a system where core sites are frozen and the core states eliminated whilst also describing the valence electrons with a set of altered pseudo-wavefunctions with fewer nodes.

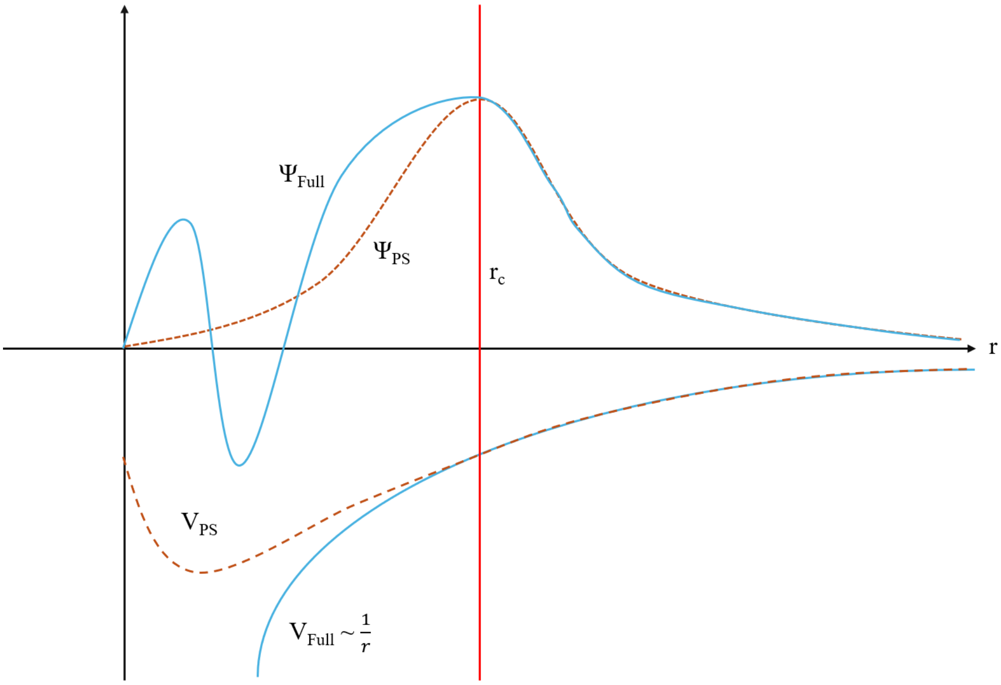

Figure. 2.4: The approximation of the pseudopotential as a function of r. r_c is the cutoff radius under which the approximation is no longer valid. Here, the dashed lines represent pseudopotential wavefunctions and potentials ψ_{PS} and V_{PS}.

The projector augmented wave (PAW) pseudopotentials are a generalisation of pseudopotentials and the linear augmented plane wave method [87]. Rapidly oscillating wavefunctions exist near the core region due to orthogonality requirements, resulting in the need for high-Fourier-order description to be accurate, as shown in Figure 2.4. To describe the addition of pseudopotentials, a transformation that allows all-electron properties to be found using a pseudo-wavefuction $|\psi'\rangle$, based on a pseudo-potential [87] is developed. The rapid oscillations need to be changed to smooth variations in order to reduce expense when using PWBS. We begin with an augmentation of the wavefunction,

$$|\psi\rangle = \hat{\tau}\,|\psi'\rangle = \hat{\tau}\sum_i |\phi'_i\rangle\, c_i, \tag{2.42}$$

where $\hat{\tau}$ is the linear translation operator. We may then write

$$c_i = \langle p_i|\psi'\rangle\,, \tag{2.43}$$

where p_i are projector functions defined by $\langle p_i|\phi'_j\rangle = \delta_{ij}$. The all-electron partial waves, $|\phi_i\rangle = \hat{\tau}\,|\phi'\rangle$, are typically solutions to the isolated atom's Kohn-Sham equation [88]. $\hat{\tau}$ is governed by the sets of $|\phi_i\rangle$, $|\phi'\rangle$ and $|p_i\rangle$, and may be written as

$$\hat{\tau} = 1 + \sum_a \hat{\tau}'_a = 1 + \sum_i (|\phi_i\rangle - |\phi'_i\rangle)\,\langle p_i|\,, \tag{2.44}$$

where $\hat{\tau}'_a$ is non-zero only within some spherical augmentation region called Ω_a that encloses atom a, and $|\phi_i\rangle$ is a pseudo partial wave and $|\phi_i\rangle = \hat{\tau}\,|\phi'_i\rangle$. Note $|\psi'\rangle$ is fictitious and $|\psi\rangle$ is the all-electron (single particle) wavefunction. The pseudo-partial waves are equal to the all-electron partial waves outside the region Ω_a and are smoothly varying within. The result is a projector augmentation of the wavefunction that preserves the orthogonality whilst altering purely the rapidly oscillating region.

2.4.3 Spin-orbit coupling and noncollinear calculations

The spin-orbit coupling (SOC) can be defined as the relativistic interaction between the spin of a particle within the atom and the potential of the nucleus. Normally we exemplify this via the orbital electrons interacting with the electrostatic potential of the nucleus and the magnetic dipole and orbital motion of the electron. As such, to correct for the SOC, we add the following term to the Hamiltonian:

$$\hat{\mathcal{H}}^{\alpha\beta}_{soc} \propto \hat{\sigma}\cdot\hat{\mathbf{L}}, \tag{2.45}$$

where σ is the Pauli spin operator, α and β are the relative spins of the two coupled particles, generally electrons in this thesis, and $\hat{\mathbf{L}}$ is the angular momentum operator [89]. This relationship is determined from the Dirac equation for a free particle in a potential,

$$i\hbar\frac{\partial\psi(\mathbf{r},t)}{\partial t} = (c\boldsymbol{\alpha}\cdot\left(\frac{\hbar}{i}\boldsymbol{\nabla} - e\mathbf{A}(\mathbf{r})\right) + \beta mc^2 + V(\mathbf{r}))\psi(\mathbf{r},t) \tag{2.46}$$

where **A** is the vector component of the field, $V(\mathbf{r})$ is the scalar potential, and α and β are the invariant matrices, modifications of the Pauli spin matrices to 4-space and a modified identity matrix respectively [90]. We can expand this in the non-relativistic limit to produce the (relativistically corrected) Dirac equation,

$$\begin{aligned} E\psi = \Bigg(&\frac{(\hat{P} - \frac{e}{c}\hat{\mathbf{A}})^2}{2m} - \frac{Ze^2}{4\pi r} - \frac{\hat{P}^4}{8m^3c^2} + \frac{Ze^2\hbar\hat{\sigma}\cdot\hat{\mathbf{L}}}{16\pi m^2c^2r^3} \\ &+ \frac{Ze^2\hbar^2}{8m^2c^2}\delta^3(\mathbf{r}) - \frac{e\boldsymbol{\sigma}\cdot\mathbf{B}}{2m} + e\boldsymbol{\phi}\Bigg)\psi, \end{aligned} \tag{2.47}$$

where $\hat{P}$ is the momentum operator, Z is the number of electrons, $\delta^3(\mathbf{r})$ is the three-dimensional delta function at position $(\mathbf{r})$, $\hat{\mathbf{A}}$ is the electromagnetic 4-potential, **B** is the magnetic field, $\boldsymbol{\sigma}$ is the Pauli matrix vector, $\boldsymbol{\phi}$ is the electric potential and c is the speed of light [91]. The fourth term, $\left(\frac{Ze^2\hbar\hat{\sigma}\cdot\hat{\mathbf{L}}}{16\pi m^2c^2r^3}\right)\psi$, is the vector spin-orbit contribution. The scalar nature of the other terms allows for them to be included even in noncollinear calculations.

Next, we restrict SOC to the PAW sphere, with the relativistic correction becoming

$$\mathbf{E}^{ij}_{soc} = \delta_{\mathbf{R}_i\mathbf{R}_j}\delta_{l_il_j}\sum_{nk} w_k f_{nk}\sum_{\alpha\beta}\langle\psi^{\alpha}_{nk}|p_i\rangle\langle\phi_i|\hat{\mathcal{H}}^{\alpha\beta}_{soc}|\phi_j\rangle\left\langle p_j\middle|\psi^{\beta}_{nk}\right\rangle \tag{2.48}$$

and w_n, f_{nk} are k-point and Fermi weights respectively [92]. ψ^{α}_{nk} is the spinor of pseudo orbital with alpha determining spin-up or down, and ϕ_i are partial waves. The relativistic correction to the SOC in a noncollinear configuration has a spinor nature. The mixing of spin-up and spin-down states provides for the noncollinear arrangement of spins, and by extension magnetic moments, within the material [93]. The wavefunction may be chosen as an eigenfunction of $\hat{\sigma}$, with the spin magnetization becoming an expectation value of the wavefunction, and we develop an uncompensated spin density [94], as seen in Figure 2.5.

In VASP, in order to model the spins on each atom, we initialise a set of magnetic moments and their configuration as a real-space 3-vector relative to some axis, known as the quantisation axis, as the starting point for a calculation. The choice of quantisation axis is best taken with some degree of commonality to the magnetic moment vectors, allowing for ease of directional definition. Including magnetic field

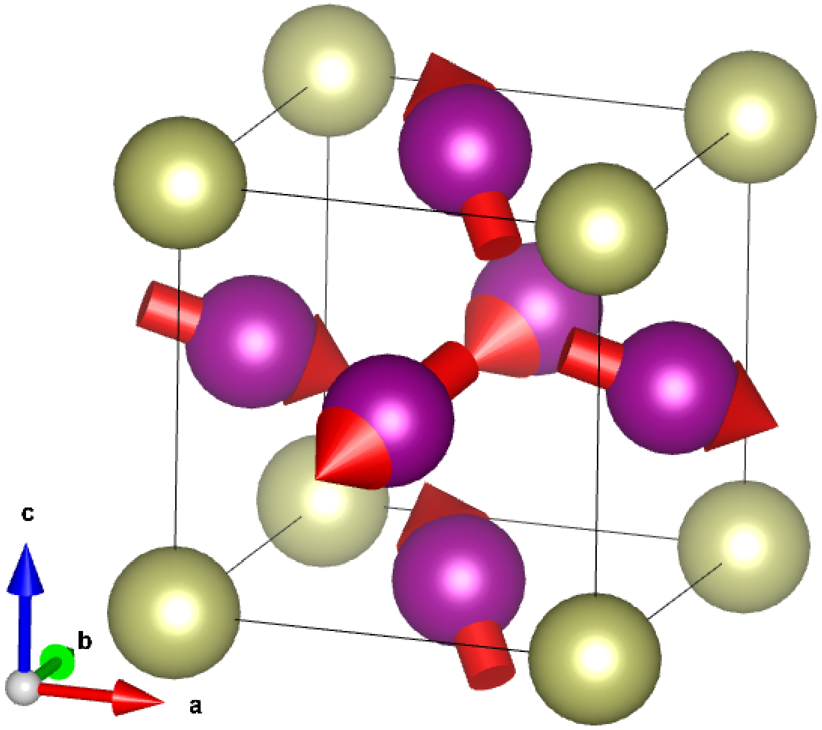

Figure. 2.5: 3D representation of noncollinearity. The red arrows represent the canting magnetic moments.

interactions, we can then generate a Kohn-Sham equation of the form

$$\begin{aligned} E[\rho(\mathbf{r})] = \sum_{i}^{N} \epsilon_i - \frac{e^2}{2} \int \frac{\rho^{\uparrow}(\mathbf{r})\rho^{\uparrow}\prime(\mathbf{r})}{|\mathbf{r}-\mathbf{r}'|} d\mathbf{r} d\mathbf{r}' - \frac{e^2}{2} \int \frac{\rho^{\downarrow}(\mathbf{r})\rho^{\downarrow}\prime(\mathbf{r})}{|\mathbf{r}-\mathbf{r}'|} d\mathbf{r} d\mathbf{r}' \\ - \int V_{XC}[\rho^{\uparrow}(\mathbf{r})]\rho^{\uparrow}(\mathbf{r}) d\mathbf{r} - \int V_{XC}[\rho^{\downarrow}(\mathbf{r})]\rho^{\downarrow}(\mathbf{r}) d\mathbf{r} \\ + \int \rho(\mathbf{r})(\epsilon_{xc}[\rho^{\uparrow}(\mathbf{r}), |\nabla(\rho^{\uparrow}(\mathbf{r}))|] + \epsilon_{xc}[\rho^{\downarrow}(\mathbf{r}), |\nabla(\rho^{\downarrow}(\mathbf{r}))|]) d^3\mathbf{r} \\ + \sum_{i} \sum_{j} \delta_{\mathbf{R}_i \mathbf{R}_j} \delta_{l_i l_j} \sum_{nk} w_k f_{nk} \sum_{\alpha\beta} \langle \psi_{nk}^{\alpha} | p_i \rangle \langle \phi_i | \hat{\mathcal{H}}_{soc}^{\alpha\beta} | \phi_j \rangle \left\langle p_j \middle| \psi_{nk}^{\beta} \right\rangle + \sum_{i} \boldsymbol{\sigma}_i \cdot \mathbf{B}(r_i). \end{aligned} \tag{2.49}$$

2.4.4 Band structure

Band structure plots are useful for illustrating the electronic properties of a system. By using the equation for the band energy $E_n(k)$ (Equation 2.47 and the correction, Equation 2.48), plotted against the reciprocal lattice vector (with particular high symmetry points noted on this axis to highlight the unique properties in these regions), we can develop a spectrum of energetic variation with location in reciprocal space, which identifies the energy bands a system has (as well as identifying forbidden bands) [95], such as in Figure 2.6.

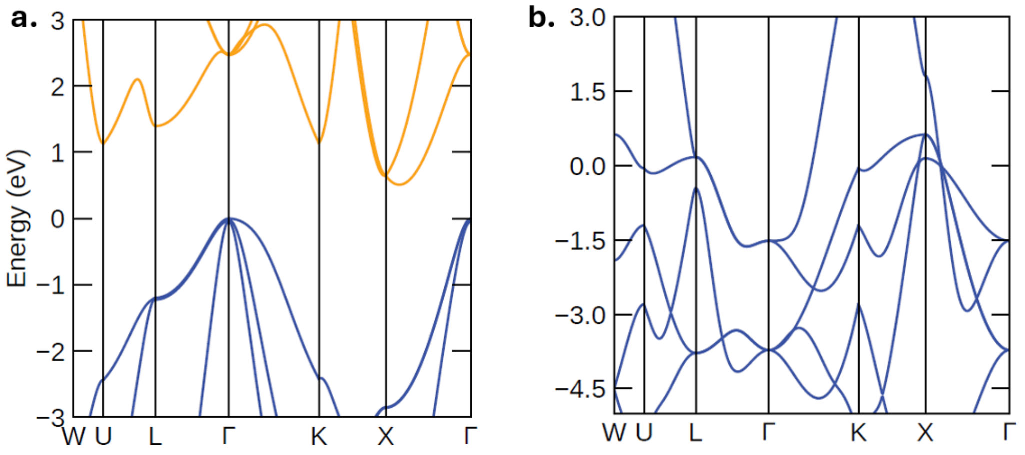

Figure. 2.6: Band structures calculated using GGA for a) silicon, a semiconductor, b) platinum, a transition metal.

We may use this band structure to determine specific properties of the system such as band gaps and the population of conduction and valence bands, which can illustrate the conductivity properties of a system (Figure 2.7). We can use specific high-symmetry points of the lattice of reference to determine the points of interest in reciprocal space, and use these points to determine a path in K-space to follow. This allows for important routes of points to be explored throughout the material.

2.5 Magnetism

A magnetic material is a material that has significant spin/magnetic moment on atoms within the configuration, has a significant exchange interaction and magnetic moments that are of regular orientation [78]. Examples of magnetic orders include ferromagnetism, in which all magnetic moments align in parallel in the ground state, or antiferromagnetism, where the overall magnetisation is zero, and the material exhibits microscopic ordering of magnetic moments that sum to give zero magnetisation.

Magnetic moments are the magnitude and orientation of magnetic field produced by local spin configuration, e.g. ions, electrons and groups thereof [78]. Magnetic moment here is the prevailing spin combination of electrons in electronic orbitals

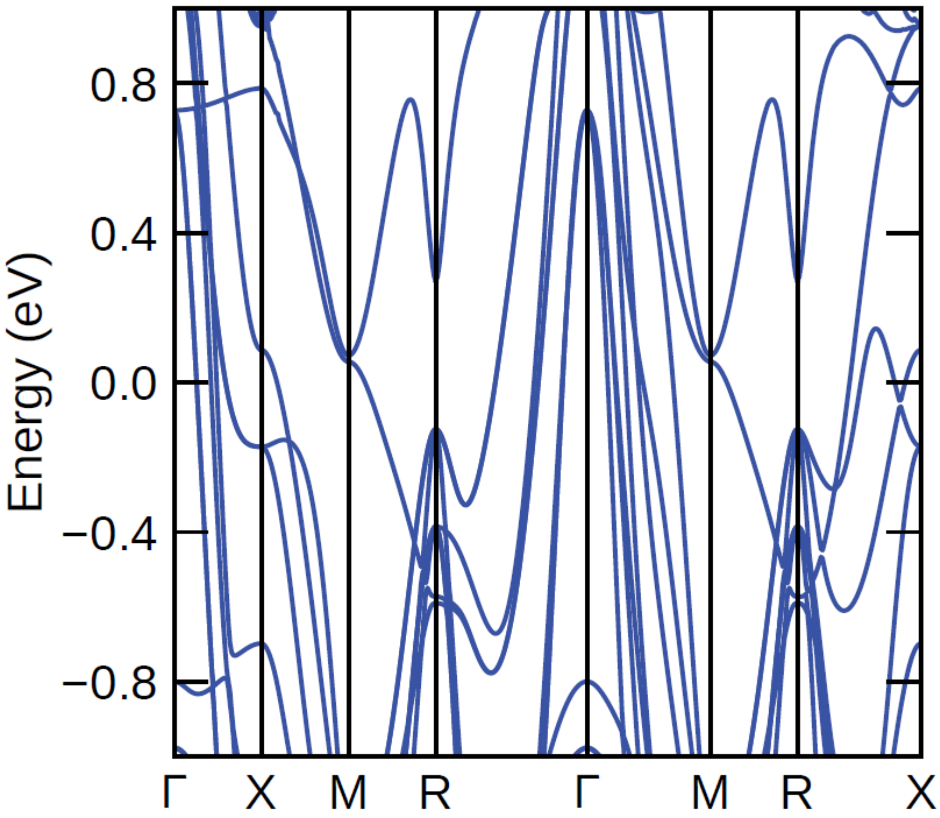

Figure. 2.7: Band structure for L1_2-Mn_3Ir over a range of 2 eV. Note the x-axis contains four high-symmetry k-points.

of the atom. The magnetic dipole moment of an atom (without nuclear magnetic moment) can be defined mathematically using quantum mechanics,

$$\mathbf{m}_{atom} = g_J \mu_B \frac{\mathbf{J}}{\hbar}, \tag{2.50}$$

where g_J is the Landé g-factor, μ_B is the Bohr magneton, and $\mathbf{J}$ is the total angular momentum [96]. For a crystal, the magnetic moment is the integral of the spin density over a single atom; the total magnetisation is the integral of the spin density over the volume of the crystal being analysed.

2.5.1 Exchange interaction

Throughout this chapter, we have mentioned the exchange interaction. In a magnetic material, this exchange interaction is governed by the Pauli exclusion principle, noting that identical spin states/quantum numbers prevent identical spatial states. As such, when orbitals overlap, some materials have preferences for relative orientations. For example, certain materials will have a relative preference to align spins when the electrostatic energy is reduced by the increased distance of the parallel spins from each other. For other materials, the antiparallel configuration (or some other noncollinear configuration of magnetic moments) reduces the electrostatic energy [97].

2.5.2 Magnetic order

Magnetic orders are a consequence of the magnetic moments forming regular repeated patterns of orientations. Depending on how they orient, the classification of the material differs; some will find an overall magnetic moment and become ferri- or ferromagnetic, or find no field overall and be antiferromagnetic. Magnetic structure is a consequence of the magnetic moments and magnetic order. The array of magnetic moments influence each other, and will settle on relative orientations that minimize the energy of the configuration. This structure will repeat within the bulk, much like the ionic structure. In order to determine the nature of the magnetic order of a configuration, we may use the quantum Heisenberg model (with the two key assumptions being aligned magnetizations produce minimum energy and the use in a one-dimensional periodic lattice to simplify this model) to determine the nature of the ordering [98, 99], whereby the Hamiltonian is given as

$$\hat{\mathcal{H}} = -\left(\frac{\hbar}{2}\right)^2 \left(\sum_{\langle i,j\rangle}^{N} J_{ij}\sigma_i \cdot \sigma_j\right), \tag{2.51}$$

where J_{nn} is the coupling constant between neighbouring dipoles n, N is the number of dipoles in the system and σ_j are the spins of dipole j, represented using Pauli spin matrices (whereby $\mathbf{S} = \frac{\hbar}{2}\sigma$) with periodic boundary conditions, i.e,. $\sigma_{N+1} = \sigma_1$,

$$\sigma^x = \begin{bmatrix} 0 & 1 \\ 1 & 0 \end{bmatrix}, \sigma^y = \begin{bmatrix} 0 & -i \\ i & 0 \end{bmatrix}, \sigma^z = \begin{bmatrix} 1 & 0 \\ 0 & -1 \end{bmatrix}. \tag{2.52}$$

We note that both conductors and insulators may gain a magnetic ordering; in itinerant electron magnetic metals like Ni, for example, a ferromagnetic order is observed. This is due to the exchange interaction in the partially filled d-shell, whereby like spins may form. Whilst NiO should seemingly form an antiferromagnetic structure and remain a conductor, it is due to the Coulomb repulsion in the d-shell that we see it remain a (Mott) insulator [100]. We can reformulate the Hamiltonian in Equation 2.51,

$$\hat{\mathcal{H}} = -\left(\frac{\hbar}{2}\right)^2 \left(\sum_{j=1}^{N} J_x \sigma_j^x \sigma_{j+1}^x + J_y \sigma_j^y \sigma_{j+1}^y + J_z \sigma_j^z \sigma_{j+1}^z + h\sigma_j^z\right), \tag{2.53}$$

where J_x, J_y, J_z are all real-valued and h is the spin constant of the external magnetic field. By setting $J_x = J_y = J_z = J$, known as the Heisenberg "XXX" model, we can define ferromagnetic models as those with with a positive value of J, and antiferromagnetic models with a negative value of J [99].

AFM materials are a long-range ordering phenomenon, and have no prevalent total magnetic moment at zero magnetization despite significant individual atomic magnetic moment. The moments may align collinearly, with atomic moments aligning antiparallel to eachother, parallel to some quantization axis. The moments may also align noncollinearly, whereby the magnetic moments of the atoms do not share a common quantization axis that is parallel/antiparallel to each moment.

To give more detail on the two key magnetic phases with respect to the crystal structure, ferromagnetic (FM) transition metal materials are defined as having prevailing collinear atomic moments, all oriented in the same direction, with long-range ordering phenomenon to generate a macroscopic magnetic field at zero external field, and obey the Stoner criterion (determined from the effect of the Pauli exclusion principle on the energetic cost for spins near the Fermi level to order in a parallel manner, i.e. in a ferromagnetic formation of like moments),

$$ID(E_F) > 1, \tag{2.54}$$

where I is the Stoner parameter, and $D(E_F)$ is the density of states at the Fermi energy, E_F [101, 102]. Transition metals such as cobalt, iron, manganese gallium (1:1 alloy), and nickel are ferromagnetic.

We mainly focus on ferromagnetic, antiferromagnetic and very low magnetisation ferrimagnetic materials in this work.

2.5.3 Temperature effects

There are many temperature-dependent aspects to magnetic properties. For the materials we study, it is worthwhile outlining the temperature effects and properties associated with these effects. Magnetic materials may change the magnetic phase they take based on the temperature of the system in which they exist. This change of magnetic ordering is called a magnetic phase transition. As such, these phase changes exhibit changes in the magnetization, which we will use here as our ordering parameter (a parameter that is defined as the ratio of a quantity in two phases [103]).

With regard to the change in magnetic moment with temperature, the general excitation of electrons as well as spin-excited phenomena with increased thermal energy causes a reduction and outright breakdown of prevailing magnetic moment at certain temperature ranges. We can define the temperatures at which this magnetic phase change occurs as the Curie and Néel temperature, which determine the temperature below which a material may maintain its ferromagnetic and antiferromagnetic nature respectively in the absence of an external field [78].

The Curie temperature for a ferromagnet can be defined mathematically for an approach in the temperature range just below the Curie temperature approximately as

$$M_s(T) \approx C|T_c - T|^{\beta}, \tag{2.55}$$

where C is a constant, T_c is the Curie temperature, $M_s(T)$ is the magnetization of the system (or for the Néel temperature, the sublattice magnetization), and β is specific to the magnetic model. For 3D Heisenberg and Ising models, the values of β are approximately 0.365 and 0.325 respectively [104]. The Néel temperature for antiferromagnets, the temperature below which a material may retain antiferromagnetic ordering, can be represented in much the same way as the Curie temperature, albeit with differing constants and values of β (Figure 2.8).

We can map the effect of the change in temperature by using the molar magnetic susceptibility, χ_ρ, defined as

$$\chi_\rho = \frac{M|\mathbf{M}|}{|\mathbf{H}|\rho}, \tag{2.56}$$

where $\mathbf{M}$ is the magnetic moment per unit volume, M is the molar mass, ρ is the material density and $\mathbf{H}$ is the magnetic field strength [105].

2.5.4 Noncollinear antiferromagnets

Noncollinear antiferromagnetic materials can simply be defined as a material with antiferromagnetic ordering (no resultant magnetic moment for the material in bulk) where the moments do not exhibit long-range collinear ordering, instead exhibiting local arrangements with zero net magnetization and no common quantization axis parallel to the moments. As the arrangement of the magnetic moments does not align with a common quantisation axis, instead they align in a manner befitting their magnetic phase, such that there is no overall magnetic moment in antiferromagnets, but with significant angular deviation between each magnetic

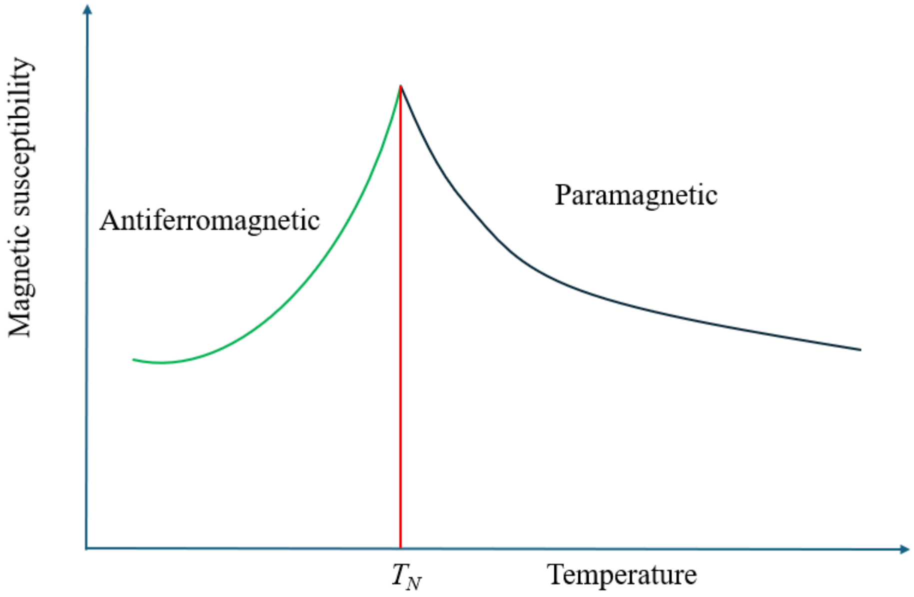

Figure. 2.8: The Néel temperature T_N, shown here as a point on a magnetic susceptibility vs temperature graph.

moment [106]. This ordering locally forms a regular series of angular distributions, sometimes with a common perpendicular axis such as those in the $L1_2$ and $D0_{19}$ distributions. Many magnetic orders may exhibit noncollinear ordering, including ferrimagnets and antiferromagnets (Figure 2.9).

2.5.5 Anisotropy

The magnetocrystalline anisotropy is the tendency for magnetic moments to align along some particular axis, whereby there is a distinct energy difference for magnetization in different orientations of the field, defined by the difference in energy between the easy axis (lowest energy) and hard axis (highest energy) [107]. This phenomenon is a consequence (to first order) of the spin-orbit interaction insofar as the electronic orbitals are coupled to the electronic spin and tend to follow it when the magnetization changes, and depend on the interaction between the orbital motion of the (d- or f-) charge cloud and the crystal electric field, the charge distribution surrounding the cloud. When the charge coupling dominates, the energy changes as a function of the spin-orbit energy, and when the spin-orbit coupling dominates, the energy varies with the electronic wavefunction in the crystal field [108]. This is expressed mathematically in spherical polar coordinates as

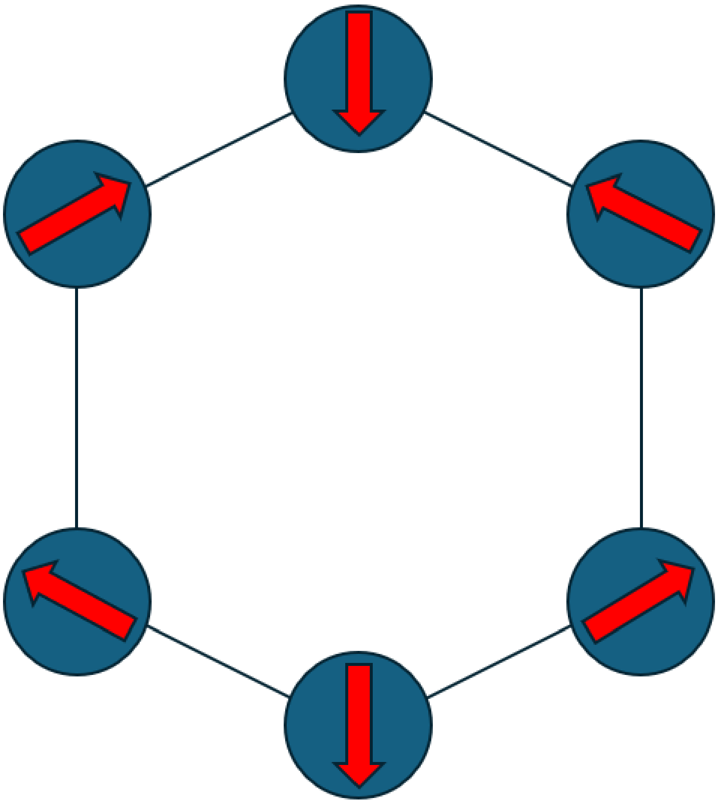

Figure. 2.9: A hexagonal noncollinear antiferromagnetic arrangement. The magnetic moments lie in-plane with differing angles.

$$\Delta E_{MCA} = E_{\theta,\phi} - E_0, \tag{2.57}$$

where E_{MCA} is the magnetocrystalline anisotropy energy, $E_{\theta,\phi}$ is the energy at some polar direction with parameters $\boldsymbol{\theta}, \boldsymbol{\phi}$, and E_0 is the energy at the most stable orientation of spin.

For the structures featured in this thesis, we investigate the tetragonal and hexagonal systems. E_{MCA} for each structural system is expressed as, to sixth order,

$$\begin{aligned} E^{Tetr}_{MCA}/V = K_1 \sin^2(\theta) + K_2 \sin^4(\theta) + K_2' \sin^4(\theta)\cos(4\phi) \\ + K_3 \sin^6(\theta) + K_3'' \sin^6(\theta)\cos(4\theta), \end{aligned} \tag{2.58}$$

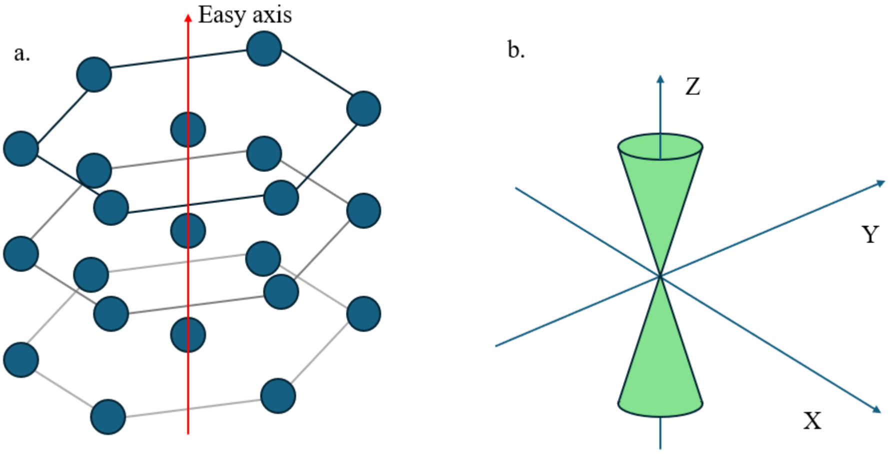

Figure. 2.10: a) A hexagonal system with the easy axis labelled, b) the minimum energies of the system, known as an "easy cone"

$$E_{MCA}^{Hex}/V = K_1 \sin^2(\theta) + K_2 \sin^4(\theta) + K_3 \sin^6(\theta) + K_3'' \sin^6(\theta) \cos(6\phi), \tag{2.59}$$

where K_n and K_n' are parameters that have the units of energy density and V is the volume of the system [109]. The minimum energy lies along an axis called the "easy axis", and likewise the maximum energy lies along the "hard axis". Sometimes, these axes may be degenerate within a plane or surface (Figure 2.10), and it should be noted cubic systems differ from tetragonal systems by fixing the ratios such that fourth-order symmetry in lateral axes is obeyed [110]. The dependence of the magnetocrystalline anisotropy on the spin-orbit interaction is found in the contribution of the interaction of $\mathbf{S} \cdot \mathbf{L}$; for nondominant spin-orbit coupling, the variation of $\mathbf{S}$ with magnetic moment, $\mathbf{M}$, is the main anisotropic effect. For dominant spin-orbit coupling, $\mathbf{L}$ and $\mathbf{S}$ follow together, and the variation of $\mathbf{L}$ with the crystal field becomes the major contribution. Both show easy and hard axes as aspects of this spin-orbit interaction [108]. It should be noted that the magnetocrystalline anisotropy energy does have some dependence on temperature and atomic number, Z, as seen in Equation 2.47. Generally, the increase in temperature toward the Néel temperature results in decreased anisotropy energy due to the reduced coupling of nearest neighbours. This is evident beyond the Néel point when the magnetic order changes, thus we see a maximum of magnetic susceptibility at the Néel temperature.

2.5.6 Magnetic dipole contributions

The magnetic dipole-dipole interaction is based on the intrinsic magnetism of fundamental particles (electrons) and their motion about the nucleus, and so it can be thought of as the pseudo-classical representation of the magnetic effect of electrons orbiting in a "current" about the nucleus. This "current" the electrons generate in an orbital generates a magnetic dipole in turn. These may then interact with other nearby magnetic dipoles [111]. The energies in DFT do not take into account the magnetic dipole-dipole interaction. As such, a correction is needed in order to accurately reflect this. The dipole energy for a given system relies on the classical dipole model. For an array of classical spins in a magnetic field, the dipoles interact as a function of distance and magnetic moment [112, 113]

$$E_d = \frac{\mu_0}{8\pi} \int \int \frac{3(\mathbf{m}(\mathbf{r}_1) \cdot \mathbf{r}_{12})(\mathbf{m}(\mathbf{r}_2) \cdot \mathbf{r}_{12}) - \mathbf{m}(\mathbf{r}_1) \cdot \mathbf{m}(\mathbf{r}_2) r_{12}^2}{r_{12}^5} d^3\mathbf{r}_1 d^3\mathbf{r}_2. \quad (2.60)$$

We note that, as the magnitude of the dipole energy is a small contribution to the total energy, we may treat it approximately. This is due to the second-order relativistic nature of the correction. Because of the strong localisation around the transition metals considered in this work, we may replace the magnetization density with a magnetic moment of uniform magnitude but varying direction, $\boldsymbol{\mu}_i = \mu \hat{\mathbf{m}}_i$ where $\hat{\mathbf{m}}_i = \sigma_i \mathbf{S}$, and $\mathbf{S}$ is a specific discretization axis and σ_i is the relative reorientation to this axis of spin i at distance r_i from the ion. We can therefore rewrite Equation 2.60 into

$$E_d = \frac{\mu_0 \mu^2}{8\pi r_1^3} \sum_i \sigma_i [3(\mathbf{S} \cdot \hat{\mathbf{r}}_i)^2 - 1](\frac{r_1}{r_i})^3. \quad (2.61)$$

The SOC magnetic anisotropy energy (MAE) contribution can be expected to be the largest share for most materials due to the dominating nature of the SOC effect from the unfilled electron shells.

We use the dipole solving program, Just Another Magnetic Simulator (JAMS) [40], to calculate these changes in energy. We perform the calculation over a single timestep and use the DFT-optimised magnetic system and unit cell to determine the dipole anisotropy of the system. We directly rotate the magnetizations in order to determine the change in energy with the magnetic structure changes.

2.5.7 Magnetic frustration and Dzyaloshinskii-Moriya interactions

Magnetic frustration has a significant but small role in the formation of the magnetic structures of manganese-rich materials, such as the ones investigated in this thesis, as well as the Dzyaloshinskii-Moriya interaction (DMI) [114, 115]. Magnetic frustration occurs when magnetic moments have no ability to simultaneously minimise their magnetic moment with nearest neighbours, resulting in orientation which provides degenerate energy states. A frustrated magnetic system is therefore a system of magnetic moments that are not held in a non-degenerate energetically minimised form. The DMI is based on the canting of magnetizations in ordered magnetic systems, and primarily governs why the magnetic moments form in a planar manner without canting out of the plane [116, 47]. For the DMI, we may define it as the contribution to the total magnetic exchange interaction between nearest neighbour magnetic spins; the DMI is also therefore known as the antisymmetric exchange, with the Hamiltonian

$$\hat{\mathcal{H}}_{\rangle|}^{\mathcal{DM}} = \mathbf{D}_{ij} \cdot (\hat{\mathbf{S}}_i \times \hat{\mathbf{S}}_j), \tag{2.62}$$

where D_{ij} is a vector defined by the symmetries of nearby ions and $\hat{\mathbf{S}}_i$ is the spin operator of ion i. These systems tend to have magnetizations ordered in multiple directions, critically only occurring in systems with broken inversion symmetry. In certain materials, such as $\mathrm{Mn_3Ir}$-$L1_2$ and $D0_{19}$ $\mathrm{Mn_3X}$ systems, the magnetizations sit in the (1-11) plane and (001) plane, with the unit cell having three separate directions of magnetization within this plane [117, 118]. The resulting structure can be ferro, ferri or antiferromagnetic. $D0_{19}$ frustrated systems have a significant magnetic contribution from the DMI insofar as the noncollinear magnetizations are stabilized at 120° from each other. The neighbouring magnetic moments in the material interact, producing a canting of the moments from an otherwise (anti-)parallel configuration. Considering the symmetry of the crystal, this interaction can contribute significantly to determining the magnetic structure, in particular the stability of the noncollinear ordering [119, 120]. $L1_2$ systems form with planes of atoms of identical species in the (1-11) plane, resulting in the DMI and the dominant magnetocrystalline anisotropy forming the noncollinear moments along the (1-11) plane. The magnetic moments form Kagome triangles, trihexagonal tiling of magnetizations, in this plane [116]. The $D0_{19}$ structures also have planes of like-species, which means the magnetic moments form planar structures in the (001)/(00-1) planes.

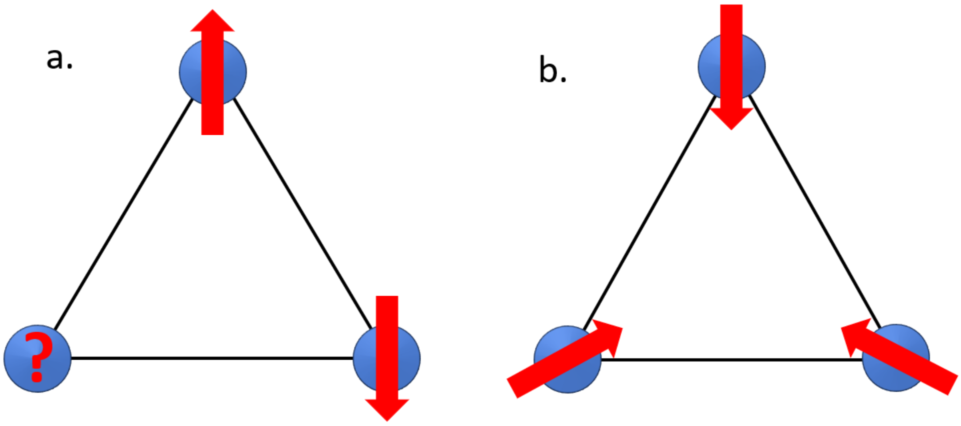

Figure. 2.11: a) A three-component triangular antiferromagnet, b) the according magnetic moments

In this work, we consider a range of Mn-alloys that exhibit a more complex magnetic order that is more frustrated than those with a collinear antiferromagnetic order, and note the contribution of DMI to these materials and their properties in terms of spin canting in otherwise ordered systems. Systemic frustration is defined classically by a system with a Hamiltonian that has competing components that cannot be simultaneously minimised [121]. Magnetic frustration is an example of systemic frustration, whereby the Hamiltonian of certain systems is frustrated by inclusion of part or all of the magnetic interaction terms; the combination of magnetic moment interactions in the Hamiltonian alongside the other exchange terms means the Hamiltonian cannot be simultaneously minimised. We present here a Hamiltonian (a simplified Heisenberg-Dirac Hamiltonian) to represent a simple system of three atoms with prevailing spin configurations S_1, S_2, and S_3,

$$\hat{\mathcal{H}} = \frac{J}{2}|\hat{\mathbf{L}}|^2 + c, \tag{2.63}$$

where the spin summation operator, $\hat{\mathbf{L}} = \hat{\mathbf{S}}_1 + \hat{\mathbf{S}}_2 + \hat{\mathbf{S}}_3$ and J is the exchange coupling term [122]. By noting that for antiferromagnetic materials, the exchange term J in the Heisenberg-Dirac Hamiltonian must be negative, the sum of the local spins $\hat{\mathbf{L}}$ in the Hamiltonian must be zero for there to be a ground state (and an antiferromagnetic ground state therefore), and therefore extending to the whole lattice (for example, by Maxwellian counting argument), we understand that the local degrees of freedom of the magnetic moments cannot take a collinear ordering without the system leaving the ground state manifold [123, 124, 125].

For an example, Figure 2.11 shows a triangular combination of three atoms of the same species in a lattice. If each atom has an identical magnetic moment, the magnetic structure of this system cannot minimize collinearly to produce an antiferromagnet. Noting again a negative J, we must therefore find a configuration that allows for antiferromagnetism. In Figure 2.11b, we see that the magnetic moments in the system may alter their direction to be noncollinear to compensate each other, providing an antiferromagnetic configuration, $\hat{\mathbf{L}} = 0$. This can be clarified further by Maxwellian counting argument as explained in Lacroix et al's Introduction to Frustrated Magnetism [122], noting that for a system of N classical Heisenberg spins that are defined in radial polar coordinates with angles θ and ϕ, the number degrees of freedom, F = 2N for the two angles. For systems with a number of clusters (groups of spins) equivalent to C, the number of constraints, K = 3C as $\hat{\mathbf{L}}$ is a three-component operator. Assuming simultaneous solution of the constraints, the ground-state degrees of freedom, D = F - K. For a triangular system, normally N = $\frac{3C}{2}$, so D = 0, however specific arrangements may be found in examples such as Heisenberg antiferromagnets where D = $\frac{N}{9}$, an extensive quantity, thus there are local degrees of freedom which may fluctuate independently without the system exiting the ground state. Whilst not all noncollinear materials are frustrated, this explanation provides key insight into understanding noncollinear antiferromagnetism generally.

The DMI and magnetocrystalline anisotropy alter the symmetry of the planar magnetic system, resulting in alterations to the MAE and electronic contributions. Due to the interaction of these moments in a planar system, we see the materials form noncollinear magnetic systems within specific planes; for $L1_2$, we see triangular systems form with moments pointing toward each other, and $D0_{19}$ systems similarly form planar orderings of magnetic moments, albeit not in explicit triangular symmetry (Figure 2.12). All magnetic moments are canted in such a way as to compensate each other antiferromagnetically, though all are noncollinear.

The variation of MAE for these materials due to the relative angular difference of the moments might be able to adopt multiple distinct minima that are equally or similarly stable. This difference may also allow for changes to the magnitude of the MAE, which is important for implementation into memory devices to find the ideal the energy of switching memory states.

2.6 Summary

To summarize, we have explored the theoretical underpinning of the approaches and relevant understanding of the research performed in this thesis in this chapter,

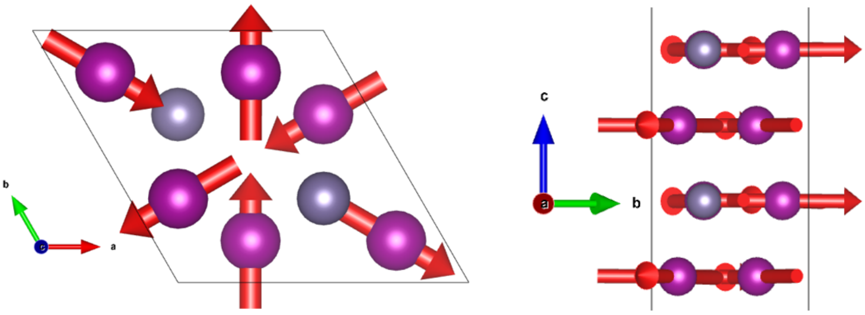

Figure. 2.12: The magnetic ordering of bulk Mn_3Ge. The purple atoms represent manganese, the grey atoms represent germanium

providing a useful basis for the reader to understand the calculation approaches and methods of later results chapters.

The first section dealt with the Schrödinger equation and its fundamental contribution to the following chapters. The DFT approach we will use for the majority of the calculations is based on the second section, where we discussed the underlying physics as well as the approximations used to improve the calculation. The implementation of the theory was discussed in the third section, in order to provide a direct understanding to the reader of how the DFT methodology can be used for our purposes. The fourth section covered the magnetic properties we aim to explore, an integral part of the investigation into these antiferromagnetic materials.

The theoretical basis that underpins this work, whilst fairly extensive, is relatively simple to implement into DFT code. VASP allows easy customisation of inputs as well as detailed output results, and so we will use this program for our calculations.

Chapter 3

Collinear Mn-alloy antiferromagnetic materials

3.1 Introduction

Magnetic Mn-alloys have been of interest to the scientific community since the early 1960s [126]. They form multiple different types of (anti)ferromagnetic arrangement, depending on composition, which range from simple configurations to highly complex ones[28].

Generally, basic antiferromagnets take collinear antiferromagnetic (AFM) structures. These systems of collinear antiferromagnets have magnetizations aligned along a common axis[127]. When altering the common axis direction to change the magnetic anisotropy, all magnetizations will alter in a similar manner. This makes characterising the magnetic anisotropy energy (MAE) into a less complex task as the reorientation requires only the common axis to be considered, rather than multiple directions of magnetizations as in noncollinear materials [43].

We should therefore characterise the easier collinear materials in order to properly construct an approach for characterising noncollinear materials. The best group to begin with would be the $L1_0$ Mn-alloys, as these collinear materials form (anti)ferromagnetic materials with common structure and species (manganese) [128, 44].

For this chapter, the main motivation is to quantify the accuracy of our calculation approach to determining the structural and magnetic parameters of these collinear $L1_0$ Mn-alloys. By confirming with these simpler magnetic structures that our approach can characterise the structural and magnetic properties of these $L1_0$ Mn-alloys, then more complex, noncollinear magnetic structures can be characterised with a more robust and well-tested methodology.

In this chapter, we aim to discuss the properties of the the $L1_0$-Strukturbericht group Mn-based alloys of 50:50 composition Mn:X, where X represents another metal (Ir, Al, Ni, Pt, Ga and Pd) [44, 129, 28, 128, 130, 131, 132]. We focus on collinear aniferromagnets using ACG notation and one ferromagnet (Figure 3.1). The properties we calculate and compare are the structural parameters, the magnetic moment on the manganese atom, the magnetic structure, and the MAE, with a focus on determining the relative magnitudes of the spin-orbit coupling and magnetic dipole-dipole contributions.

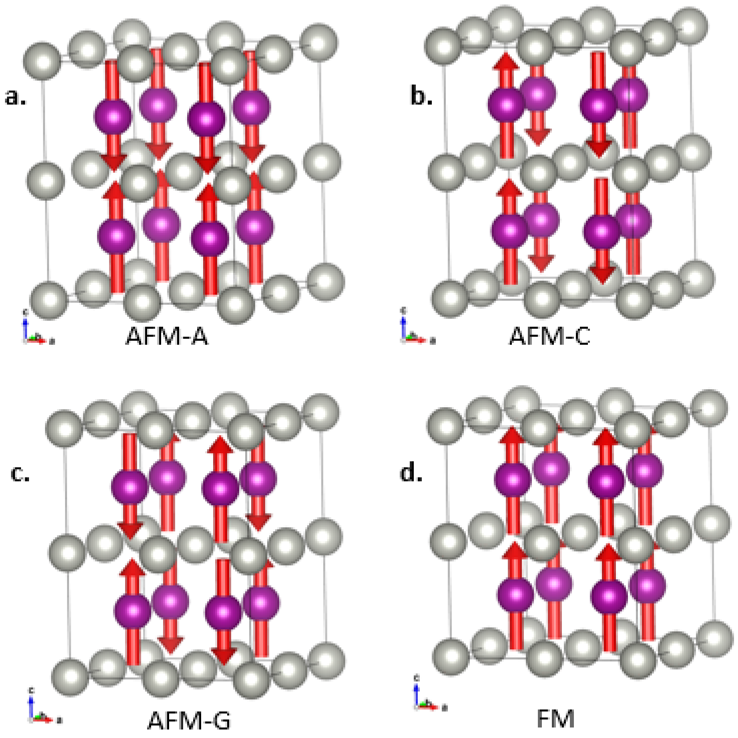

Figure. 3.1: The various magnetic configurations investigated. From top left, clockwise; a) A-phase antiferromagnetic, b) C-phase antiferromagnetic, c) G-phase antiferromagnetic, d) ferromagnetic

We compare the calculated results we acquire to existing information from other studies, both experimental (section 3.2) and theoretical (section 3.3), which use different methods to determine the same parameters. We can then be confident in the method if we can retrieve similar results to other theoretical approaches and experimental studies, which we elucidate on in section 3.4. We will discuss and compare the previous experimental and theoretical literature to the calculated results in section 3.5, and will conclude the chapter in section 3.6. We note that the theoretical approximations will cause differences for some approaches and parameters when compared to similar studies.

Our method includes a series of simulations operating at $10 \times 10 \times 10$ k-points for a single primitive cell in a Monkhorst-Pack sampling grid. We use an energy cutoff of 350eV, and various density functional theory with Hubbard U (DFT+U) correction values, varying from 0 to 4 (and specified as to which applies) on the Mn atoms. We do not use symmetry constraints on the system, and use projector augmented wave (PAW)-Perdew, Burke and Ernzerhof (PBE) pseudopotentials. The force tolerance is 10^{-3} eV/A^{-1} and the energy tolerance is 10^{-5} eV/atom.

3.2 Previous experimental results

Previous experimental investigation of $L1_0$ Mn alloys has revealed a wealth of data on the lattice parameters and magnetic structure of these materials (Table 3.1). However, the magnetocrystalline anisotropy energy, a specific aspect of the MAE based on the symmetry of the crystal, is difficult to measure experimentally in antiferromagnets due to compensated antiferromagnets having zero net magnetization, producing less reaction to the external magnetic field, and thus few studies give an experimental value for MAE [43]. The materials we focus on are stoichiometric materials (alloys with a 50:50 ratio of the two elements). The lack of stoichiometric antiferromagnetic materials with an exact MAE defined in experimental literature is a significant issue when seeking to compare information (Table 3.1). In order to rectify this, one of the main reference materials we use to confirm the capability of our calculations for this group of materials is MnGa, an $L1_0$-type ferromagnetic (FM) material, as this has experimental studies that give a figure for the MAE. Because MnGa is an $L1_0$ material, we can use it to ensure the predicted properties are consistent with experiment.

Material	a (nm)	c (nm)	Magnetic structure	Moment on Mn (μ_B)	MAE (meV/FU)	References
MnIr	0.386	0.364	AFM	-	-	[127, 130]
MnAl	0.393	0.359	AFM-A	1.86 (3.86)	-	[129, 131]
MnNi	0.374	0.352	AFM-C	3.80	-	[128]
MnPt	0.403	0.369	AFM-C	4.30	-	[128, 133]
MnGa	0.400	0.371	FM	2.32	0.58	[134, 132, 135]
MnPd	0.407	0.358	AFM-C	-	-	[128, 136]

Table 3.1: Experimentally determined properties of $L1_0$ Mn-alloys including lattice parameters, magnetic structure, and MAE.

The experimental results from literature employ a variety of approaches for creating samples. As such, it is important to describe each experiment and to note the important considerations here.

We begin with MnIr. In a study by Umetsu et al, the $L1_0$-MnIr sample was generated by arc-melting high-purity iridium and manganese in argon gas. The sample was then annealed at 1073K for 72 hours with stoichiometry determined via inductively coupled plasma mass spectrometry (ICP-MS), where multiple ratios are used in the study including equiatomic quantities. The lattice parameters were found to be a=0.386 nm, c=0.364 nm, measured via x-ray diffraction (XRD) (Table 3.1). An antiferromagnetic configuration of undefined order and easy axis is found via XRD and identification of the Néel temperature, T_N, via temperature-dependent electrical resistivity calculation [130]. In another study of the magnetic properties by Pearson et al, a sample of high-purity weighed iridium and manganese was prepared by melting equal quantities of iridium and manganese followed by a two-stage annealing process. In this study, it is noted that the easy axis lies in the (001) plane, determined via x-ray/neutron diffraction [127]. MnIr is included in many studies of magnetic and structural data, but for the MAE the $L1_0$ system is often difficult or less preferable to measure. This is likely due to the increased stability of the $L1_2$ Mn_3Ir system, resulting in more apparent MAE than that of the $L1_0$ system due to the increased MAE magnitude and more stable noncollinear structure.

Next, we describe the work done with MnAl by Takeuchi et al [131]. Using a sample preparation method that sputters together the manganese and aluminium with stoichiometry determined by ICP-MS, the study finds a=0.393 nm, c=0.359 nm measured via XRD. It can also be noted that in the study by Sato et al, MnAl, measured via neutron diffraction and Rietveld fitting respectively in the $L1_0$-antiferromagnetic phase, has an A-phase structure to the magnetic moments (Figure 3.1), each of an average 1.86 μ_B (but a peak value of 3.86 μ_B) [129]. MnAl is very frequently studied, but mostly into its metastable ferromagnetic state. As such, this material has remarkably little information on its ground state antiferromagnetic parameters in experiment.

We now assess the literature regarding MnNi. In the study by Tarnóczi et al, the sample is prepared by melting nickel and manganese in argon atmosphere, homogenizing the sample at 800°C for 24 hours to ensure uniform material distribution. The study finds a=0.374 nm, c=0.352 nm, measured via neutron and X-ray powder diffraction with a magnetic moment magnitude of 3.8 μ_B. The magnetic structure is also found to be C-phase (Figure 3.1); MnNi has a wealth of research detailing the magnetic and structural data, but not the anisotropy data[128].

Considering the work on MnPt, Andreas et al use a method of material synthesis that sputters together platinum and manganese in an argon atmosphere at 475°C followed by annealing for 1 hour at 375°C with a field strength of 1T and subsequently field cooled. The magnetic moment magnitude is determined using a sample melted in argon atmosphere, and homogenized at 800°C for 24 hours. The study finds a=0.403 nm and c=0.369 nm, measured via neutron and X-ray powder diffraction. The magnetic easy axis is aligned parallel to the (001) plane and canted 45 degrees to the [100] direction, measured by polarized neutron diffraction [133]. The magnetic moment magnitude is 4.3 μ_B. In a separate study by Tarnóczi et al, the sample is prepared by melting platinum and manganese in argon atmosphere, homogenizing at 800°C for 24 hours. The magnetic order is found to be C-phase, measured via neutron and X-ray powder diffraction [128]. Despite the growing popularity of MnPt as a material in the spintronics community, experimental MAE results are surprisingly hard to come by.

MnGa is the most experimentally well characterised material for the $L1_0$ Mn-alloys surveyed here. In the study by J.P. Corbett et al, using a sample annealed at 1100°C and generated via molecular beam epitaxy (MBE), the lattice parameters are found to be a=0.400 nm, c=0.371 nm [134], measured via scanning tunnelling microscopy (STM) and XRD. In the study by X.P. Zhao et al, using a sample that is grown at 250°C via MBE and cooled to room temperature, it is found that MnGa has 2.32 μ_B magnetic moment magnitude and ferromagnetic ordering [135]. The structure is measured via XRD, and the magnetic properties are measured via superconducting quantum interference device (SQUID), set to a specific temperature (5K, 100K, 200K, 280K) and hysteresis loops are measured. In the study by Z. Jiao et al, the sample was created using arc melting in an argon atmosphere and annealed at 723K for 24 hours. MnGa has been determined in this study to have lattice parameters of a=0.388 nm, c=0.370 nm and an MAE of 0.58 meV/FU with an easy plane of (001) [132]. The lattice parameters were measured via XRD, and the magnetic properties by vibrating sample magnetometry. Due to the comprehensive profile of MnGa data, this is the primary experimental reference point. This material has all the data we will require for evaluation.

Lastly, experimental literature on MnPd is evaluated. MnPd samples that were created via melting in argon atmosphere, homogenized at 800°C for 24 hours, are found to have lattice parameters of a=0.407nm, c=0.358 nm via the work by Tarnóczi et al [128], measured via neutron and X-ray powder diffraction, and C-phase antiferromagnetic ordering via the work done by Tang et al [136], where samples were generated by room-temperature ultra-high vacuum deposition systems at room temperature. The stoichiometry was confirmed using Auger electron spectrometry and magnetic data aquired via magneto-optical Kerr effect (MOKE). MnPd has structural and some magnetic data, but no data on the MAE (In much the same position as MnNi). The easy axis is [100], measured in the (001) plane by neutron diffraction [128].

3.3 Previous theoretical results

Theoretical results for many $L1_0$ Mn-alloys and their structural and magnetic parameters are well-described and determined (Table 3.2). We use these results to compare to the materials that are without experimental data; whilst not as generally applicable as an experimental result due to the necessary approximations used, these theoretical results are important to compare and contrast the results of differing theoretical methodologies. Here, we summarise the material properties that have been gathered from these theory-focused studies in Table 3.2, which we shall compare to the parameters in Table 3.1.

Material	a (nm)	c (nm)	Magnetic structure	Moment on Mn (μ_B)	MAE (meV/FU)	Easy axes	References
MnIr	0.385	0.364	AFM-C	3.74	3.370-3.525	[100]	[44, 43]
MnAl	0.392	0.357	AFM-A	3.21	-	-	[129]
MnNi	0.372	0.352	AFM-C	3.22	0.145-0.250	[100]	[137, 44, 43]
MnPt	0.383	0.384	AFM-C	3.91	0.255	[001]	[138, 44]
MnGa	0.389	0.362	FM	2.58	0.846	[001]	[28]
MnPd	0.407	0.358	AFM-C	3.67	0.285-0.360	[100]	[44, 43]

Table 3.2: Theoretical parameters for $L1_0$ Mn-alloys, including lattice parameters, magnetic structure, and MAE.

In a study on multiple $L1_0$ materials by Umetsu et al, the approach used to investigate lattice parameter ratio and MAE/anisotropy constants was that of linear muffin tin orbital with atomic Sphere approximation, an implementation of density functional theory (DFT) within the local spin density approximation. They determine anisotropy energies of -3.53, -0.145, 0.255, -0.285 meV/FU for MnIr, MnNi, MnPt and MnPd, respectively with easy axes in the [100] direction for MnNi, MnIr and MnPd and a [001] easy axis for MnPt [44].

In a study by Josten et al, the *ab initio* simulation data is used to support experiment on strongly pinned magnetic moments in MnNi in a magnetic field. The first calculation method includes coherent potential approximation to determine magnetization direction preference and MAE. Spin and orbital contributions are included in this study. The second calculation method used spin polarized relativistic Korringa-Kohn-Rostoker (KKR) with PBE to evaluate changes in the composition of the alloy, inducing a defect. The calculated parameters included the magnetic ordering and magnetic moment of the MnNi system (C-phase, 3.22 μ_B) as well as the MAE (-0.154 meV/FU) with easy axis [110] [137].

The study by Mohn et al uses full-potential linear augmented plane-wave (FP-LAPW) methodology including spin-orbit coupling. Spin and orbital contributions are included in this study. The study focuses on finding materials parameters (magnetic moment, MAE, also spin density) for MnNi, MnPd, and MnIr whilst also evaluating the effect of a change of magnetic moment direction in spin density distribution; the study finds magnetic moments for the aforementioned alloys of 3.15, 1.56, 3.74 μ_B per Mn, and -0.250, -0.360, -3.370 meV/FU respectively. Each MAE minima lies at 45 degrees to the [001] direction [43].

The study by Al-Aqtash and Sabirianov used augmented plane wave PBE with Blöchl tetrahedron method, along with spin-orbit coupling included[28] to study MnGa. The study investigated the structure, magnetic order, magnetic moment, and MAE, as well as band structure calculations. The calculated values for the lattice constants include a = 0.389 nm, c = 0.362 nm, the magnetic ordering is ferromagnetic, the magnetic moment is 2.58 μ_B per Mn, and the MAE is 0.846 meV/FU with an easy axis in the c-direction [28].

Makkaka, Mukumba and Lethole's study employs DFT calculations with PBE, using ultrasoft pseudopotentials. Spin and orbital contributions are included in this study. The study solves for structure, magnetic moment and further electronic and structural properties of MnPt (as well as CoPt and NiPt), finding a = 0.383 nm, c = 0.384 nm. The magnetic moment is 3.91 μ_B per Mn and easy axis in the [001] direction [138].

For MnIr, the calculation methods are linear muffin tin orbital with atomic sphere approximation (LMTO-ASA) + local spin-density approximation (LSDA) from the study by Umetsu et al, and FP-LAPW + spin-orbit coupling (SOC) working within the local spin density approximation from Mohn et al's work. The MAE is reported as 3.370 meV/FU-3.525 meV/FU [44, 43], a high MAE overall. The small variation in MAE between approaches indicates a good agreement between studies, with a C-axis perpendicular easy axis and easy plane of (001) respectively also indicating good agreement (Figure 3.2).

Now using MnAl as a reference material, this study by Sato et al provides both a quoted and calculated value for for the lattice parameters (0.392 nm and 0.357 nm for a and c respectively), a magnetic structure and a magnetic moment magnitude (3.21 μ_B) as well as stability of configuration and projected density of states (PDOS), though there's no MAE prediction given in this study. Using frozen-core full-potential projected augmented wave method, with Hubbard U that is determined by matching the calculated lattice parameters to experimental lattice parameters. However, agreement is found between the experimental lattice parameters (Table 3.1) and the theoretical lattice parameters (Table 3.2), as well as on the antiferromagnetic nature and magnetic order of the material [129]. Spin and orbital contributions are included in this study.

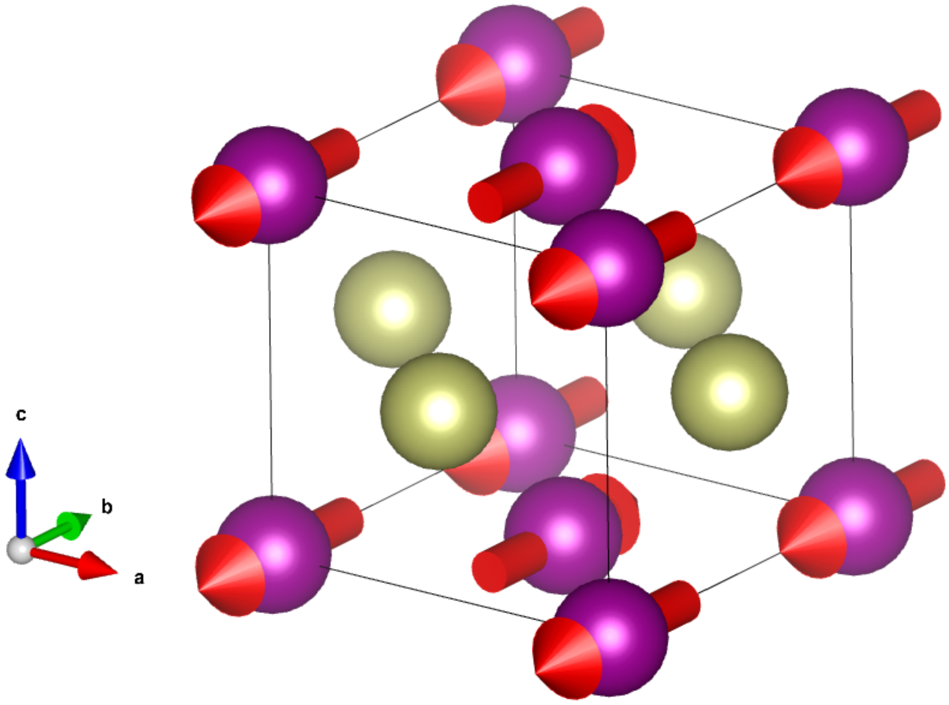

Figure. 3.2: An example of the unit cell we use. Collinear $L1_0$-MnIr unit cell complete with ground-state magnetic moment vectors on display. Purple atoms represent Mn, green atoms represent Ir

With MnNi, we focus on comparing three studies; Umetsu et al, Josten et al and Mohn et al. The study by Josten et al uses the CPA calculation method to determine magnetization direction and MAE with spin-polarized relativistic (SPR)-KKR using PBE, and PAW-PBE in VASP using a supercell. It identifies the MAE of MnNi as -0.154 meV/FU. The study by Mohn et al employs FP-LAPW methodology including spin-orbit coupling. Both approaches in this study find a [110] easy axis and -0.25 meV/FU is reported as the MAE. Another study by Umetsu et al uses LMTO-ASA + LSDA, with -0.145 meV/FU MAE where the the easy plane is (001). The studies reveal a wide variation of anisotropies, likely due to the relatively low value of the anisotropy in the material. Whilst this range of anisotropies is energetically advantageous for experimental use, this can be an issue for effective comparison [137, 44, 43].

Now for MnPt, the study by Umetsu et al used the methodology LMTO-ASA + LSDA. The calculated MAE is 0.255 meV/FU, a low value for the MAE, and the C-axis is the easy axis [44]. The easy axis is the same as that found in experiment (Table 3.1).

Next, comparing MnGa, the study by Al-Aqtash and Sabirianov involved DFT with a PAW PBE, with SOC included. The study finds a higher magnitude MAE than experiment (Table 3.1) with 0.846 meV/FU, and that the lattice parameters are close, though not identical to experiment. The magnetic moment magnitude differs by 11%, and the MAE is significantly larger [28].

Lastly, we compare the studies on MnPd, which involve LMTO-ASA + LSDA, and FP-LAPW + SOC from the studies by Umetsu et al and Mohn et al respectively. These calculations present a range of MAEs; 0.285 meV/FU-0.360 meV/FU, [44, 43], a small variation of anisotropy results indicating reasonable theoretical agreement between approaches, which is a small MAE overall with a (001) easy plane.

3.4 Structure and magnetic properties

3.4.1 Supercell for calculation

The supercell used for calculation is a 2 × 2 × 2 expansion of the primitive cell, containing 8 Mn atoms and 8 atoms of the alloyed metal. The 8 Mn atoms can be used to describe various magnetic configurations as the Mn site is the dominant location of the magnetic moments (Figure 3.1). We focus on 4 magnetic configurations; A, C, and G antiferromagnets based on the ACG notation system [126], and a ferromagnetic reference configuration (Figure 3.1). We then perform full supercell optimization calculations to determine the configuration with the minimum energy. This is done by comparing the total energy for each magnetic order. We then use the most stable magnetic order and structure for each material going forward. We provide the magnetic configurations via initial conditions for the magnetic moment. We also provide estimations of the magnitude of the magnetic moment to initialise the calculation, usually overestimating the value of the initial magnetic moment, which ensures the simulation has ample capability to find the best magnetic moment and so minimize the energy.

3.4.2 U-value and functional

We select a variety of exchange correlation functionals (generalized gradient approximation (GGA)s PBE [69], PBE functional revised for solids (PBEsol) [139], Perdew-Wang (PW91) [67], revised PBE (rPBE) [70], Armiento-Mattsson 2005 (AM05) [140, 141, 142], as well as meta-GGAs like Strongly Constrained and Appropriately Normed (SCAN) [143], revised SCAN (rSCAN) [144], revised Tao, Perdew, Staroverov, Scuseria (rTPSS) [145, 146, 147], and Minnesota 2006 local function (M06-L) [148]), and test each with a range of Hubbard U-values (0 eV, 1 eV, 2 eV, 4 eV) to compare predictions against experimental results. The functional with the best combined estimate of the experimental material parameters will be selected going forward for use in further simulations.

We begin with $L1_0$-MnGa, which has an FM magnetic structure [135]. If a given exchange correlation functional does not predict a stable FM state, it can be easily dismissed. In this case, we dismiss all functionals using U=2 and U=4, which do not produce a stable ferromagnetic configuration (Figure 3.4). For assessment of functionals, we use three further key factors; the lattice parameters, the magnetic moment magnitude, and the magnetic anisotropy magnitude (Figure 3.3).

For the lattice parameters, we find that the best match apparent is U=0 with rPBE, followed by M06-L. It sits near-exactly on the experimental value, whilst the other (meta-)GGAs with U=0 are further off, by 0.01 nm comparatively for the next-closest functional, SCAN. However, for U=1, the competitors that are closest are PBEsol, PW91, PBE (with one lattice parameter underestimated and one overestimated). AM05, rSCAN and rTPSS, then M06-L are next, and SCAN dramatically under- and overestimates the two parameters. The best overall agreement with experiment is rPBE (U=0).

For magnetic moment, the best agreement with experiment is U=1 with PBE; PBEsol, PW91, rTPSS, rSCAN and M06-L underestimate the magnetic moment slightly, and SCAN and rPBE overestimate it. The PBE calculated magnetic moment is almost exactly the same as experimental figures and as such is well within experimental error. Close competitors are, jointly, U=1 PBEsol, and AM05. All U=0 GGAs underestimate the magnetic moment magnitude considerably (by a minimum of 0.4 μ_B for rPBE and M06-L).

For MAE (dipole anisotropy energy (DAE) + SOC anisotropy), the best agreement

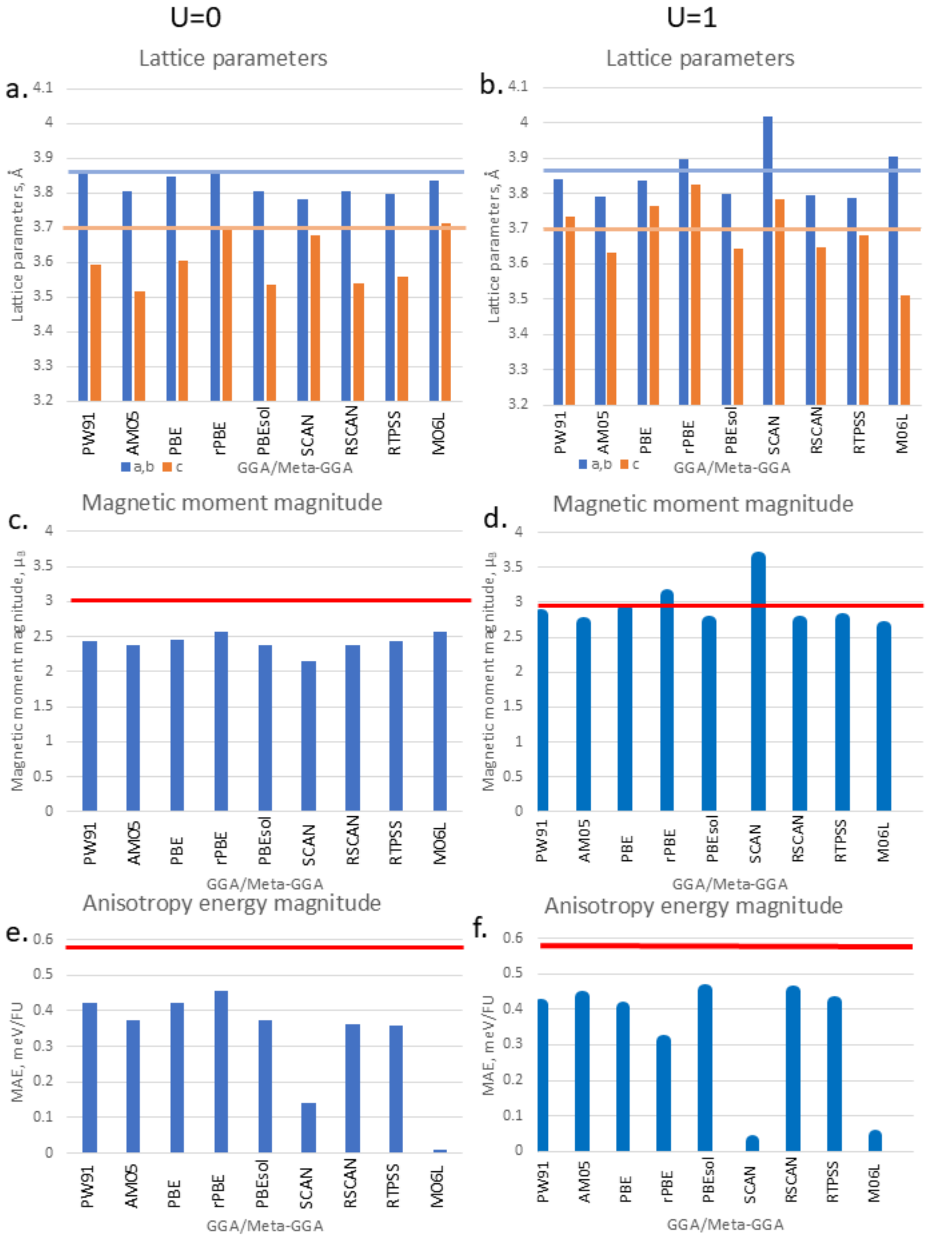

Figure. 3.3: Calculated properties of $L1_0$ MnGa using different functionals and Hubbard U values. a, b) Lattice parameters for various functionals, where the blue line represents the experimental a lattice parameter and the gold line represents the experimental c lattice parameter. c, d) Magnetic moments for various functionals, where the red line is the experimental magnetic moment. e, f) the MAE magnitude, where the red line is the experimental MAE.

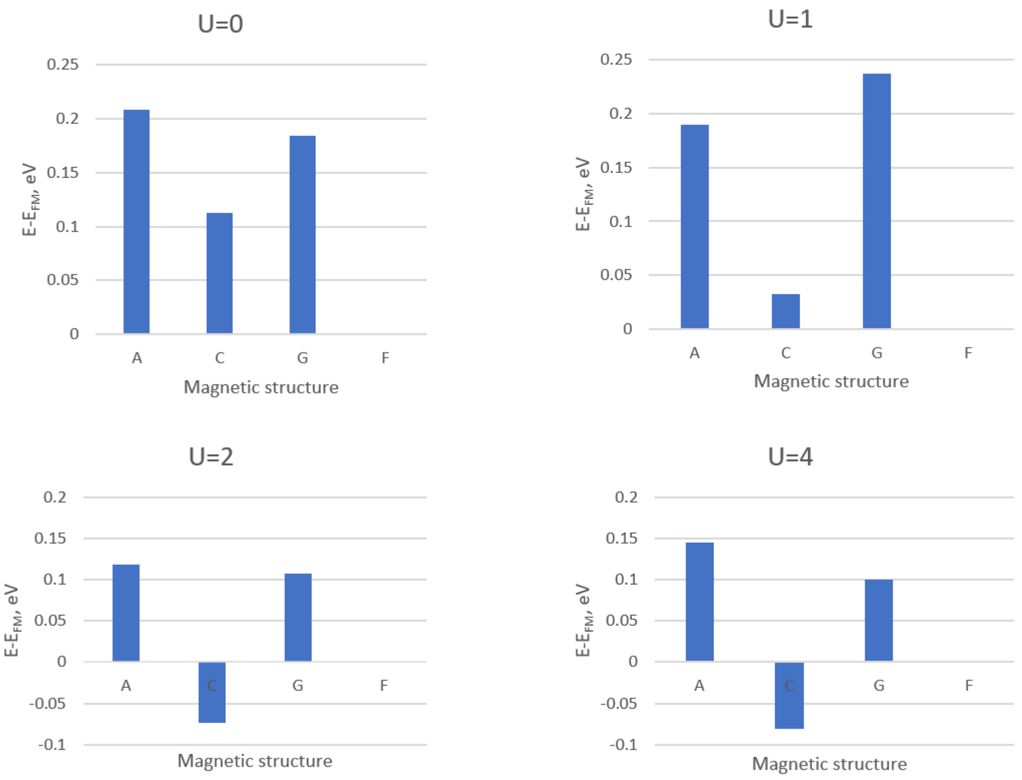

Figure. 3.4: Calculated magnetic ordering of $L1_0$ MnGa using different U values, in this example using PBEsol as a GGA. Positive values indicate higher-energy ordering than the FM configuration.

with experiment is for PBEsol, with U=1, though this is an underestimate by 0.12 meV/FU. rSCAN with U=1 is the next closest, (0.13meV/FU below), followed AM05, then rTPSS then PW91 and PBE. For U=0, rPBE is closest, underestimating by 0.13 meV/FU, followed by PW91 and PBE. All the rest significantly underestimate the magnetic anisotropy.

On this basis, the best compromise to find accurate parameters for MnGa would be to use PBEsol with U=1, due to the lattice parameters and moment being quite close and relative best SOC-MAE prediction, with significant improvement over PBE for the last category. We use this as the functional in the following sections, maintaining comparison to both theoretical and experimental parameters in order to ensure the model maintains a consistent capability.

3.4.3 Calculated properties of L1_0 materials

Results in Table 3.3 show that the lattice parameters for MnIr are a=0.382 nm, c=0.360 nm, which are close to the experimental values from the experimental

Material	a (nm)	c (nm)	Reference a (nm)	Reference c (nm)	magnetic configuration	Total Magnetic moment (μ_B on Mn)	Reference magnetic moment (μ_B on Mn)
MnIr	0.382	0.360	0.386	0.364	AFM-C	3.1	3.74
MnAl	0.391	0.348	0.393	0.359	AFM-A	2.72	-
MnNi	0.362	0.351	0.374	0.352	AFM-C	3.41	3.80
MnPt	0.393	0.391	0.403	0.369	AFM-C	3.83	4.30
MnGa	0.380	0.364	0.400	0.371	FM	2.70	2.32
MnPd	0.395	0.363	0.407	0.358	AFM-C	3.91	3.67

Table 3.3: Results for structural and magnetic properties with comparison to the relevant experimental values

study by Umetsu et al, a=0.386 nm (1% difference), c=0.364 nm (1% difference) [130]. As well as this, MnIr has a small magnetization difference to the figure given in the theoretical study by Umetsu et al (Table 3.1). The study predicts $L1_0$-MnIr has C-phase magnetic structure, and the magnetization magnitude is different to calculated results in Table 3.2 by 0.64 μ_B, or 17% [127]. This C-phase magnetic structure (Figure 3.1) is identical between the study and the result of the calculations (Table 3.3).

We calculate that the MnAl lattice parameters are a=0.391 nm, c=0.348 nm. This is close to the experimental figures obtained in the study by Takeuchi et al, a=0.393 nm (0.5% difference), c=0.359 nm (3% difference) [131], indicating agreement to the experimental structural values. MnAl's AFM configuration is that of the A-phase, as predicted in previous theoretical work by Sato et al [129] (Table 3.2). The magnetic moment is 2.7 μ_B per Mn, a reasonable agreement to theory differing by 16% (Table 3.2).

When investigating parameters for MnNi, we calculate that the lattice parameters are a=0.362 nm, c=0.351 nm. These values are close to the study by Tarnóczi et al [128], a=0.374 nm (3% difference), c=0.352 nm (0.2% difference), with c-lattice nearly perfectly matching the experimental value (Table 3.1). The calculated magnetic moment of MnNi is very similar to Tarnóczi et al's value for this parameter. The AFM structure matches the Tarnóczi et al's magnetic structure, whereby this study has 3.8 μ_B and C-phase, compared to the calculated 3.4 μ_B, a difference of 11% [128].

The lattice parameters of MnPt were calculated to be a=0.393 nm, c=0.391 nm. These values differ by 0.01 nm and 0.022nm from the experimental results obtained by Solina et al's work (Table 3.1), the study showing that a=0.403 nm (2% difference) and c=0.369 nm (6% difference) [133]. MnPt has an experimental value for the magnetic moment of 4.3 μ_B per Mn and C-phase magnetic structure, as noted in the study by Pál et al. The calculated magnetic moment we have determined differs from Pál et al by 12% (3.8 μ_B per Mn and C-phase) [133, 128].

We calculate the lattice parameters of MnGa to be a=0.380 nm, c=0.364 nm; these parameters are reasonable when compared to the experimental studies by Corbett et al (Table 3.1). The study gives figures a=0.400 nm (5% difference), c=0.371 nm (2% difference) for the experimental value [134]. MnGa has a ferromagnetic ordering in both the experimental study and our own calculations, with 2.724 μ_B as the calculated magnetic moment compared to the experimental value from Zhao et al of 2.32 μ_B [135]. This is a reasonable agreement (15% difference) between the two figures.

Lastly, for MnPd, we obtain lattice parameters of a=0.395 nm, c=0.363 nm; these calculated parameters are within 3 % and 1.3% of the experiment parameters given by Pál et al at a=0.407 nm, c=0.358 nm respectively (Table 3.1) [128]. The ordering in the theoretical study by Tang et al is C-phase and magnetization of 3.67 μ_B (Table 3.2) [136]. We find the magnetic moment to be 3.91 μ_B, with C-phase magnetic structure, which is within 7%. Identical magnetic structure and similar magnetic moment indicates a good agreement between calculation and reference.

The calculated parameters of the materials match the experimental and theoretical studies well, with differences in the values being as low as 12%. The largest difference was in MnGa, where its lattice parameter differed from experiment study by up to 0.02 nm, though all other figures are closer to experimental values (within 0.02 nm or less). This indicates generally strong agreement with experimental structural values for all materials, and thus a good indication the calculations are reasonable.

3.4.4 Magnetic anisotropy

Understanding the magnetic anisotropy of the $L1_0$ materials gives us an insight into the spintronic switching capabilities of these alloys. By calculating the magnetic anisotropy we can predict the easy and hard axes of these materials as well as determine salient magnetic features in the change of direction of the magnetic quantization axis of the materials.

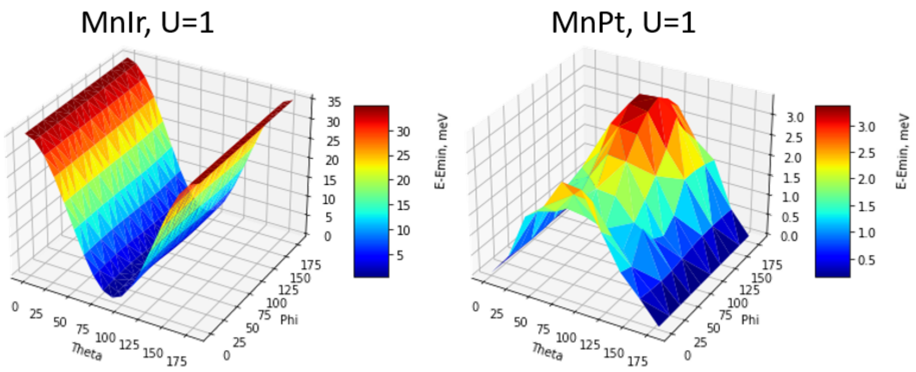

MnIr, U=1

MnPt, U=1

Figure. 3.5: Calculated spin-orbit contribution of the magnetic anisotropy of $L1_0$ MnIr and MnPt within a supercell of eight primitive cells, where theta (θ) represents the angle away from the perpendicular to [001], and phi (ϕ) the angle from [100]

The dipole contribution to the anisotropy is given in Table 3.4. This is a component of the previously displayed MAE, which is determined by the spin dipole contribution in relation to the magnetic moments.

In the case of MnIr, the calculated MAE, -4.187 meV/FU appears to differ from the theoretical MAE (compared to theoretical studies by Umetsu et al, which find -3.5 meV/FU[44]) by -0.687 meV/FU, or 20%. Both the study in Table 3.4 and our calculations predict an easy plane in the (001) plane as seen in Figure 3.5, where the minimum at $\theta = 90^\circ$ indicates the easy axis sits within the (001) plane (Figure 3.2).

We now discuss MnAl. Our calculation determines the MAE to be $+0.215$ meV/FU (Table 3.4), which displays a [001] uniaxial easy axis. There is no theoretical or experimental reference that discusses the anisotropy contributions, SOC or otherwise, for AFM MnAl; this is due to the ferromagnetic metastable state of MnAl being far more thoroughly researched in recent history [149].

MnNi also has no experimentally determined MAE, but does have theoretical figures with a range of -0.145 to -0.250 meV/FU (Table 3.2). We calculate an SOC anisotropy of -0.132 meV/FU (Table 3.4); the theoretical reference values in Table 3.2 are quite well-matched, differing by 9% at minimum. We find the easy plane is in the (001) plane [137, 44, 43].

For MnPt, the calculation is different to the theoretical reference. We find a value for the MAE of $+0.493$ meV/FU (Table 3.4) compared to $+0.255$ meV/FU given in Table 3.2 [30, 44], a difference of 48%, and the easy direction is calculated to be uniaxial along the c-axis. In Figure 3.5, we see MnPt's uniaxial anisotropy represented by the minimum energy at $\theta = 0^\circ$ and 180°. The magnetic easy direction matches the theoretical reference well.

With the ferromagnetic material MnGa, we note reference MAE is $+0.580$ meV/FU, which is close to the calculated value of $+0.372$ meV/FU [132], (Table 3.4) and the easy axis is [001] in calculation, in agreement with Table 3.1.

MnPd has no experimental reference MAE, though does have a theoretical MAE range of -0.285 to -0.360 meV/FU (Table 3.2). In the calculated results the MAE is determined to be -0.142 meV/FU (Table 3.4). The value from calculation differs from theoretical reference [44] by a factor of approximately 2. The easy axis is predicted to lie along [110].

For the majority of these materials there is little in the way of explicit information in experiment or calculation on dipole anisotropies. The general order of magnitude of the DAE is often considered to be negligible, and this is generally the case in the results in Table 3.4. Exceptions include MnPd, and to a lesser extent MnPt

Material	Calc. SOC anisotropy, meV/FU	Calc. easy direction	DAE, meV/FU	DAE easy direction	Calc. MAE, meV/FU	Ref. MAE, meV/FU	Ref. easy direction
MnIr	-4.250	Easy plane, ab	+0.063	easy plane, ab	-4.187	-3.500	easy plane, ab
MnAl	+0.225	[001]	-0.010	[001]	+0.215	-	-
MnNi	-0.175	Easy plane, ab	+0.043	[001]	-0.132	-0.145 to -0.250	Easy plane, ab
MnPt	+0.400	[001]	0.093	[001]	+0.493	+0.255	[001]
MnGa	+0.460	[001]	-0.088	Easy plane, ab	+ 0.372	+0.580	[001]
MnPd	-0.240	[110]	0.098	[001]	-0.142	-0.285 to -0.360	Easy plane, ab

Table 3.4: SOC anisotropy results and DAE contributions for the calculations, with comparison to reference data

and MnGa, whereby the DAE is a significant component of the MAE.

3.5 Discussion

To ensure the calculation was optimising to a global minimum rather than finding a local minimum, the calculations were repeated using a poor set of initial parameters, including inaccurate initial lattice parameters and poor magnetic moment ordering. The result was identical to the initial calculation with far better starting parameters, indicating that we found the global minimum. We can therefore find the local energetic minima for a number of $L1_0$ systems, as well as determine the magnetic characteristics of the system to within experimental error. Results are also comparable to values in theory for both similar and different approximations/methods.

Material	Experimental parameters, nm		Theoretical parameters, nm		Calculated parameters, nm	
-	a	b	a	b	a	b
MnIr	0.386	0.364	0.385	0.364	0.382	0.360
MnAl	0.393	0.359	0.392	0.357	0.391	0.348
MnNi	0.374	0.352	0.372	0.352	0.362	0.351
MnPt	0.403	0.369	0.383	0.384	0.393	0.391
MnGa	0.400	0.371	0.389	0.362	0.380	0.364
MnPd	0.407	0.358	0.407	0.358	0.395	0.363

Table 3.5: Comparison of the structural parameters of each of the materials in this chapter compared to experimental and theoretical parameters

Predictions are in reasonable agreement with experiment on structural and magnetic parameters (Tables 3.5, 3.6). The calculated results are also very similar to those of reference calculations. For MnIr, the lattice parameters match experiment to within 0.004 nm. This is an excellent agreement. For magnetic moment, which we take from LMTO-ASA + LSDA and FP-LAPW + SOC theory, we see some difference to theory at around $\pm 0.64\ \mu_B$ though the magnetic structure matches perfectly, and MAE is different by 0.75 meV/FU. Antiferromagnetic MnAl does not have much information recorded about it. The a-lattice parameter is within 0.001 nm which is again excellent agreement to experiment; the c-lattice parameter is off by 0.011 nm, which is still reasonable. The magnetic moment of MnAl is calculated to be 2.7 μ_B. The magnetic structure, A-phase antiferromagnetism, matches well to theoretical reference. The MAE is +0.225 meV/FU (Table 3.7).

Material	Experimental moment, μ_B	Theoretical moment, μ_B	Calculated moment, μ_B
MnIr	-	3.74	3.10
MnAl	1.86 (3.86)	3.21	2.72
MnNi	3.80	3.22	3.41
MnPt	4.30	3.91	3.83
MnGa	2.32	2.58	2.70
MnPd	-	3.67	3.91

Table 3.6: Comparisons of the magnetic moments of experimental and theoretical literature vs. the calculated results

MnNi has calculated differences in the a-lattice parameter of 0.012 nm and c-lattice parameter of 0.002 nm to reference, both matching experiment well (Table 3.5). Its magnetic moment is off by 0.041 μ_B. MnNi's MAE is close to the range of theoretical values described in Table 3.7. MnPt has lattice parameters that are 0.01 nm and 0.022 nm different to experiment for a- and c-lattice parameters respectively, and a magnetic moment that's within experimental error (Table 3.5), with matching theory, and matches the magnetic structure well. The MAE differs by 0.24 meV/FU to theory. MnGa matches experiment and theory well, with lattice parameters smaller by 0.01 nm, magnetic moment matching structure and off by 0.38 μ_B from experiment and is well within theory ranges of magnetic moment, and MAE within 0.21 meV/FU of experiment. MnPd has reasonable lattice parameters within 0.012 nm, and magnetic moment differs from theory by 0.24 μ_B. Theory matches the calculation, as does the rough experimental range, though the MAE has some significant difference. We may expect MnPt and MnIr to differ so greatly in terms of their SOC MAE, despite similar atomic numbers, formula unit volumes and DAE contributions, due to the nature of the Mn moment being unsaturated/weakly itinerant. This results in the moments and MAE contribution from Mn being diminished in MnIr, whereas the moments are well-localised in other materials like MnPt [43], giving rise to a large MAE overall. This also goes some considerable way to evaluating differences to the other materials as well, with additional effects from the differing atomic number and the orbitals that the unpaired electrons occupy; For example, MnPt has one unpaired electron in the 5d and 6s cloud, whereas Mn has three unpaired electrons in the 5d cloud, resulting in a higher angular momentum contribution from the Mn unpaired electrons.

DAE, a contributing component to the MAE, was often not included in litera-

Material	Experimental values		Theoretical values		Calculated values			
	MAE	Easy direction	MAE	Easy direction	SOC MAE	DAE MAE	Overall MAE	Easy direction
MnIr	-	-	3.370-3.525	[100]	-4.250	+0.063	-4.187	(001) plane
MnAl	-	-	-	-	+0.225	-0.010	+0.215	[001]
MnNi	-	-	0.145-0.250	[100]	-0.175	+0.043	-0.132	(001) plane
MnPt	-	-	0.255	[001]	+0.400	+0.093	+0.493	[001]
MnGa	0.580	1	0.846	[001]	+0.460	-0.088	+0.372	[001]
MnPd	-	-	0.285-0.360	[100]	-0.240	+0.098	-0.142	(001) plane

Table 3.7: Comparisons of the MAE of experimental and theoretical literature vs. the calculated results

ture (though is still important to calculate explicitly to match the MAE), however from symmetry arguments we can see that the DAE distribution over a range of angles should form with opposite sign to the magnetic anisotropy and with the same distribution shape. This was a convenient phenomenon for assessing the DAE's validity with respect to the MAE, and is a fairly logical one considering the identical reorientation of the magnetizations. In this case, we can see that the dipole anisotropy is generally on the order of 10^{-5}eV, smaller than the magnetic anisotropy when non-zero (Table 3.7). This indicates SOC anisotropy is the dominant contribution to the MAE (Figure 3.6). We can consider the dipole anisotropy contribution to be insignificant for certain materials like MnIr. For other materials, like MnNi and MnGa, this anisotropy must also be included due to the contribution becoming comparable to the magnitude of the MAE. However, it should be noted that in all cases, the largest DAE proportion as a percentage is in MnPd at 41%.

3.5.1 Sources of inaccuracy

One issue with the functional selection may be the coarseness of U-value sampling. It may be better to use a finer array of U-values to determine more specific optimal processes. Due to the integer values of U, we may be missing a more refined observation of the effects of the non-integer values of the Hubbard U on the

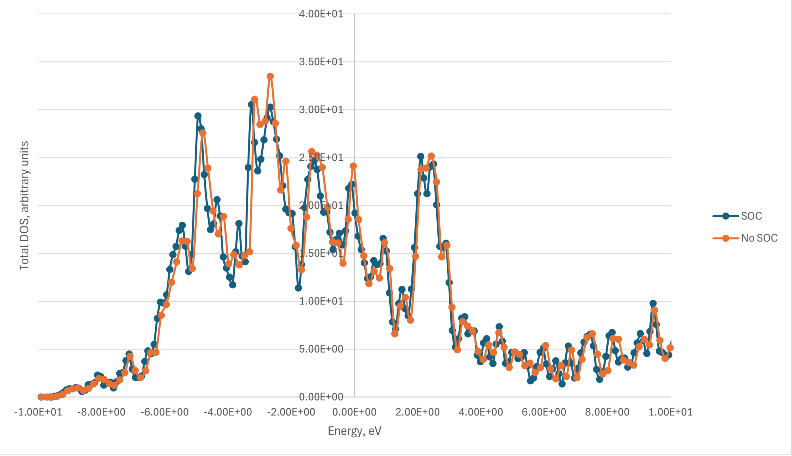

Figure. 3.6: Total density of states for MnIr. We note the effect of simulating SOC effects has small but significant changes to the density of states, in particular shifting peaks.

simulation of $L1_0$ materials. The optimal U-value for each individual material varies greatly so it is likely the best U overall may be non-integer in order to compensate.

Materials used in experiment will not always be perfectly stoichiometric, having slight differences in the quoted element ratios. Not only this, but defects in the material are often difficult to fully analyse, resulting in electronic property issues and differences that may not be apparent in simulations due to the ideal nature of the materials being simulated. These composition issues can result in sometimes significant differences to the predicted properties from calculation.

The experimental studies referenced take place at a variety of temperatures. The calculations take place at 0K for ionic relaxation, and as such will have defined differences to experiment because of the dissimilar temperatures used. This difference can affect all properties of the system and cannot be experimentally matched due to the inability to measure at 0K.

Predictions from different exchange-correlation approximations differ significantly from each other and experiment, depending on the parameter being compared. We cannot get DFT to represent every system perfectly using only one U-value. In addition this, due to limits in accounting for all electronic interactions due to the approximations needed, the electronic model is not perfect, leading to small differences in results compared to other models that account for these interactions differently. This can compound on select figures in simulation, such as smaller artefacts of dipole anisotropy and its effect on the total anisotropy of the material. Theoretical approaches to determining parameters also suffer from a lack of comparability when they use different DFT methods and functionals. Due to these specific limitations in theory, it becomes challenging to use differing DFT approaches as appropriate references. As such, a number of experimentally unrealised factors, like the MAE, may be missed due to lack of comparability between the approaches and between materials consequentially.

3.6 Conclusions

The systematic comparisons presented in this chapter indicate that the best overall level of theory for the prediction of lattice parameters, acceptable magnetic moment and magnetic structure, and MAE is PBEsol at U=1eV (Figures 3.3, 3.4). Differences to MnGa between predicted and experimental lattice parameters are within 0.02 nm, the experimental error, and the magnetic properties bear the larger differences, though these are still relatively small at $0.38\mu_B$ per Mn and 0.208 meV/FU from experiment, both within experimental error (Tables 3.1, 3.3). We may note that the other calculated structures are very similar to to experimental values, with the largest difference being 22 pm (0.022 nm) off from experimental studies (Table 3.5). This important step primarily allows for the effective simulation of position- and crystallographically-dependent parameters such as the magnetic moment and MAE, as well as providing an important foundation to compare to existing literature; we could easily determine the effectiveness of the calculation if the lattice parameters were to be compared to literature for each material.

MAE was very much comparable to experiment and theory, where studies had determined an MAE (Tables 3.5, 3.6, 3.7). The implication of this for our work will be that MAE calculation is very much feasible and therefore can be expanded to more complex materials. The utility of MAE comparison here is the ability to cross-compare this material property with a unified approach, which has been difficult to do for some time. The unique inclusion of DAE means we could detail the significance to the MAE overall compared to the SOC-MAE contribution, resulting in the determination that for materials like MnNi and MnPd, DAE is critical to determining the overall MAE.

We note that the calculated magnetic easy axes agree with the majority of experimental results (Tables 3.1, 3.4). For MnIr, we calculate the easy axis to be in the a-b plane, with no preferred direction within this plane. This agrees well with experiment, where the easy axis is undefined within this a-b plane. As for MnPt, we find the calculations and the experimental and theoretical studies agree that the main plane of the easy axis is in [001], though the canting component seen in experiment, 45 degrees from the a-b plane in the (100) plane, is not found. The easy plane of MnGa is agreed as being on the [001] axis. With similar energetic minimums in the exact angle of MnPd's easy axis between [100] and [110], we agree with the easy plane being on the a-b plane and find the [110] axis to be the easy axis. As such, we can determine reasonably well the general plane of the easy axes, with only one material not equivalent to experiment. We may therefore conclude that the predictive methodology is effective at determining the easy axes of these materials.

As for magnetic order, the experimental and theoretical studies determine similar results to the calculations (Tables 3.1, 3.4, 3.2). As MnIr is not defined specifically in experiment further than being an antiferromagnet, the calculations at least agree on the antiferromagnetic nature of the material. With regard to MnAl, we get explicit agreement with the A-phase antiferromagnetic structure, which is also confirmed by separate theoretical approaches. For MnNi, we also retrieve identical magnetic structure in the C-phase antiferromagnetic order. Similarly, for MnPt, we retrieve the C-phase antiferromagnetic order, though it is worth noting we do not retrieve the canting seen in the magnetic anisotropy despite this. As for MnGa, we retrieve the ferromagnetic nature of the material in agreement with experiment. Finally, experiment agrees with the calculation that MnPd has a C-phase antiferromagnetic order. All distributions match experiment in their ordering, and as such can be used to conclude that magnetic order is calculated well by our approach.

We may conclude from the calculations that we are able to effectively simulate and characterise $L1_0$ materials. MAE should be considered reasonable due to the procedurally optimised volume parameters being used rather than the unoptimized parameters of other studies. Whilst the MAE differs from these studies to some degree, it is worth noting the initial parameters of a number of studies referenced here do not optimise structure from first principles. As this is the case, our work can be taken to be a better prediction of the actual value.

The material parameters we calculate are within reasonable similarity to those determined in experimental (Table 3.1) and theoretical (Table 3.2) studies, where the calculated result is within or close to the error tolerance of the experimental result. The theoretical values for these parameters align with experimental values and those of the calculations, and as such we have confidence that the calculations characterise these materials well. As the simulated results optimise the structure from an initial estimate also, we can be even more confident in the calculations when considering this match to both theory and experiment.

As such, from the MAE data given in the MnGa results, we may conclude that the results here have been successful, and are within 2×10^{-1} meV/FU for the MAE with the correct shape of variation [132, 150], with a factor of around $\sqrt{2}$ being the main difference. The lattice parameters (10^{-2} nm) [134] and magnetic moment (2×10^{-1} μ_B) [151] are of comparable precision. As we have seen this effect is similar for the other materials' lattice parameters and magnetic data, we can be reasonably confident the calculated MAE is within a similarly reasonable tolerance.

Chapter 4

Noncollinear antiferromagnetic Mn-alloy materials

4.1 Introduction

Due to the utility of spintronic materials in magnetic memory devices [50], such as the spin-valve [51], research into magnetic materials that can improve on existing material performance or offer new functionality has been of great interest. This is especially true in the realm of antiferromagnetic (AFM) spintronic devices, such as tunnelling spin valves, that are constructed with both active layers of the tunnel junction made from antiferromagnetic materials (and those with a ferromagnetic layer of the tunnel junction and antiferromagnetic pinning layer) [152, 21]. Candidate materials that are of significant interest are the binary manganese AFM alloys, such as Mn-transition metal alloys, due to their wide range of AFM properties. In the previous chapter, we discussed binary alloys of component ratio 1:1 which exhibit collinear magnetic order. Here, we discuss a set of binary alloys of component ratio 3:1 that exhibit noncollinear magnetic order in order to characterise how these materials may be beneficial to spintronic applications.

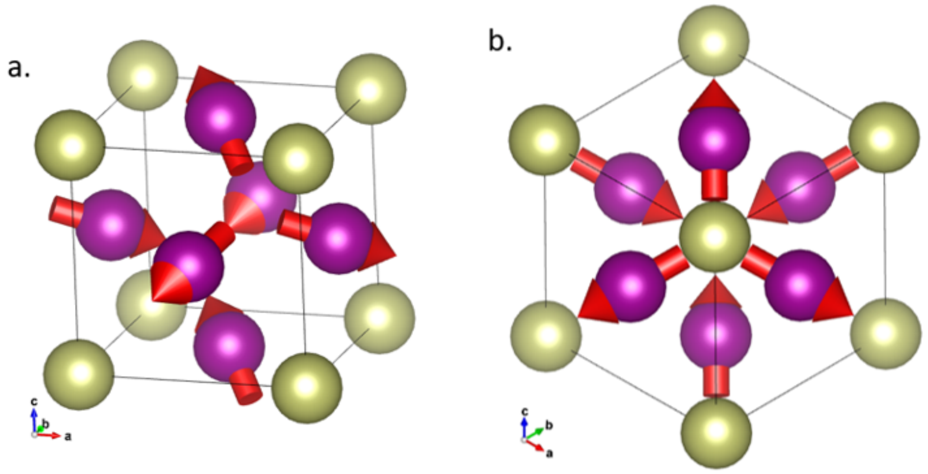

Figure. 4.1: Magnetic moment configuration for $L1_2$ Mn_3Ir a) viewed from the side b) viewed along [1-11]. The green atoms are Ir, and the purple atoms are Mn.

An effective spin model Hamiltonian describing the system of magnetic moments in a material, omitting the Zeeman term, is:

$$\hat{\mathcal{H}} = -\frac{1}{2}\sum_{i \neq j} J_{ij}\mathbf{S}_i \cdot \mathbf{S}_j + \hat{\mathcal{H}}_{MCA}, \tag{4.1}$$

where J_{ij} is the nearest-neighbour exchange term between atoms i and j, $\mathbf{S}_i$ is the spin of atom i and is equivalent to $\hbar\sigma_i$, and $\mathcal{H}_{MCA}$ is the Hamiltonian for the specific magnetocrystalline anisotropy energy. The ground state is the spin configuration that minimises the energy of the Hamiltonian, however this summation is only valid for certain magnetic moment orientations with relation to the orientation of the spin due to the dot product between these spin vectors. This forces only certain magnetic configurations to become the lowest energy states, with significant contribution from the anisotropy term. This effective spin model can be applied to Kagome lattices, such as those sublattices of manganese in Mn_3Ir, Mn_3Ge, Mn_3Ga and Mn_3Sn [122], which have similar symmetry to the example in Figures 4.1 and 4.2. These systems may have magnetic moments in differing orientations relative to each other due to the on-site anisotropy term, producing considerably different magnetic properties to simple collinear systems. In the case of Mn_3Ir, Mn_3Ge, Mn_3Ga and Mn_3Sn, the excess manganese permits the manganese sublattices to form hexagonal structures that do not adopt collinear magnetic structures

[153, 154]. For a triangular system of three magnetic ions such as those in Mn_3Ir, a simple noncollinear system of nearest neighbours [155, 156] will be directly applicable. Because of the antiferromagnetic nature, the materials' magnetic moments must also rearrange themselves in order to minimize the energy, resulting in the magnetic moments orienting noncollinearly with a more extended system (Figure 4.2) [157].

Noncollinear systems will form the mainstay of the results presented in this chapter. Four main materials are examined; Mn_3Ir, Mn_3Sn, Mn_3Ge and Mn_3Ga. Mn_3Ir takes on an $L1_2$ crystal structure [158], and the rest adopt both $D0_{19}$ and $D0_{22}$ structures. The $D0_{19}$ structures are noncollinear antiferromagnets, and the $D0_{22}$ structures are collinear [159, 160, 161, 162]. The differing crystal structures lead to significantly different magnetic structures. With the $L1_2$ material, we find three-fold rotation symmetry within the (1-11) plane (Figure 4.1) [116]. For the $D0_{19}$ structures, planar three-fold symmetry is apparent along the (001) plane [119, 163, 164]. The magnetic moments of these materials align parallel to these planes.

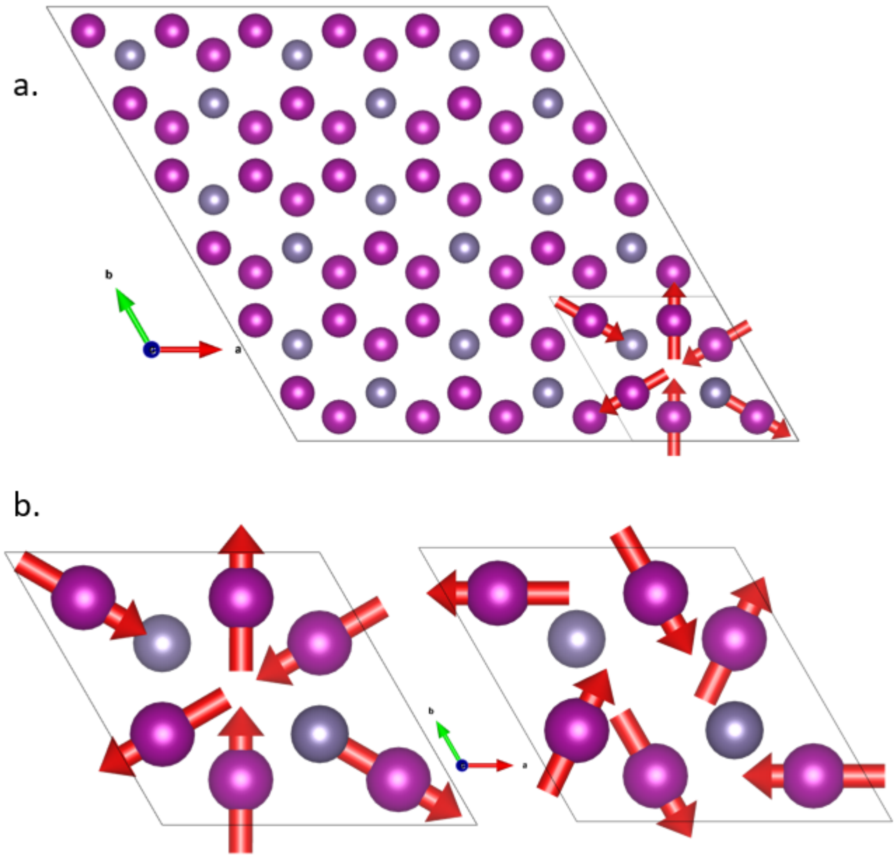

Figure. 4.2: a) Atomic configurations for Mn_3Ga, Mn_3Ge and Mn_3Sn, where purple atoms are the Mn atoms and the grey atoms are the Ga/Ge/Sn (inset; magnetic moment configuration), b) a magnetic moment configuration of such alloys rotated by 150°, where the purple atoms are the Mn and the grey atoms are the Ga/Ge/Sn.

We now present a discussion on why these complex materials are desirable for spintronics. Due to the different structure and composition of the materials (including structural configurations such as the $L1_2$ and $D0_{19}$ materials (Figures 4.1, 4.2)), these materials will have properties that are significantly different to the previous collinear materials investigated in the last chapter due to the noncollinear magnetic order. Some of these properties, like the on-site anisotropy constants defined in the second term of equation 4.1, may be advantageous to determine in order to compare to the previous chapter on collinear systems. They would also be useful for consideration for practical use in heterostructure devices in order to determine energetic cost of magnetic order changes [21]. Shi et al use Mn_3Pt, a noncollinear antiferromagnet, to construct an all-AFM memory bit, which utilises the inverting of the magnetic moment directions as a memory state change. Investigations of the magnetic structure and anisotropy of the noncollinear systems [165, 166, 167, 161] reveal interesting electron transport properties via the materials' spin-Hall and anomalous Hall conductivity (an important transport property with its surface spin charge accumulations) [168, 169, 170], with the noncollinear nature of the material affecting symmetry, including the breaking of symmetry to induce AHE [170].

The magnetic anisotropy energy (MAE) of a noncollinear material is a complex consideration, with the full characterisation of the magnetic anisotropy requiring magnetic moments are compared in every possible angular combination. By using a uniaxial approach as in equation 4.1, we see the local uniaxial symmetry axes can be expressed as three differing directions based on local tetragonal symmetry, reducing complexity significantly by reducing the considered directions of the system. Noting the rotational symmetry about the [1-11] axis, symmetric constraints on nearest neighbour interactions can be applied to simplify the Hamiltonian. To simplify this process, we may assess only symmetrical planes within which the three magnetic moment axes lie, a similar calculation approach to that outlined in the study by Szunyogh et al [42]. This approach reduces the calculation to assessing the magnetic moments rotated about some common axis perpendicular to the plane, producing a planar change of magnetic moment and thus a form of MAE. This quantity will be called the 'planar MAE' going forward. These properties are important to determine for these materials to be potentially useful for spintronic and computational applications such as bit memory devices [21] which rely on changes to the direction of the magnetizing field to operate. This planar MAE is useful but does not give a full understanding of the effects of magnetic anisotropy. We note the materials we discuss can be simulated effectively using a variety of methodologies [42, 119, 171, 172]. As well as this, the magnetic structure is critical to determining and predicting magnetic properties such as the anisotropy energy. The methods used in previous work such as by Szunyogh et al, Yang et al, Hernandez et al and Pradhan et al, focusing on screened Korringa-Kohn-Rostoker (SKKR), full-potential linear augmented plane-wave (FP-LAPW) and generalized gradient approximation (GGA) (Perdew, Burke and Ernzerhof (PBE)), differ such that direct comparison of results depends on the specifics of the simulation. To address this, we use a unified approach to simulate all materials we note in this chapter, and compare to previous studies so that the structural properties are correctly reproduced and match existing data.

Despite some experimental estimations of the MAE [161, 173, 167, 166, 42, 164], a more thorough investigation of the magnetic anisotropy is needed in these noncollinear materials, especially as there are few theoretical studies based on first-principles calculation involving relativistic effects using the higher order terms in the MA hamiltonian. To address these issues in this chapter we determine the planar MAE for a select range of noncollinear materials.

Though the study of the band structures of stable configurations of noncollinear materials has been undertaken before [171, 118], strain effects are needed to understand the change in electronic properties when strain is present, such as in a heterostructure where lattice parameters do not match perfectly. Structural changes in materials are common when the materials are placed upon mismatched substrates, and the structural changes will induce strain within the material [153, 174, 175, 176, 177, 178]. As such, we will later focus on the change in structural and band structure properties at a variety of strains, in particular examining the changes in the location of Weyl points within the band structure in order to track the effects of the change in strain. Weyl points are important aspects of momentum space, whereby they are specific features of the Berry phase, specifically the Berry curvature (whereby the former is the phase change of a system during a cycle and the latter is a gauge transformation associated with this phase), existing as monopoles (and anti-monopoles) within the Berry curvature. These monopoles and the associated Weyl fermions can then be understood as topological charges, resulting in high electron mobility due to the lack of dependence on symmetries excluding translation symmetry [179]. The inclusion of spin-orbit coupling (SOC) on the Weyl points sees changes in the band structure, critically splitting at the Weyl points [180]. It is worth noting the Weyl points are topologically protected, retaining the same invariant quantities with or without SOC [181]. We assess the effect of changing strain on these materials, questioning as to how it affects structural and electronic properties of the material. We aim to use this idea to determine the magnetic properties of these materials.

Straining a material is an interesting avenue of investigation, as it gives us an estimate of the effects of growth of this material on a substrate with differing structural parameters. This straining will alter the structural parameters of the (antiferro)magnetic material, resulting in an electronic reconfiguration and in our case may alter the magnetic properties. The work by Xiong et al demonstrates the practical effect of a strained material, providing us with an example of the method in action [182]. In Farkous et al's study, we see the use of density functional theory (DFT) in determining the effect of strain, and how we can determine directionally dependent strains [183].

The rest of this chapter is organised as follows. We describe the methodological details specific to this chapter in section 4.2. In section 4.3, we then move onto a survey of previously gathered experimental results in literature. In section 4.4, a summary of previous theoretical results are presented. In section 4.5.1, we present results for the structural, magnetic and anisotropic properties of Mn_3Ir, Mn_3Sn, Mn_3Ge and Mn_3Ga, and compare this to the experimental and theoretical results that are available in the literature in order to ensure the simulations are reasonable. In subsection 4.5.2, we present results on the effect of strain (both compressive and extensive strain) on the band structure of these materials. In section 4.6 we provide a discussion of the results, and a conclusion in section 4.7 summarizes the major findings of this chapter. We will explore the magnetic anisotropy in the chapter via study of the planar MAE in Mn_3Ir, Mn_3Sn, Mn_3Ge and Mn_3Ga.

4.2 Methods

We optimise the structural parameters, including volume and atomic positions, for the noncollinear materials. Without proper volume optimization, the subsequent analysis of other material properties will be inaccurate. The method of optimising the structure is identical to the previous chapter. As part of the initial conditions for the DFT calculation, the magnetic moments must be set to be noncollinear in specific directions for the correct magnetic phase to be obtained in order to avoid trivial solutions where all moments are zero or highly disordered configurations that are not well optimised and less stable magnetic phases e.g. ferromagnetic phases.

One strategy mentioned previously for finding the MAE in a crystal with noncollinear magnetic moments is to find a common axis about which all magnetic moments can be rotated coherently within a 2D plane. For example, this approach was employed by Szunyogh et al [42]. As a particular example, for Mn_3Ir the high symmetry rotation axes [1-11] and [110] were used. Rotation about the [1-11] axis is illustrated in Figure 4.3. For the other noncollinear materials considered in this chapter we adopt a similar approach with previously determined magnetic order, used to evaluate the magnetic high-symmetry planes of the material and therefore the best axes about which to reorient the magnetic moments (Figure 4.3). We examine such high-symmetry planes to define a planar anisotropy instead of assessing the unfeasibly large number of possible magnetic moment configurations that could participate in physical magnetization reversal processes. We begin by calculating the optimal bulk parameters of the material. We use the PBE functional revised for solids (PBEsol) exchange-correlation (XC) functional with spin-orbit

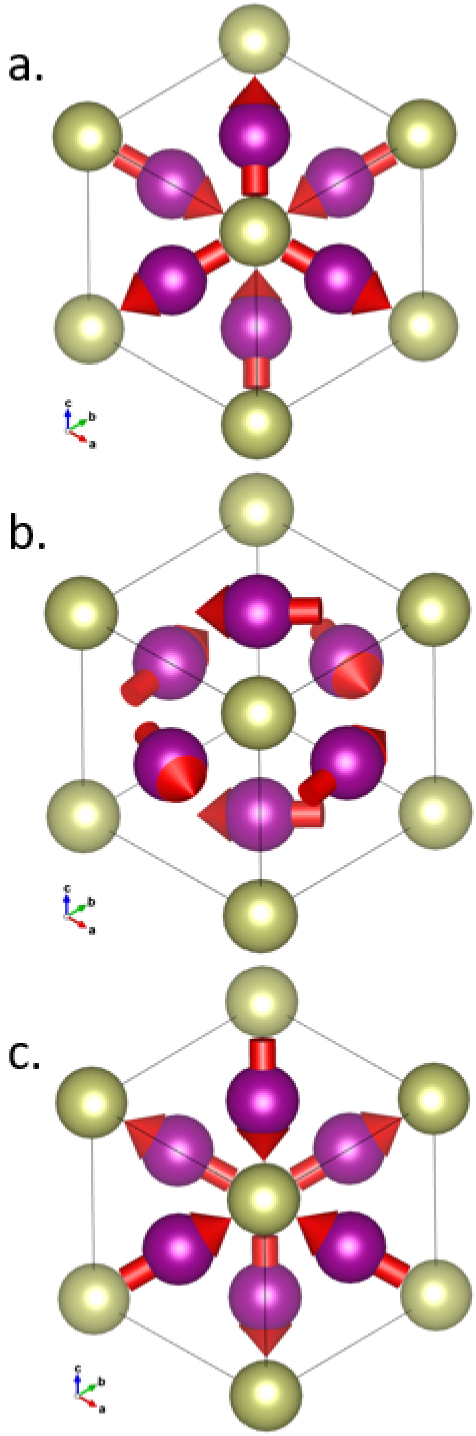

Figure. 4.3: Rotation of magnetic moments about the [1-11] axis for Mn_3Ir: a) 0°, b) 90° anticlockwise, c) 180° anticlockwise. The green atoms are Ir, and the purple atoms are Mn.

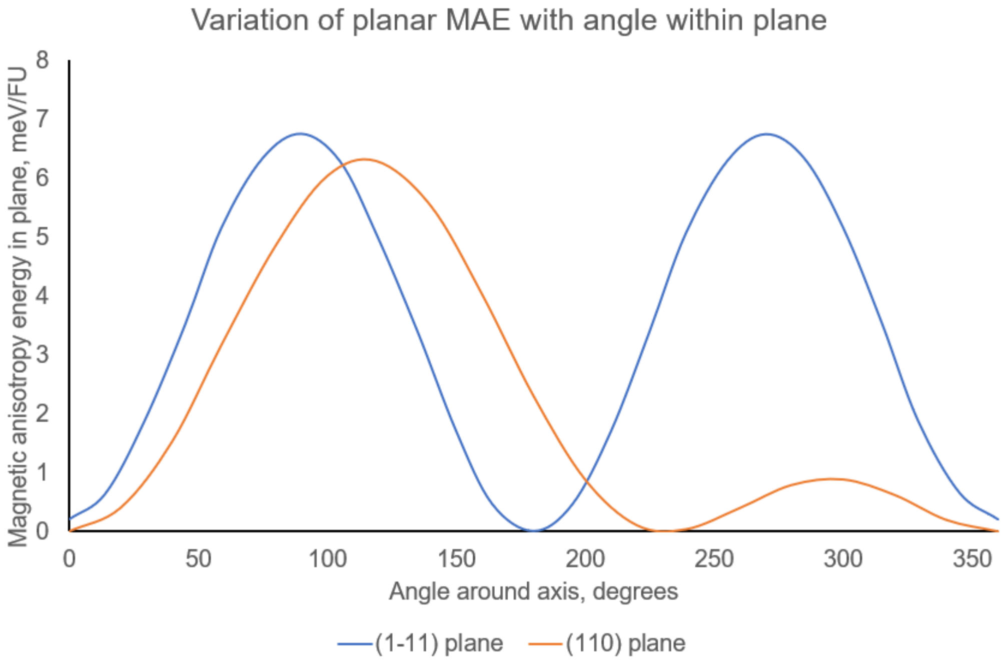

Figure. 4.4: Example of the effect of the rotation of the quantization axis in-plane for Mn_3Ir.

coupling included and a Hubbard U of 1eV to simulate the cell allowing volume, ion position and symmetry to change. We allow the magnetic moments to relax into the calculated optimal directions and magnitudes. Once these are determined, we may then reset the simulation grid and begin calculating the change in planar anisotropy energy. By allocating a series of changes to the shared quantisation axis of the magnetic moments, we can rotate the magnetic moments easily about a selected axis. By doing this, we preserve the relative magnetic order also. In this way, we may identify the relation between MAE and the relative rotation about the axis.

As an illustrative example, Figure 4.4 shows how the spin-orbit contribution to the anisotropy energy changes with angle in Mn_3Ir. As discussed in Szunyogh et al [42], the magnitude of the oscillation of the planar MAE with angle should be equal to the on-site anisotropy constant, and the rotation in-plane should produce a smooth variation of 180° symmetry (Figure 4.4). Rotating around lower-symmetry axes would be less useful due to the high probability of high-energy configurations being formed. This approach to evaluating MAEs is useful for systematic comparisons between materials even if the physical process may be different.

To supplement the planar magnetic anisotropy, we also simulate the magnetic dipole contribution to the anisotropy. Using the same magnetic parameters as the planar anisotropy energy, we run a calculation with a cutoff radius of 50 nm and a single timestep.

We also calculate the electronic properties of the $D0_{19}$ materials, specifically the band structure, as well as changes induced by biaxial strain applied in the (001) plane. This strain necessitates changes of structure and so we alter the lattice parameters such that we induce a strain, optimise the material in the c-direction, then determine the band structure. We do this by altering the lattice parameters a and b by some percentage to induce a strain in this plane. The a and b directions are constrained and will not be optimised. We then run a similar calculation to the previous methodology, a volume optimisation with a Hubbard U of 1 eV and spin-orbit coupling included that only allows the c lattice parameter and magnetic moments to alter. The band structure is then calculated for this new strained configuration. We monitor specific points in the band structure, in this case Weyl points, to track changes with strain in a range of $\pm$ 6% strain overall.

Our method includes a series of simulations operating at $5 \times 5 \times 5$ k-points (due to the larger primitive cells) in a Monkhorst-Pack sampling grid. We use an energy cutoff of 350eV, and a density functional theory with Hubbard U (DFT+U) correction value of 1 eV on the Mn atoms. We do not use symmetry constraints on the system, and use the projector augmented wave (PAW)-PBEsol pseudopotential. The force tolerance is 10^{-3} eV/A^{-1} and the energy tolerance is 10^{-5} eV/atom.

4.3 Previous experimental results

4.3.1 L1$_2$ materials

Values of the lattice parameter reported in literature (Table 4.1) range between 0.377 nm and 0.380 nm. In particular, the study by Taylor et al used magnetron sputtering to grow Mn_3Ir films. The component ratio of the sputtered materials was 72:28, determined via Rutherford backscattering spectrometry (RBS) and x-ray diffraction (XRD). The study finds a cubic lattice parameter of 0.380 nm via XRD [165]. A separate study by Tomeno et al used a 3:1 ratio of materials to grow a crystal via Bridgman method with a 1000 K, three-week annealing period. In this case the lattice constant measured via neutron scattering was 0.377 nm. Between the two studies discussed above is the lattice parameter result from the study by Mao et al, where the epitaxial growth of 15 nm of Mn_3Ir on MgO [111] at 600 °C resulted in lattice parameters of 0.379 nm and 0.380 nm for the bulk and film respectively (measured via XRD). The overall agreement is remarkably clear, with results differing by 0.003 nm, with an average value of a=0.378 nm.

Material	a (nm)	c (nm)	Crystal structure type	Magnetic structure	Moment (μ_B)	MAE (meV/FU)	References
Mn_3Ir	0.378	0.378	$L1_2$	AFM, (1-11)	-	-	[165, 184, 147, 117]
Mn_3Ga	0.531-0.540	0.435-0.439	$D0_{19}$	AFM, (001)	2.40	0.0300	[185, 186, 166, 169]
Mn_3Ge	0.533	0.431	$D0_{19}$	AFM, (001)	2.23	0.0100	[163, 167, 187]
Mn_3Sn	0.559-0.568	0.451	$D0_{19}$	AFM, (001)	3.00	0.0002-0.0003	[173, 188, 189, 190, 191, 161]

Table 4.1: Experimental parameters for $L1_2$ and $D0_{19}$ materials, including lattice parameters, magnetic structure and plane where magnetic moments are flat, and MAE.

This indicates the structure is well-known, and would be a useful parameter to compare to.
Mn_3Ir adopts an $L1_2$ crystal structure with a planar magnetic moment configuration, whereby all moments lie within the (1-11) plane. The planes within which the magnetic moments lie are formed of a unit cell of three manganese atoms forming a triangle of magnetic moments that all point toward or away from the centre of said triangle, as in Figure 4.3. The studies in Table 4.1 agree on the magnetic ordering, finding an antiferromagnetic magnetic order with moments parallel to the (1-11) planes. Particularly in Tomeno et al's study, the strong exchange interaction seen within the (111) plane indicated orthogonal magnetic moments. In the study by Kohn et al, neutron diffraction measurements on a 200 nm ordered Mn_3Ir film revealed the $L1_2$ structure had antiferromagnetic ((1-11) plane) magnetic structure, making for an excellent agreement to the study by Tomeno et al and indicating a good consensus on the magnetic structure of this material.

4.3.2 $D0_{19}$ materials

We consider Mn_3Ga, Mn_3Ge and Mn_3Sn as examples of $D0_{19}$ materials. The magnetic moments sit parallel to the (001) plane, with two distinct sublattices offset vertically. The two arrays of three manganese atoms produce the triangular sublattices of atoms with antiferromagnetic ordering (Figure 4.2).

Mn_3Ga

In Kurt et al's work on Mn_3Ga (Table 4.1), the sample of Mn_3Ga is produced via sputtering deposition, with XRD and tunnelling electron microscopy (TEM) being used to determine the structural and magnetic properties of the sample which has a species ratio of 3:1 [185]. Films of Mn_3Ga are grown on Si wafers and sputtered Ru index-matching layers. The lattice parameters for Mn_3Ga are noted to be 0.531 nm and 0.435 nm for a and c respectively. Kurt et al's study references the work by Kren and Kadar. This study generates the sample via metal melt technique using two high-purity species, producing a sample of 2.85:1.15 stoichiometry, determined by chemical analysis [186]. The lattice parameters this work determined are a=0.536 nm and c= 0.432 nm and were determined by XRD. In Liu et al's study, a sample of Mn_3Ga is heat-treated at 893K and the lattice parameters are measured via XRD at room temperature [169]. The lattice parameters are found to be a= 0.540 nm and c=0.439 nm. The results from this study agree well with Kurt et al's study, differing by less than 0.01 nm. This indicates a strong structural agreement for the lattice parameters to be within a= 0.531-0.540 nm and c=0.435-0.439 nm.

This work by Kurt et al also finds the magnetic moment to be 2.4 μ_B/Mn. Neutron diffraction is used for property characterisation. The magnetic moments lie parallel to the (100) plane. Identical results are found in the work by Kren et al. Wu et al find an estimation of the MAE to be 0.03meV/FU from the frequency and grain size relation of the temperature-dependent exchange bias, using a sample grown on a silicon substrate with energy dispersive x-ray (EDX) measurements to characterise stoichiometry of 2.8:1.2, and vibrating sample magnetometer (VSM) is used to confirm magnetic properties [166].

Mn_3Ge

For Mn_3Ge, the study by Chen et al used metal melting to construct the sample, with the constituent species melted at a 3:1.025 ratio, heated to 1050 °C for two days then cooled to 740 °C and annealed at this temperature for seven days [163]. The properties were determined via XRD and neutron diffraction. The study determined that the lattice parameters are a= 0.533 nm and c= 0.430 nm (Table 4.1). In the work by Kiyohara et al, purified manganese and gallium was arc-melted and annealed at 860 °C for three days, then quenched in water [187]. scanning electron microscopy (SEM) EDX probing in this study concludes the material ratio is 3.05:0.95 Mn:Ge and hexagonal. XRD measurements show the lattice parameters are a= 0.534 nm and c= 0.431 nm, which agree remarkably well with Chen et al and indicate a very strong structural agreement. Similar studies include Rai et al, where the Mn_3Ge material was prepared in a 3.09:0.91 ratio via induction melting, heated in quartz to 1273K for 10 hours, cooled by 2K/hour to 1073K then quenched [187]. The material composition was assessed by inductively coupled plasma optical emission spectroscopy (ICP-OES), and the lattice parameters were found to be a=0.533 nm and c=0.431 nm via XRD.

The magnetic moment of Mn_3Ge is determined by the study by Chen et al to be 2.21 μ_B/Mn. The magnetic moments are all parallel to the (001) plane. In Rai et al's study, the magnetic moment was assessed by neutron diffraction to be 2.25 μ_B on each Mn atom, two very similar magnetic moments. In the work by Liu et al, metal melting of equal quantities of metals for Mn_3Ge was used to generate the sample using the Bridgman-Stockbarger technique, with properties determined via piezoresistive torque magnetometer [167]. The study notes the magnetic anisotropy Hamiltonian gives a six-fold symmetry term of 0.01 meV calculated from the torque magnetometry the study undertakes, making for a useful indirect comparison to the magnetic anisotropy calculations.

Mn_3Sn

Mn_3Sn is characterised in the work by Yang et al (Table 4.1) [189, 190]. The study by Yang et al uses the Sn-flux growth method to produce their samples, as per the work of Sung, Ronning, Thompson and Bauer [192]. This work used a magnetic property measurement system (MPMS) to determine structural information, and found that the lattice parameters are a= 0.568 nm, c= 0.452 nm. Brown et al's study on Mn_3Sn reveals similar information on Mn_3Sn's structural and magnetic properties (Table 4.1) [173]. The study finds a= 0.559 nm, c= 0.450 nm.

Sakamoto et al's work uses magneto-optical Kerr effect (MOKE) to measure the magnetic properties of Mn_3Sn [188]. Mn_3Sn is produced via metal melting under vacuum at 1050 °C. Single crystals were generated by crushing the Mn_3Sn and heating under 1080 °C. Inductively coupled plasma spectroscopy showed a material ratio of 3.07:0.93 Mn:Sn. The magnetic moment is found to be around 3 μ_B/Mn via MOKE. The magnetic moments lie parallel to the (001) plane.

The magnetic moment from the study by Brown et al was found to be 3.00 μ_B/Mn, similar to Sakamoto et al's approximate value, and the moments are parallel to the (001) plane also. The sample properties are measured via neutron scattering.

In the study by Low et al, the sample is generated by powder melt in argon atmosphere, with a ratio of species of 7:3. The sample is heated to 1000 °C, cooled to 900 °C, and air quenched [191]. XRD and energy dispersive x-ray spectroscopy (EDXS) measurements confirm the composition. electrical transport option (ETO) and VSM are used to measure the magnetic properties. It is determined that the magnetic moment is 3 μ_B/Mn.

Miwa et al's study uses bulk single-crystal Mn_3Sn as a sample, with time-resolved magneto-optical Kerr effect (TR-MOKE) used to measure properties [161]. This work supports the previously discussed studies by finding the magnetic moment on Mn to be $3\mu_B$. This is in excellent agreement to the studies by Sakamoto et al and Brown et al, and the six-fold MAE found from torque measurements when rotating the magnetic field around the (0001) axis is estimated as 0.0003meV/FU. In the work by Duan et al, the sample was prepared by melting metal species together to form polycrystalline Mn_3Sn, then melted at 1273 K in a quartz tube with argon gas to form monocrystalline Mn_3Sn, crushed and a hexagonal ($D0_{19}$) sample selected [190]. Quantitative electron probe microanalysis (EPMA) analysis showed that the composition of the single crystal is 3.13:1 Mn and Sn. Cu-K-alpha (XRD), scanning electron microscopy (SEM, XL30, PHILIPS), and EPMA (1610, SHIMADZU) were used to determine the structural properties, and magnetic properties were determined via VSM, torque-magnetometer and heat capacity systems, and the study calculates a periodic MAE in the (0001) plane from torque measurements to be 0.0002meV/FU, similarly low to Miwa et al.

4.4 Previous theoretical results

4.4.1 L1_2 Mn-alloys

Similar to the experimental results in Table 4.1, Szunyogh et al identify, in their study, that Mn_3Ir is a cubic structure of lattice parameter a= 0.379 nm [42]. The study uses self-consistent SKKR with a local spin density approximation as parameterized by Vosko et al. In Opahle et al, the lattice parameter is determined to be 0.371nm, using DFT, with a PBE GGA to exchange correlation with spin-orbit coupling included [45]. The agreement is strong, putting the lattice parameter in the range of 0.371-0.379nm (a very tight range). Comparing these predictions (Table 4.2) to those in Table 4.1, we can see the lattice parameters differ by 0.26% and 1.8% for lower and upper ranges respectively.

In the study by Szunyogh et al, the manganese atoms have a magnetic moment of 2.66 μ_B/Mn, in a triangular configuration in the (1-11) plane. The anisotropy about (1-11) is 10meV.

4.4.2 D0_{19} Mn-alloys

Mn_3Ga

For lattice parameters, Hernandez et al's study of Mn_3Ga gives a useful pair of values (Table 4.2) [119]. The study uses DFT, with a PBE GGA to exchange correlation. Spin-orbit coupling was included, and a supercell of 9 to 10 stacked layers separated by vacuum (a thin film calculation). The lattice parameters found for Mn_3Ga in the study by Hernandez et al are a= 0.525 nm, c= 0.424 nm. The magnetic moment is 2.48 μ_B/Mn, in the (001) plane. Compared to the results in Table 4.1, the lattice parameters differ by 1.1% for a and 2.6% for c, and the magnetic moment differs by 3%. This is an excellent agreement between theoretical and experimental studies.

Mn_3Ge

From the study by Yang et al, the theoretical study of Mn_3Ge determines that the lattice parameters of Mn_3Ge are a= 0.535 nm, c= 0.431 nm [171]. The study

Material	a (nm)	c (nm)	Magnetic structure	Moment (μ_B)	MAE (meV/FU)	References
Mn_3Ir	0.371-0.379	0.371-0.379	AFM, (1-11)	2.66	+10	[42, 45]
Mn_3Ga	0.525	0.424	AFM, (001)	2.48	-	[119]
Mn_3Ge	0.535	0.431	AFM, (001)	2.29-2.70	-	[171, 193]
Mn_3Sn	0.567	0.453	AFM, (001)	3.12-3.17	-	[171, 172]

Table 4.2: Theoretical parameters for $L1_2$ Mn-alloys, including lattice parameters, magnetic structure and plane where magnetic moments are parallel, and MAE.

uses DFT, with a PBE GGA to exchange correlation. In the work by McCoombs et al, which also uses DFT (specifically using a PBE GGA to exchange correlation with spin-orbit coupling included [193]), the lattice parameters of Mn_3Ge are a= 0.535 nm and c= 0.431 nm (Table 4.2). The theoretical studies by Yang et al and McCoombs et al bear remarkable agreement, indicating the lattice parameters are well understood for the theoretical approach they share. They also are very close to the determined experimental lattice parameters, differing by 0.001 nm. We compare data on Mn_3Ge (Table 4.1), and see minor differences in lattice parameters,by 0.75% for a, a very small difference, and matches near-perfectly for c.

The magnetic moment is calculated to be 2.70 μ_B/Mn in Yang et al's study, with all moments parallel to the (001) plane (Table 4.2). The magnetic moment also differs by 10% to that in Table 4.1, which is in reasonable agreement to the experimental study. The work by McCoombs et al retrieves a magnetic moment of 2.29 μ_B/Mn, a fairly significant difference. This indicates there is some uncertainty as to the magnetic moment between studies. Both differ from experiment (Table 4.1), with Yang et al's study differing from experiment by 21% and McCoombs et al's study differing by 2.7%.

Mn_3Sn

Also from Yang et al's work, the study into the properties of Mn_3Sn contains results that note the lattice parameters are a= 0.567 nm, c= 0.453 nm (Table 4.2) [171]. The study uses DFT, with a PBE GGA to exchange correlation. In Pradhan et al's study, they used DFT codes based on both FP-LAPW and PAW, using experimental lattice parameters 0.566 nm and 0.452 nm [194] for a and c respectively [172]. The theoretical studies match well with the upper end of the experimental lattice parameter determination for a (Table 4.1). Comparing the theoretical predictions to experimental average we find the difference of lattice parameters is 0.33% and 0.49%, excellent agreement for a and c respectively.

The study by Yang et al also determines that the magnetic moment is 3.17 μ_B/Mn, parallel to (001) plane (Table 4.2). A 6.7% difference in terms of the magnitude of the magnetic moment to Table 4.1 indicates that these theoretical predictions are a very good match to experiment. Pradhan et al's study of the magnetic moment on Mn in Mn_3Sn has resulted in a magnetic moment magnitude of 3.12 μ_B, a 4% difference to the experimental average. The studies by Yang et al and Pradhan et al are well-matched, and match well to experiment (Table 4.1).

4.5 Results

4.5.1 Structure, magnetic and bulk properties

Firstly, Mn_3Ir is simulated in a bulk configuration. We determine that the lattice parameter is 0.364 nm for Mn_3Ir, for a cubic face-centred configuration. We also determine a spin-orbit contribution to the planar MAE of 6.29 meV/FU when rotating about (1-11), and a magnetic dipole contribution of -0.003 meV/FU, for a total planar MAE of 6.26meV/FU. The magnetic structure is given in Figure 4.5, and the magnetic moments are parallel to planes perpendicular to [1-11].

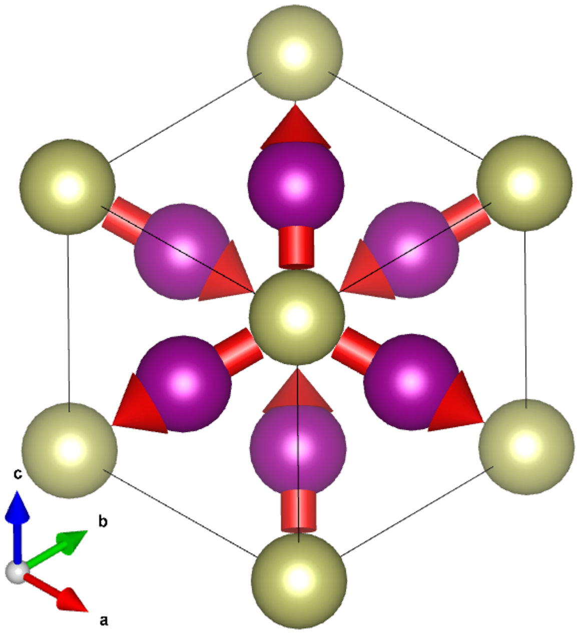

Figure. 4.5: Mn_3Ir simulated structure with magnetic moments, positioned along the [1-11] axis.

We investigate the simulated parameters of Mn_3Ga (Table 4.3). We find that the structure forms hexagonally, and determine that the lattice parameters are 0.525 and 0.428 nm for a and c respectively as in Figure 4.6. The magnetic moment on the manganese atoms is determined to be 3.18 μ_B, and all form a magnetic structure that's parallel to the (001) plane. The planar MAE is 0.0289 meV/FU from the spin-orbit contribution and -0.0012 meV/FU from the magnetic dipole contribution, resulting in a total planar MAE of 0.0277meV.

We now consider the results for Mn_3Ge (Table 4.3). We determine that the lattice parameters are 0.514 and 0.426 nm for a and c respectively. The magnetic moment on the manganese atoms is determined to be 3.09 μ_B and the magnetic structure

Material	a (nm)	c (nm)	Magnetic structure	Moment (μ_B)	planar MAE (meV/FU)	dipole anisotropy energy (DAE)
Mn_3Ir	0.364	0.364	AFM, (1-11)	2.79	+6.2900	-0.0030
Mn_3Ga	0.530	0.428	AFM, (001)	3.18	+0.0289	-0.0012
Mn_3Ge	0.514	0.426	AFM, (001)	3.09	+0.0019	-0.0011
Mn_3Sn	0.559	0.446	AFM, (001)	3.37	-0.0029	+0.0059

Table 4.3: Calculated parameters for $D0_{19}$ materials, including lattice parameters, magnetic structure, and MAE

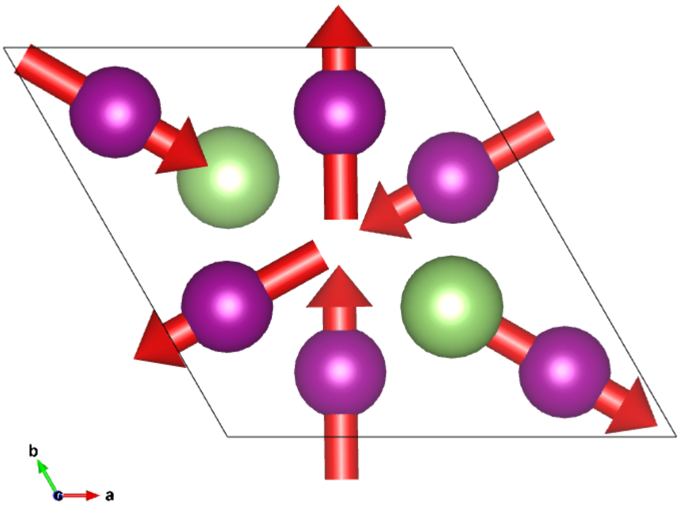

Figure. 4.6: Mn_3Ga simulated structure with magnetic moments, viewed in the (001) plane. The green atoms are Ga, the purple atoms are Mn.

is an offset planar structure in (001) (Figure 4.7). The simulated planar MAE has a 0.0019 meV spin-orbit contribution, though this is higher than the total planar MAE after DAE compensation of +0.0008 meV.

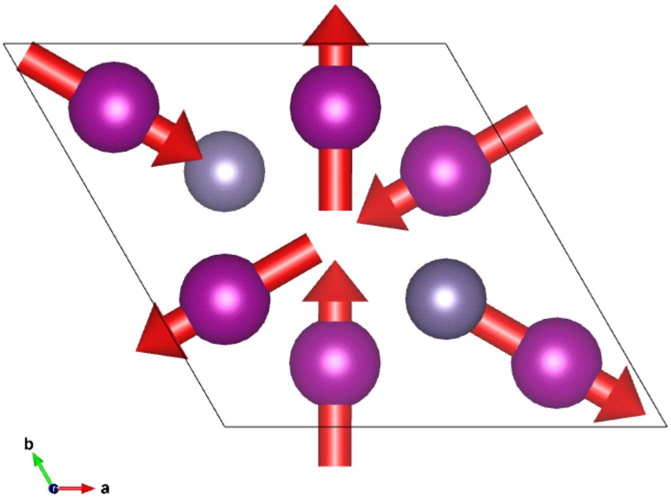

Figure. 4.7: Mn_3Ge simulated structure with magnetic moments, viewed in the (001) plane. The grey atoms are Ge, the purple atoms are Mn.

We then look at results for the simulation of Mn_3Sn (Table 4.3). We determine that the lattice parameters are 0.567 nm and 0.446 nm for a and c, and the magnetic moment on the manganese atoms is determined to be 3.37 μ_B from the calculations, visualised in Figure 4.8. The magnetic structure is an offset planar structure with moments all parallel to the (001) plane. The planar MAE is -0.0029 meV/FU.

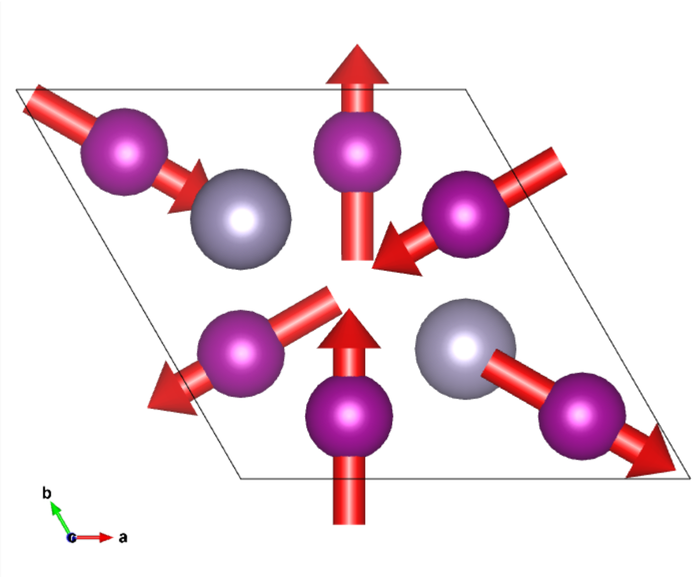

Figure. 4.8: Mn_3Sn simulated structure with magnetic moments, viewed in the (001) plane. The grey atoms are Sn, the purple atoms are Mn.

4.5.2 Strain and band structure

A common effect when creating heterostructures from materials that do not have perfectly matching lattices is that some level of strain is introduced, which will have significant impact on the electronic properties of the material. This impact is manifested in changes to the structure, magnetic properties, and bulk properties like band structure. We will evaluate the change in structural, magnetic and electronic properties during this straining procedure on the $D0_{19}$ AFM materials, in order to see the effect heterostructure-induced straining would have on these antiferromagnets.

Strain

To properly investigate the strain, we first determine a region of strain that is reasonable to use that will not be likely to change the phase of the material; we determine a ±6% change in lattice parameters in the a and b direction results in purely a planar strain without any risk of phase change, and analyse every percentage point of strain in-between. The lattice parameters change enough to be significant in effect at these strain limits. We must also determine how these samples are "grown"; in this case, we can note that these materials generally form an alternately layered system in the c-direction, so we may allow only the c-axis to alter during optimisation. We may then define strain in a,b via altering the lattice parameters directly in the calculation. Comprehensive optimisation will be needed at each strain to adequately determine the ground-state configuration of the magnetic material with these new lattice parameters. Because we are not altering the phase of the material, we assume identical magnetic orders between each phase. Otherwise, we use identical settings other than a change in lattice parameters for all calculations of this type. We complete changes in strain for noncollinear materials Mn_3Ga, Mn_3Ge and Mn_3Sn, and each strain value for these materials. We expect to see a minimum at 0% strain and a linear change in c; an energy minima forming at 0% strain would be a necessary consequence of proper optimisation and a useful indicator of the calculations' validity. The linear change in c lattice parameter will correspond with the linear change in a and b.

Effects on magnetic configuration are unlikely to be useful as we consider the magnetic system to remain unchanged in the Strukturbericht notation in the range of strains we use, though not strictly the magnetic moment itself (Figure 4.9). Whilst we expect to see fractional changes in the angle of magnetic moments, we would largely be concerned with ensuring the magnetic ordering remains the same. We need to be aware of phase changes occurring as this will result in the strain data becoming incomparable; this should largely be avoided by the choice of strain range, however it is important to be aware of any potential changes to avoid irrelevant data. Phase changes may be signified by departure from a smoothly varying strain curve, and represent alterations of standard cell structure or magnetic phase. Good estimates for c-lattice parameter are critical in determining the proper c-lattice value post-strain. These estimates can be determined formulaically by changing the c-lattice parameter by the negative of the percentage change of a and b.

We determine further band structure changes and changes in the density of states in order to track the changes in electronic properties, focusing on specific points for each material. This will be done as a function of strain. The strain calculations can then be used to identify thin-film or near-boundary effects, and so tune material heterostructures to produce desired effects via choice of substrate. We can use the changes in structure to develop strain-related models of the planar MAE and DAE also, to determine how strain alters key magnetic properties and therefore how they can be altered by the choice of substrate.

Three primary materials are tested in the hexagonal $D0_{19}$ order; Mn_3Sn, Mn_3Ge,

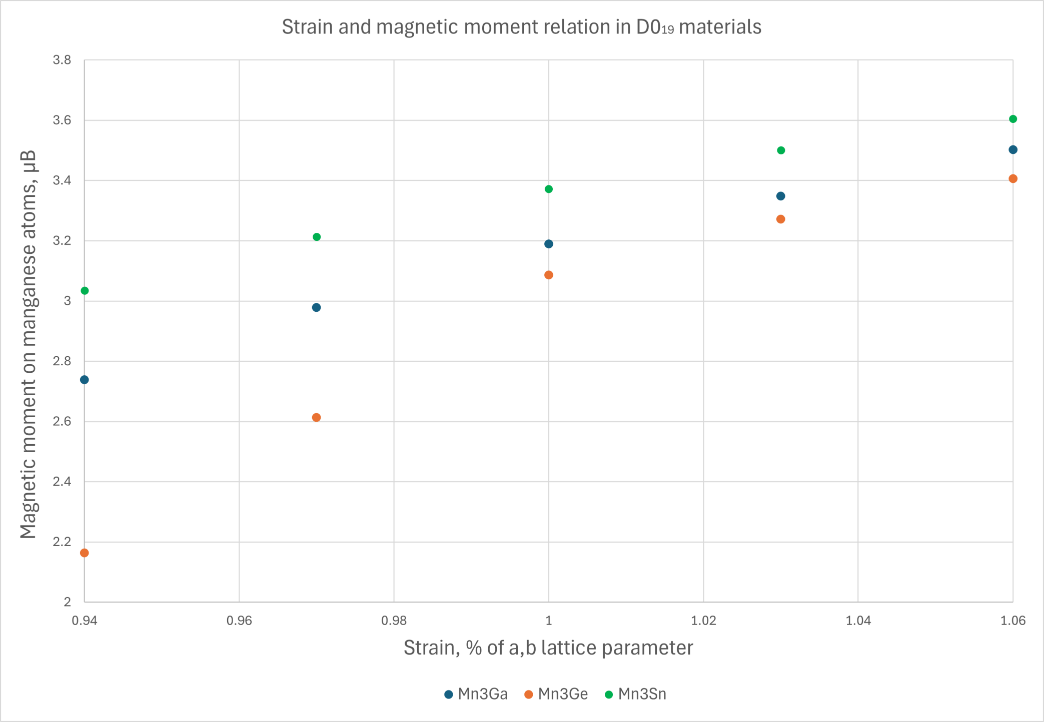

Figure. 4.9: Variation of magnetic moment with strain for the $D0_{19}$ materials.

Mn_3Ga. All materials form a minimum within the expected strain range of ±6%. The distribution of energy of formation will not be exactly symmetric; positive and negative strains will affect the material in different ways, and as such may not do so equally. All materials form a minima of formation energy vs. strain at 0% strain; this is is a useful confirmation of the method, and an expected result as straining a material should perturb the optimal equilibrium structure (Figure 4.10). Magnetic structure is largely the same across all strains, with minimal distortion in the $D0_{19}$ structures. This indicates the range of strains is adequate for the calculations. We can determine from the low magnetic distortion that the materials remain stable in their current structural and magnetic phase. We note the magnetic moments increase with strain, though not strictly linearly (Figure 4.9).

Mn_3Ga has an amplitude of 0.7 eV for the smoothly varying change in formation energy (Table 4.4). The alteration of the c-lattice parameter is linear. Similarly, Mn_3Ge has an amplitude of 0.8 eV, and the c-lattice parameter varies equally smoothly. Mn_3Sn has an amplitude of 0.6 eV, and the change in the c-lattice parameter is mostly smooth, with some small oscillations present.

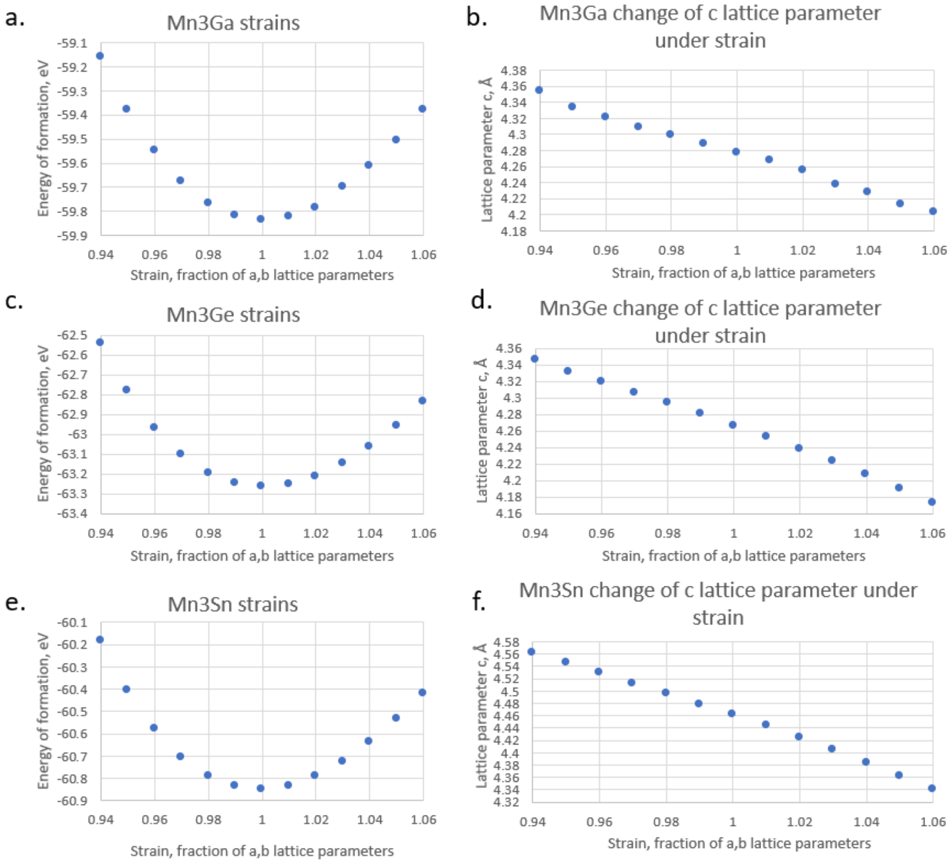

Figure. 4.10: Energy of formation trends and c lattice parameter variation for strained $D0_{19}$ materials a,b) Mn_3Ga, c,d) Mn_3Ge, e,f) Mn_3Sn.

Material	Energy of formation change, eV	Strain minima, %	c (nm)
Mn_3Ga	0.7	0	0.428
Mn_3Ge	0.8	0	0.427
Mn_3Sn	0.6	0	0.446

Table 4.4: Calculated parameters for $D0_{19}$ materials under strain, extracting data from Figure 4.10. The resultant amplitude of the energy of formation, the energy of formation minimum of the strain and the c-lattice parameter at the minimum are given to elucidate on the primary effects of the strain.

Band structure

Band structures contain information on many electronic properties and are therefore important to evaluate. For changing strains, the properties will alter significantly. Tracking these changes will be important to understand the evolution of these systems under mechanical changes.

To determine the effect of this strain on these electronic properties, we evaluate band structure changes at a range of different strains, as the band structure can be used to determine a wide array of properties.

After the optimization process from the calculated strain effects, a band structure calculation is performed in order to generate the band structure. We determine set k-points to compare to the band structure at 0% strain in order to determine whether the additional strain provides desirable outcomes.

Certain noncollinear structures have Weyl points; these are consistent features in the band structure that seem to remain apparent for a number of strains, so tracking changes to these features is an excellent way of tracking band structure change. These Weyl points are a useful reference point that could be mapped across the strain to determine trends of changes in the band structure. We evaluate the changes to the Weyl points and see if they can be found in literature and also see if they prevail across the strain distribution.

We perform this series of calculations from -6% strain through to +6% strain, altering the a and b lattice parameters by the according strain percentile to induce lateral strain as before. We gather the band structure and assess the change in pre-selected Weyl points. We may then produce a comparative path of strain vs. Weyl point of band structure (Figure 4.11).

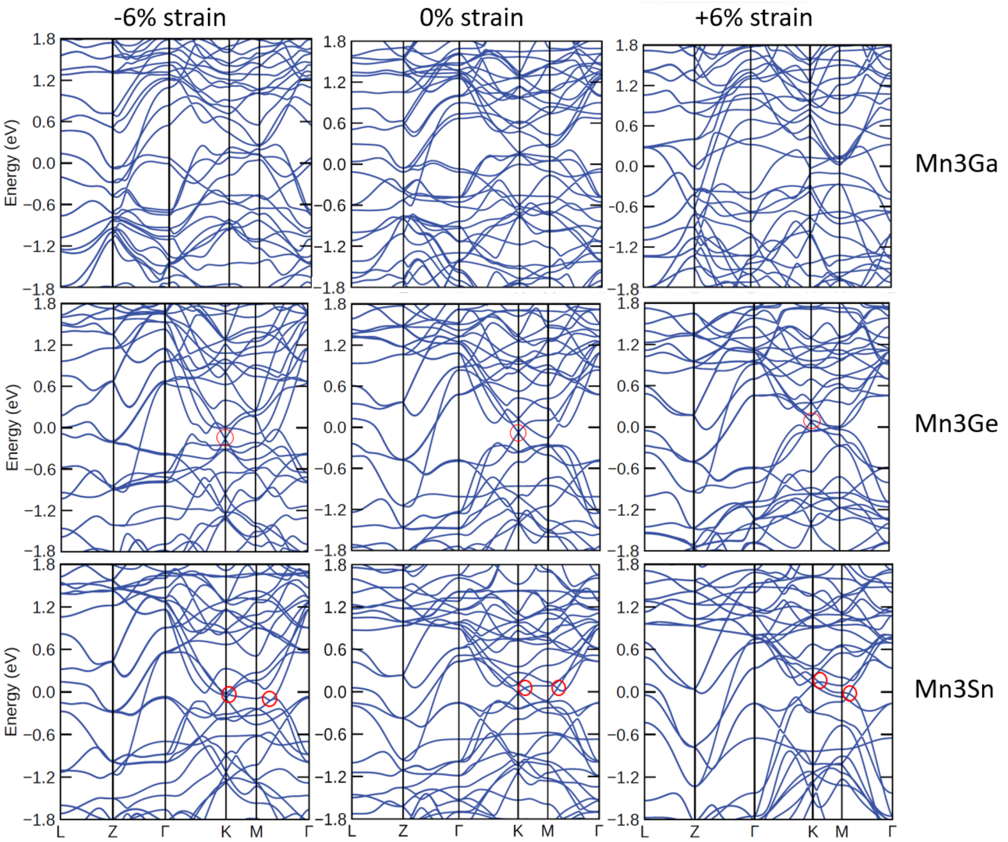

Figure. 4.11: Band structures for various strains and materials. The red circles indicate the Weyl points present in these band structures.

In Mn_3Ga's band structures, we note that no point corresponds to a Weyl point. We can instead note the changes to the bands visible around the M point, which has an indirect bandgap 0% strain. at -6%, we note the bandgap closes together somewhat, and at +6% strain the bandgap fully closes (Figure 4.11).

In Mn_3Ge, we track a single Weyl point on K. At -6%, we see the Weyl point settle at -0.15eV in relation to the Fermi energy. At 0%, the Weyl point is 0.07eV under the Fermi energy, and retains the rising limb and falling limb of its band structure on the right. At +6%, the Weyl point has shifted to +0.07eV, and the rightmost upper band has collapsed. The total magnitude of change is 0.22eV. The Weyl point changes at +6% to have two falling limbs on the right (Figure 4.11).

The k-points at M and K have features near the Fermi energy that resemble Weyl points in Mn_3Sn (Figure 4.11). We assess their change in energy, position and nature throughout the straining process, and find that the Weyl point rises with respect to fermi energy for the Weyl point close to K. The amplitude of the rise in energy is small, mustering around 0.01 eV overall from -6% to 0% and 0.01eV

from 0% to 6%. The Weyl point nature at +6% changes with the rightmost rising limb becoming a falling limb. There is also a change for the M points with strain, increasing by around 0.01 eV from -6% to 0%, however the M Weyl point reduces in energy above 0%.
The Weyl point has a chiral nature, which coincidentally affects the conductivity of a material whilst within a magnetic field. We would therefore expect to maintain the electron mobility due to the consistent number of Weyl points remaining across our strain distribution.

4.6 Discussion

The material structures we have calculated are highly comparable to previous studies, and the lattice parameters and magnetic parameters match well to experiment and theory studies to within a few percentage points for each lattice parameter value. With such close results, we can be confident the simulated model is correct for the structure of the material. We will now elaborate further on these comparisons.

Material	Experimental parameters, nm		Theoretical parameters, nm		Calculated parameters, nm	
-	a	b	a	b	a	b
Mn_3Ir	0.378	0.378	0.371-0.379	0.371-0.379	0.364	0.364
Mn_3Ga	0.531-0.540	0.435-0.439	0.525	0.424	0.530	0.428
Mn_3Ge	0.533	0.431	0.535	0.431	0.514	0.426
Mn_3Sn	0.559-0.568	0.451	0.567	0.453	0.559	0.446

Table 4.5: Comparison of the structural parameters of each of the materials in this chapter compared to experimental and theoretical parameters

$L1_2$-Mn_3Ir has been studied theoretically using the planar MAE approach described earlier in the study by Szunyogh et al (Table 4.2). This gives us a useful theoretical comparison. We therefore use the $L1_2$-Mn_3Ir to determine how well the method works. We find the calculated results (Table 4.5) very comparable to the theoretical study by Szunyogh et al, in terms of the periodic variation and the magnitude of the MAE as well as general properties of the material. We determine that the lattice parameter is 0.364 nm, similar to Szunyogh et al's study's 0.379 nm. The experimental studies by Taylor et al and Tomeno et al also find a similar lattice parameter very close to the calculated result (Table 4.5). Ophale et al's theoretical study finds the lattice parameter to be 0.371 nm, differing by 1.9%. The simulated magnetic characterisation includes a magnetic moment per Manganese atom of 2.79 μ_B compared to Szunyogh et al's study's 2.66 μ_B (Table 4.6), and the magnetic structure takes a noncollinear AFM arrangement parallel to the (1-11) plane, in excellent agreement with the study. The experimental work by Tomeno et al and Kohn et al finds similar magnetic structure with the magnetic structure with (111) and (1-11) planes of magnetic moments. The calculated planar MAE of 6.26 meV/FU is similar to the planar MAE in Szunyogh et al's study of 10 meV/FU (Table 4.6).

Material	Experimental		Theoretical		Calculated		
	Magnetic moment, μ_B	MAE, meV/FU	Magnetic moment, μ_B	MAE, meV/FU	Magnetic moment, μ_B	MAE, meV/FU	DAE, meV/FU
Mn_3Ir	-	-	2.66	+10	2.79	+6.2900	-0.00300
Mn_3Ga	2.40	0.03	2.48	-	3.18	+0.0289	-0.00115
Mn_3Ge	2.23	0.01	2.29-2.70	-	3.09	+0.0019	-0.00110
Mn_3Sn	3.00	0.0002-0.0003	3.12-3.17	-	3.37	+0.0029	-0.00590

Table 4.6: Comparisons of the magnetic moments and MAE of experimental and theoretical literature vs. the calculated results

We determine that the lattice parameters for Mn_3Ga are a=0.525 nm and c=0.428 nm; comparing to the results in Table 4.5, we see that the lattice parameters from Kurt et al's experimental work are predicted to be a= 0.531 nm and c= 0.435 nm, differences of 1% and 1.6% respectively. We find that the experimental work by Kren and Kadar finds similar lattice parameters to our own (a=0.536 nm and c= 0.432 nm, a difference of 2% and 0.9% respectively), though Liu et al's experimental study finds lattice parameters that are slightly further from ours (a= 0.540 nm and c=0.439 nm, a difference of 2.9% and 2.6% respectively). For theoretical studies (Table 4.5), we find Hernandez et al's study gives a= 0.525 nm, c= 0.424 nm, a perfect match for a and a difference of 0.94% for c. The magnetic moment on the manganese atoms is found to be 3.18 μ_B, differing from Kurt et al's experimental study, which retrieved 2.40 μ_B (Table 4.6), a difference of 32.5%, and the magnetic structure is an offset planar structure in the (001) plane, implying that simulation finds stronger field than experiment. We note therefore there are still significant differences between the magnetic effects modelled in our work and the reality of the experiment. In the theoretical work by Hernandez et al, we find the magnetic moment to be 2.48 μ_B, a difference of 28%, a difference likely due to the lack of U-value and the thin-film approach taken in Hernandez et al's model. The planar MAE is 0.0289 meV/FU, comparable to Wu et al's experimental value of 0.03 meV/FU, a difference of 3.8% (Table 4.6).

We determine that the lattice parameters of Mn_3Ge are 0.514 and 0.426 nm for a and c respectively (Table 4.3), which differ from Chen et al's experimental study's lattice parameters (Table 4.5) by 3.6% for a (0.533 nm) and by 0.9% for c (0.430 nm), and similar still to the experimental work by Kiyohara et al (a= 0.534 nm, c= 0.431 nm). Yang et al's theoretical work (a= 0.535 nm, c= 0.431 nm) and McCoombs et al's theoretical work (a= 0.534 nm and c= 0.431 nm), which calculate remarkably similar lattice parameters that differ from the calculated values by 4% for a and 1.1% for c respectively (Table 4.5). The magnetic moment on the manganese atoms is determined to be 3.09 μ_B compared to Chen et al's experimental study's 2.21 μ_B, a difference of 28.5%, and the magnetic structure is an offset planar structure in (001). Yang et al's study finds a value of 2.7 μ_B, a difference of 14%. We find closer agreement to theory, which is to be expected as the method is quite similar, and again find a significant difference to experiment. McCoombs et al's work finds a magnetic moment very similar to that of Chen et al's study. The planar MAE found by Liu et al's experimental work is 0.010 meV/FU, significantly larger than the calculated planar MAE of 0.0019 meV/FU (0.0008 meV/FU after DAE compensation) (Table 4.6).

We then look at Mn_3Sn. We determine that the lattice parameters are 0.567 and 0.446 nm for a and c respectively (Table 4.3), differing from the theoretical work by Yang et al (Table 4.2). Yang et al's experimental study determines the lattice parameters to be a= 0.568 nm and c= 0.452 nm, differing by 0.17% and 1.3% respectively. Brown et al's experimental work is similarly close (Table 4.5), with lattice parameters (a= 0.559 nm, c= 0.450 nm) differing by 1.4% and 0.8% respectively. Pradhan et al's theoretical study finds a=0.566 nm and c=0.452 nm, differing by 0.27% and 1.4%. The magnetic moment on the manganese atoms is determined to be 3.37 μ_B from the calculations, differing from Yang et al's theoretical work by 6%, with their value of 3.17 μ_B (Table 4.6). This result also differs from Sakamoto et al, Brown et al, Lowe et al and Miwa et al's experimental work, finding 3 μ_B each, by 12%. The work done by Pradhan et al finds a magnetic moment of 3.17 μ_B for Mn in Mn_3Sn, a difference of 8%. The magnetic structure is an offset planar structure in (001). The planar MAE is -0.0029 meV/FU, which is comparably low as per the work of Miwa et al, where a value of 0.0003meV/FU was found, and in a similar position to Duan et al's work, finding 0.0002meV/FU (Table 4.6).

Predicted magnetic properties are consistent with previous studies (Tables 4.5, 4.6); the calculated magnetic moments are within 33% of values in previous studies at most, and the calculated magnetic structures match the theoretical and experimental studies well. This indicates the first-principles approach can more than capably deal with the magnetic structure evident in these materials.

Reference planar MAEs for these materials differ to varying degrees, likely due to differences in definition or procedure as well as very low value (Tables 4.1, 4.3). The former is a very reasonable consideration, as our exploration of anisotropic trends is significantly limited by only considering the magnetically symmetric plane. In addition to this, we note the anisotropy energy for Mn_3Sn from the experimental studies is a calculation based on the experimental parameters retrieved from the torque measurements, indicating direct measurement is still quite a challenge to compare to [161, 190]. The high MAE of Mn_3Ir and significant difference to the $D0_{19}$ materials' MAE may be attributed to the high spin-orbit coupling between Mn and Ir. However, there is some attribution to the method of determining the MAE for why the MAE is so high; per Jenkins et al [11], the rigid rotation method we employ may well miss the local minima of the free-energy surface. We may therefore consider the potential for further MAE minimisation.

Straining alters properties in a logical manner (Figures 4.9 and 4.10), with relatively small magnitude of energy change with strain but consistent 0% minima in energy, and for all materials we see linear changes of the c lattice parameter with strain. We note that Mn_3Ge has the largest change in energy with strain, closely followed by Mn_3Ga, whilst Mn_3Sn has the lowest amplitude of energy. The c lattice parameters decrease linearly, a logical consequence to compensate for for the change in volume. The c lattice parameter at zero strain matches previous calculations (Table 4.4).

For the strain calculations, we see the band structures alter with strain (Figure 4.11). The number of Weyl points vary for each $D0_{19}$ material. For example, Mn_3Ga has no Weyl points in the band structures we calculate, but Mn_3Ge and Mn_3Sn have 1 and 2 respectively. The changes of the Weyl points, particularly energy changes, vary both linearly (Mn_3Ge) and nonlinearly (Mn_3Sn) with strain changes. Changes to the nature of the Weyl points remain fairly few, indicating generally consistent Weyl point migration with energy. Due to the potential high mobility of the Weyl fermion, the changes in Weyl point energy within the band structure mean a great deal for a spintronic device using read and write currents at their inherently high switching frequencies. As such, the combination of high mobility electrons in Weyl points and spintronic applications can be viewed as crucial to work in tandem together in a high-frequency memory device.

4.6.1 Sources of inaccuracy

The simulations show considerable difference to experiment for the magnetic moment magnitudes. It is possible this difference may cause properties we have calculated, such as the anisotropy in plane and the strains, to be less accurate than desired. However, we note that the simulated magnetic moments match existing theoretical studies well. This indicates the difference is an artefact of approach, and thus is likely a systematic error.

We make an assumption regarding changes in properties in relation to strain; we assume they come about from the optimization of the c-lattice parameter. We assume the lack of optimization in the other axes will not cause issues due to uniform straining, and due to the repeating nature of the cell (and rarity of dislocations) it is unlikely any relaxation should occur.

As before with the $L1_0$ systems, the experimental studies we reference are performed at a variety of temperatures. We cannot match these experimental temperatures exactly as we do not consider temperature effects, therefore we may note some difference to these studies. This may affect all parameters simulated.

Real materials may also have defects within the sample. As we model an ideal material in DFT simulations, different results are expected to the experimental studies because of this. Whilst all properties are potentially affected, significant deviations will occur in the magnetic and electronic properties.

4.7 Conclusion

The calculations of structural properties of the investigated materials (Table 4.3) match well to previous studies (Tables 4.1, 4.2), indicating that we successfully use a calculated approach to comprehensively characterise these materials. This also maintains a consistent and comparable approach between materials, and so we have successfully generated a comparable methodology for characterising these materials from first principles. We note the structure of each material matches the experimental and theoretical studies, which allows us to conclude that the structure is well-represented in the simulated data and can be predicted using our methodology.

The novel findings of this structural research reveal linear variation in lattice properties across moderate strain within $D0_{19}$ materials (Figures 4.9 and 4.10). These varied properties indicate the effects of applied strain will have a predictable effect on the properties of these materials, with particular utility to heterostructure devices.

The ground state calculations of magnetic structure of the investigated materials (Table 4.3) are very much comparable to previous experimental studies (Tables 4.1, 4.2). Use of a common approach to comprehensively characterise the noncollinear materials has yielded magnetic structures that are precisely aligned with the theoretical and experimental studies, indicating strong agreement. As such, the conclusion is that the magnetic structure is simulated with reasonable agreement to experiment. The calculated magnetic parameters of the materials are also found to be reasonably close to experimental studies, and closer still to theoretical studies. The material with the largest consistent difference in magnetic moment to theoretical studies is Mn_3Ga, with Mn_3Ge differing the most from experimental works. Mn_3Sn's magnetic moment is largely very similar to previous experimental and theoretical studies.

From the planar MAE calculations (Table 4.3), we can see the calculated values for the in-plane MAE match well with those from previous experimental and theoretical studies, indicating a universally applicable exploration of these values (Tables 4.1, 4.2). This implies the planar MAE of noncollinear magnetic materials may be predicted well using this method, and that the variation of the planar MAE may be predicted with confidence.

Novel findings note the peak of magnetic moment resides at maximum strain (Figure 4.9). Alongside this, the change in planar anisotropy energy for the $D0_{19}$ materials steadily decreases with strain (Table 4.4). We conclude that the applied strain will therefore increase the magnetic moment, and will result in lower MAE if strain is extensive. The band structures acquired for the ground state match well to studies of the non-strained environment (Figure 4.11). The strained band structures are sensible with regard to the Weyl point changes, with the number of Weyl points determined and clear Weyl points in the band structure. In particular, the alterations to Weyl points in these systems are reasonable, with the number of Weyl points remaining consistent, indicating well-determined band structure, which we can conclude reflects the topological nature of the Weyl point. The changes to the energy of the Weyl point vary in different ways, though we can note this variation alters with strain; we may conclude therefore that low strain will affect only the energetic properties of the Weyl points and thus maintain electron mobility of these materials, maintaining the high-frequency conductive properties.

Chapter 5

Interface effects on antiferromagnets

5.1 Introduction

In any nanoscale device, accounting for the effects of the nearby boundaries of a material is crucial for proper characterisation [195]. Alongside this, most nanoscale devices are designed to interface various layers of materials in a heterostructure in order to modify the properties of the device overall, such as certain types of transistor [196, 197]. We may expect the interaction of these interfaces to have some local electronic effect that will alter properties of the device as a whole, such as local polarisation affecting conductivity [198, 199]. As such, it is important to understand the effects of these interfaces on the properties of a thin slab of material in order to determine the changes these interfaces produce when compared to the bulk materials [200]. Surfaces and interfaces of materials can exhibit interesting and unique properties that differ greatly from bulk materials, such as altered charge densities, changes to magnetic ordering and structural changes, such as the changes seen through varying thickness of Mn_3Ge in the work by Wang et al [201]. These are important to characterise for devices with heterostructure configurations and thin film natures as the terminations of the materials can significantly alter the magnetic and electronic properties of the heterostructure as a whole. Surfaces are of course encountered in nearly any material, however interfaces are important for device construction due to the effects substrate materials can have on the films above them, such as the variation in platinum substrate thickness, shown in Jiang et al's work [202]. For most memory devices using spin-orbit torque (SOT)-antiferromagnetic (AFM) architecture, we expect to interface the AFM materials with nonmagnetic conductors like platinum. As such, it is crucial to be able to predict these interface properties. A large number of possible surfaces and combinations are available for us to explore, however we will focus on epitaxial-like combinations of materials in order to provide combinations that may be grown together.

The magnetic properties, structural properties and electronic properties of a material all differ at an interface or surface region. An important question is how the material properties change; for example, by altering the magnetic moment orientation or shifting atoms at the interface or surface, which would result in the properties deviating from the material bulk at this localised interface area [203]. Specifically, it may be queried what the most energetically stable interface is, and which material deviates the least structurally from bulk in order to preserve uniformity. Correspondingly, it is important to ask what material has the most bulk-like magnetic structure at the interface in order to maintain bulk-like SOT variation. To this end, it is necessary to establish how the magnetic moments are affected by the introduction of an interface and whether there is a breakdown in magnetic ordering, and how the surface magnetic moments are affected. In addition to this, because of the potential mismatch between materials epitaxially grown onto each other, strain is applied to the materials [153]. This will result in significant structural changes at the interface of materials. The electronic properties will of course differ with these changes; we can even predict the change in the density of states within the bulk-like, surface and interface regions.

When considering the finite nature of a material, it is important to question whether the surfaces of this material have some effect on the material properties at large; specifically, how does an interface affect conductivity via charge transfer and electronic state redistribution. The change in charge across such a surface needs to be assessed for potential charge transfer, which will affect conductivity. We assess the surfaces of three $D0_{19}$ materials, and the interface of platinum with the $D0_{19}$ materials. We will calculate the expansion per unit layer, formation energy for specific terminations that are symmetrically inequivalent, the Bader charge analysis and the partial density of states. Evaluating the epitaxial-like construction of two-layer systems is critical to characterising heterostructures of antiferromagnets and nonmagnetic metals, a very important part of any SOT-AFM spintronic device. The interaction at such an interface will have significant effect on the charge formation and density of states, resulting in significant alteration of performance. We aim to evaluate the magnetic and electronic properties of a $D0_{19}$ material on a platinum layer, such as the change in projected density of states (PDOS) and the charge transfer at the interface, and assess the magnetic order changes associated with the layer interface.

We note the $D0_{19}$ materials have a hexagonal structure, with the materials forming in layer-like systems with metallic bonds. This manner of structure indicates a wide array of symmetric systems. We will investigate the symmetrically inequivalent systems of the $D0_{19}$ materials in order to fully compare the interfaces.

In section 5.2, the theory and methodology for this work is introduced. Section 5.3 will contain data from previous studies, allowing us to compare the calculated properties. In section 5.4, we discuss the results of the calculations, both for single-material films and for heterostructures. Lastly, we will discuss the calculated results in section 5.5 and conclude the chapter in section 5.6.

5.2 Theory and methodology

5.2.1 Surface energy

Within the bulk, we expect the ions and magnetic moments to position and align in a perfectly periodic manner. At the surface, however, the discontinuity of the crystal will see structural and magnetic properties change in the material. To simulate a surface interface, we take the approach of using a large vacuum gap, more than 10 Å , between 2 surfaces of the material, thereby breaking down the infinite periodicity of the material in one direction. These semi-infinite "slabs" of material are used to calculate surface effects over a set area.

To find the surface energy (E_{surf}), for realistic surfaces, it is necessary to simulate cases of stoichiometric and non-stoichiometric slabs. For the latter, two conditions are given; manganese-rich, whereby the manganese chemical potential is used to calculate the non-manganese elements chemical potential, and manganese-poor, where the non-manganese element is used to calculate the manganese chemical potential. The surface energy is defined as

$$E_{surf} = \frac{E_{tot} - \sum_i N_i \mu_i}{2A}, \tag{5.1}$$

where A is the cross-sectional area of the semi-infinite slab being calculated, E_{tot} is the total energy of the slab over A, N_i is the number of atoms of species i, and μ_i is the chemical potential of species i [204]. In this case, μ_i will be different for manganese rich and poor cases, resulting in two limits for the surface energy.

Our method includes a series of simulations operating at 5 × 5 × 5 k-points (for each primitive cell, with alterations for larger slab sections) in a Monkhorst-Pack sampling grid. We use an energy cutoff of 350eV, and a density functional theory with Hubbard U (DFT+U) correction value of 1 eV on the Mn atoms. We do not use symmetry constraints on the system, and use the projector augmented wave

(PAW)-PBE functional revised for solids (PBEsol) pseudopotential. The force tolerance is 10^{-2} eV/A^{-1} and the energy tolerance is 10^{-3} eV/atom.

5.2.2 Magnetic moment alignment

The surface moments are expected to significantly reorient compared to the bulk orientation. The depth of the reorientation varies between materials. This is due to the lack of bulk-like ordering on one side of the configuration, resulting in the relaxation of the ordering out of the plane. The magnetic moments near or at the interface/surface are no longer constrained on one side due to the lack of magnetic moments applying the magnetic constraint to them, and will begin to reorient in such a way that they further minimise their energy. This reorientation occurs mechanically via the minimisation of energy and thus applied torque from the magnetic structure, whereby the minimum energy is only achieved by the reorientation of the moments to reduce the spin-torque that evolves from the altered system. However, this reorientation at the interface/surface will cause deeper magnetic moments to adjust to compensate and further lower their energy, resulting in a system with some depth to the reorientation and distortion of magnetic moment. We also expect in-plane reorientation of the magnetic moments, again to compensate for the out-of-plane reorientation and to minimise energy. The centre of the Mn-alloy layer should appear bulk-like, with minimal distortion. It is possible to use density functional theory (DFT) to simulate the magnetic configuration in the layer and compare the trend in angular displacement to the bulk configuration to find the point at which the material becomes approximately bulk-like. We may then analyse the changes as a function of the direction of interest, resulting in the determination of the change in angle from the bulk-like region at the surface and how deeply the surface influences the alteration of the magnetic configuration.

In terms of optimisation of magnetic moments, we determine two distinct types of optimisation. Local optimisation (whereby initial configurations of magnetic moments are initialised and optimised only for local perturbations from the default) is used for the majority of this chapter. However, locally optimised ordering does not determine the effect of more disorganised surface configurations. In our case, comprehensive global optimisation (whereby the magnetization remains zero but the moments are initialized in differing configurations) for every magnetic moment would be excessively time-consuming. Instead, restricting changes to the most-likely affected magnetic moments, namely those at the surface, and providing a limited region of randomization of direction will be more efficient. To do this, a fully random direction with a magnitude scaled to a set fraction of the magnetic moment

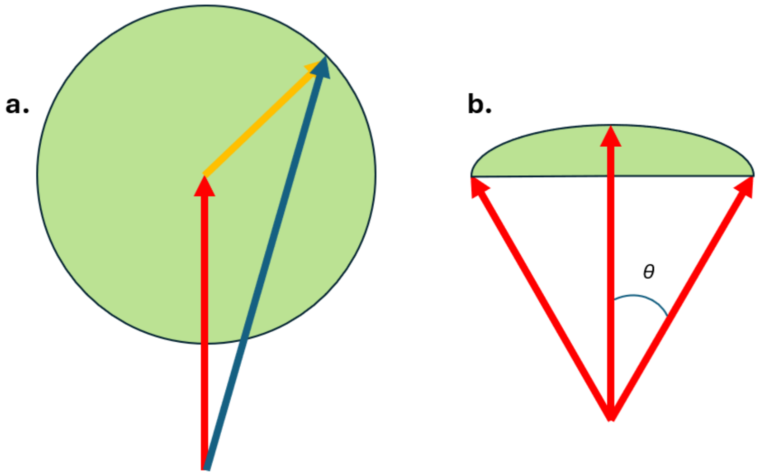

Figure. 5.1: Randomisation procedure for magnetic moments within a limit. a) vector sum of random vector (gold) and bulk moment (red), with resultant moment (blue). b) new moment rescaled to correct magnitude in limited region, θ; in this work, θ is limited to ±16°.

is added to the magnetic moment (Figure 5.1). The new magnetic moment is then normalized and re-scaled to the original magnetic moment, providing a limited range of potential directions within a boundary set by the ratio of magnitudes of the two vectors. This "randomization" will be quantized by the size of the magnitude of the randomized vector with relation to the magnitude of the original magnetic moment, such that

$$\mathit{Randomisation} = \frac{|\mathbf{v}_{ran}|}{|\mathbf{m}|}, \tag{5.2}$$

where $\mathbf{v}_{ran}$ is the randomised vector and $\mathbf{m}$ is the magnetic moment.

5.2.3 Bader charge analysis

Bader charge analysis is an aspect of Richard Bader's work into the quantum theory of atoms in molecules (QTAiM) [205]. It is a method of assessing charge and charge density across a system by using localised charge distributions within Bader volumes (defined as the volume enclosed within a surface of vanishing gradient flux at every surface, within which a virial relation for the atomic subsystem is found). By integrating the charge density within the Bader volume, we can find the localised charge at an atomic point in the system. We may then use this to map the changes for atomic charge throughout the system. The code used here is by the Henkelman Group, which partitions charge density grids from Vienna ab-initio simulation program (VASP) into Bader volumes using steepest ascent paths up to a maximum charge density [206, 207, 208]. Subsequently, these maxima are assigned grid points. Further paths terminate at these grid points. This code is remarkably efficient over the large charge density grids generated in VASP.

5.2.4 Projected density of states

Three Mn_3X systems studied in this chapter and all are Weyl semimetals [209]. This is a key feature of the electronic structure of these materials, as has been seen in Chapter 4, and is a major contributor to the topological effects this material displays whilst otherwise acting as a metal. We note that Mn_3Ge and Mn_3Sn are reported to be, unusually, Weyl semimetals of low carrier mobility [210]. We therefore would benefit from an investigation into the density of states in order to determine the electronic effects on these Weyl semimetals. We define the density of states to be the number of allowed states per unit energy range. The density of states can therefore be represented as a function of energy. As such, we may see how this density of states varies for differing combinations of materials. However, it should be understood that the contributions from the orbitals of certain elements and atoms can be determined, and so contributions from specific elements may also be projected as part of this density of states, and at differing positions, in order to determine the differences in contributions to the density of states, such as the decomposition of Mn_3Ge contributions seen in the study by Changdar et al [211]. The density of states is read in from the output of a VASP calculation, then plotted against the corresponding energy, as in Figure 5.2.

5.3 Previous experimental and theoretical data

It is worthwhile to analyse data from previous studies to compare the surface/ interface interactions of the $D0_{19}$ materials that we simulate to previous experimental and theoretical studies. In particular, we focus on the theoretical, namely the total density of states (DOS) of the bulk material, and the experimental expansion and strain characteristics of these materials, whereby the latter focuses on applications on platinum. We will evaluate and compare these studies for each material. For the film expansion, we take the measured thickness of the film and find the difference in height from the measured c-lattice parameter.

For Mn_3Ga (Table 5.1), we see the major PDOS peaks, as compared to theoretical work by Khmelevskyi, Ruban and Mohn using an local spin-density approximation

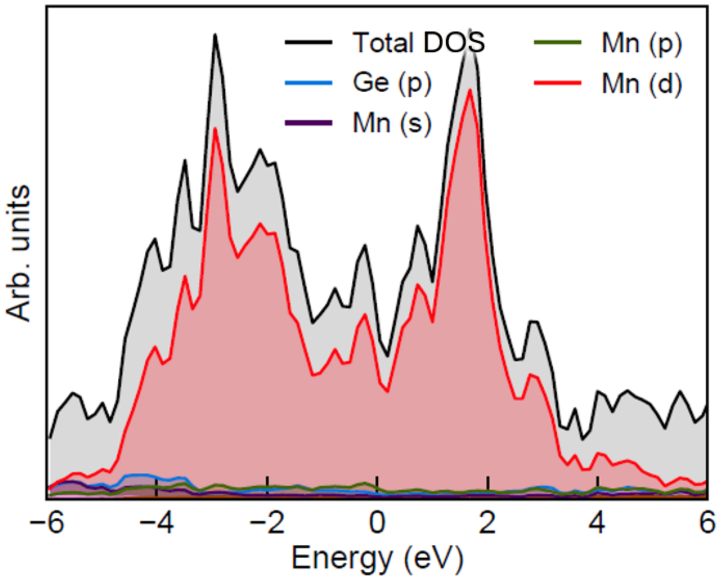

Figure. 5.2: Projected density of states of Mn_3Ge in bulk. The density of states is broken down into the various electronic cloud contributions for Mn and Ge. As can be seen in the figure, the largest contribution to the density of states is the Mn d-cloud.

Material	Lattice mismatch with Platinum, %	Major bulk PDOS peaks, eV	Estimated layer expansion in (001), pm/layer	References
Mn_3Ga	2.45	-2.72, 1.36	0.317	[212, 153]
Mn_3Ge	4.15	1, -2, -3	0.831	[160, 175, 177]
Mn_3Sn	1	-2.5, 0.5, 0.4 | -3, -2.5, -2.1, 1.4	0.253-1.860	[213, 174, 164, 214, 215]

Table 5.1: Summary of the data from previous experimental and theoretical studies

(LSDA) approach with Korringa-Kohn-Rostoker (KKR) using atomic sphere approximation (ASA), appear at -2.72 eV and 1.36 eV [212]. The expansion per layer over a layer grown on MgO(001)/Pt(111) in the study by Holguin-Momaca et al sees a value of 0.317 pm/layer over a critical thickness of 10nm in a layer 50nm thick, measured by 30kV reflection high-energy electron diffraction (RHEED). On Pt, the work by Holguin-Momaca et al shows a lattice mismatch of 2.45% measured using 30kV RHEED on a material grown via radio-frequency magnetron sputtering, with a temperature of 400°C and a growth pressure of 3 mTorr [153]. For Mn_3Ge, we see that the major PDOS peaks, as compared to the theoretical work by Wang et al, appear at -2.64 eV and 1 eV. The calculation uses DFT; a Perdew, Burke and Ernzerhof (PBE)-generalized gradient approximation (GGA) at a cutoff of 350 eV and a k-point grid of $7{\times}7{\times}8$ [160]. The expansion per layer over a layer grown on $LaAlO_3$ in the study by Hong et al sees a value of 0.831 pm/layer with the lattice constants measured via x-ray diffraction (XRD) over a 20nm layer measured using AFM. Crystals are grown using molecular beam epitaxy (MBE) at 570°C [175]. On Pt, the work by Olayiwola et al shows a lattice mismatch of 4.15% measured via XRD on a sample grown via magnetron sputtering [177].
For Mn_3Sn, we see that the major PDOS peaks, as compared to the theoretical work by Zhang et al, appear at -2.5 eV and 0.5 eV using DFT, a PBE-GGA+U with a cutoff of 450 eV [213] and $U-J$ value of 0.78 eV. Yang et al's study, based of DFT using GGA and a $7 \times 7 \times 5$ k-point grid, sees peaks at -2.5 eV and 1.4 eV [215]. The expansion per layer over a layer grown on MgO(110)[001] in the study by Liu et al sees a value of 1.860 pm/layer on a 12nm film grown via MBE at 420°C at $3{\times}10^{-9}$ mbar and measured using both RHEED and high-resolution XRD. This is compared to Markou et al's work which had an expansion of 0.253 pm/layer on MgO (10-10) over 10 nm, with crystals grown via magnetron sputtering at $3{\times}10^{-9}$ mbar and a temperature of 500°C, lattice parameters measured by XRD and the thickness measured by quartz crystal microbalance and z-ray reflectivity [174, 164]. On Pt, the work by Cheng et al shows a lattice mismatch of 1%, with the crystal grown at 260°C for Pt and 210°C for Mn_3Sn via off-axis sputtering and measured by XRD [214].

5.4 Results

5.4.1 Layer optimisation at the surface

Differing surface terminations arise from different material planes, such as the (100), (010) and (001) planes, as well as from differing atomic configurations

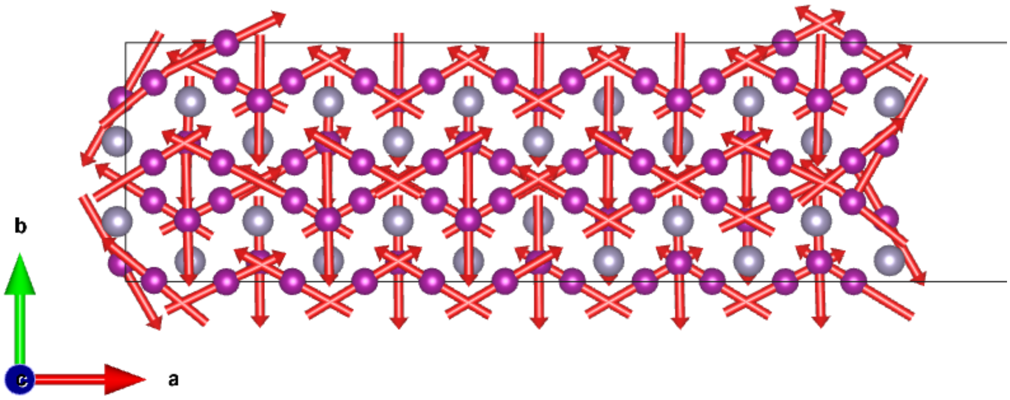

Figure. 5.3: Mn_3Sn, (100)-A, with two surfaces exposed to vacuum. The grey atoms represent Sn, and the purple atoms represent Mn

at these surfaces. Because of these differing terminations for the same surface, the aforementioned surfaces will be the focus of investigation, along with the specific symmetrically nonidentical terminations they have. We will begin with an initial optimisation of slabs of the materials with magnetic moments initialised in a hexagonal planar configuration (such as that in Figure 5.3) to best mimic the bulk, then discuss the effects of the surface terminations.

Structural optimisation of a film must be monitored to not only determine the change of structure a surface causes but to ensure the expansion of the surface, defined as the difference in length along some axis between a continuous bulk and a slab of the same number and configuration of atoms, within the calculation is of a reasonable value. As such, the key results we need to determine for the structural characterisation of the surface are the expansion per unit layer, defined as the expansion of the slab divided by the number of material layers (Figure 5.4), and the surface relaxation, defined as the displacement of atoms out of bulk-like positioning at or near the surface; this may be from single surfaces expanding from the bulk, or the surface rumpling (defined as single atoms displacing from the average position at the surface). It is also worth noting the overall slab expansion to see how far the surface deviates from bulk in order to determine the extent of the surface changes. In this section, we use DFT to determine the properties of surfaces on a $D0_{19}$ material slab for a variety of surfaces in planes (100), (010) and (001) (Figure 5.5), over a slab of material with a vacuum gap over 10 Å wide (Figure 5.3).

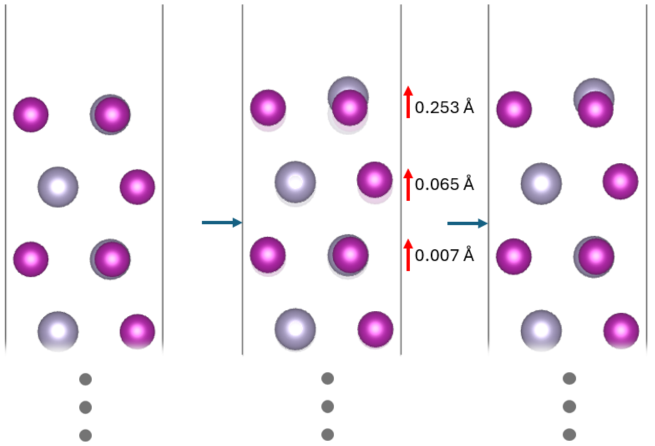

Figure. 5.4: The change in thickness, marked by a red arrow, at the surface over each layer for the (001)-Mn_3Sn termination. The ellipsis indicates continuation of the supercell.

Material	Surface normal	Surface index	Surface layer (1) expansion, Å	Layer 2 expansion, Å	Layer 3 expansion, Å
Mn_3Ga	(001)	A	0.069	0.012	0
Mn_3Ga	(100)	A	0.119	0.050	0
Mn_3Ga	(100)	B	0.041	0.064	0.040
Mn_3Ga	(010)	A	0.079	0.038	0.023
Mn_3Ga	(010)	B	0.311	0.155	0.075
Mn_3Ge	(001)	A	0.240	0.031	0
Mn_3Ge	(100)	A	0.072	0.030	0
Mn_3Ge	(100)	B	0.001	0	0
Mn_3Ge	(010)	A	0.105	0.072	0
Mn_3Ge	(010)	B	0.038	0.024	0.010
Mn_3Sn	(001)	A	0.253	0.065	0.007
Mn_3Sn	(100)	A	0.005	0.010	0.008
Mn_3Sn	(100)	B	0.004	0.008	0.004
Mn_3Sn	(010)	A	0.195	0.152	0.043
Mn_3Sn	(010)	B	0.080	0.032	0

Table 5.2: Expansion length for the first three layers of each material and surface.

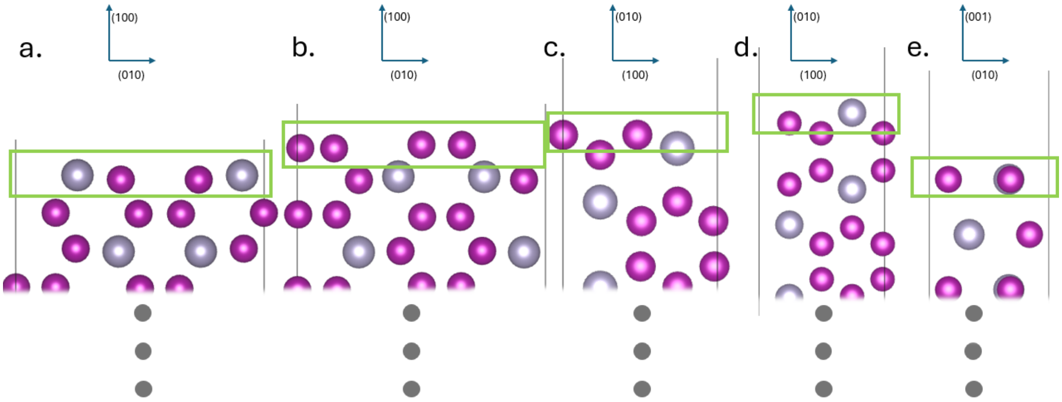

Figure. 5.5: The surface terminations for the $D0_{19}$ materials with Mn_3Sn used as an example. a) and b) are the (100) terminations, respectively called (100)-A and (100)-B, c) and d) are the (010) terminations, labelled (010)-A and (010)-B respectively, and e) is the (001) termination, called A. The grey ellipsis indicates the continuation of the supercell of atoms and the green box indicates the surface layer.

Mn_3Ga

The (001) surface has a small expansion of an average of 0.876 pm per layer of material over 1.82 nm, with the maximum surface displacement of 0.069 Å from bulk (Tables 5.3, 5.2). As the calculation involves two surfaces, we can note this is the overall expansion of this slab. The calculated energy of formation is 0.106 eV/Å^2. For the surface rumpling, we see minimal deviation from bulk, with the Ga species at the surface forming more prominently than Mn by 5 pm. (Figure 5.6).

For the (100) surface, we use two inequivalent surface terminations (100)-A and (100)-B (Figure 5.5). The expansions of the two different terminations of surfaces resulted in 0.119 Å and 0.041 Å of expansion for (100)-A and (100)-B respectively at the surface layer, with (100)-B having deeper expansion at lower layers (Table 5.2). The energies of formation of the surfaces are 0.0950 and 0.138 eV/Å^2 for Mn-rich and Mn-poor respectively for (100)-A and 0.159 and 0.116 eV/Å^2 for (100)-B (Table 5.3). This indicates the surface with minimum overall energy is the Mn-poor configuration of the (100)-A surface (Figure 5.7). Surface rumpling shows for both surfaces that the Mn species is displaced relative to the Ga species; for (100)-B this is seen in the layer below the surface with 9 pm of space between

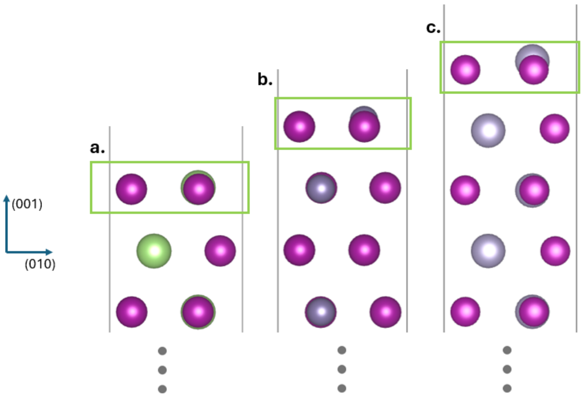

Figure. 5.6: Mn_3X slabs with (001) surfaces, pictured in the (100) plane to show surfaces from the side, to observe the displacement from the surface. a) Mn_3Ga, where the green atoms represent Ga, b) Mn_3Ge, where the dark grey atoms represent Ge, c) Mn_3Sn, where the light grey atoms represent Sn. Purple atoms represent Mn. The grey ellipsis indicates the continuation of the supercell of atoms and the green box indicates the surface layer.

the Ga and Mn, though only (100)-A sees significant rising at the surface by Mn by 6 pm (Figure 5.8). As such, we see the lowest energy surface termination is the Mn-rich (100)-A and the termination of lowest expansion per layer is the (100)-B surface.

For the (010) surface, we consider two inequivalent surface terminations (010)-A and (010)-B. For these surface terminations, we see expansions of 0.079 Å and 0.311 Å for the surface layer, with (010)-B expanding further at lower layers (Table 5.2). For each configuration's surface energy, we see 0.115 eV/Å^2 and 0.111 eV/Å^2 for the (010)-A and (010)-B surfaces respectively, and as such the latter is the more energetically stable surface (Table 5.3). The surface rumpling is largely unremarkable for both surfaces (Figure 5.9). As such, we see the lowest energy termination is the (010)-B and the termination of lowest expansion per layer is the (010)-B surface.

Mn_3Ge

For the (001) surface, the expansion is 3.39 pm per layer for two surfaces over 1.84 nm with expansion at the first layer up to 0.240 Å , which is significantly larger than for Mn_3Ga, and a surface energy of 0.012 eV/Å^2 (Tables 5.3, 5.2). This exceptionally low surface energy of formation is far lower than Mn_3Ge's (001) configuration. Surface rumpling shows the Ge at the surface rises above the Mn

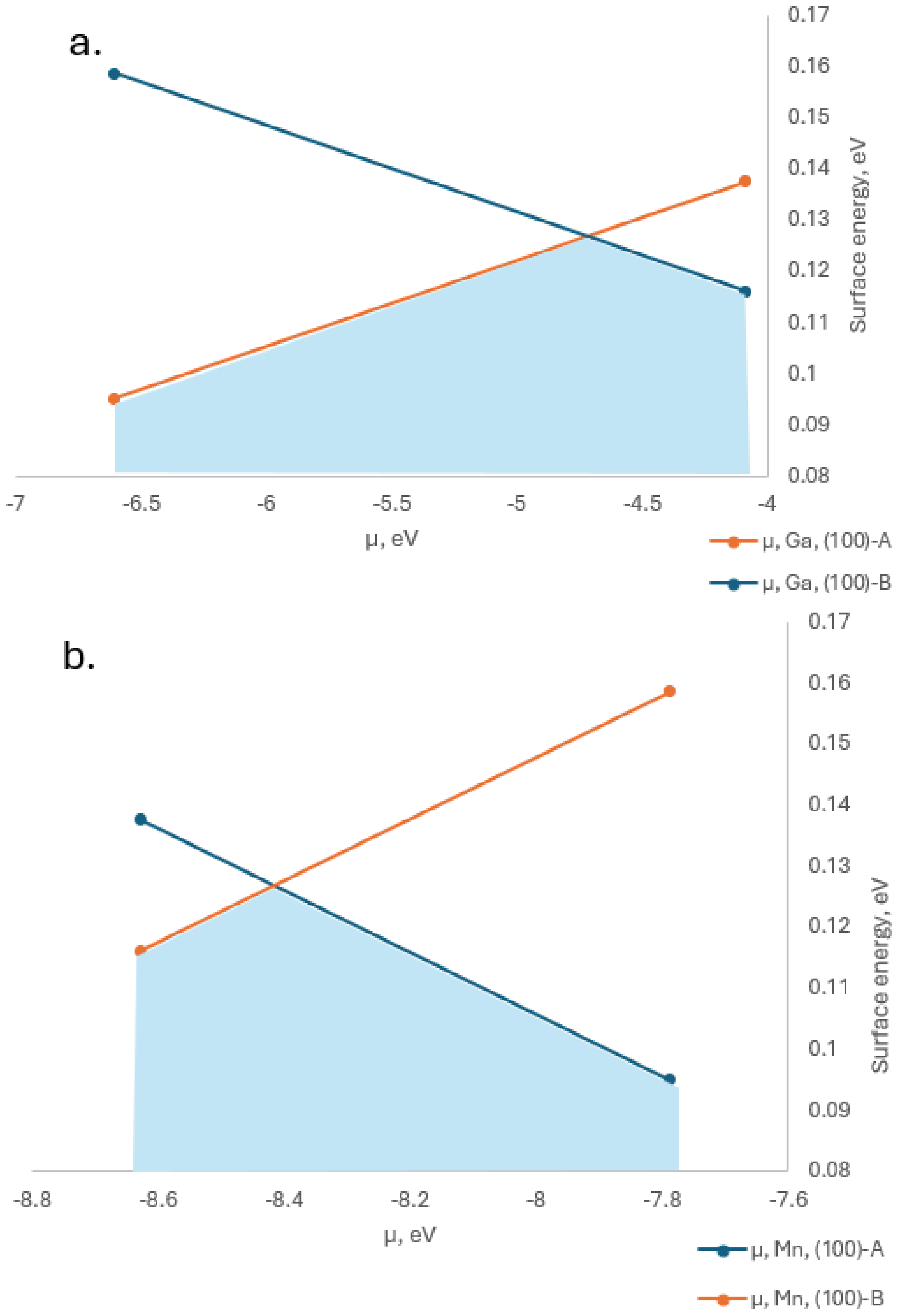

Figure. 5.7: The variation of the chemical potential μ with the surface termination and Mn-richness on the (100)-Mn_3Ga surface. The blue region indicates the stable chemical potential values. a) the variation in the chemical potential in Ga, b) the variation in chemical potential for Mn.

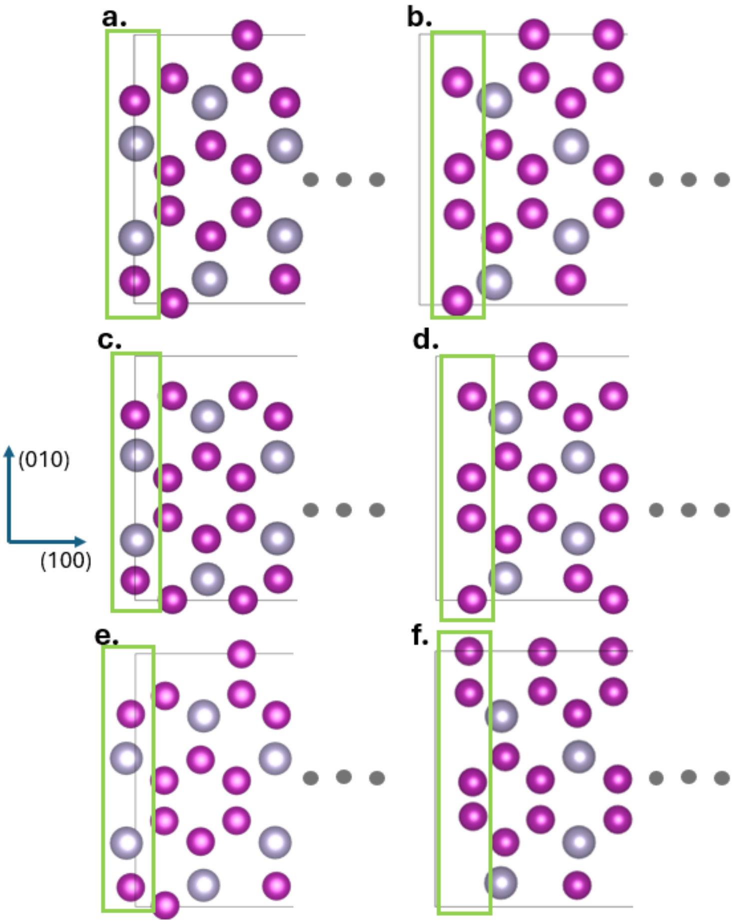

Figure. 5.8: Mn_3X slabs with (100) surfaces, pictured in the (001) plane to show surfaces from the side, to observe the displacement from the surface. a) Mn_3Ga (100)-A, b) Mn_3Ga (100)-B, c) Mn_3Ge (100)-A, d) Mn_3Ge (100)-B, e) Mn_3Sn (100)-A, f) Mn_3Sn (100)-B. Grey atoms represent Ga, Ge and Sn, purple atoms represent Mn. The grey ellipsis indicates the continuation of the supercell of atoms and the green box indicates the surface layer.

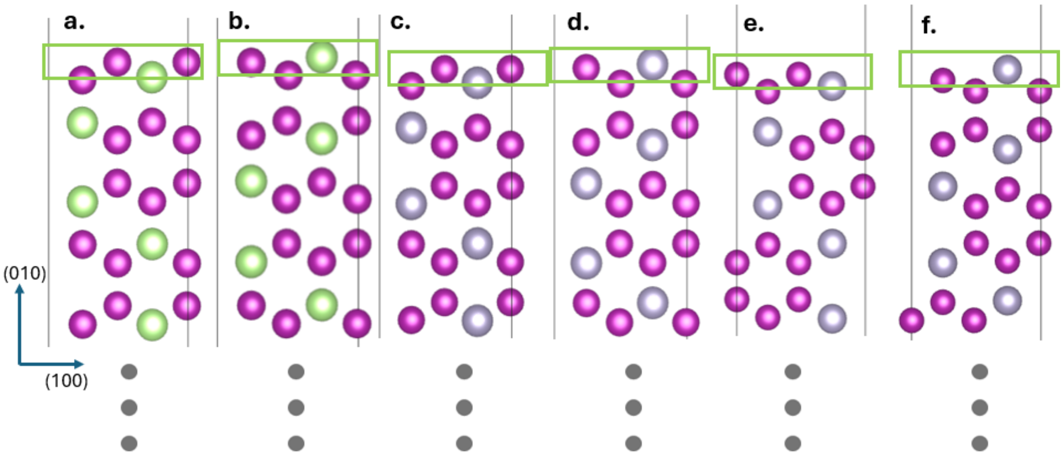

Figure. 5.9: Mn_3X slabs with (010) surfaces, pictured in the (001) plane to show surfaces from the side, to observe the displacement from the surface. a) Mn_3Ga (010)-A, b) Mn_3Ga (010)-B, c) Mn_3Ge (010)-A, d) Mn_3Ge (010)-B, e) Mn_3Sn (010)-A, f) Mn_3Sn (010)-B. The grey ellipsis indicates the continuation of the supercell of atoms and the green box indicates the surface layer. Green atoms represent Ga, grey atoms represent Ge/Sn, and purple atoms represent Mn.

Material	Surface normal	Surface index	Expansion per layer (pm)	Formation energy, eV/Å^2
Mn_3Ga	(001)	A	0.876	0.106
Mn_3Ga	(100)	A	1.050	Mn-rich: 0.095, Mn-poor: 0.138
Mn_3Ga	(100)	B	0.872	Mn-rich: 0.159, Mn-poor: 0.116
Mn_3Ga	(010)	A	0.207	0.115
Mn_3Ga	(010)	B	0.505	0.111
Mn_3Ge	(001)	A	3.390	0.012
Mn_3Ge	(100)	A	0.887	Mn-rich: 0.144, Mn-poor: 0.073
Mn_3Ge	(100)	B	0.010	Mn-rich: 0.091, Mn-poor: 0.163
Mn_3Ge	(010)	A	1.475	0.109
Mn_3Ge	(010)	B	0.655	0.097
Mn_3Sn	(001)	A	1.320	0.083
Mn_3Sn	(100)	A	1.490	Mn-rich: 0.136, Mn-poor: 0.071
Mn_3Sn	(100)	B	5.870	Mn-rich: 0.103, Mn-poor: 0.168
Mn_3Sn	(010)	A	0.166	0.106
Mn_3Sn	(010)	B	0.715	0.096

Table 5.3: Calculated results for structural and magnetic properties of the $D0_{19}$ materials

by 23 pm (Figure 5.6).

For the (100) direction, the expansion at the surface is 0.072 Å and 0.001 Å respectively. From this, we see dramatically different expansions, and can conclude that (100)-B is more bulk-like to the smaller expansion (Table 5.2). Energetically, we see the (100)-A configuration reach 0.144 eV/Å^2 in the Mn-rich phase and 0.0728 eV/Å^2 in the Mn-poor phase, and for the (100)-B configuration, we see 0.0914 eV/Å^2 for Mn-rich and 0.163 eV/Å^2 for Mn-poor configurations, indicating the first configuration in the Mn-poor category is most stable (Table 5.3). Surface rumpling shows for (100)-B, the Mn species is displaced slightly above the Ga species at the layer below the surface by 7 pm, though only (100)-A sees significant rising at the surface by Mn by 7 pm (Figure 5.8). As such, we see the lowest energy surface termination is the Mn-poor (100)-A and the expansion is the same for both surfaces.

For the (010) direction, the surface expansion is 0.105 Å and 0.038 Å for (010)-A and (010)-B respectively (Table 5.2). Again, the expansion differs by a significant factor between the two terminations, indicating (010)-B to be less unstable. For the first and second configurations, we see surface energies of 0.109 eV/Å^2 and 0.0969 eV/Å^2, indicating the second surface is the most stable (Table 5.3). The surface rumpling is largely unremarkable for both surfaces (Figure 5.9). As such, we see the lowest energy surface termination is the (010)-B and the termination with the lowest expansion per layer is the (100)-B surface.

Mn_3Sn

For the (001) direction, the expansion is 1.32 pm per layer for two surfaces over 4.38 nm with surface expansion of 0.253 Å maximum, and is relatively comparable to Mn_3Ge, though still larger than the surface layer expansion of Mn_3Ga (Tables 5.3, 5.2). Energetically, we have a low energy of formation at 0.0827 eV/Å^2, lower than for Mn_3Ga but higher than Mn_3Ge. Surface rumpling shows the Sn at the surface displaces above the Mn by 31 pm (Figure 5.6).

For the (100) surface, the surface layer expansion is 0.005 Å and 0.004 Å for (100)-A and (100)-B, smaller than Mn_3Ga and indicating that the (100)-A configuration is more bulk-like than the (100)-B as it expands less (Table 5.2). The energy of formation for the surface is, for the (100)-A surface, 0.136 eV/Å^2 and 0.071 eV/Å^2 for the Mn-rich and Mn-poor system respectively. For the (100)-B surface, the surface energies of formation are 0.103 eV/Å^2 and 0.168 eV/Å^2 for the Mn-rich and Mn-poor system respectively (Table 5.3). The most stable is the (100)-A surface termination in the Mn-poor system, similar to Mn_3Ge. Surface rumpling shows for the (100)-B surface that the Mn species displaces slightly above the Ga species in the layer below the surface by 13 pm, though only (100)-A sees significant displacement at the surface by Ga by 16 pm (Figure 5.8). As such, we see the lowest energy termination is the Mn-poor (100)-A and the termination with the lowest expansion per unit area is the (100)-A surface.

For the (010) direction, the surface layer expansion is 0.195 Å and 0.080 Å for the (010)-A and (010)-B surfaces respectively, comparable to Mn_3Ge and confirming that the (010)-A is more structurally comparable to bulk (Table 5.2). The surface energies of formation for the (010)-A and (010)-B surfaces are 0.106 eV/Å^2 and 0.0963 eV/Å^2, whereby the (010)-B surface is more energetically stable (Table 5.3). The surface relaxation is largely unremarkable for both surfaces, though (010)-B has an Mn displace below the surface by 46 pm (Figure 5.9). As such, we see the lowest energy termination is the (010)-B and the termination with the lowest expansion per unit area is the (010)-A surface.

5.4.2 Magnetic and electronic effects at the surface

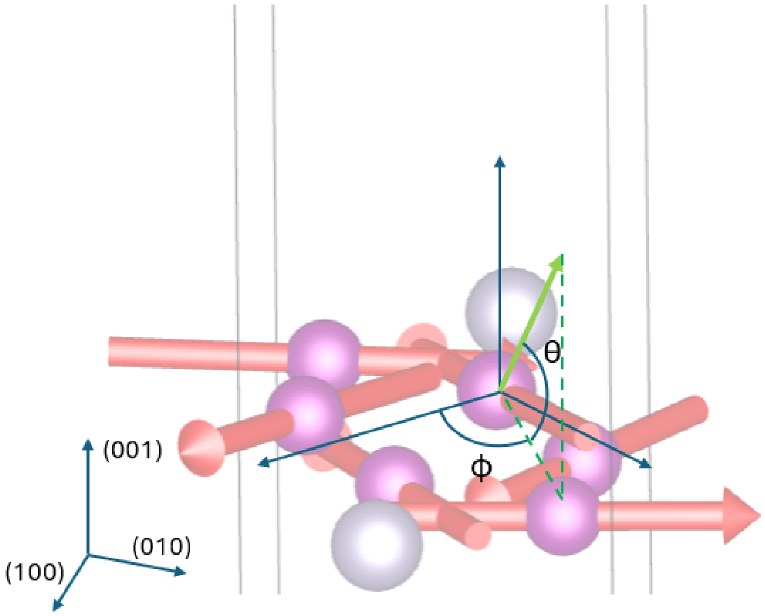

Figure. 5.10: The angles θ and ϕ used to describe the canting of magnetic moments, projected onto a (001) Mn_3X surface. The green arrow is an example of a magnetic moment with significant variation in θ and ϕ, where the green dashed lines illustrate the displacement.

The magnetic and electronic properties at the surface are also important to assess;

Material	Surface normal	Surface index	Average θ, degrees	Average ϕ, degrees	Maximum θ, degrees	Maximum ϕ, degrees
Mn_3Ga	(001)	A	0.58	2.06	1.79	4.80
Mn_3Ga	(100)	A	0.77	10.66	4.88	29.35
Mn_3Ga	(100)	B	0.49	11.75	3.61	44.66
Mn_3Ga	(010)	A	0.17	1.63	0.76	4.61
Mn_3Ga	(010)	B	0.33	6.66	2.14	12.79
Mn_3Ge	(001)	A	1.46	3.22	4.12	6.20
Mn_3Ge	(100)	A	0.26	8.63	0.31	34.31
Mn_3Ge	(100)	B	0.37	8.76	2.71	22.55
Mn_3Ge	(010)	A	0.16	3.26	0.63	13.02
Mn_3Ge	(010)	B	0.24	1.86	1.46	3.26
Mn_3Sn	(001)	A	0.56	2.76	2.58	4.88
Mn_3Sn	(100)	A	0.38	7.99	2.94	30.07
Mn_3Sn	(100)	B	0.42	10.19	3.15	29.00
Mn_3Sn	(010)	A	0.34	1.76	1.94	4.64
Mn_3Sn	(010)	B	0.82	2.25	6.46	4.69

Table 5.4: Angular deviation at the surfaces from bulk.

the distortion at the surface of the magnetic moments tells us how the surface affects ordering within its proximity. The electronic properties at the surface can be mapped via the use of PDOS and Bader charge analysis, which allow us to assess the specific positions close to the surface. We will examine the magnetic canting, the PDOS, and the Bader charge analysis at the surface. We describe the angular deviation as a combination of two angles; θ, the deviation normal to the (001) plane, and ϕ, the deviation in the (001) plane (Figure 5.10).

Mn_3Ga

For the (001) surface, very little deviation of the magnetic moments at the surface occurs. There is very little deviation out of plane, with the most significant deviation being in ϕ (Figure 5.12). Notably θ raises to 2.06° at the surface and ϕ peaks at 4.80° (Table 5.4). The Bader charge analysis (Table 5.5) shows that Mn atoms see a decrease in charge from the bulk average by 0.056 e at the surface, whereas Ga atoms see an increase by 0.115 e at the surface and 0.030 e at the second layer over bulk average (Figure 5.13). The standard deviations for the two species are 0.012 e for Mn and 0.003 e for Ga atoms. For the Mn-PDOS (Figure 5.11a), we see peaks in the Mn bulk at -3.66 eV, -2.95 eV, -1.92 eV, 0 eV, 1.74 eV and 3 eV. At the surface, we see peaks shift; the peak at -3.66 eV merges with

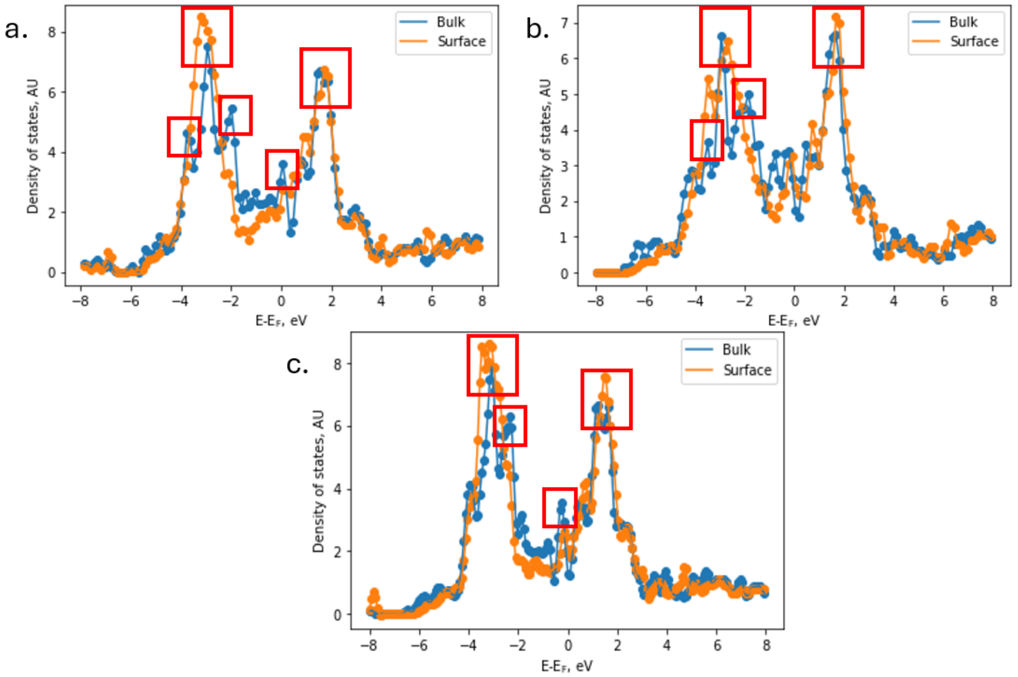

Figure. 5.11: PDOS graphs in the (001) direction. a) Mn_3Ga, b) Mn_3Ge, c) Mn_3Sn. The red boxes indicate the regions of interest for PDOS analysis, due to the peaks contained within.

the peak at -2.95 eV, the peak at -2.95 eV shifts to -3.24 eV, the peak at -1.92 eV merges into the main peak at -3.24 eV, the 0 eV peak simply sees a small reduction in magnitude, and the peak at 1.74 eV retains its position.

The (100) configuration has significant canting. There is canting present down to the fifth layer from the surface. For the (100)-A surface, the angular deviation is up to 29.35° out-of-plane in ϕ at the surface, which falls quickly after the second layer to the bulk configuration. The (100)-B surface sees canting to 44.66° in ϕ at the layer below the surface, a similarly severe amount of angular deviation of the moment (Figure 5.15). As such, the minimum deviation is seen in (100)-A (Table 5.4). For the (100)-A surface, the surface Mn layer drops by 0.204 e in terms of Bader charge then rising to 0.085 e over the bulk average for the layer below the surface, with the Ga species remaining largely unchanged (Table 5.5). The standard deviation for this surface termination for each species is 0.039 e for Mn, and 0.028 e for Ga. The (100)-B surface shows a drop by 0.109 e, then a rise over bulk charge by 0.155 e under Bader analysis, with the centre region falling to the bulk average for Mn. For Ga, the (100)-B surface sees a rise by 0.108 e on average at the surface layer. The standard deviations for the bulk-like regions were

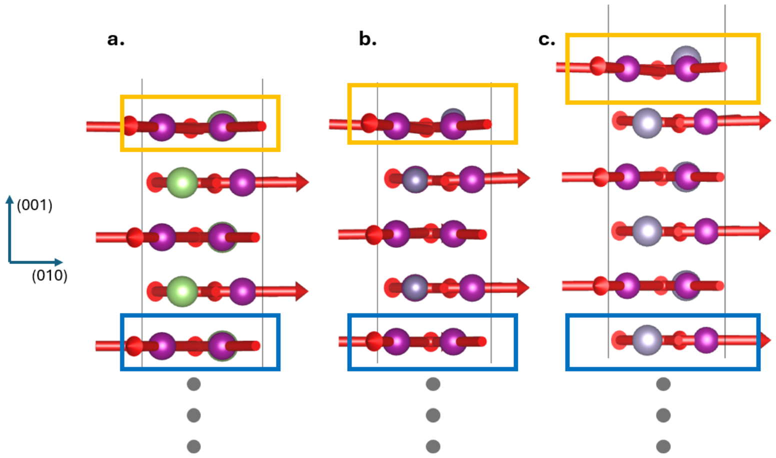

Figure. 5.12: The magnetic moments and PDOS selection regions for Mn_3X alloys along the (001) direction. a) Mn_3Ga, b) Mn_3Ge, c) Mn_3Sn. The grey ellipsis indicates the continuation of the supercell of atoms. The gold box represents the surface layer, and the blue box represents the bulk layer.

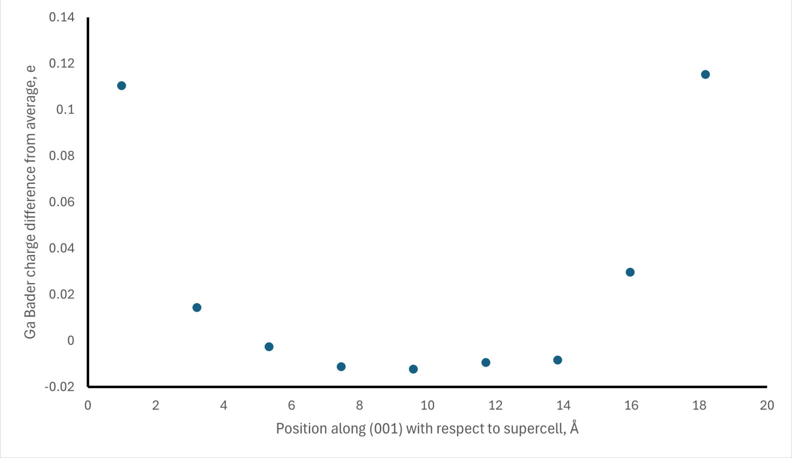

Figure. 5.13: Bader charge deviation from bulk average for the Ga atoms within the (001) surface slab.

Material	Surface normal	Termination	Bader charge variation, e
Mn_3Ga	(001)	A	Mn: -0.056 to +0.013, Ga: 0.115
Mn_3Ga	(100)	A	Mn: -0.204 to +0.085, Ga: +0
Mn_3Ga	(100)	B	Mn:-0.109 to +0.155, Ga: 0.108
Mn_3Ga	(010)	A	Mn: -0.075 to +0.044, Ga: +0.130
Mn_3Ga	(010)	B	Mn: -0.078 to +0.041, Ga: +0.054
Mn_3Ge	(001)	A	Mn: -0.045 to -0.015, Ge: -0.010 to +0.037
Mn_3Ge	(100)	A	Mn: -0.214 to +0.130, Ge: -0.1
Mn_3Ge	(100)	B	Mn:-0.088 to +0.169, Ge: -0.027 to +0.134
Mn_3Ge	(010)	A	Mn:-0.059 to +0.023, Ge: -0.008 to +0.043
Mn_3Ge	(010)	B	Mn:-0.045 to +0.027, Ge: -0.0048
Mn_3Sn	(001)	A	Mn:-0.053 to +0.016, Sn: -0.010 +0.048
Mn_3Sn	(100)	A	Mn:-0.177 to +0.082, Sn: -0.026 to +0.025
Mn_3Sn	(100)	B	Mn:-0.099 to +0.088, Sn: -0.008 to +0.107
Mn_3Sn	(010)	A	Mn:-0.078 to +0.014, Sn: -0.025 to +0.134
Mn_3Sn	(010)	B	Mn:-0.061 to +0.026, Sn: -0.018 to +0.024

Table 5.5: Bader charge variation for the differing terminations of surfaces

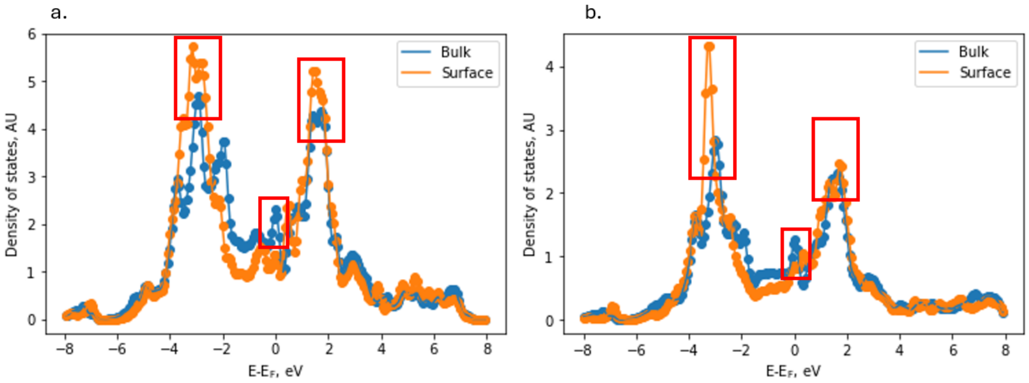

Figure. 5.14: The PDOS of the Mn_3Ga (100) surface in comparison to the bulk for a) (100)-A and b) (100)-B. The red boxes indicate the regions of interest for PDOS analysis, due to the peaks contained within.

0.029 e and 0.034 e for Ga and Mn respectively. As such, the minimum deviation is seen in (100)-B for Mn and (100)-A for Ga. PDOS of the bulk system shows peaks at -2.95 eV, 0.0 eV and 1.61 eV. For the (100)-A surface, PDOS shows little translation of the peaks at -2.95 eV, 0.00 eV and 1.61 eV (Figure 5.14), with the former splitting (-3.15 eV and -2.79 eV). PDOS for the (100)-B surface shows that the bulk and surface differ; the peak at -2.95 eV shifts to -3.22 eV, the peak at 0.00 eV shifts to 0.41 eV, and the peak at 1.61 eV splits to 1.33 eV and 1.79 eV.

For the (010) surface, we see some angular deviation from the bulk configuration down to the second layer of material for both surfaces for the (010)-A surface termination, up to 4.61° in ϕ (Table 5.4). The (010)-B surface has more in-plane canting with an angular maximum of 12.79° in ϕ (Figure 5.17). The minimum deviation of moments is seen in (010)-A. Bader charge analysis shows the (010)-A surface has a drop of 0.075 e compared to the average bulk Bader charge, then a rise to 0.044 e above bulk on the second layer, moving to a drop of 0.06 e on the next layer, before returning to the bulk value (Table 5.5). An increase of 0.130 e from bulk occurs for Ga at the (010)-A surface. The standard deviations for each species is 0.008 e and 0.015 e for Ga and Mn respectively. For the (010)-B surface, the Mn species drops by 0.078 e below bulk at the surface, then increasing by 0.041 e above bulk on the layer below, and the Ga species increasing by 0.054 e at the surface, with standard deviations of 0.009 e and 0.013 e for Ga and Mn respectively. As such, the minimum deviation is seen in (010)-B, but both surfaces are very similar. For the PDOS in the Mn-bulk, we see major peaks located at -2.95 eV and 1.61 eV (Figure 5.16). At the surface layer for the (010)-A surface,

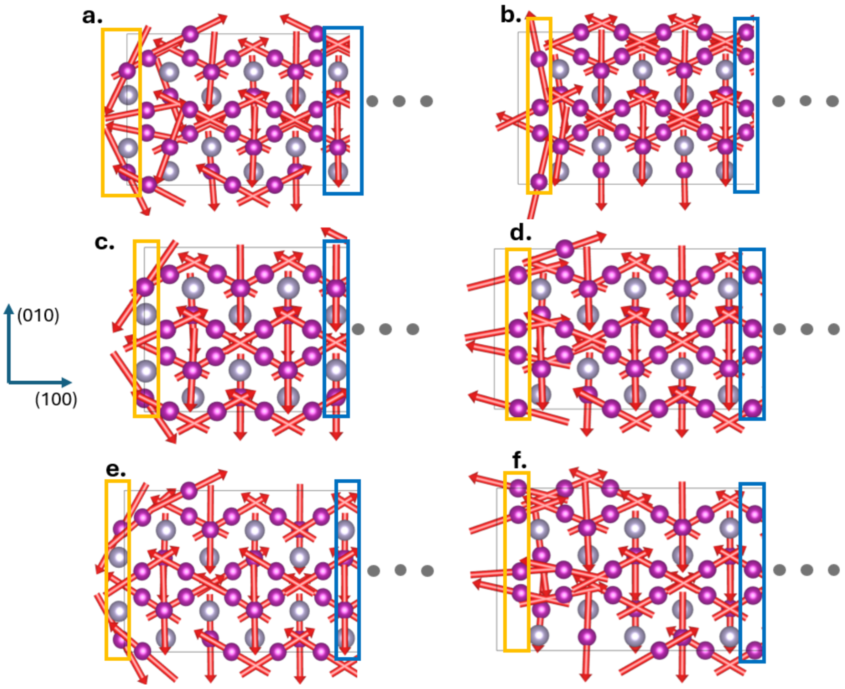

Figure. 5.15: The magnetic moments and PDOS selection regions for Mn_3X alloys along the (100) direction. a) Mn_3Ga (100)-A, b) Mn_3Ga (100)-B, c) Mn_3Ge (100)-A, d) Mn_3Ge (100)-B, e) Mn_3Sn (100)-A, f) Mn_3Sn (100)-B. The grey ellipsis indicates the continuation of the supercell of atoms. The gold box represents the surface layer next to vacuum, and the blue box represents the bulk layer. The grey atoms represent Ga. Ge and Sn. The purple atoms represent Mn. The surfaces for secondary materials (X) with the same chemical group have similar surface magnetization formation angles, indicating surface canting has some direct dependence on the group electronic structure.

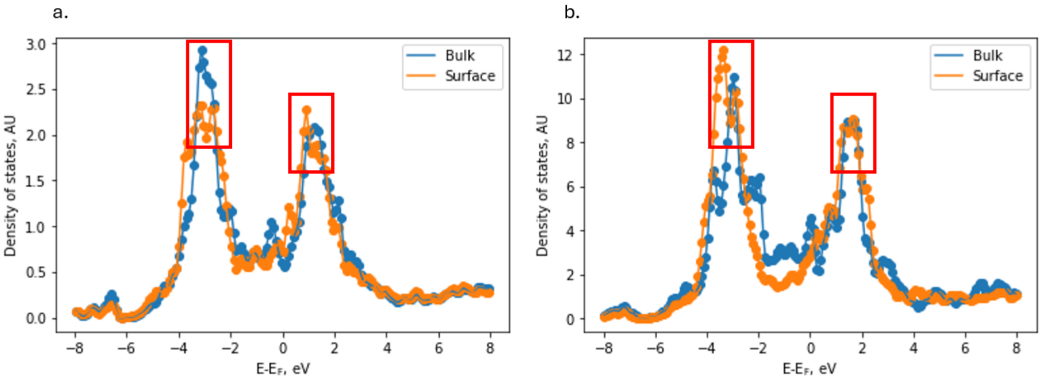

Figure. 5.16: The PDOS of the Mn_3Ga (010) surface in comparison to the bulk for a) (010)-A and b) (010)-B. The red boxes indicate the regions of interest for PDOS analysis, due to the peaks contained within.

which exhibits peaks in the same regions, the -2.95 eV peak does shift to -2.93 eV and splits to -3.12 eV and -2.64 eV. The peak at 1.61 eV shifts to 1.2 eV. The (010)-B surface differs, with a splitting of the -2.95 eV peak to -3.36 eV and -2.89 eV and the 1.61 eV peak splits to 1.27 eV and 1.73 eV. The 0 eV peak shifts to 0.34 eV.

Mn_3Ge

For the (001) surface, we see the small amounts of significant canting of the surface extend down to the third layer. The surface canting is mostly in-plane, though there is some small amounts of out-of-plane canting in the top three layers (Table 5.4). The maximum angle is in θ, raising to 4° at the surface (Figure 5.12). For Bader charge analysis, we see a decrease in charge by 0.045 e at the surface for Mn. For Ga, we see an decrease in charge at the surface and increase at the second layer by 0.010 e and 0.033-0.037 e respectively (Table 5.5). The standard deviations are 0.010 e and 0.007 e for Mn and Ga respectively. The difference in PDOS between the bulk and the surface is relatively minor (Figure 5.11b), with the major peaks at -3.04 eV and 1.55 eV having some shift, with the former shifting slightly to -2.67 eV and the latter shifting to 1.82 eV. The peak at -3.49 eV remains in the same place, and the peak at -1.85 eV merges with the peak at -2.67 eV.

For the (100) direction, we see no significant canting of either configurations below the surface. The (100)-A surface sees significant canting at the surface layer, up to 34.31° in ϕ. The (100)-B surface sees high angular deviation for the surface layer and the third layer below, up to 22.6° ϕ rotation, followed by up to 13.28° for

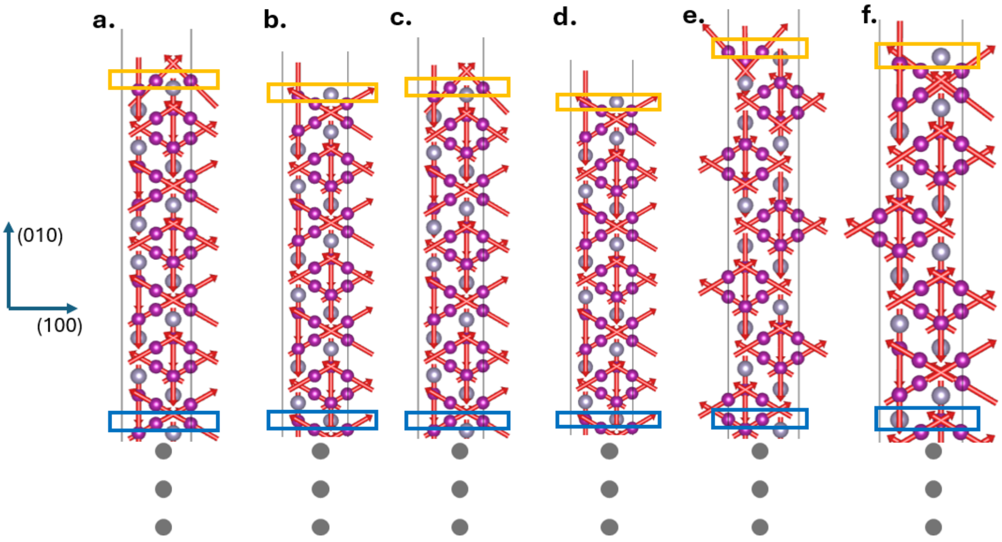

Figure. 5.17: The magnetic moments and PDOS selection regions for Mn_3X alloys along the (010) direction. a) Mn_3Ga (010)-A, b) Mn_3Ga (010)-B, c) Mn_3Ge (010)-A, d) Mn_3Ge (010)-B, e) Mn_3Sn (010)-A, f) Mn_3Sn (010)-B. The grey ellipsis indicates the continuation of the supercell of atoms. The gold box represents the surface layer next to vacuum, and the blue box represents the bulk layer.

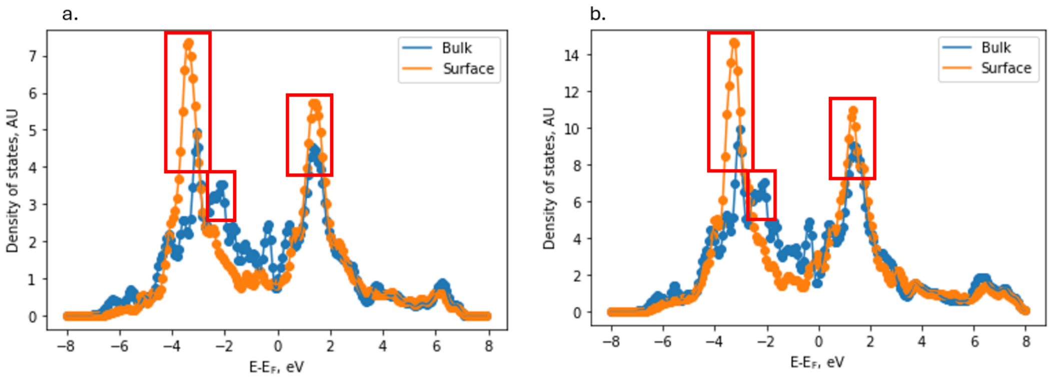

Figure. 5.18: The PDOS of Mn_3Ge's (100) surface in comparison to the bulk for a) (100)-A and b) (100)-B. The red boxes indicate the regions of interest for PDOS analysis, due to the peaks contained within.

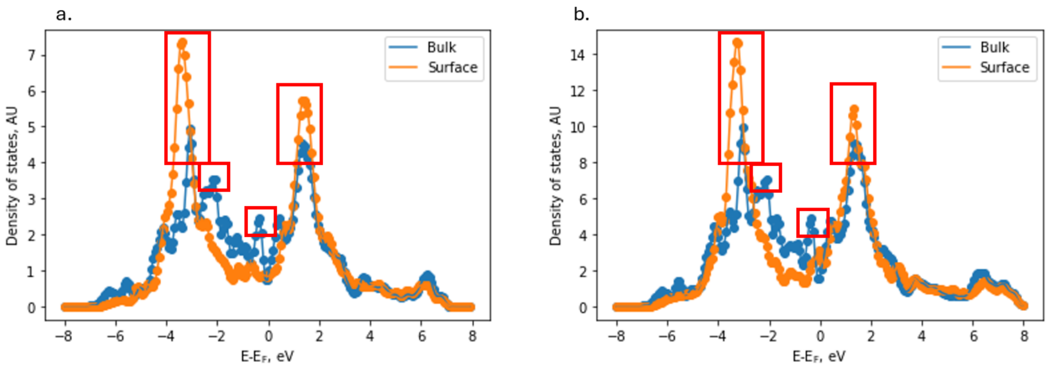

Figure. 5.19: The PDOS of Mn_3Ge's (010) surface in comparison to the bulk for a) (010)-A and b) (010)-B. The red boxes indicate the regions of interest for PDOS analysis, due to the peaks contained within.

the third layer, then flattening out to bulk configuration (Figure 5.15). From the average deviation (Table 5.4), the minimum deviation is seen in (100)-A. For the (100)-A surface, Bader charge analysis shows a drop from bulk average by 0.214 e at the surface, followed by an increase of 0.130 e on the layer below for Mn, and for Ge, we see a drop by 0.105 e, with the species' standard deviations of Bader charge being 0.024 e and 0.030 e for Mn and Ge respectively (Table 5.5). For the (100)-B surface, we see the surface layer has an Mn Bader charge reduction of 0.088 e, and an increase by 0.169 e on the next layer, returning to within 0.05 e of the bulk average on the third layer onward, with an increase in Ge charge by 0.134 near the surface. The standard deviation for the (100)-B surface was 0.023 e and 0.020 e for Mn and Ge respectively. As such, the minimum deviation is seen in (100)-B. For the Mn-bulk, PDOS shows peaks around -3.04 eV, -2.08 eV and 1.56 eV (Figure 5.18). PDOS analysis shows similar peaks at -3.37 and 1.48 eV at the (100)-A surface, however the (100)-B surface has peaks of similar position at -3.21 eV and 1.34 eV. In both cases, the peak at -2.08 eV merges with the peak at -3.37 and -3.21 eV. The PDOS shows the two surfaces exemplify remarkably similar distributions.

For the (010) surfaces, the (010)-A surface has some canting on the first surface layer, up to 13.02° out-of-plane in ϕ (Table 5.4). We also see some canting in ϕ at the (010)-B surface, but this is only up to 3.26° at maximum, and is as such marginal (Figure 5.17). As such, the minimum deviation is seen in (010)-B. Bader analysis for Mn shows the (010)-A surface charge density dropping by 0.059 e at the surface layer then peaking by 0.023 e on the second layer compared to the bulk, and raising by 0.043 e for Ge at the surface (Table 5.5). Standard deviations are 0.008 e and 0.004 e for Mn and Ge respectively. The (010)-B surface shows a drop of 0.045 at the surface for Mn, followed by an increase by 0.027 e, and a drop for Ge of 0.005 e. All other points are within 0.02 e of the mean, at a standard deviation of 0.009 e and 0.005 e for Mn and Ge from the mean respectively. As such, the minimum deviation is seen in (010)-A, but (010)-B deviates least at the surface itself. For the Mn PDOS, we see the main two Mn-bulk peaks emerge at -3.04 eV and 1.56 eV (Figure 5.19), with two additional peaks at -2.08 eV and -0.34 eV. The (010)-A surface shows virtually no shift, only a splitting of the peak at -3.04 eV, to -3.20 eV and -2.85 eV. The (010)-B surface showing shifts of these peaks to -3.31 eV and 1.72 eV. The peak at -2.08 eV merges with the main peak at -3.20 and -3.31 eV, and the peak at -0.34 eV diffuses into the distribution.

Mn_3Sn

We see for the surface perpendicular to (001) that the magnetic moments cant out-of-plane. This canting persists down to the second layer, after which the angle of the canting is below 2.60° in θ, yet also has larger variation in ϕ, at 4.88° (Table 5.4). This repeats symmetrically on the other surface of the supercell. Notably, θ raises to 1.31° at the surface and 2.60° at the layer below the surface (Figure 5.12). The Bader charge analysis shows a decrease at the first layer below bulk charge of between 0.053 e and 0.030 e for Mn (Table 5.5). All other layers sit evenly about the bulk average. For Sn, the first two layers see elevated charge at 0.037 e above the bulk average. The standard deviations for both species are 0.008 and 0.004 e respectively. PDOS of the surface and bulk shows that the Mn density of states are only minorly affected, with splitting of the major peak at -3 eV and shifting to -3.30 eV, splitting into peaks at -3.47 eV and -3.14 eV, and the unifying of the split peak at 1.47 eV (Figure 5.11c). The peak at -2.34 eV merges with the peak at -2.67 eV. The peak at 0 eV shifts to -0.2 eV.

We see canting of the magnetic moments at the (100) surfaces as well. For the (100)-A surface, we see the surface layer moments cant at a high angle to two layers below on both surfaces (30.07° and 6.7°) in ϕ before dropping below the average. For the (100)-B surface, we see the surface moments cant in ϕ as low as three layers down, with the surface layer canting by 29.00°, the second layer by 7.64°, then the third layer cants by up to 21.56° (Figure 5.15). The minimum deviation is seen in (100)-A (Table 5.4). For the (100)-A surface, the PDOS we retrieve for this surface shows a significant difference between the number of peaks for bulk Mn_3Sn and the upper layers of Mn_3Sn. The bulk has peaks around -3.96 eV, -3.11 eV and -2.34 eV, showing the triple peak, as well as a split peak at 1.38

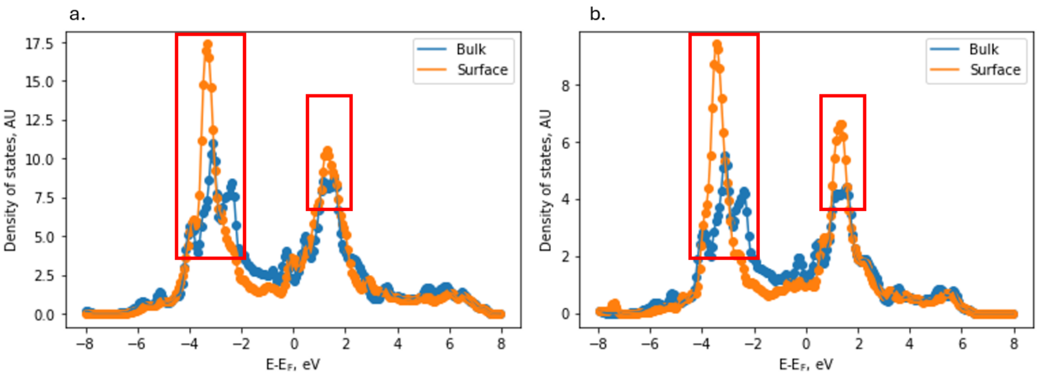

Figure. 5.20: The PDOS of Mn_3Sn's (100) surface in comparison to the bulk for a) (100)-A and b) (100)-B. The red boxes indicate the regions of interest for PDOS analysis, due to the peaks contained within.

eV, with peaks at 1.10 eV and 1.58 eV. The surface has dominating peaks at -3.39 eV and 1.38 eV, showing the peaks around -3.11 eV have shifted or merged at the surface, and that the 1.38 eV peaks have merged. The (100)-B surface shows remarkably similar PDOS peaks to the (100)-A termination; PDOS shows the two surfaces have the almost the same location of peak, with the peaks on the (100)-B surface appearing at -3.32 eV and 1.28 eV (Figure 5.20). Bader analysis shows a reduction in charge at both surfaces (Table 5.5). For the (100)-A surface, we see a drop from bulk value of charge for the surface layer for Mn by 0.177 e followed by an increase to 0.082 e above the bulk charge average, with no major change for Sn; standard deviations of the charges are 0.020 e and 0.014 e for Mn and Sn respectively. For the (100)-B surface, we see a drop from the bulk charge value by 0.099 e at the surface layer, followed by an increase by 0.088 e the layer below for Mn with Sn increasing by +0.107 e at the surface. The (100)-B surface has a standard deviation for Mn and Sn of 0.023 e and 0.006 e respectively. As such, the minimum deviation is seen in (100)-B.

For the (010) surfaces, we see very little canting for the (010)-A surface, indicating a very stable magnetic surface; the most canting occurs at the surface layer, up to 4.64° in ϕ. The (010)-B surface cants significantly only in the first layer, with a maximum of 4.69° in ϕ and 6.46° in θ. The magnetic moments remain virtually uncanted throughout the films otherwise (Figure 5.17). As such, the minimum deviation is seen in (010)-B (Table 5.4). In terms of Bader charge analysis, the (010)-A surface sees a drop by 0.078 e from bulk average for Mn, with Sn seeing a rise at the surface by 0.14 e above the average bulk charge, decreasing to a rise of 0.041 e above the surface at the next layer (Table 5.5). The standard

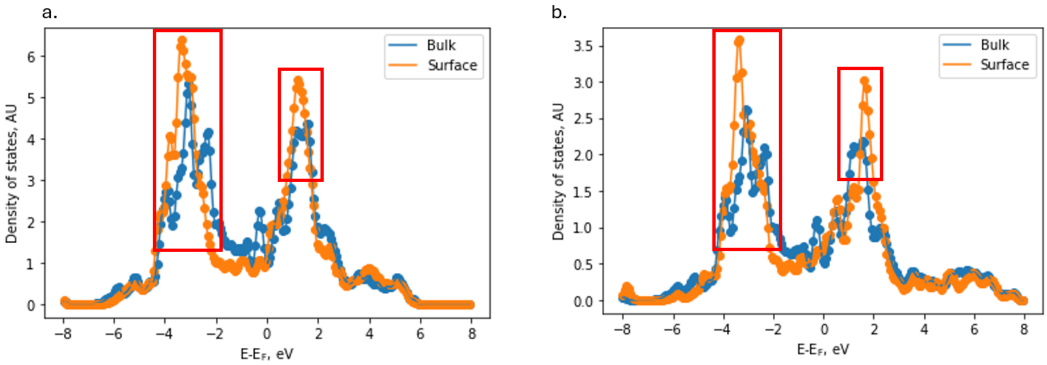

Figure. 5.21: The PDOS of Mn_3Sn's (010) surface in comparison to the bulk for a) (010)-A and b) (010)-B. The red boxes indicate the regions of interest for PDOS analysis, due to the peaks contained within.

deviations of the charges are 0.017 e for Sn and 0.007 e for Mn. The (010)-B surface sees virtually no change for either species, with Mn dropping the charge by 0.061 e from average bulk charge at the layer below the surface, and for Sn a very gradual dispersion from 0.024 e at the surface dropping to the bulk average is seen. Standard deviations for the two species are 0.013 and 0.014 for Sn and Mn respectively. As such, the minimum deviation is seen in (010)-B. For the PDOS in the bulk, we see peaks at -3.96 eV, -3.11 eV and -2.34 eV in bulk, as well as a split peak centred at 1.38 eV, with peaks at 1.10 eV and 1.58 eV. At the surface, whilst both terminations exhibit peaks in the similar regions, the (010)-A surface sees only the 3.11 eV peak shift to 3.34 eV, whereas the split peak centred at 1.38 eV unifies at 1.27 eV; the (010)-B surface sees the centre of the group of peaks at -3.11 eV shift, with distributions moving from -3.11 eV to -3.34 eV and a unified peak shifting from 1.38 to 1.62 eV (Figure 5.21).

5.4.3 Randomised magnetic moments at the surface

Whilst the ideal magnetic moments are useful to use for these materials, it is worthwhile trying to determine what potential surface distortions for the magnetic moments might result in a lower energy per unit area. Here, we find the formation energy for partially randomised magnetic moments at the surface and compare this to the ordered ground state energy, with variations of 30%, which allow for up to 16° variation from the original moment (Figure 5.22). 90 different configurations were trialled for the randomisation, in order to determine the best arrangement and to find a configuration that converged effectively.

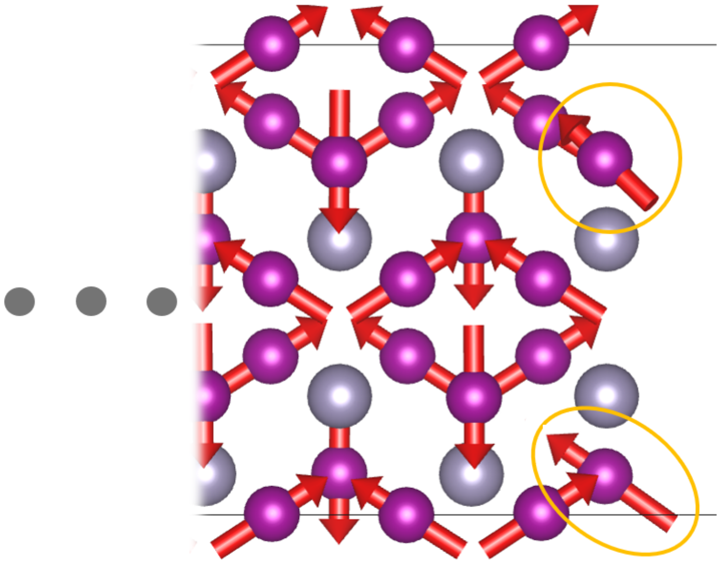

Figure. 5.22: Example of 30%, or up to 16° randomized magnetic moment at the surface of a (100) Mn_3Sn slab. The moments in the gold circles are those that are randomized. The grey ellipsis indicates the continuation of the supercell of atoms.

Mn_3Ga

The moments at the surface of the Mn_3Ga were randomized to 30%. The result of the most-stable randomized configuration for Mn_3Ga was no major improvement on the energetic minimum for Mn_3Ga. The difference in energy between the bulk-like configuration and the most stable randomized moments was +1.48 meV. This energy difference indicates there is no randomized configuration for these materials more stable than the bulk-like ordering.

Mn_3Ge

For Mn_3Ge, the result of the randomized magnetic moments for Mn_3Ga was no major improvement of the energetic minimum for Mn_3Ge. Whilst the randomized magnetic moments generally converged, we see a significant difference in the minimum energies of +0.05 to +1.66 eV.

Mn_3Sn

Mn_3Sn was similarly randomised, and the result of the randomised magnetic moments for Mn_3Sn was no major improvement of the energetic minimum for Mn_3Sn.

These randomised results had a minimum energy that differed to the standard configuration by $+0.15$ to $+1.67$ eV, indicating no better stability.

5.4.4 Comparison of substrate interfaces

The interface, when two materials interact, normally has some ionic displacement due to the differing lattice constants between the two materials. The mismatch may result in stress or strain applied to the new material it interfaces with, and conversely applies to the material itself. The result of this strain is the shifting of ions to compensate for this strain, and thus the electronic reorganisation within the material as a consequence. At this interface the properties of the two materials will differ greatly from bulk. We may use these interface properties to induce a change in the behaviour of the materials in the heterostructure. Analysing this effect is a key contribution to the effective simulation microscale devices in future. In this calculation, we add a metallic, nonmagnetic material layer (platinum) to the antiferromagnetic films. The aim is to determine the changes in the magnetic interaction at such an interface. We will explore the Bader charge, partial density of states (such as Figure 5.23) and the magnetic moment per atom at this interface, with translations to define the most stable combination of the heterostructure. In our case, due to the similar symmetry of the systems we use, we trialled five different translations of the platinum and the $D0_{19}$ relative to each other along the crystallographic a,b axes.

In terms of the lowest energy configuration of the various translations between the Mn_3X materials and platinum, it can be noted that, despite the small magnitude of difference in energy per unit area from configuration I, configuration II is the lowest energy state for all materials, by a difference of 0.08 J/m^2, 0.15 J/m^2, and 0.10 J/m^2 for Mn_3Ga, Mn_3Ge and Mn_3Sn respectively. This will be the configuration we use going forward (Figure 5.24).

Mn_3Ga

For Mn_3Ga, we see the Bader charge has significant variation at the boundary with charge being heavily affected by the heterostructure (Table 5.6). The boundary between the Mn_3Ga and the Pt sees a change in Pt, Mn and Ga charges, by 0.388-0.699 e, -0.441 e and -1.544 e respectively. This indicates a charge transfer across the two materials.

The Mn-PDOS of the most stable configuration shows major peaks in the bulk at -3.02 eV, -2.24 eV and 1.36 eV. These shift at the interface, with the peak at

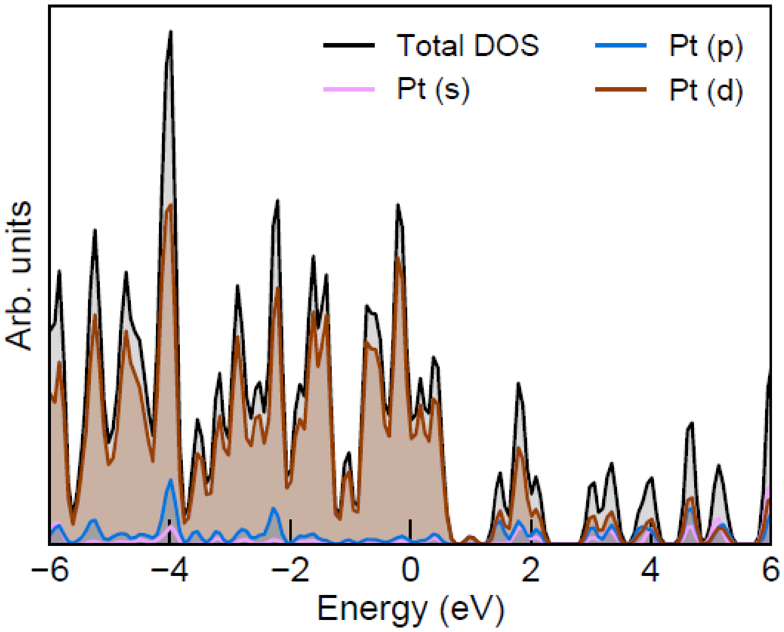

Figure. 5.23: Platinum DOS. We can see the most significant region of this density of states exists below 0 eV.

-3.02 eV merging with the peak at -2.34 eV, the peak at -2.24 eV shifting to -2.34 eV and the peak at 1.36 eV shifting to 1.65 eV. This indicates a significant change in the density of states, giving a shift by -0.1 eV and +0.29 eV respectively. The PDOS of the deeper bulk-like layers compared to that of a continuous bulk are the same, indicating no shift of the Fermi level (Figure 5.25).

For the heterostructure, the magnetic moments were virtually planar (Table 5.7). Average out-of-plane deviation, θ, is 1.03°, peaking at 2.10°. In-plane, ϕ, average deviation is 4.31° with a peak value of 5.42° at the interface (Figure 5.26).

Mn_3Ge

For Mn_3Ge, we see the Bader charge has significant charge transfer at the interface (Table 5.6). The boundary between the Mn_3Ga and the Pt sees an increase in Pt charge and a decrease in Mn and Ga charges, by 0.386 e, -0.342 e and -0.757 e respectively.

The heterostructure modelled shows some changes in the PDOS at the surface, with peak translation of -2.35 eV down to -2.51 eV, and from 1.22 up to 1.54 eV from bulk to interface. The peak at -3.15 eV reduces dramatically. Using the shifted peak value as the reference, this indicates the overall shift of -0.16 eV and +0.32 eV respectively, similar to Mn_3Ga. The deeper bulk-like layers compared

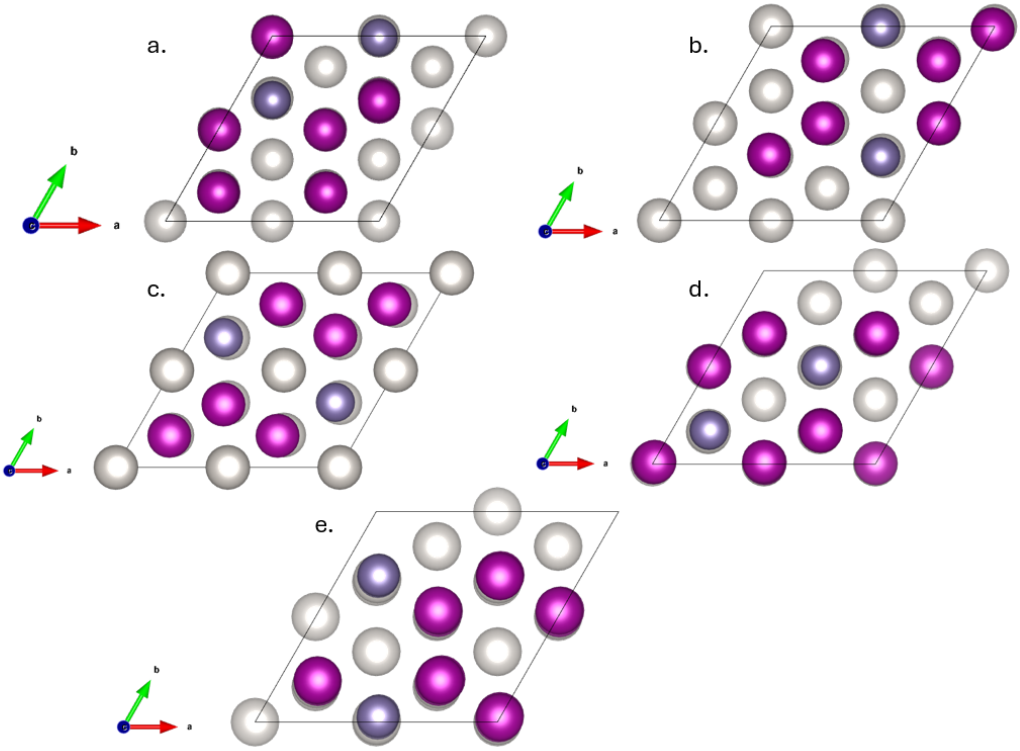

Figure. 5.24: Translations of the $D0_{19}$ (purple and grey atoms) materials relative to platinum (white). a) the zero translation configuration, I. b) configuration II and c) configuration III, translations along the b-direction. d) configuration IV and e) configuration V along the a-direction.

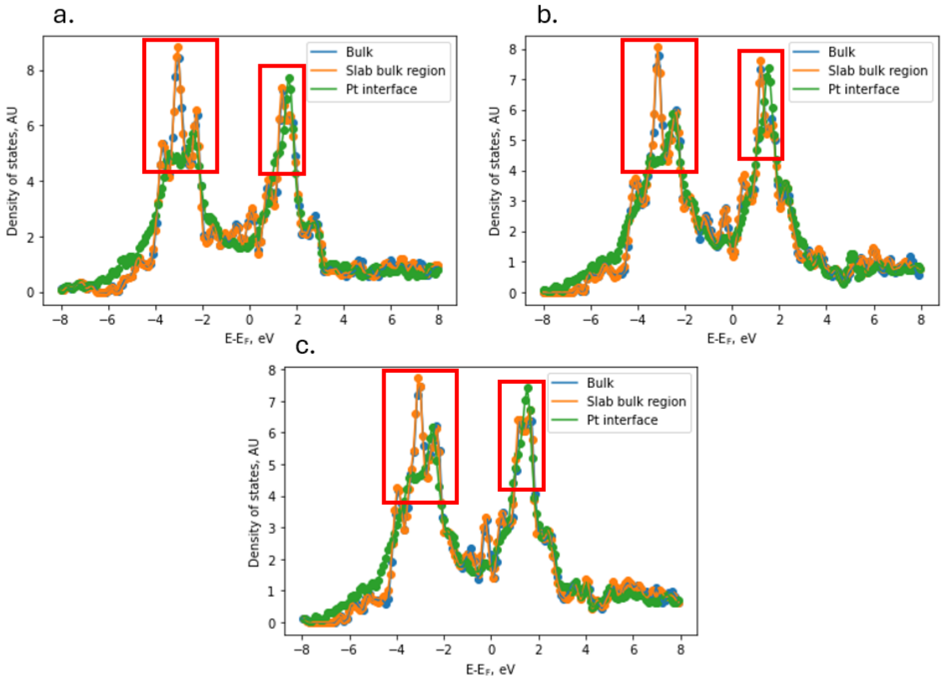

Figure. 5.25: The Mn-PDOS graphs of the $D0_{19}$ materials interfacing with platinum. a) is Mn_3Ga, b) is Mn_3Ge, and c) is Mn_3Sn. The red boxes indicate regions of interest for PDOS analysis, due to the peaks contained within.

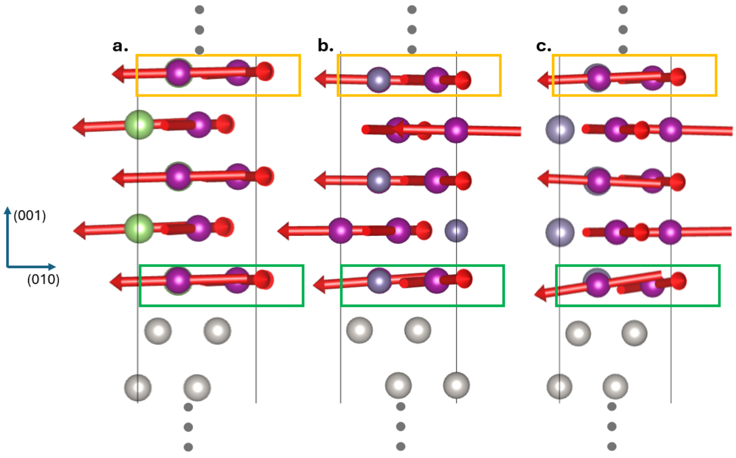

Figure. 5.26: Magnetic moments and PDOS regions for the Pt-Mn_3X heterostructure models. a) Mn_3Ga (green and purple atoms), b) Mn_3Ge (grey and purple atoms), c) Mn_3Sn (grey and purple atoms). The gold boxes represent the PDOS bulk region within the Mn_3X material, and the green boxes represent the PDOS interface region for the Mn_3X material.

Material	Mn charge difference, e	Pt Bader charge difference, e	Metal X charge difference, e
Mn_3Ga	-0.441	0.388-0.699	-1.544
Mn_3Ge	-0.342	0.386	-0.757
Mn_3Sn	-0.381	0.394-0.773	-1.795

Table 5.6: Bader charge difference at the interface with platinum, where metal X represents Ga, Ge and Sn.

to a continuous bulk have peaks in the same position, indicating no shift of the Fermi level (Figure 5.25).

In terms of magnetic moments in this heterostructure (Table 5.7), this system has very little angular deviation. The average rotation in-plane, ϕ, is 3.84° and out-of-plane, θ, is 0.95°, with the peak out-of-plane change being 3.15° at the interface (Figure 5.26).

Mn_3Sn

For Mn_3Sn, the Bader charge analysis shows significant deviation at the boundary (Table 5.6). Charge at the boundary layer for platinum sees a significant increase by 0.394-0.773 e, and decreases for Mn and Sn at the boundary of 0.381 e and 1.795 e respectively.

For the PDOS, the heterostructure analysis shows the comparison of bulk to the interface layer has a slight deviation of the peak at -2.30 eV to -2.50 eV, and the peak split at 1.43 eV (1.24 and 1.63 eV) combines and shifts to 1.53 eV. This indicates a shift by -0.20 eV and on average +0.1 eV respectively, differing significantly from Mn_3Ga and Mn_3Ge. The deeper bulk-like layers compared to a continuous bulk are the same, indicating no shift of the Fermi level (Figure 5.25).

For the magnetic moments, we see distinct canting at the interface (Table 5.7). The average in-plane canting, ϕ, is 4.95° with the interface seeing a 6.69° maximum at the interface, and out-of-plane we see an average of 3.58° with out-of-plane canting, θ, at the interface reaching 4.85° as a maximum (Figure 5.26).

5.5 Discussion

The properties calculated in this chapter are compared to the previous data (Table 5.1). For surface expansion, we calculate 0.876 pm/layer for Mn_3Ga and compare that to the value found in Holguin-Momaca et al's experimental work of 0.317 pm/layer, whereby the experimental value is 36% of the calculated value [153].

Material	Average θ, degrees	Average ϕ, degrees	Maximum θ, degrees	Maximum ϕ, degrees
Mn_3Ga	4.31	1.03	5.42	2.10
Mn_3Ge	3.84	0.95	6.04	3.15
Mn_3Sn	4.95	3.58	6.69	4.85

Table 5.7: Angular deviation at the interface with platinum.

Slab thickness and lattice parameter evolution were measured using RHEED in Holguin-Momaca et al's study. This difference in quantity shows the simulation approach is potentially allowing the system to expand significantly more than experimentally observed.

However, for Mn_3Ge and Mn_3Sn, we calculate expansions of 3.390 pm/layer and 1.320 pm/layer respectively. The expansion for Mn_3Ge is contrasted by the results from the study by Hong et al of 8.310 pm/layer (measured using XRD and AFM) [175]. For Mn_3Sn, experimental studies find expansions of 0.253-1.860 pm/layer. These studies are by Liu et al (and measured using both RHEED and high-resolution XRD) and Markou et al (lattice parameters measured by XRD and the thickness measured by quartz crystal microbalance and z-ray reflectivity) [174, 164] respectively. We can see that the calculated expansion for Mn_3Ge is 24% of value in Hong et al's study. This indicates that the calculation may limit expansion of this surface, in contrition to the calculation for Mn_3Ga.

Liu et al's study shows an expansion that is 5.21 times smaller than the calculated value for Mn_3Sn, whereas the expansion from Markou et al is 1.41 times larger, giving a wide range of values; this indicates experimental approaches have some disagreement, though the calculated expansion is within the region of agreement for the two expansion values. However, we may contend that the expansion from experiment is measured over one surface whereas the calculated expansion is taken over two surfaces, meaning the expansion may not align perfectly over the two surfaces, which will affect the comparison to calculation by a factor of 2. As well as this, noting how the thickness of the calculated surfaces is different to that of the experimental surfaces will affect the expansion due to the wider bulk region, affecting the scaling.

With the calculation method, we're able to directly compare several materials using an identical approach to determine relative property differences, a unique aspect to this research. As such, the simulated comparison of PDOS peaks allows us to see the relative changes of the density of states between materials. As well as this, determining the PDOS at the interface and surface of these materials

Material	Surface charge transfer in non-Mn species, e	Average surface moment canting, θ, °	Average surface moment canting, ϕ, °	Maximum surface moment canting, θ, °	Maximum surface moment canting, ϕ, °	Interface charge transfer in non-Mn species, e	Average interface moment canting, θ, °	Average interface moment canting, ϕ, °	Maximum interface moment canting, θ, °	Maximum interface moment canting, ϕ, °
Mn3Ga	0.115	0.58	2.06	1.79	4.80	-1.544	4.31	1.03	5.42	2.10
Mn_3Ge	-0.010 to +0.037	1.46	3.22	4.12	6.20	-0.757	3.84	0.95	6.04	3.15
Mn_3Sn	-0.010 to +0.048	0.56	2.76	2.58	4.88	-1.795	4.95	3.58	6.69	4.85

Table 5.8: Comparison of charge transfer effects for the (001)-direction material surfaces and iterfaces with platinum.

allows for comparison of specific regions within these materials. For the following comparisons, we compare bulk regions to theoretical studies in literature. The major PDOS peaks identified in literature (Table 5.1) may be compared to the calculated peaks in bulk. We see that the major peaks for Mn_3Ga from the theoretical work by Khmelevskyi, Ruban and Mohn match very well to the peaks we calculated in terms of their energetic location [212]. However, the nature of the peaks should be noted to be slightly different around -3 eV, as Khmelevskyi, Ruban and Mohn's study indicates a largely featureless and wide peak. We see several individual peaks that are well-isolated. This indicates reasonable agreement between the KKR-LSDA and PBEsol-DFT methodologies used in the reference and calculation respectively, though the results from each are not identical.

For Mn_3Ge, we see major peaks at -3, -2 and +1 eV from Wang et al's theoretical work [160]. This correlates well with the simulated PDOS in bulk, with major peaks at -3.09 eV, -2.35 eV and 1.19 eV. The nature of the peaks is largely the same, and as such is in reasonable agreement to Wang et al's study in bulk in the (001) direction, confirming the validity of our approach; as seen in chapter 3, we note the similarity of PBE and PBEsol GGAs in characterisation, and so we may determine the agreement here is to be expected to some extent, though we should note the novel approach we take using a GGA+U method will provide differences in the PDOS distribution.

For Mn_3Sn, Zhang et al's theoretical study predicts peaks at -2.50 eV, 0.51 eV and 0.4 eV, and Yang et al's work predicts peaks at -3, -2.51, -2.10 and 1.41 eV[213, 215]. Whilst these studies disagree somewhat, there is notable agreement for features around -2.50 eV. The calculated results indicate peaks at -3.87, -3.09 and -2.30 eV, as well as a positive peak that flattens around 1.24-1.63 eV. Whilst shifted significantly in the negative region of energy, these results are largely similar in nature to those of Yang et al's study, indicating a reasonable agreement for most peaks. Zhang et al's work is mostly dissimilar in the positive region of energy. Our own approach differs slightly from both, with a PBEsol-GGA+U with U=1 eV. The comparatively similar methodology for each piece of literature provides distinctly different answers to each other, yet the agreement is quite strong between Yang et al's theoretical study and the calculated results, which is to be expected from the somewhat similar approach. However, the combination of a differing GGA, a differing U-value and a higher cutoff seems to have a distinct effect on the positive region of the PDOS in the work by Zhang et al; this produces distinct differences between the calculated results and Zhang et al's theoretical study.

The shift in PDOS peaks at the surface are generally small, but most are shifted away from the Fermi surface. We note that the largest shift on Mn_3Ga is 0 eV to 0.41 eV at the (100)-A surface, a very large shift in peak position, indicating comparatively radical changes in Mn electronic structure at the surface. This material also sees comparatively large shifts on other surfaces. For Mn_3Ge, less radical shifts of peaks occur, with both (100) surface terminations shifting by 0.33 eV, with shifts on other surfaces reaching similar quantities. For Mn_3Sn, the shift is even smaller at 0.28 eV for the (100)-A surface termination, with other surfaces struggling to approach the same magnitude of shift. However, though the shifts are relatively small, it should be noted all are still significant shifts, indicating the surfaces produce significant changes to the Mn electronic structure.

Formation energy for Mn_3Ga is largely very similar across all surfaces investigated. The variation in energy across the various surfaces is small, with a range of 0.064 eV. The lowest energy surface is the first configuration of Mn-rich surface in the (100)-A configuration at 0.095 eV/Å^2, and the highest is the second Mn-rich (100)-B direction configuration at 0.159 eV/Å^2. This is indicative of the surface formation being similarly stable for all orientations, and as such having no majorly preferred orientation.

Mn_3Ge has a remarkably stable (001)-direction termination at 0.012 eV/Å^2, 12.4 times lower than the least stable configuration of the Mn-rich phase of the (100)-A configuration at 0.144 eV/Å^2. This indicates a departure from Mn_3Ga in that there is a dedicated most stable direction, (001), which is also orthogonal to that of Mn_3Ga.

Formation energy in Mn_3Sn has a similarly small variation of energy to Mn_3Ga, with minimum energy being 0.071 eV/Å^2 and maximum of 0.168 eV/Å^2 at the (100)-B Mn-poor configuration, however in this case the minimum energy configuration is the (100)-A type for the Mn-poor region. Whilst the range is larger than that of Mn_3Ga at 0.097 eV/Å^2, it's still a small enough range to determine no major preference in direction.

For the alteration of magnetic ordering at the surface, we note that in general the configurations have very varied canting in-plane and out-of-plane (Table 5.8). For θ and ϕ for Mn_3Ga, we see average canting of 0.49° and 11.75° for (100)-B, 0.17° and 1.63° for (010)-A. From the data we calculated, we can determine the most bulk-like surface of the magnetic ordering is the (010)-A direction. The largest deviation is the (100)-B surface at 44.66° in ϕ at the surface, indicating this surface is particularly heavily affected by the breakdown in periodicity. For θ and ϕ for Mn_3Ge, we see average canting of 0.26° and 8.63° for (100)-A, 0.24° and 1.86° for (010)-B. From this, we can determine the most bulk-like surface of the magnetic ordering is the (010)-B direction. The largest deviation is the (100)-A surface at 34.31° in ϕ at the surface, indicating this surface is again particularly heavily affected by the breakdown in periodicity, maintaining a consistently deviated magnetic order. For θ and ϕ for Mn_3Sn, we see average canting of 0.38° and 7.99° for (100)-A, 0.34° and 1.76° for (010)-A. From this, we can determine the most bulk-like surface of the magnetic ordering is the (010)-A direction. The largest deviation is the (100)-A surface at 30.07° in ϕ at the surface, indicating the (100) surface is of remarkable deviation across all materials to a consistent extent.

Bader charge variation indicates the charge redistribution at the surface of a material (Table 5.8). This alteration in charge will affect the interface polarization of a material at a given thickness. For Mn_3Ga, we see that the largest change in charge at a given surface is for the (100) direction of the (100)-A type. Specifically, the charge on Mn atoms varies by 0.289 e over two surfaces. This is followed closely by the (100)-B termination at 0.255 e change for Mn over two surfaces. The major differences for the (010) surfaces are small Mn variations of 0.119 e. For the charge on Ga at the surface, the (010)-A increases by 0.066 e on the (010)-A termination over the (010)-B termination, and for the (001) configuration we see similar Ga variations to (010) by 0.115 e and very small Mn differences of -0.068 e, opposite in variation to (010). We can therefore say the (001) direction is the most consistent with bulk at the surface for Mn and of reasonably small charge variation for Ga, making (001) useful orientation for terminating thin films (Table 5.8).

For Mn_3Ge, we find the (100) direction's (100)-A has a very large variance of charge over the first two layers of 0.227 e for Mn, with at 0.100 e drop for Ge. For the second termination, we find an Mn difference of 0.259 e and an increase in Ge of 0.161 e. For (010), the magnitudes of the Mn charge variations are 0.082 e and 0.072 e for the (010)-A and (010)-B terminations, with Ge varying far less in the (010)-B termination. For the (001) direction, we see a maximal charge variation of 0.060 e for Mn and 0.047 for Ge, varying over two layers (Table 5.8). Overall, the (001) layer is the least varied orientation for thin films charge-wise.

For Mn_3Sn, we note the (100) terminations' charge variations of 0.259 e and 0.187 e for the (100)-A and (100)-B respectively for Mn, with no significant Sn charge deviation. The (010) direction has less charge variation at the surface than (100) with the terminations varying by 0.092 e and 0.087 e for the for the (010)-A and (010)-B respectively for Mn. For Sn, variations are 0.156 e and 0.042 e for the (010)-A and (010)-B respectively, larger than any (100) change for Sn. For (001), the first layer has charge variation up to 0.069 e for Mn, with Sn variation up to 0.058 e, bucking the trend for these materials and making the (001) direction fractionally more variable in terms of surface charge than the (010)-B for (010) (Table 5.8).

Substrate interaction is then the next point of interest. We determine that the lowest energy relative translation state for the platinum and the $D0_{19}$ materials is configuration II. It should be noted that, as the $D0_{19}$ materials are all similar in structure, the fact they all share the same minimum energy translation is not a point of concern, moreso a point of useful comparison and confirmation. The energy minimum differences from configuration I are all sufficiently low, on the typical order of configurational differences in DFT at around 0.1 J/m^2.

For Mn_3Ga on Pt, the interface sees a shift in the magnetic moments of up to 8.12° in-plane (θ) and 2.10° out-of-plane (ϕ) (Table 5.8). This matches the surface interaction out of plane insofar as the change of magnetic moments is small. In-plane magnetization changes are significantly higher by a factor of 4. Mn_3Ge has a much lower in-plane rotation maintaining a peak near the average (3.84°), and out-of-plane only peaking at 3.15°, somewhat similar to Mn_3Ga. For Mn_3Sn, however, the angle of canting is between both Mn_3Ga and Mn_3Ge with an in-plane peak of 6.69°, but exceeds both Mn_3Ga and Mn_3Ge out-of-plane with a 4.85° maximum. The indication here is that Mn_3Sn sees the most effect from the substrate and as such is more sensitive to changes in the substrate; those materials with very small canting are minimally affected by the substrate and as such will have a more consistent SOT contribution than those with higher canting angles.

Bader charge analysis shows some significant charge transfer occurring at the interface of materials. For Mn_3Ge, we see a far lower change in the charge transfer from the interface Ge atoms than for the Ga and Sn atoms of the other heterostructures, at 0.757 e vs 1.544 e and 1.795 e for Ge, Ga and Sn respectively (Table 5.8). The changes for platinum and manganese remain largely the same between the heterostructures, as would be expected, making these useful comparisons. The charge transfer produces an electronic polarisation across the interface by generating regions of high and low charge. We may therefore note that Mn_3Ge has the least charge transfer making it the least polarised, with Mn_3Sn being the most polarised. This correlates with the magnetic moment canting, insofar as the minimal canting and minimal charge transfer occur in the same material, Mn_3Ge.

The PDOS shows significant effect by platinum to affect the density of states. Generally we see the centre of the peak shift further toward the extremes. Mn_3Ga sees a shift by up to -0.1 eV and +0.29 eV compared to bulk. For Mn_3Ge, the

PDOS sees shifts by up to -0.16 eV and +0.32 eV. Mn_3Sn sees shifts by -0.2 eV and +0.1 eV. The platinum therefore moves the states further from the Fermi energy on epitaxial combination. As the larger peaks shift away from each other, we note the conductivity will decrease due to the reduction in conductive bands proximable to each other. It should be noted that the presence of platinum does not shift the Fermi energy in any of the DO_{19} materials, indicating it does not affect the conductivity of the material for the heterostructure to be involved.

We note that the surfaces see minimal charge transfer at the interface and have very significant canting of the moments, whereas the heterostructure interface with Pt has significant charge transfer with smaller canting. We note that the (100) surfaces for all three materials generally incur the largest maximum and average canting, with the (010) surfaces following, then the (001) surfaces, and that the lowest charge transfer is at the (001) surface, with larger charge transfer at the (100) and (010) surfaces. The only exceptions to this trend are surfaces of similar charge transfer. For the Pt interface, the largest charge transfer does take the largest average moment canting in Mn_3Sn, and similarly the lowest charge transfer sees the lowest canting in Mn_3Ge. The ordering does significantly mitigate canting in the (001) surfaces, where we see lower moment canting for both systems.

5.5.1 Sources of inaccuracy

For the structural calculations, as well as the calculations of the layer expansion, the sources of potential error may come from the limitations of VASP due to the thickness the layer. There is a limited number of atoms VASP can efficiently simulate based on the computing power available, resulting in the limitation of thickness of the layer. This makes comparison to some studies using thicker materials difficult. Similarly, magnetic ordering may have some error attributed to the layer sizing and periodic nature of the simulation. By using a far thicker layer, we may assess a more reasonable bulk-to-surface progression of magnetic ordering. Other limitations in the calculated approach may be the approximate nature of DFT; the exchange-correlation functional cannot be computed exactly, and as such may result in a systematic error when comparing to experimental data.

Bader charge analysis may have significant differences to comparable studies due to the potential difference in the number of charge centres to be integrated over. Assessment closer to the surface should still be reasonable as the distribution of charge should compare well locally but for nonlocal comparisons or for assessing effects over wider bulks this effect can become significant. As well as this, the charge centering may differ based on the method used and thus dramatically affect the charge localisation of the materials, resulting in configurations that are unrealistic. Whilst this should only be a minor error in this work, it is important to note the contribution charge localisation may provide to this calculation.

For the PDOS, the difference in simulation methodology in comparison to other studies may be responsible for the mismatch in peak location due to the differing treatment of electronic state calculation. As well as this, the selection of symmetrically inequivalent layers will dramatically change the result of the simulation, as well as differences in the supercells between the reference study and the calculation. On this basis, whilst we choose to do single-layer projections for most comparisons, multilayer comparisons may find differing peak locations and magnitude, thus this discrepancy should be taken into account. As we mainly reference the largest peaks, this shouldn't be of major significance.

Temperature effects have also been ignored. The calculations we perform operate under the zero temperature condition, and therefore may not duplicate systems of higher temperature well. As such, we will have a systematic error associated with comparison to higher temperature systems.

The interface between materials has also been idealised. Due to the semi-infinite nature of our model slab, the interface is restricted to a small infinitely-repeating cell which cannot be extended to encounter point defects such as vacancies or extended defects such as dislocations. Consequentially, effects unique to these defects will not be taken into account and may therefore provide distinct electronic and structural differences to experiment.

5.6 Conclusion

We note that the findings of previous research (Table 5.1) match well to the calculated values for the expansion of the $D0_{19}$ materials, within picometres of experimental value for expansion (Table 5.3). The PDOS of the bulk of the $D0_{19}$ materials generally match well, with exception of Zhang et al [213] with the positive region differing by 0.9 eV. We can therefore conclude that the calculated properties of the $D0_{19}$ materials at a surface, such as the layer expansion, are reasonable, and can go forward with the rest of the surface characterisations. We have determined here the properties of interfaces in anticipation for potential optimisation of heterostructure devices.

The material properties deviate from bulk at the surface both structurally and magnetically. We see the surface rumpling alter the positions of atoms significantly, with the most extreme rumpling being Mn_3Sn's (001) configuration at 31 pm displacement of Sn (section 5.4.2). The least affected are the (010) configurations, which had less that 1 pm displacement of any atom. This allows us to conclude the (010) configurations are the most similar to bulk in terms of structure, which should preserve the structural properties up to the surface. However, the most energetically stable surface is Mn_3Ge's (001) configuration (Table 5.3), and as such the relaxed surfaces with more significant displacement may still be the most stable. Expansion perpendicular to the surfaces is also calculated, with the largest expansion being Mn_3Sn's (100)-B surface at 5.87 pm/layer, though all expansions are relatively low, indicating the layer expansion does not play a significant role at the surface. Novel findings of this section include the variation in the magnetic moments immediately at the surface, whereby the least affected surfaces are the (001) configurations for Mn3Ga and Mn_3Sn, and the (010)-B surface for Mn_3Ge. These values are all below 5° average variation, with some variation being less that 1°, indicating significant similarity to bulk and thus similar SOT variation. We can compare this to the PDOS changes at the surface and note that the changes to the magnetic moment support the conclusion that the electronic structure must be significantly affected by the surface, with PDOS shifts in Mn_3Ga of up to 0.41 eV.

For the platinum-substrate $D0_{19}$ heterostructures, we have evaluated the magnetic and electronic properties as well as confirming the structural ordering preference of the two materials with respect to each other via translation. We can conclude that the presence of the platinum layer significantly affects the magnetic moment, particularly in-plane, causing all materials to deviate from bulk significantly. We note that Mn_3Sn had the largest in-plane change of magnetic moment angle at 4.85° at the surface, nearly double Mn_3Ga's value of 2.10°(Table 5.7). This implies significant magnetic effects come from the interface and so thicker films of Mn_3Sn will be needed than the other $D0_{19}$ materials in order to preserve bulk-like SOT variation. Novel findings include the charge transfer at the interface. The charge transfer details the significance of the near-interface electric field and the depth to which the resistive nature of the combination may be affected; we see the smallest charge transfers at the surface of order 0.1 e, implying charge redistribution at the surface is not responsible for significant conductivity effects. However, the largest charge transfer exists at the interface of Pt and Mn_3Sn for Sn at 1.795 e, with all Pt interfaces showing significant charge transfer, resulting in charge polarization of the interface (Table 5.6). As well as this, the bulk PDOS is affected by the interface. For the Pt interface, we see little effect on the bulk implying the Fermi energy is not affected by the platinum layer and thus conductivity is largely unaffected, but at the interface we see the shifts in peaks become significant, deviating away from the Fermi energy by up to 0.32 eV, indicating the Mn structure becomes strained somewhat and shifts slightly at the interface due to the heterostructure being formed.

Chapter 6

Conclusion

To conclude this thesis, we will summarize the major results of the research chapters and discuss the future research opportunities. This thesis covers a deep range of results and so we will dedicate discussion and comparison of these to this section. We firstly recap on the overall impetus of this research. For spin-orbit torque (SOT)-antiferromagnetic (AFM) memory devices, we are interested in the screening of AFM Mn-alloys to determine their material properties and the effects of interfaces for their application in AFM read and write layers for spintronic memory devices. We begin with discussing the results for the bulk $L1_0$ materials. We then discuss how these materials compare and what the calculations determine may be useful as applications for these materials. After this, we discuss the $L1_2$ and $D0_{19}$ bulk properties, with care to elaborate on the utility of investigating the strain. We compare these to the $L1_0$ materials in order to compare and contrast the utility in an SOT-AFM device. Finally, we discuss the further $D0_{19}$ calculations, and their application to device-specific properties so that it is seen as to how this research best relates to more practical designs of SOT-AFM devices.

In chapter 3, six $L1_0$ Mn-alloys were characterised for their structural and magnetic properties in order to determine the most effective characterisation approach using density functional theory (DFT). We compare the simulated results to a wealth of experimental and theoretical data as well as making predictions as to the properties of the materials that do not have existing literature. The $L1_0$ materials are all collinear, with MnGa being the only ferromagnet of the six alloys. The remaining materials were all collinear antiferromagnets. Using MnGa to form the basis of comparison to experimental and theoretical literature (Tables 3.1, 3.2), we determined the optimal calculation methodology to be PBE functional revised for solids (PBEsol)+U and U=1 eV respectively. Comparison of structural properties to previous studies (Table 3.3) shows general agreement to the calculations to within 0.02 nm or less for lattice parameters, which reinforces the correct selection of the method and the predictive capability of the simulated approach. It therefore indicates we can use this to structurally characterise and compare each material using this unified approach. Magnetic ordering shows general agreement across the board to experiment to within 0.5 μ_B, down to the ordering configuration for the antiferromagnets (Table 3.4). Whilst some materials do not reconcile with the exact magnetic moment ordering in terms of the ground state orientation that are determined in previous studies, such as MnPt's 45° canting from the (001) plane as in Andreas et al's study [43], we can conclude that magnetic properties can be predicted using the simulated approach; we can predict exact ordering and values of the magnetic moments to within 0.5 μ_B.

We see a large value of the magnetic anisotropy energy (MAE) for MnIr at -4.187 meV/FU, compared to more typical values of MAE of around one order of magnitude less, such as 0.372 meV/FU for MnGa (Table 3.4). Easy axes are identified that align with previous studies though some experimentally observed features are not seen due to low energy, such as the 45° canting for MnIr seen in the theoretical study by Mohn et al and for MnPt seen in the experimental study by Andreas et al [133, 43]. We may conclude from the comparable results to previous theoretical and experimental studies that the simulated method has a reliable predictive capability for the MAE. The calculated prediction for MnIr's MAE was within 0.69 eV/FU, or 20% of the reference value from the study by Umetsu et al [44]. Other characteristics of Mn-alloy antiferromagnets can be predicted with similar degrees of precision.

In chapter 4, the $L1_2$ and $D0_{19}$ noncollinear antiferromagnets were investigated. For these materials, we investigate the structural and magnetic properties like the MAE, as well as further electronic properties like the band structure; we also investigated the effects of strain on the materials to investigate the effects on the structural, magnetic and electronic properties. We restrict this to strain to the (001) plane in order to maintain symmetry and support comparison with existing literature. Both the $D0_{19}$ and $L1_2$ materials were simulated to determine the structure, magnetic ordering, magnetic moment, and plane-restricted magnetocrystalline anisotropy energy. $D0_{19}$ materials were also simulated to determine the effects of planar straining, specifically the structure, formation energy and the changes in band structure with particular focus on the shifting of Weyl points.

We find the calculated structural properties compare to experimental and theoretical findings well (Tables 4.1, 4.2), with experimental and theoretical literature volunteering structural parameters differing by 10's of pm at most (Table 4.3). Magnetic properties are of some significant disagreement though, with experimental studies like that of Chen et al showing up to 40% difference from the calculated value for Mn_3Ge (2.21 μ_B from the experimental study by Chen et al vs the calculated value 3.09 μ_B), though we may also note that the literature also has a wide range of values, such as Yang et al's theoretical study (2.7 μ_B). We note that the MAE is predicted to be of far lower magnitude for the evaluated $D0_{19}$ materials than for the $L1_2$ material (e.g. 6.26 meV/FU for Mn_3Ir vs. 27.70 μeV/FU for Mn_3Ga), a likely consequence of the high atomic number of Ir, indicating that switching the magnetic ordering between high and low energy states would be less energetically expensive for the $D0_{19}$ materials per formula unit, though the functionality at room temperature will depend on the volume of the material used. We calculated the effects of straining the $D0_{19}$ lattices (Table 4.4), which is necessary to simulate epitaxial growth on a substrate material, such as in a heterostructure device. For each material, this strain results in an asymmetric change in formation energy of the strained structure (with a minimum at 0% strain) and reduction in the c-lattice parameter with increasing strain (Figure 4.10). The existence and change in location of Weyl points is then determined from band structure calculations at 0% strain and ±6% strain (Figure 4.11). We note that Mn_3Ga has no Weyl points in our band structures, but Mn_3Ge and Mn_3Sn do have 1 and 2 Weyl points respectively. Mn_3Ga does however show significant variation with strain in terms of band structure. In Mn_3Ge, the Weyl point steadily rises in energy with an increase in strain by +0.220 eV. In Mn_3Sn, the Weyl points both follow differing trends, with the Weyl point nearest the K k-point rising very slightly in energy above 0% strain, but the number of Weyl points remains the same across the strain range. For the Weyl point closest to the M k-point, the energy varies greatly, rising before 0% and then falling with strain, though retaining the same nature throughout. We also see the magnetic moment magnitude changes consistently with strain, though not strictly linearly, indicating strain may be used to adjust this magnetic property. As well as this, the number of the Weyl points will not be affected by low strain, maintaining the potential high mobility and thus high switching speeds within the noncollinear antiferromagnets.

In chapter 5, the surface and heterostructure interface effects for $D0_{19}$ materials were investigated. We selected to use a simulation of epitaxially combined Mn-alloy and platinum. We characterised the magnetic distortion, charge transfer and densities of states at the surface, as well as the structural properties and deviations from the bulk. The expansion of materials matched reasonably well to the experimentally predicted expansion (Table 5.1), whereby we find the calculated results (Table 5.3) to be within the order of magnitude of experimental expansion, with individual layer expansions at the surface (Table 5.2) rarely exceeding 0.2 Å, and for calculated expansion of Mn_3Sn to be within the range of experimental results from Markou et al and Liu et al [174, 164]. We may conclude the simulated model can predict overall expansion to within tens of picometres per layer and that the surface relaxation is reasonable for these materials. We determined the magnetic distortion at the surfaces was generally quite significant (Table 5.4), with the maximal canting up to 44.66° in ϕ for Mn_3Ga's (100)-B termination. This is likely to affect changes in the MAE at the surface and at material interfaces, meaning limitations to minimum thickness may be necessary to avoid MAE variations away from bulk behaviour. This is very important in nanoscale thin film devices to ensure effective switching with predictable states.

The Bader charge analysis revealed significant charge transfer at the material interface between $D0_{19}$ materials and platinum (Table 5.6), with up to -1.795 e charge transfer in Sn for Mn_3Sn on Pt and up to -0.441 e charge transfer in Mn in Mn_3Ga on Pt across the first layers of Pt and Mn_3Ga. Large charge transfer implies electric field generation at the boundary which will affect conductivity through the boundary, altering the resistive state of any heterostructure. At the surface (Table 5.5), whilst some charge effects are visible, the surface charge deviation is fairly minimal with a maximum charge variation of 0.344 e over the first two layers in Mn for Mn_3Ge compared to the larger charge transfer at the material interface. The depth of significant charge transfer at the surface is useful to determine a minimum thickness of the $D0_{19}$ material to maintain bulk-like behaviour and determine the reduction in conductivity at interfaces; we may conclude that interfaces beyond 2 layers deep are commonly very bulk-like in terms of charge distribution.

The projected density of states (PDOS) shows significant effects of both the surface and platinum interface on the density of states, with shifts up to 0.41 eV at the surface for Mn_3Ga (section 5.4.4). The shift at the surface indicates a significant electronic relocation within the Mn system, which is important to understand as the Mn is the species with non-zero magnetic moment and often has a significantly smaller rumpling than the non-Mn species, making structural changes hard to identify. Whilst the Fermi energy remains the same for the platinum layer and the $D0_{19}$ material, indicating no major change in the conductivity of the interface, the shift of densities of state by up to 0.32 eV reinforces the Mn does have some rumpling, with state densities becoming significantly more disparate.

This research supplies significant data on the predictive capability of simulating antiferromagnets and comparing them directly. Whilst a wide array of materials have been considered, further research could be generalised for an even wider array of antiferromagnets. It would be advantageous to generate a large database of comparable antiferromagnets for use in characterising and tuning AFM experiments and devices, specifically noncollinear antiferromagnets when considering the interesting changes in MAE found in this research such as strain sensitivity, charge polarization at Pt interfaces and Weyl fermion effects. Further antiferromagnet characterisation is also a useful aspect of any continued research. The data on interface interaction gathered in this research will influence the understanding of the boundary effects in SOT-AFM devices so that these devices may be better optimised in their construction and in the understanding of the underlying electronic effects. Further research into the specific interactions at an interface would therefore be a useful avenue of exploration, especially when considering the findings regarding conductivity and Weyl points for heterostructures in this thesis.

Further research into the effects of different nonmagnetic metals as substrates for the Mn-alloys, and to complete anomalous Hall effect calculations [22] into the AFM materials and interface heterostructures for more comprehensive device-based characterisation, would further expand on the interface research within this thesis. It would also provide further insight into potential low-cost substrates and substrate tuning.

Overall, we have successfully produced a method of predictively characterising AFM materials for their structural, magnetic and electronic properties. We have investigated both collinear and noncollinear Mn-alloy AFM materials, investigated strain effects and interface effects, and determined the magnetocrystalline anisotropy and the nature of the anisotropy from this model. This thesis provides a useful platform for developing comprehensive data on AFM materials for potential use in heterostructure devices, with evaluation of strain and interface properties calculated for a range of materials. This research will aid in the screening and characterisation of antiferromagnets and heterostructures with a view to implementation in future SOT-AFM devices.

Acronyms

AFM antiferromagnetic. 4–6, 10, 12, 35, 45, 47, 50, 57, 58, 60, 69, 72, 79, 84, 87, 89, 96, 101, 102, 108, 136, 146, 150

AM05 Armiento-Mattsson 2005. 54, 56

CASTEP Cambridge serial total energy package. 9

DAE dipole anisotropy energy. 54, 60–64, 66, 87, 88, 90, 96, 97

DFT density functional theory. 8, 9, 12, 13, 15, 20, 22, 40, 44, 50, 51, 53, 65, 66, 74, 75, 83, 85, 99, 104, 108, 109, 138, 141, 142, 146

DFT+U density functional theory with Hubbard U. 22, 47, 78, 103

DMI Dzyaloshinskii-Moriya interaction. 41–43

DOS density of states. 106, 132, XIII

EDX energy dispersive x-ray. 81

EDXS energy dispersive x-ray spectroscopy. 82

EPMA electron probe microanalysis. 82

ETO electrical transport option. 82

FM ferromagnetic. 2, 4, 5, 35, 47, 50, 54, 57

FP-LAPW full-potential linear augmented plane-wave. 51–53, 62, 73, 85

GGA generalized gradient approximation. 9, 21, 32, 54, 73, 83, 85, 108, 138, VIII

ICP-MS inductively coupled plasma mass spectrometry. 48

ICP-OES inductively coupled plasma optical emission spectroscopy. 81

JAMS Just Another Magnetic Simulator. 9, 10, 40

KKR Korringa-Kohn-Rostoker. 51, 52, 108, 138

LDA local density approximation. 9, 20, 21, 23

LMTO-ASA linear muffin tin orbital with atomic sphere approximation. 51, 53, 62

LSDA local spin-density approximation. 51, 53, 62, 106, 138

M06-L Minnesota 2006 local function. 54

MAE magnetic anisotropy energy. 40, 43, 45–54, 56, 60–64, 66–68, 73–75, 77, 79, 81–84, 86–90, 95–98, 100, 147–150, XIV, XV

MBE molecular beam epitaxy. 49, 108

MOKE magneto-optical Kerr effect. 50, 82

MPMS magnetic property measurement system. 82

MRAM magnetoresistive random access memory. 1–5

PAW projector augmented wave. 28, 30, 47, 52, 53, 78, 103

PBE Perdew, Burke and Ernzerhof. 21, 47, 51–54, 56, 73, 83, 85, 108, 138

PBEsol PBE functional revised for solids. 54, 56, 66, 75, 78, 104, 138, 146

PDOS projected density of states. 9, 52, 102, 106–108, 118, 122, 124, 126–129, 131, 132, 135, 136, 138, 141–144, 149

PW91 Perdew-Wang. 54, 56

PWBS plane-wave basis set. 25, 29

RBS Rutherford backscattering spectrometry. 78

RHEED reflection high-energy electron diffraction. 108, 136

rPBE revised PBE. 21, 54, 56

rSCAN revised SCAN. 54, 56

rTPSS revised Tao, Perdew, Staroverov, Scuseria. 54, 56

SCAN Strongly Constrained and Appropriately Normed. 54

SCF self-consistent field. 20, 26

SEM scanning electron microscopy. 81, 82

SIE self-interaction error. 22

SKKR screened Korringa-Kohn-Rostoker. 73, 83

SOC spin-orbit coupling. 29, 30, 40, 51, 53, 54, 56, 60–66, 74, IX

SOT spin-orbit torque. 4, 11, 101, 102, 141, 144, 146, 150

SPR spin-polarized relativistic. 52

SQUID superconducting quantum interference device. 49

STM scanning tunnelling microscopy. 49

STT spin transfer torque. 4

TEM tunnelling electron microscopy. 80

TMR tunnelling magnetoresistance. 2–6

TR-MOKE time-resolved magneto-optical Kerr effect. 82

VASP Vienna ab-initio simulation program. 9, 13, 22, 30, 44, 106, 142

VSM vibrating sample magnetometer. 81–83

XC exchange-correlation. 13, 19–22, 75

XRD x-ray diffraction. 48, 49, 78, 80–82, 108, 136

Bibliography

[1] Jamie H. Warner, Franziska Schäffel, Alicja Bachmatiuk, and Mark H. Rümmeli. Chapter 6 - applications of graphene. In *Graphene*, pages 333–437. Elsevier, 2013.

[2] M. Julliere. Tunneling between ferromagnetic films. *Physics Letters A*, 54(3):225–226, 1975.

[3] Mark Johnson and R. H. Silsbee. Interfacial charge-spin coupling: Injection and detection of spin magnetization in metals. *Physics Review Letters*, 55:1790–1793, 1985.

[4] G. Binasch, P. Grünberg, F. Saurenbach, and W. Zinn. Enhanced magnetoresistance in layered magnetic structures with antiferromagnetic interlayer exchange. *Physics Review B*, 39:4828–4830, 1989.

[5] M. N. Baibich, J. M. Broto, A. Fert, F. Nguyen Van Dau, F. Petroff, P. Etienne, G. Creuzet, A. Friederich, and J. Chazelas. Giant Magnetoresistance of (001)Fe/(001)Cr Magnetic Superlattices. *Physics Review Letters*, 61:2472–2475, 1988.

[6] J.M. Daughton. GMR applications. *Journal of Magnetism and Magnetic Materials*, 192(2):334–342, 1999.

[7] Sabpreet Bhatti, Rachid Sbiaa, Atsufumi Hirohata, Hideo Ohno, Shunsuke Fukami, and S.N. Piramanayagam. Spintronics based random access memory: a review. *Materials Today*, 20(9):530–548, 2017.

[8] Vincent Petit, Steven Carlini, and Victor Avelar. Digital economy and climate impact, 2021.

[9] Steve Sandler. Faster-Switching GaN : Presenting a number of interesting measurement challenges. *IEEE Power Electronics Magazine*, 2(2):24–31, 2015.

[10] Han Yan et al. Electric-field-controlled antiferromagnetic spintronic devices. *Advanced Materials*, 32(12):1905603, 2020.

[11] Sarah Jenkins, Roy W. Chantrell, Timothy J. Klemmer, and Richard F. L. Evans. Magnetic anisotropy of the noncollinear antiferromagnet $\mathrm{IrMn_3}$. *Physics Review B*, 100:220405, 2019.

[12] P. Wadley et al. Electrical switching of an antiferromagnet. *Science*, 351(6273):587–590, 2016.

[13] V. Baltz, A. Manchon, M. Tsoi, T. Moriyama, T. Ono, and Y. Tserkovnyak. Antiferromagnetic spintronics. *Reviews of Modern Physics*, 90:015005, 2018.

[14] Cheng Song, Yunfeng You, Xianzhe Chen, Xiaofeng Zhou, Yuyan Wang, and Feng Pan. How to manipulate magnetic states of antiferromagnets. *Nanotechnology*, 29(11):112001, 2018.

[15] Ding-Fu Shao and Evgeny Y. Tsymbal. Antiferromagnetic tunnel junctions for spintronics. *npj Spintronics*, 2(1):13, 2024.

[16] Enlong Liu et al. Synthetic-ferromagnet pinning layers enabling top-pinned magnetic tunnel junctions for high-density embedded magnetic random-access memory. *Physics Review Applied*, 10:054054, 2018.

[17] Yeongkyo Seo and Kon-Woo Kwon. Ultra High-Density SOT-MRAM Design for Last-Level On-Chip Cache Application. *Electronics*, 12(20), 2023.

[18] Dmytro Apalkov et al. Spin-transfer torque magnetic random access memory (STT-MRAM). *Journal of Emerging Technologies in Computing Systems*, 9(2), 2013.

[19] Danrong Xiong et al. Antiferromagnetic spintronics: An overview and outlook. *Fundamental Research*, 2(4):522–534, 2022.

[20] Victor Lopez-Dominguez, Yixin Shao, and Pedram Khalili Amiri. Perspectives on field-free spin–orbit torque devices for memory and computing applications. *Journal of Applied Physics*, 133(4):040902, 2023.

[21] Jiacheng Shi et al. Electrically Controlled All-Antiferromagnetic Tunnel Junctions on Silicon with Large Room-Temperature Magnetoresistance. *Advanced Materials*, 36(24):2312008, 2024.

[22] Xiaoning Wang, Han Yan, Xiaorong Zhou, Hongyu Chen, Zexin Feng, Peixin Qin, Ziang Meng, Li Liu, and Zhiqi Liu. Noncollinear Mn_3Sn for antiferromagnetic spintronics. *Materials Today Physics*, 28:100878, 2022.

[23] Han Yan et al. A piezoelectric, strain-controlled antiferromagnetic memory insensitive to magnetic fields. *Nature Nanotechnology*, 14(2):131–136, 2019.

[24] Ju-Young Yoon et al. Handedness anomaly in a non-collinear antiferromagnet under spin-orbit torque. *Nature Materials*, 22(9):1106–1113, 2023.

[25] C. Hermann and Paul Peter Ewald. *Strukturbericht 1913-1928 : Zeitschrift fur Kristallographie, Kristallgeometrie, Kristallphysik, Kristallchemie ... Erganzungsband*. Akademische Verlagsgesellschaft, Leipzig, 1931.

[26] Michael J. Mehl. A brief history of strukturbericht symbols and other crystallographic classification schemes. *Journal of Physics: Conference Series*, 1290(1):012016, 2019.

[27] Rajesh Dutta. Ab-initio DFTU study on the electronic correlation in multiferroic XY-antiferromagnetic $Ba_2CoGe_2O_7$. *Journal of Magnetism and Magnetic Materials*, 596:171955, 2024.

[28] Nabil Al-Aqtash and Renat Sabirianov. Strain control of magnetocrystalline anisotropy and energy product of MnGa alloys. *Journal of Magnetism and Magnetic Materials*, 391:26–33, 2015.

[29] Masoud Rahbar Niazi, Sohrab Sanjabi, and Yousef Jamali. Ab initio study of the effect of thickness and epitaxial strain on the magnetic structure of NiMn freestanding films. *Physics Letters A*, 383(14):1660–1665, 2019.

[30] Rie Y. Umetsu, Kazuaki Fukamichi, and Akimasa Sakuma. Electrical and Magnetic Properties, and Electronic Structures of Pseudo-Gap-Type Antiferromagnetic $L1_0$-Type MnPt Alloys. *Materials Transactions*, 47(1):2–10, 2006.

[31] G. Kresse and J. Hafner. Ab initio molecular-dynamics simulation of the liquid-metal-amorphous-semiconductor transition in germanium. *Physics Review B*, 49:14251–14269, 1994.

[32] G. Kresse and J. Furthmüller. Efficiency of ab-initio total energy calculations for metals and semiconductors using a plane-wave basis set. *Computational Materials Science*, 6(1):15–50, 1996.

[33] G. Kresse and J. Furthmüller. Efficient iterative schemes for ab initio total-energy calculations using a plane-wave basis set. *Physics Review B*, 54:11169–11186, 1996.

[34] G. Kresse and D. Joubert. From ultrasoft pseudopotentials to the projector augmented-wave method. *Physics Review B*, 59:1758–1775, 1999.

[35] Stewart J. Clark, Matthew D. Segall, Chris J. Pickard, Phil J. Hasnip, Matt I. J. Probert, Keith Refson, and Mike C. Payne. First principles methods using CASTEP. *Zeitschrift für Kristallographie - Crystalline Materials*, 220(5-6):567–570, 2005.

[36] Bongani Ngobe, Ramogohlo Diale, Maje Phasha, Mahlaga Molepo, and Hasani Chauke. Ab-initio techniques, VASP and CASTEP, are used to investigate the electronic properties of B2 compounds formed between Ti and group VIII elements - a comparative study. *MATEC Web of Conferences*, 370:02005, 2022.

[37] Thomas D. Kühne et al. CP2K: An electronic structure and molecular dynamics software package - Quickstep: Efficient and accurate electronic structure calculations. *The Journal of Chemical Physics*, 152(19):194103, 2020.

[38] R F L Evans, W J Fan, P Chureemart, T A Ostler, M O A Ellis, and R W Chantrell. Atomistic spin model simulations of magnetic nanomaterials. *Journal of Physics: Condensed Matter*, 26(10):103202, 2014.

[39] Sarah Jenkins, Roy. W. Chantrell, and Richard F. L. Evans. Atomistic simulations of the magnetic properties of $\mathrm{Ir}_x\mathrm{Mn}_{1-x}$ alloys. *Physical Review Materials*, 5:034406, 2021.

[40] Joseph Barker. Just Another Magnetic Simulator, 2019.

[41] Sarah Jenkins, Andrea Meo, Luke E Elliott, Stephan K Piotrowski, Mukund Bapna, Roy W Chantrell, Sara A Majetich, and Richard F L Evans. Magnetic stray fields in nanoscale magnetic tunnel junctions. *Journal of Physics D: Applied Physics*, 53(4):044001, 2019.

[42] L. Szunyogh, B. Lazarovits, L. Udvardi, J. Jackson, and U. Nowak. Giant magnetic anisotropy of the bulk antiferromagnets IrMn and IrMn_3 from first principles. *Physics Review B*, 79:020403, 2009.

[43] S. Khmelevskyi, A. B. Shick, and P. Mohn. Element-specific analysis of the magnetic anisotropy in Mn-based antiferromagnetic alloys from first principles. *Physical Review B*, 83(22):224419, 2011. PRB.

[44] R. Y. Umetsu, A. Sakuma, and K. Fukamichi. Magnetic anisotropy energy of antiferromagnetic $L1_0$-type equiatomic Mn alloys. *Applied Physics Letters*, 89(5):052504, 2006.

[45] Ingo Opahle, Harish K. Singh, Jan Zemen, Oliver Gutfleisch, and Hongbin Zhang. Effect of N, C, and B interstitials on the structural and magnetic properties of alloys with Cu_3Au structure. *Physics Review Res.*, 2:023134, 2020.

[46] V. Puliafito, R. Khymyn, M. Carpentieri, B. Azzerboni, V. Tiberkevich, A. Slavin, and G. Finocchio. Micromagnetic modeling of terahertz oscillations in an antiferromagnetic material driven by the spin Hall effect. *Physics Review B*, 99:024405, 2019.

[47] J. S. R. McCoombs, A. Zelenskiy, M. L. Plumer, B. W. Southern, and T. L. Monchesky. Impact of Dzyaloshinskii-Moriya and anisotropic exchange interactions on the cubic kagome antiferromagnets Mn_3X and Mn_3AB. *Physics Review B*, 107:064407, 2023.

[48] Michael Donahue. OOMMF User's Guide, Version 1.0, 1999.

[49] S.C. Westmoreland, R.F.L. Evans, G. Hrkac, T. Schrefl, G.T. Zimanyi, M. Winklhofer, N. Sakuma, M. Yano, A. Kato, T. Shoji, A. Manabe, M. Ito, and R.W. Chantrell. Multiscale model approaches to the design of advanced permanent magnets. *Scripta Materialia*, 148:56–62, 2018.

[50] Xinyu Huang et al. Manipulating exchange bias in 2d magnetic heterojunction for high-performance robust memory applications. *Nature Communications*, 14(1):2190, 2023.

[51] Mengjuan Mi, Han Xiao, Lixuan Yu, Yingxu Zhang, Yuanshuo Wang, Qiang Cao, and Yilin Wang. Two-dimensional magnetic materials for spintronic devices. *Materials Today Nano*, 24:100408, 2023.

[52] E. Schrödinger. An undulatory theory of the mechanics of atoms and molecules. *Physics Review*, 28:1049–1070, 1926.

[53] Anoop Kumar Kushwaha. A brief review of density functional theory and solvation model. *ChemRxiv*, 2022.

[54] M. Born and R. Oppenheimer. Zur quantentheorie der molekeln. *Annalen der Physik*, 389(20):457–484, 1927.

[55] M. Verdaguer and V. Robert. 8.04 - fundamentals, principles, and concepts of molecular magnetism and spintronics. In Jan Reedijk and Kenneth Poeppelmeier, editors, *Comprehensive Inorganic Chemistry II (Second Edition)*, pages 131–189. Elsevier, Amsterdam, second edition edition, 2013.

[56] Pablo Echenique and J. L. Alonso. A mathematical and computational review of hartree–fock scf methods in quantum chemistry. *Molecular Physics*, 105(23-24):3057–3098, 2007.

[57] D. R. Hartree. The wave mechanics of an atom with a non-coulomb central field. part ii. some results and discussion. *Mathematical Proceedings of the Cambridge Philosophical Society*, 24(1):111–132, 1928.

[58] Erin R. Johnson and Axel D. Becke. A post-Hartree-Fock model of intermolecular interactions: Inclusion of higher-order corrections. *The Journal of Chemical Physics*, 124(17):174104, 2006.

[59] P. Hohenberg and W. Kohn. Inhomogeneous electron gas. *Physics Review*, 136:B864–B871, 1964.

[60] C.C.M. Rindt and S.V. Gaastra-Nedea. 15 - modeling thermochemical reactions in thermal energy storage systems. In Luisa F. Cabeza, editor, *Advances in Thermal Energy Storage Systems*, Woodhead Publishing Series in Energy, pages 375–415. Woodhead Publishing, 2015.

[61] W. Kohn and L. J. Sham. Self-consistent equations including exchange and correlation effects. *Physics Review*, 140:A1133–A1138, 1965.

[62] Lin Lin, Jianfeng Lu, and Lexing Ying. Numerical methods for kohn–sham density functional theory. *Acta Numerica*, 28:405–539, 2019.

[63] Miguel A.L. Marques, Micael J.T. Oliveira, and Tobias Burnus. Libxc: A library of exchange and correlation functionals for density functional theory. *Computer Physics Communications*, 183(10):2272–2281, 2012.

[64] Julien Toulouse. *Review of Approximations for the Exchange-Correlation Energy in Density-Functional Theory*, pages 1–90. Springer International Publishing, Cham, 2023.

[65] M. T. Entwistle, M. Casula, and R. W. Godby. Comparison of local density functionals based on electron gas and finite systems. *Physics Review B*, 97:235143, 2018.

[66] D. M. Ceperley and B. J. Alder. Ground state of the electron gas by a stochastic method. *Physics Review Letters*, 45:566–569, 1980.

[67] John P. Perdew, J. A. Chevary, S. H. Vosko, Koblar A. Jackson, Mark R. Pederson, D. J. Singh, and Carlos Fiolhais. Atoms, molecules, solids, and surfaces: Applications of the generalized gradient approximation for exchange and correlation. *Physics Review B*, 46:6671–6687, 1992.

[68] P. Ziesche, H. Eschrig, Technische Universität Dresden. Institut für Theoretische Physik, and European Physical Society. *Electronic Structure of Solids '91: Proceedings of the 75. WE-Heraeus-Seminar and 21st Annual International Symposium on Electronic Structure of Solids Held in Gaussig (Germany), March 11-15, 1991*. Physical research. Walter de Gruyter GmbH, 1991.

[69] John P. Perdew, Kieron Burke, and Matthias Ernzerhof. Generalized Gradient Approximation Made Simple. *Physics Review Letters*, 77:3865–3868, 1996.

[70] Yingkai Zhang and Weitao Yang. Comment on "Generalized Gradient Approximation Made Simple". *Physics Review Letters*, 80:890, 1998.

[71] Mike Towler. Self-interaction in DFT; via vallico.net, Apuan Alps Centre for Physics.

[72] Junwei Lucas Bao, Laura Gagliardi, and Donald G. Truhlar. Self-Interaction Error in Density Functional Theory: An Appraisal. *The Journal of Physical Chemistry Letters*, 9(9):2353–2358, 2018.

[73] J Hubbard. Electron correlations in narrow energy bands. *Proceedings of the Royal Society of London. Series A. Mathematical and Physical Sciences*, 276(1365):238–257, 1963.

[74] Matteo Cococcioni and Stefano de Gironcoli. Linear response approach to the calculation of the effective interaction parameters in the LDA+U method. *Physics Review B*, 71:035105, 2005.

[75] S. L. Dudarev, G. A. Botton, S. Y. Savrasov, C. J. Humphreys, and A. P. Sutton. Electron-energy-loss spectra and the structural stability of nickel oxide: An LSDA+U study. *Physics Review B*, 57:1505–1509, 1998.

[76] Yue-Chao Wang, Ze-Hua Chen, and Hong Jiang. The local projection in the density functional theory plus u approach: A critical assessment. *The Journal of Chemical Physics*, 144(14):144106, 04 2016.

[77] Auguste Bravais. Systems formed by points distributed regularly on a plane or in space. *Crystallographic Society of America*, pages 1–128, 1850.

[78] N. W. Ashcroft and N. D. Mermin. *Solid State Physics*. Holt-Saunders, 1976.

[79] J.M. Martínez-Duart, R.J. Martín-Palma, and F. Agulló-Rueda. Chapter 2 - survey of solid state physics. In J.M. Martínez-Duart, R.J. Martín-Palma, and F. Agulló-Rueda, editors, *Nanotechnology for Microelectronics and Optoelectronics*, European Materials Research Society Series, pages 21–53. Elsevier, Amsterdam, 2006.

[80] Hong Jiang and Huai-Yang Sun. Chapter 2 - density-functional theory. In Pavlo O. Dral, editor, *Quantum Chemistry in the Age of Machine Learning*, pages 27–65. Elsevier, 2023.

[81] Kamal Choudhary and Francesca Tavazza. Convergence and machine learning predictions of monkhorst-pack k-points and plane-wave cut-off in high-throughput dft calculations. *Computational Materials Science*, 161:300–308, 2019.

[82] Richard M. Martin. *Electronic Structure: Basic Theory and Practical Methods*. Cambridge University Press, 2020.

[83] Prasanta K. Misra. Chapter 1 - basic properties of crystals. In Prasanta K. Misra, editor, *Physics of Condensed Matter*, pages 1–35. Academic Press, Boston, 2012.

[84] Wenhao Sun and Gerbrand Ceder. Efficient creation and convergence of surface slabs. *Surface Science*, 617:53–59, 2013.

[85] Hendrik J. Monkhorst and James D. Pack. Special points for Brillouin-zone integrations. *Physics Review B*, 13:5188–5192, 1976.

[86] Victor Wen-zhe Yu, Jonathan Moussa, and Volker Blum. Accurate frozen core approximation for all-electron density-functional theory. *The Journal of Chemical Physics*, 154(22):224107, 2021.

[87] P. E. Blöchl. Projector augmented-wave method. *Physics Review B*, 50:17953–17979, 1994.

[88] Marc Torrent, François Jollet, François Bottin, Gilles Zérah, and Xavier Gonze. Implementation of the projector augmented-wave method in the abinit code: Application to the study of iron under pressure. *Computational Materials Science*, 42(2):337–351, 2008.

[89] Soner Steiner, Sergii Khmelevskyi, Martijn Marsmann, and Georg Kresse. Calculation of the magnetic anisotropy with projected-augmented-wave methodology and the case study of disordered FeCo alloys. *Physics Review B*, 93:224425, 2016.

[90] Paul Strange. *Relativistic Quantum Mechanics: With Applications in Condensed Matter and Atomic Physics*. Cambridge University Press, 1998.

[91] Christof Keebaugh, Emily Marshman, and Chandralekha Singh. Improving student understanding of corrections to the energy spectrum of the hydrogen atom for the zeeman effect. *Physical Review Physics Education Research*, 15:010113, 2019.

[92] Amin Mirzai and Aylin Ahadi. First-principles study of luminescence and electronic properties of Ce-doped Y_2SiO_5. *The Journal of Chemical Physics*, 159(16):164301, 2023.

[93] Christoph Van Wüllen. Spin densities in two-component relativistic density functional calculations: Noncollinear versus collinear approach. *Journal of computational chemistry.*, 23(8):779–785, 2002.

[94] Viktor N. Staroverov and Ernest R. Davidson. A density functional method for degenerate spin-multiplet components. *Chemical Physics Letters*, 340(1):142–150, 2001.

[95] Fatima, Yangchao Liao, Sara A. Tolba, Luis Alberto Ruiz Pestana, and Wenjie Xia. Chapter one - electronic structure and density functional theory.

In Wenjie Xia and Luis Alberto Ruiz Pestana, editors, *Fundamentals of Multiscale Modeling of Structural Materials*, pages 3–35. Elsevier, 2023.

[96] T. Miyagi, X. Cao, R. Seutin, S. Bacca, R. F. Garcia Ruiz, K. Hebeler, J. D. Holt, and A. Schwenk. Impact of two-body currents on magnetic dipole moments of nuclei. *Physical Review Letters*, 132:232503, 2024.

[97] Pawel Gruszecki, Chandrima Banerjee, Michal Mruczkiewicz, Olav Hellwig, Anjan Barman, and Maciej Krawczyk. Chapter two - the influence of the internal domain wall structure on spin wave band structure in periodic magnetic stripe domain patterns. In Robert E. Camley and Robert L. Stamps, editors, *Solid State Physics*, volume 72 of *Solid State Physics*, pages 29–82. Academic Press, 2021.

[98] Freeman J. Dyson, Elliott H. Lieb, and Barry Simon. Phase transitions in the quantum heisenberg model. *Physical Review Letters*, 37:120–123, 1976.

[99] T. Werlang and Gustavo Rigolin. Thermal and magnetic quantum discord in heisenberg models. *Physical Review A*, 81:044101, 2010.

[100] Alexander G Gavriliuk, Viktor V Struzhkin, Anna G Ivanova, Vitali B Prakapenka, Anna A Mironovich, Sergey N Aksenov, Ivan A Troyan, and Wolfgang Morgenroth. The first-order structural transition in NiO at high pressure. *Commun. Phys.*, 6(1), January 2023.

[101] Edmund C. Stoner. Collective electron ferromagnetism. *Proceedings of the Royal Society of London. Series A. Mathematical and Physical Sciences*, 165(922):372–414, 1938.

[102] Gernot Stollhoff, Andrzej M. Oleś, and Volker Heine. Stoner exchange interaction in transition metals. *Physical Review B*, 41:7028–7041, 1990.

[103] K. Fabian, V. P. Shcherbakov, and S. A. McEnroe. Measuring the curie temperature. *Geochemistry, Geophysics, Geosystems*, 14(4):947–961, 2013.

[104] N.V. Khiem, P.T. Phong, L.V. Bau, D.N.H. Nam, L.V. Hong, and N.X. Phuc. Critical parameters near the ferromagnetic–paramagnetic phase transition in la0.7a0.3(mn1xbx)o3 (a=sr; b=ti and al; x=0.0 and 0.05) compounds. *Journal of Magnetism and Magnetic Materials*, 321(13):2027–2031, 2009.

[105] J. Valenta, F. Honda, M. Valiska, P. Opletal, J. Kastil, M. Misek, M. Divis, L. Sandratskii, J. Prchal, and V. Sechovsky. Antiferromagnetism and phase transitions in noncentrosymmetric $UIrSi_3$. *Physical Review B*, 97:144423, 2018.

[106] Steven H. Simon. Chapter 20 - spontaneous magnetic order: Ferro-, anti-ferro, and ferri-magnetism. In Mark Holborn and Marvin Heiferman, editors, *Oxford Solid State Basics*, pages 223–231. Oxford University Press, Oxford, 2013.

[107] Nina Kostevšek and Igor Serša. Chapter nine - characterization of metal-based nanoparticles as contrast agents for magnetic resonance imaging. In Radmila Milačič, Janez Ščančar, Heidi Goenaga-Infante, and Janja Vidmar, editors, *Analysis and Characterisation of Metal-Based Nanomaterials*, volume 93 of *Comprehensive Analytical Chemistry*, pages 303–343. Elsevier, 2021.

[108] Giorgio Bertotti. Chapter 5 - exchange and anisotropy. In Giorgio Bertotti, editor, *Hysteresis in Magnetism*, Electromagnetism, pages 129–162. Academic Press, San Diego, 1998.

[109] Ralph Skomski. *Simple Models of Magnetism*. Oxford University Press, 2008.

[110] Jack B. Collings, Ricardo Rama-Eiroa, Ruben M. Otxoa, Richard F. L. Evans, and Roy W. Chantrell. Generalized form of the magnetic anisotropy field in micromagnetic and atomistic spin models. *Phys. Rev. B*, 107:064413, 2023.

[111] Jiaxuan Wang, Hui Dong, and Sheng-Wen Li. Magnetic dipole-dipole interaction induced by the electromagnetic field. *Physical Review A*, 97:013819, 2018.

[112] A. Schrön, C. Rödl, and F. Bechstedt. Crystalline and magnetic anisotropy of the 3*d*-transition metal monoxides MnO, FeO, CoO, and NiO. *Physics Review B*, 86:115134, 2012.

[113] John David Jackson. *Classical electrodynamics; 2nd ed.* Wiley, New York, NY, 1975.

[114] I. Dzyaloshinsky. A thermodynamic theory of “weak” ferromagnetism of antiferromagnetics. *Journal of Physics and Chemistry of Solids*, 4(4):241–255, 1958.

[115] Tôru Moriya. Anisotropic superexchange interaction and weak ferromagnetism. *Physics Review*, 120:91–98, 1960.

[116] Hua Chen, Tzu-Cheng Wang, Di Xiao, Guang-Yu Guo, Qian Niu, and Allan H. MacDonald. Manipulating anomalous hall antiferromagnets with magnetic fields. *Physics Review B*, 101:104418, 2020.

[117] A. Kohn, A. Kovács, R. Fan, G. J. McIntyre, R. C. C. Ward, and J. P. Goff. The antiferromagnetic structures of $\mathrm{IrMn_3}$ and their influence on exchange-bias. *Scientific Reports*, 3(1):2412, 2013.

[118] Yang Zhang, Yan Sun, Hao Yang, Jakub Železný, Stuart P. P. Parkin, Claudia Felser, and Binghai Yan. Strong anisotropic anomalous Hall effect and spin Hall effect in the chiral antiferromagnetic compounds $\mathrm{Mn_3Ge}$, Sn, Ga, Ir, Rh, and Pt). *Physics Review B*, 95:075128, 2017.

[119] Jose Mario Galicia Hernandez, J. Guerrero-Sanchez, R. Ponce-Perez, and Noboru Takeuchi. Assessing the stability of Kagome D019-Mn3Ga (0001) surfaces: A first-principles study. *Surfaces and Interfaces*, 41:103167, 2023.

[120] Zhongping Zhao, Qi Guo, Fenghua Chen, Kewei Zhang, and Yong Jiang. Magnetic properties and anomalous Hall effect in antiferromagnetic $\mathrm{Mn_3Sn}$ films. *Physica B: Condensed Matter*, 604:412692, 2021.

[121] J Cumings, L J Heyderman, C H Marrows, and R L Stamps. Focus on artificial frustrated systems. *New Journal of Physics*, 16(7):075016, 2014.

[122] Claudine Lacroix, Philippe Mendels, and Frédéric Mila. *Introduction to Frustrated Magnetism: Materials, Experiments, Theory*. Springer Berlin Heidelberg, 2011.

[123] Peiyu Cai, Wenmiao Chen, Gregory S. Day, Hannah F. Drake, Elizabeth A. Joseph, Zachary T. Perry, Zhifeng Xiao, and Hong-Cai Zhou. 2.03 - metal-organic frameworks: New functional materials and applications. In David L. Andrews, Robert H. Lipson, and Thomas Nann, editors, *Comprehensive Nanoscience and Nanotechnology (Second Edition)*, pages 35–54. Academic Press, Oxford, second edition edition, 2019.

[124] Roderich Moessner and Arthur P. Ramirez. Geometrical frustration. *Physics Today*, 59(2):24–29, 2006.

[125] David Billington et al. Magnetic frustration, short-range correlations and the role of the paramagnetic Fermi surface of $PdCrO_2$. *Scientific Reports*, 5(1):12428, 2015.

[126] E. F. Bertaut, R. Pauthenet, and M. Mercier. Proprietes magnetiques et structures du manganite d'yttrium. *Physics Letters*, 7(2):110–111, 1963.

[127] Kari Selte, A. Kjekshus, A. F. Andresen, and W. B. Pearson. Equiatomic Transition Metal Alloys of Manganese. VII. A Neutron Diffraction Study of Magnetic Ordering in the IrMn Phase. *Acta Chemica Scandinavica*, 22(9):3039–3042, 1968.

[128] L. Pál, E. Krén, G. Kádár, P. Szabó, and T. Tarnóczi. Magnetic Structures and Phase Transformations in Mn-Based CuAu-I Type Alloys. *Journal of Applied Physics*, 39(2):538–544, 2008.

[129] Suguru Sato, Shuichiro Irie, Yuki Nagamine, Takashi Miyazaki, and Yuji Umeda. Antiferromagnetism in perfectly ordered $L1_0$-MnAl with stoichiometric composition and its mechanism. *Scientific Reports*, 10(1):12489, 2020.

[130] R. Y. Umetsu, M. Miyakawa, K. Fukamichi, and A. Sakuma. Pseudogap in the density of states and the highest Néel temperature of the $L1_0$-type MnIr alloy system. *Physical Review B*, 69(10):104411, 2004.

[131] Yutaro Takeuchi, Ryotaro Okuda, Junta Igarashi, Butsurin Jinnai, Takaharu Saino, Shoji Ikeda, Shunsuke Fukami, and Hideo Ohno. Nanometer-thin L1-MnAl film with B2-CoAl underlayer for high-speed and high-density STT-MRAM: Structure and magnetic properties. *Applied Physics Letters*, 120(5):052404, 2022.

[132] Zhengying Jiao, Jingmin Wang, Zhongheng Fu, Ruifeng Zhang, and Chengbao Jiang. Magnetocrystalline anisotropy regulations in bulk $L1_0$-MnGa alloys by tailoring the tetragonal lattice parameter c: Selectively alloying Al and C atoms. *Journal of Alloys and Compounds*, 881:160646, 2021.

[133] Danica Solina, Wolfgang Schmidt, Rainer Kaltofen, Cornelia Krien, Chih-Huang Lai, and Andreas Schreyer. The magnetic structure of $L1_0$ ordered

MnPt at room temperature determined using polarized neutron diffraction. *Materials Research Express*, 6(7):076105, 2019.

[134] J. P. Corbett, J. Guerrero-Sanchez, A. L. Richard, D. C. Ingram, N. Takeuchi, and A. R. Smith. Surface structures of L10-MnGa (001) by scanning tunneling microscopy and first-principles theory. *Applied Surface Science*, 422:985–989, 2017.

[135] X. P. Zhao, J. Lu, S. W. Mao, Z. F. Yu, D. H. Wei, and J. H. Zhao. Spontaneous perpendicular exchange bias effect in L1-MnGa/FeMn bilayers grown by molecular-beam epitaxy. *Applied Physics Letters*, 112(4):042403, 2018.

[136] Y. J. Tang et al. Structure and magnetic properties of exchange-biased polycrystalline Fe/MnPd bilayers. *Physical Review B*, 62(13):8654–8657, 2000. PRB.

[137] Nicolas Josten, Sakia Noorzayee, Olga Miroshkina, Benjamin Zingsem, Mehmet Acet, Ulf Wiedwald, Aslı Çakır, Markus E. Gruner, and Michael Farle. Emergence of net magnetization by magnetic field biased diffusion in antiferromagnetic $L1_0$ NiMn. *Physical Review B*, 107(17):174417, 2023. PRB.

[138] N. L. Lethole, P. Mukumba, and G. Makaka. First-principles calculations to investigate magnetic, electronic, mechanical and dynamical properties of the bimetallic M-Pt (M: Mn, Co, and Ni) alloys. *Journal of Magnetism and Magnetic Materials*, 565:170298, 2023.

[139] John P. Perdew, Adrienn Ruzsinszky, Gábor I. Csonka, Oleg A. Vydrov, Gustavo E. Scuseria, Lucian A. Constantin, Xiaolan Zhou, and Kieron Burke. Restoring the Density-Gradient Expansion for Exchange in Solids and Surfaces. *Physics Review Letters*, 100:136406, 2008.

[140] R. Armiento and A. E. Mattsson. Functional designed to include surface effects in self-consistent density functional theory. *Physics Review B*, 72:085108, 2005.

[141] Ann E. Mattsson, Rickard Armiento, Joachim Paier, Georg Kresse, John M. Wills, and Thomas R. Mattsson. The AM05 density functional applied to solids. *The Journal of Chemical Physics*, 128(8):084714, 2008.

[142] Ann E. Mattsson and Rickard Armiento. Implementing and testing the AM05 spin density functional. *Physics Review B*, 79:155101, 2009.

[143] Jianwei Sun, Adrienn Ruzsinszky, and John P. Perdew. Strongly Constrained and Appropriately Normed Semilocal Density Functional. *Physics Review Letters*, 115:036402, 2015.

[144] Albert P. Bartók and Jonathan R. Yates. Regularized SCAN functional. *The Journal of Chemical Physics*, 150(16):161101, 2019.

[145] Jianwei Sun, Martijn Marsman, Gábor I. Csonka, Adrienn Ruzsinszky, Pan Hao, Yoon-Suk Kim, Georg Kresse, and John P. Perdew. Self-consistent meta-generalized gradient approximation within the projector-augmented-wave method. *Physics Review B*, 84:035117, 2011.

[146] Jianmin Tao, John P. Perdew, Viktor N. Staroverov, and Gustavo E. Scuseria. Climbing the Density Functional Ladder: Nonempirical Meta–Generalized Gradient Approximation Designed for Molecules and Solids. *Physics Review Letters*, 91:146401, 2003.

[147] John P. Perdew, Jianmin Tao, Viktor N. Staroverov, and Gustavo E. Scuseria. Meta-generalized gradient approximation: Explanation of a realistic nonempirical density functional. *The Journal of Chemical Physics*, 120(15):6898–6911, 2004.

[148] Yan Zhao and Donald G. Truhlar. A new local density functional for main-group thermochemistry, transition metal bonding, thermochemical kinetics, and noncovalent interactions. *The Journal of Chemical Physics*, 125(19):194101, 2006.

[149] Shogo Yamashita and Akimasa Sakuma. Study of ground state magnetic structure of L10-type MnAl via spin-spiral density wave. *Applied Physics Express*, 16(8):083002, 2023.

[150] Lijun Zhu and Jianhua Zhao. Perpendicularly magnetized $\mathrm{Mn}_x\mathrm{Ga}$ films: promising materials for future spintronic devices, magnetic recording and permanent magnets. *Applied Physics A*, 111(2):379–387, 2013.

[151] Zhengying Jiao, Zhongheng Fu, Jingmin Wang, Ruifeng Zhang, and Chengbao Jiang. Uniaxial magnetocrystalline anisotropy of tetragonal $\mathrm{Mn}_x\mathrm{Ga}_{100-x}$ (50x75) alloys. *Journal of Magnetism and Magnetic Materials*, 489:165308, 2019.

[152] Marília Silva, Diana C. Leitao, Susana Cardoso, and Paulo Freitas. MnNi-based spin valve sensors combining high thermal stability, small footprint and pTesla detectivities. *AIP Advances*, 8(5):056644, 2018.

[153] José T. Holguín-Momaca, Christian J. Muñoz-Carnero, Himanshu Sharma, Carlos R. Santillán-Rodríguez, José A. Matutes-Aquino, C.V. Tomy, and Sion F. Olive-Méndez. Tuning the ferromagnetism of epitaxial-strained $D0_{19}$-Mn_3Ga thin films. *Journal of Magnetism and Magnetic Materials*, 471:329–333, 2019.

[154] J Kubler, K H Hock, J Sticht, and A R Williams. Density functional theory of non-collinear magnetism. *Journal of Physics F: Metal Physics*, 18(3):469, 1988.

[155] Ronald Wiesendanger. Noncollinear spins, via Nanostructure and Solid State Physics: Universität Hamburg, 2020.

[156] A.T. Melo, D.M.S. Brito, A.F. Lima, and M.V. Lalic. Non-collinear spin DFT study of the ground state magnetic structure, optical and electronic properties of the hexagonal $LuFeO_3$ multiferroic. *Journal of Alloys and Compounds*, 813:152227, 2020.

[157] T. Nan et al. Controlling spin current polarization through non-collinear antiferromagnetism. *Nature Communications*, 11(1):4671, 2020.

[158] M.-T. Suzuki, T. Koretsune, M. Ochi, and R. Arita. Cluster multipole theory for anomalous Hall effect in antiferromagnets. *Physics Review B*, 95:094406, 2017.

[159] Fanghai Hu et al. Tunable magnetic and transport properties of Mn_3Ga thin films on Ta/Ru seed layer. *Journal of Applied Physics*, 123:103902, 2018.

[160] Xiaolei Wang, Chen Zhang, Qianqian Yang, Lei Liu, Dong Pan, Xue Chen, Jinxiang Deng, Tianrui Zhai, and Hui-Xiong Deng. Manipulation of crystalline structure, magnetic performance, and topological feature in Mn_3Ge films. *APL Materials*, 9(11):111107, 2021.

[161] Shinji Miwa, Satoshi Iihama, Takuya Nomoto, Takahiro Tomita, Tomoya Higo, Muhammad Ikhlas, Shoya Sakamoto, Yoshi Chika Otani, Shigemi Mizukami, Ryotaro Arita, et al. Giant effective damping of octupole oscillation in an antiferromagnetic weyl semimetal. *Small Science*, 1(5):2000062, 2021.

[162] Takahiro Ogasawara, Jun young Kim, Yasuo Ando, and Atsufumi Hirohata. Structural and antiferromagnetic characterization of noncollinear $D0_{19}$ Mn_3Ge polycrystalline film. *Journal of Magnetism and Magnetic Materials*, 473:7–11, 2019.

[163] Y. Chen et al. Antichiral spin order, its soft modes, and their hybridization with phonons in the topological semimetal Mn_3Ge. *Physics Review B*, 102:054403, 2020.

[164] A. Markou, J. M. Taylor, A. Kalache, P. Werner, S. S. P. Parkin, and C. Felser. Noncollinear antiferromagnetic Mn_3Sn films. *Physics Review Mater.*, 2:051001, 2018.

[165] James M. Taylor et al. Epitaxial growth, structural characterization, and exchange bias of noncollinear antiferromagnetic Mn_3Ir thin films. *Physics Review Materials*, 3:074409, 2019.

[166] Haokaifeng Wu, Iori Sudoh, Ruihan Xu, Wenshuo Si, C A Vaz, Jun-young Kim, Gonzalo Vallejo-Fernandez, and Atsufumi Hirohata. Large exchange bias induced by polycrystalline Mn_3Ga antiferromagnetic films with controlled layer thickness. *Journal of Physics D: Applied Physics*, 51:215003, 2018.

[167] Y.S. Liu, H. Xiao, A.B. Yu, Y.F. Wu, K. Manna, Claudia Felser, C.M. Schneider, Hong-Yi Xie, and T. Hu. Probing magnetic anisotropy in Kagome antiferromagnetic Mn_3Ge with torque magnetometry. *Journal of Magnetism and Magnetic Materials*, 563:170018, 2022.

[168] Ajaya K. Nayak et al. Large anomalous Hall effect driven by a nonvanishing Berry curvature in the noncolinear antiferromagnet Mn_3Ge. *Science Advances*, 2(4):e1501870, 2016.

[169] Z. H. Liu, Y. J. Zhang, G. D. Liu, B. Ding, E. K. Liu, Hasnain Mehdi Jafri, Z. P. Hou, W. H. Wang, X. Q. Ma, and G. H. Wu. Transition from Anomalous Hall Effect to Topological Hall Effect in Hexagonal Non-Collinear Magnet Mn_3Ga. *Scientific Reports*, 7(1):515, 2017.

[170] Satoru Nakatsuji, Naoki Kiyohara, and Tomoya Higo. Large anomalous hall effect in a non-collinear antiferromagnet at room temperature. *Nature*, 527(7577):212–215, 2015.

[171] Hao Yang, Yan Sun, Yang Zhang, Wu-Jun Shi, Stuart S P Parkin, and Binghai Yan. Topological Weyl semimetals in the chiral antiferromagnetic materials Mn3Ge and Mn3Sn. *New Journal of Physics*, 19(1):015008, 2017.

[172] Subhadip Pradhan, Kartik Samanta, Kush Saha, and Ashis K. Nandy. Vector-chirality driven topological phase transitions in noncollinear antiferromagnets and its impact on anomalous Hall effect, 2023.

[173] P. Brown, V Nunez, F Tasset, J Forsyth, and P Radhakrishna. Determination of the magnetic structure of Mn3Sn using generalized neutron polarization analysis. *Journal of Physics: Condensed Matter*, 2(47):9409, 1990.

[174] Jiahui Liu et al. The anomalous Hall effect controlled by residual epitaxial strain in antiferromagnetic Weyl semimetal Mn_3Sn thin films grown by molecular beam epitaxy. *Results in Physics*, 52:106803, 2023.

[175] Deshun Hong, Changjiang Liu, Jianguo Wen, Qianheng Du, Brandon Fisher, J. S. Jiang, John E. Pearson, and Anand Bhattacharya. Synthesis of antiferromagnetic Weyl semimetal Mn3Ge on insulating substrates by electron beam assisted molecular beam epitaxy. *APL Materials*, 10(10):101113, 2022.

[176] Deshun Hong, Naween Anand, Changjiang Liu, Haihua Liu, Ilke Arslan, John E. Pearson, Anand Bhattacharya, and J. S. Jiang. Large anomalous Nernst and inverse spin-Hall effects in epitaxial thin films of kagome semimetal Mn_3Ge. *Physics Review Mater.*, 4:094201, 2020.

[177] Idris Opeyemi Olayiwola, Carlos R. Santillán-Rodríguez, José A. Matutes-Aquino, Isis M. Cota-Martínez, Rocío M. Gutiérrez-Pérez, José T. Holguín-Momaca, and Sion F. Olive-Méndez. Room temperature positive exchange bias in CoFeB/$D0_{19}$-Mn_3Ge noncollinear antiferromagnetic thin films. *Journal of Alloys and Compounds*, 955:170279, 2023.

[178] James M. Taylor, Anastasios Markou, Edouard Lesne, Pranava Keerthi Sivakumar, Chen Luo, Florin Radu, Peter Werner, Claudia Felser, and Stuart S. P. Parkin. Anomalous and topological Hall effects in epitaxial thin films of the noncollinear antiferromagnet Mn_3Sn. *Physics Review B*, 101:094404, 2020.

[179] N. P. Armitage, E. J. Mele, and Ashvin Vishwanath. Weyl and dirac semimetals in three-dimensional solids. *Review of Modern Physics*, 90:015001, 2018.

[180] Hao Yang, Yan Sun, Yang Zhang, Wu-Jun Shi, Stuart S P Parkin, and Binghai Yan. Topological weyl semimetals in the chiral antiferromagnetic materials Mn3Ge and Mn3Sn. *New Journal of Physics*, 19(1):015008, 2017.

[181] Zoltán Scherübl and et al. Observation of spin–orbit coupling induced weyl points in a two-electron double quantum dot. *Communications Physics*, 2(1), 2019.

[182] Pan Xiong et al. Strain engineering of two-dimensional multilayered heterostructures for beyond-lithium-based rechargeable batteries. *Nature Communications*, 11(1):3297, 2020.

[183] M. Farkous et al. Strain effects on the electronic and optical properties of Van der Waals heterostructure MoS_2/WS_2: A first-principles study. *Physica E: Low-dimensional Systems and Nanostructures*, 116:113799, 2020.

[184] Huiling Mao, Yuta Sasaki, Yuta Kobayashi, Shinji Isogami, Teruo Ono, Takahiro Moriyama, Yukiko K. Takahashi, and Kihiro T. Yamada. Ultrafast spin-to-charge conversion in antiferromagnetic [111]-oriented $L1_2$-Mn_3Ir. *Applied Physics Letters*, 123(21):212401, 2023.

[185] H. Kurt, K. Rode, H. Tokuc, P. Stamenov, M. Venkatesan, and J. M. D. Coey. Exchange-biased magnetic tunnel junctions with antiferromagnetic E-Mn_3Ga. *Applied Physics Letters*, 101(23):232402, 2012.

[186] E. Krén and G. Kádár. Neutron diffraction study of Mn3Ga. *Solid State Communications*, 8(20):1653–1655, 1970.

[187] V. Rai, S. Jana, M. Meven, R. Dutta, J. Persson, and S. Nandi. Unconventional magnetoresistance and electronic transition in Mn_3Ge Weyl semimetal. *Physics Review B*, 106:195114, 2022.

[188] S. Sakamoto, T. Higo, M. Shiga, K. Amemiya, S. Nakatsuji, and S. Miwa. Observation of spontaneous x-ray magnetic circular dichroism in a chiral antiferromagnet. *Physics Review B*, 104:134431, 2021.

[189] Xiaoyan Yang, Yi Qiu, Jie Su, Yalei Huang, Jincang Zhang, Xiao Liang, and Guixin Cao. Coexistence of in-plane and out-of-plane exchange bias in correlated kagome antiferromagnet mn3- xcrxsn, 2022.

[190] T. F. Duan, W. J. Ren, W. L. Liu, S. J. Li, W. Liu, and Z. D. Zhang. Magnetic anisotropy of single-crystalline Mn_3Sn in triangular and helix-phase states. *Applied Physics Letters*, 107(8):082403, 2015.

[191] Achintya Low, Susanta Ghosh, Susmita Changdar, Sayan Routh, Shubham Purwar, and S. Thirupathaiah. Tuning of topological properties in the strongly correlated antiferromagnet Mn_3Sn via Fe doping. *Physics Review B*, 106:144429, 2022.

[192] N. H. Sung, F. Ronning, J. D. Thompson, and E. D. Bauer. Magnetic phase dependence of the anomalous Hall effect in Mn_3Sn single crystals. *Applied Physics Letters*, 112(13):132406, 2018.

[193] J. S. R. McCoombs et al. Giant anomalous Hall effect in epitaxial $Mn_{3.2}Ge$ films with a cubic kagome structure, 2023.

[194] Charanpreet Singh, Vikram Singh, Gyandeep Pradhan, Velaga Srihari, Himanshu Kumar Poswal, Ramesh Nath, Ashis K. Nandy, and Ajaya K. Nayak. Pressure controlled trimerization for switching of anomalous Hall effect in triangular antiferromagnet Mn_3Sn. *Physics Review Research*, 2:043366, 2020.

[195] Charmaine Chia, Stefanie S. Jeffrey, and Roger T. Howe. Scalable methods for ultra-smooth platinum in nanoscale devices. *Micro and Nano Engineering*, 3:50–58, 2019.

[196] Enrique G. Marin, Damiano Marian, Marta Perucchini, Gianluca Fiori, and Giuseppe Iannaccone. Lateral heterostructure field-effect transistors based on two-dimensional material stacks with varying thickness and energy filtering source. *ACS Nano*, 14(2):1982–1989, 2020.

[197] Higo Tomoya et al. Perpendicular full switching of chiral antiferromagnetic order by current. *Nature*, 607(7919):474–479, 2022.

[198] E. Z. Zhang, Y. C. Deng, X. H. Liu, X. Z. Zhan, T. Zhu, and K. Y. Wang. Manipulating antiferromagnetic interfacial states by spin-orbit torques. *Physics Review B*, 104:134408, 2021.

[199] X. H. Liu, K. W. Edmonds, Z. P. Zhou, and K. Y. Wang. Tuning Interfacial Spins in Antiferromagnetic/Ferromagnetic/Heavy-Metal Heterostructures via Spin-Orbit Torque. *Physics Review Applied*, 13:014059, 2020.

[200] Xionghua Liu, Dong Zhang, Yongcheng Deng, Nai Jiang, Enze Zhang, Chao Shen, Kai Chang, and Kaiyou Wang. Tunable spin textures in a kagome antiferromagnetic semimetal via symmetry design. *ACS Nano*, 18(1):1013–1021, 2024.

[201] Xiaolei Wang et al. Investigating the strain controlled epitaxial growth of Mn_3Ge films through thickness modulation. *Applied Surface Science*, 602:154247, 2022.

[202] Nai Jiang, Yongcheng Deng, Xionghua Liu, Dong Zhang, Enze Zhang, Houzhi Zheng, Kai Chang, Chao Shen, and Kaiyou Wang. Variable spin texture in Mn3Sn/Pt heterostructures revealed by magnetic circular dichroism. *Applied Physics Letters*, 123(7):072401, 2023.

[203] Sophie F. Weber, Andrea Urru, Sayantika Bhowal, Claude Ederer, and Nicola A. Spaldin. Surface magnetization in antiferromagnets: Classification, example materials, and relation to magnetoelectric responses. *Physics Review X*, 14:021033, 2024.

[204] Chuen-Keung Sin, Jingzhao Zhang, Kinfai Tse, and Junyi Zhu. A brief review of formation energies calculation of surfaces and edges in semiconductors. *Journal of Semiconductors*, 41(6):061101, 2020.

[205] R.F.W. Bader and R.F. Bader. *Atoms in Molecules- A Quantum Theory*. International series of monographs on chemistry. Clarendon Press, 1990.

[206] Edward Sanville, Steven D. Kenny, Roger Smith, and Graeme Henkelman. Improved grid-based algorithm for bader charge allocation. *Journal of Computational Chemistry*, 28(5):899–908, 2007.

[207] W Tang, E Sanville, and G Henkelman. A grid-based bader analysis algorithm without lattice bias. *Journal of Physics: Condensed Matter*, 21(8):084204, 2009.

[208] Graeme Henkelman, Andri Arnaldsson, and Hannes Jónsson. A fast and robust algorithm for bader decomposition of charge density. *Computational Materials Science*, 36(3):354–360, 2006.

[209] M. Raju, Ralph Romero, Daisuke Nishio-Hamane, Ryota Uesugi, Mihiro Asakura, Zhenisbek Tagay, Tomoya Higo, N. P. Armitage, Collin Broholm, and Satoru Nakatsuji. Anisotropic anomalous transport in the kagome-based topological antiferromagnetic Mn_3Ga epitaxial thin films. *Physical Review Materials*, 8:014204, Jan 2024.

[210] Taishi Chen et al. Anomalous transport due to Weyl fermions in the chiral antiferromagnets Mn_3X, $X = Sn, Ge$. *Nature Communications*, 12(1):572, 2021.

[211] Susmita Changdar, Susanta Ghosh, Anumita Bose, Indrani Kar, Achintya Low, Patrick Le Fèvre, François Bertran, Awadhesh Narayan, and Setti Thirupathaiah. Weak electronic correlations observed in magnetic Weyl Semimetal Mn_3Ge. *Journal of Physics: Condensed Matter*, 36(12):125502, 2023.

[212] Sergii Khmelevskyi, Andrei V. Ruban, and Peter Mohn. Magnetic ordering and exchange interactions in structural modifications of mn_3ga alloys: Interplay of frustration, atomic order, and off-stoichiometry. *Physics Review B*, 93:184404, 2016.

[213] Junran Zhang, Yunhao Lu, and Yanchun Li. The structural stability of Mn_3Sn Heusler compound under high pressure. *Journal of Physics: Condensed Matter*, 36(19):195403, 2024.

[214] Yang Cheng, Sisheng Yu, Menglin Zhu, Jinwoo Hwang, and Fengyuan Yang. Tunable topological Hall effects in noncollinear antiferromagnet Mn_3Sn/Pt bilayers. *APL Materials*, 9(5):051121, 2021.

[215] Hung-Hsiang Yang, Chi-Cheng Lee, Yasuo Yoshida, Muhammad Ikhlas, Takahiro Tomita, Agustinus Nugroho, Taisuke Ozaki, Satoru Nakatsuji, and Yukio Hasegawa. Scanning tunneling microscopy on cleaved Mn_3Sn(0001) surface. *Scientific Reports*, 9(1):9677, 2019.